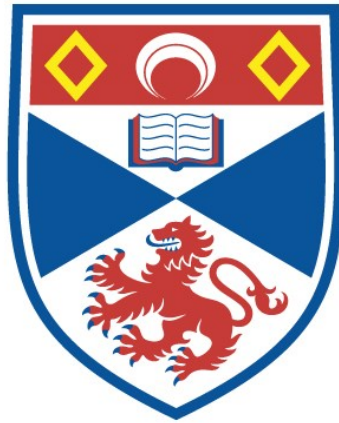


AN ASSESSMENT OF MODIS PRODUCTS IN THE
SOUTHERN OCEAN USING TAGGED SOUTHERN
ELEPHANT SEALS, IN THE CONTEXT OF AN
INCREASINGLY POSITIVE SOUTHERN ANNULAR
MODE

Lauren Biermann

A Thesis Submitted for the Degree of PhD
at the
University of St Andrews



2018

Full metadata for this item is available in
St Andrews Research Repository
at:

<http://research-repository.st-andrews.ac.uk/>

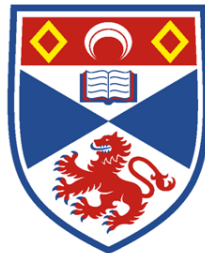
Please use this identifier to cite or link to this item:

<http://hdl.handle.net/10023/15613>

This item is protected by original copyright

AN ASSESSMENT OF MODIS PRODUCTS IN THE
SOUTHERN OCEAN USING TAGGED SOUTHERN
ELEPHANT SEALS, IN THE CONTEXT OF AN
INCREASINGLY POSITIVE SOUTHERN ANNULAR MODE

LAUREN BIERMANN



University of
St Andrews

This thesis is submitted in partial fulfilment for the degree of PhD

at the

University of St Andrews

February 2016

Lauren Biermann: *An assessment of MODIS products in the Southern Ocean using tagged southern elephant seals, in the context of an increasingly positive Southern Annular Mode* ©
February 2016

ABSTRACT

The Southern Ocean maintains a complex, dynamic marine food web based on its stock of photosynthesising phytoplankton. For the same reason, it is our most significant sink of carbon, vital to functioning of global atmospheric systems. However, this key polar ocean is also responsive to atmospheric variability dominated by the Southern Annular Mode (SAM), with unknown implications for phytoplankton patterns in space and over time.

MODIS surface chlorophyll-a concentration ([Chl-a]) and the depth of the 1% light level (Z_{eu}) were evaluated against *in situ* fluorescence and light data collected by tagged southern elephant seals. Light data were processed to minimize self-shading and environmental sources of variability, and Lee Z_{eu} outperformed Morel Z_{eu} when examined relative to the resultant *in situ* measures of the 1% light level. Based on these results, fluorescence data were corrected for quenching at the surface using Lee Z_{eu} as a reference depth; conserving deep chlorophyll maxima within hydrographically defined mixed layers. [Chl-a] was evaluated against quenching-corrected fluorescence and satellite products mirrored *in situ* trends over time.

The MODIS timeseries was interrogated for spatio-temporal shifts to phytoplankton abundance in surface waters. Trends over 13 years of austral summers point to overall declines and perturbations to the timing of the bloom, with changes that were significantly related to the SAM presenting as regional rather than annular. In this context, to assess if perturbations may impact top predators, the at-sea behaviour of tagged seals were examined relative to the fluorescence and light data they collected. Using a cumulative sums analysis of speed, foraging phases were distinguishable from 'outbound' and 'homebound' travel. When all phases were examined relative to fluorescence and the 1% light level, foraging appeared to be associated with increased phytoplankton abundance. This suggests that the future of these marine predators may be linked to shifting phytoplankton patterns.

PUBLICATIONS

Biermann, L., Guinet, C., Bester, M., Brierley, A. S., & Boehme, L. (2015). An alternative method for correcting fluorescence quenching. *Ocean Science*. DOI: doi:10.5194/os-11-83-2015.

ACKNOWLEDGMENTS

A few years ago, while I was still in sunny Cape Town and struggling to decide between getting a real job, or following a PhD dream that would see me moving to Scotland, my dad suggested I close my eyes and imagine the daily routine of each option. I think he hoped this exercise would help me realise I didn't really want another few years of imposter syndrome! However, despite that and in spite of my reluctance to leave South Africa, when I did close my eyes and think of the life ahead of me, I couldn't imagine not doing this work.

I thank my grandparents, who I miss so fiercely, for planting the seeds that grew into my love for nature and science. I gratefully acknowledge my parents who have loved and supported all the dreams that stemmed from it. Thanks to you both, I have been a black-belt, a journalist, an ichthyologist, a chemical engineer, a wetland rehabilitator, a biological oceanographer and, finally, now a doctor-in-that-thing-I-love-most.

There's also the family I adopted along the way who have made this all possible. Natalie Burls, you made me brave. Anna Versfeld, you steered me through every step of this and I couldn't have done it without you. Dearest Hayley Evers-King, Ben Loveday, Sarah Nicholson and Emily McGregor - you guys fed me cheese, fixed my code, and kept me sane. Thank you. Theoni Photopoulou, Janice Deary, Frances Trahar, Emily Davis, Toast Coetzer, Nadya Josephy-Collins and Bear, Mel Froude, AFJ and Ella Nilsen, you wonderful humans helped me survive homesickness with liberal doses of humour, adventure, excellent advice, coffee and unwavering friendship. Finally, my colleagues and friends Silje Kristen Jensen, Luca Pumpkin Lamoni, Hugh Venables, Kelly God-You Bunting, Mick Roomie Wu, Debbie Bivins, Mel Froude, Little Jo Kershaw, Hannah Wood, and team Onoufriou. Thank you for making me part of the family. I miss all your faces.

I must also thank Mike Fedak for keeping tabs on me, helping me through some tricky times, and, vitally, letting me use the coffee grinder.

Lastly, to my person and my love, Bastien PF Queste. I literally could not have done this without you.

This is a very well-travelled body of work. Chapters were written in South Africa, Scotland, England and France. Bits and pieces were tagged on in Norway, Spain, Italy and Morocco. I loved doing this work, and I enjoyed writing it up. When I look at this thesis, I am reminded of all the people and places that were part of it, and I am grateful.

This work received funding from the MASTS pooling initiative (The Marine Alliance for Science and Technology for Scotland) and their support is gratefully acknowledged. MASTS is funded by the Scottish Funding Council (grant reference HR09011) and contributing institutions. A number of field assistants were involved in the deployment of tags and I am grateful to everyone who worked so hard behind the scenes. Fluorescence and light data were generously provided by Christophe Guinet through the CEBC-CNRS, as part of the research program supported by CNES-TOSCA, ANR-VMC, Total Foundation and IPEV. The Mammal Research Institute at the University of Pretoria covered Marion Island Argos transmission costs and I thank Marthan Bester and Trevor McIntyre for facilitating this.

CONTENTS

1	INTRODUCTION	1
1.1	The Southern Ocean	1
1.2	The Southern Annular Mode	2
1.3	Phytoplankton	5
1.4	Ocean Colour	8
1.5	Elephant seals as semi-Lagrangian sampling platforms	9
1.6	In conclusion	12
1.7	PhD objectives	13
2	EVALUATING THE ACCURACY OF MODIS Z_{EU} USING <i>in situ</i> LIGHT DATA RETRIEVED BY TAGGED SOUTHERN ELEPHANT SEALS.	17
2.1	Background	17
2.2	Materials and Methods	23
2.2.1	In-situ measures of the 1% light level	23
2.2.2	MODIS Z_{eu}	31
2.3	Results	37
2.4	Discussion	42
3	CORRECTING NON-PHOTOCHEMICAL QUENCHING OF FLUORESCENCE DATA RETRIEVED BY TAGGED SOUTHERN ELEPHANT SEALS, USING MODIS LEE Z_{EU} .	55
3.1	Introduction	55
3.2	Materials and Methods	60
3.2.1	Collection of in-situ data	60
3.2.2	Satellite data	65
3.2.3	Correcting for quenching	66
3.3	Results	67
3.4	Discussion	69
4	ON THE PRESENCE AND RELEVANCE OF DEEP CHLOROPHYLL MAXIMA IN DEEPLY MIXED INDIAN SECTOR WATERS OF THE SOUTHERN OCEAN	73
4.1	Introduction	73
4.2	Methods	78

4.2.1	Calculating mixed layer depth	78
4.2.2	Resolving vertical fluorescence	78
4.2.3	Test 1: Do DCM have surface Chl-a signatures?	80
4.2.4	Are DCM associated with fronts or particular water masses?	80
4.2.5	Is fluorescence abundance related to MLD?	80
4.3	Results	81
4.4	Discussion	97
5	EVALUATING THE ACCURACY OF MODIS [CHL-A] USING VERTICALLY-INTEGRATED FLUORESCENCE DATA RETRIEVED BY TAGGED SOUTHERN ELEPHANT SEALS	101
5.1	Introduction	101
5.2	Materials and Methods	104
5.2.1	Collection of in-situ data	104
5.2.2	MODIS Chl-a data	106
5.2.3	Fluorescence data	107
5.2.4	Comparing Fluorescence and MODIS Chl-a	110
5.3	Results	110
5.4	Discussion	131
6	EVALUATING THE MODIS TIMESERIES FOR TRENDS OVER TIME, AND FOR CHANGES RELATIVE TO THE SOUTHERN ANNULAR MODE	135
6.1	Introduction	135
6.2	Methods and Materials	139
6.2.1	SAM Index	139
6.2.2	MODIS Data	140
6.2.3	Processing MODIS Data	141
6.2.4	Examining MODIS Data relative to the SAM	142
6.3	Results and Discussion	143
6.3.1	Climatologies	143
6.3.2	Trends in MODIS [Chl-a], Lee Z_{eu} and cloud fraction over time	150
6.3.3	Anomalies in MODIS [Chl-a], Lee Z_{eu} and cloud fraction relative to the SAM	158
6.4	Conclusions	176

7	FROM THE BOTTOM TO THE TOP: LINKING PHYTOPLANKTON ABUNDANCE TO FORAGING PATTERNS OF THE SOUTHERN ELEPHANT SEAL	185
7.1	Background	185
7.2	Methods	190
7.2.1	In-situ datasets	190
7.2.2	CUSUM Analysis	192
7.2.3	Spatial Division of Tracks	193
7.2.4	CUSUM Chart	193
7.2.5	Processing of the fluorescence and 1% light level data	194
7.3	Results	195
7.4	Discussion	207
8	SUMMARY	211
8.1	Context	211
8.2	Some light on the matter	212
8.3	Quenching Correction	212
8.4	Vertical Dimension and DCM	213
8.5	Horizontal dynamics	214
8.6	A changing ocean?	214
8.7	Seals and little green cells	216
8.8	Recommendations for future deployments	218
	BIBLIOGRAPHY	219

LIST OF FIGURES

- Figure 1 (a) Bathymetry of Indian and Pacific sectors of the Southern Ocean with depth in meters in greyscale, and land shown in black. (b) Mean kinetic energy ($\text{m}^2 \text{s}^{-2}$) of the ACC at a depth of 250m. Bathymetric features evident in (a), which present upstream and within boxes A-D generate the topographically-steered boundary currents, jets and eddies seen in (b). Figure from Thompson and Richards (2011). 2
- Figure 2 Atmospheric circulation in the Southern Hemisphere during the austral summer (December - February). Figure from Zheng et al. (2014). 3
- Figure 3 Circulation anomalies in the Southern Hemisphere when the SAM is positive over summer months (December - February). Figure from Zheng et al. (2014) 4
- Figure 4 Mean MODIS daytime cloud fraction for December 2014. This map illustrates how the Southern Ocean is persistently blanketed by cloud over the austral summer, with white showing 100% mean cloud coverage and black representing little to none. 20
- Figure 5 Merged composites of two MODIS Z_{eu} products, both measured in meters (m) and both 'representative' of the depth of the 1% light level. The depth of the 1% light level is shown as an 8-day merged product in the top row of figures (a) and (b). The bottom row of figures (c) and (d) represents the 1% light level for all of January 2015 (monthly product). These temporally-merged data are available as level 3 products, calculated using either the Morel et al. (2007) algorithm (first row) or the Lee et al. (2007) algorithm (second row). 22

- Figure 6 Tracks of 35 southern elephant seals (in black) tagged with light meters over the austral summers spanning 2009 to early 2015. The general positions of the Sub Antarctic Front and the Polar Front are shown in green and blue, respectively (Orsi and Harris, 2014). 24
- Figure 7 Logarithmic conversion of the light intensity measured by the TDR-MK loggers to light level values. Axes are delineated into 10 different classes of light intensity, which are representative of the range of different surface light conditions possibly experienced by the tagged seals. These range from full sunlight (highest possible light) to overcast night (lowest possible light). Figure from Jaud et al. (2012). 25
- Figure 8 Examples of *in situ* 1% light level depths collected by two instrumented elephant seals from Kerguelen with tracks coloured by the depth of the 1% light level smoothed by a moving mean with widow size = 1. Corresponding plots (a) and (b) show the unsmoothed 1% light level depth data in grey, results when smoothed using the smallest moving mean (window = 1) in blue, and smoothed by a window of 4 in red. 30
- Figure 9 Linear regression between 8-day Morel Z_{eu} and 8-day Lee Z_{eu} grouped by year. The 1:1 line is in dashed red illustrating a perfect relationship, and the true linear fit is shown by the dashed grey line. The R value, p-value and the number of datasets collected by seal per year are reported in the top left-hand corner of each plot, and the linear equation with intercept and slope are reported in bold above. 33
- Figure 10 Elephant seal track for the duration of a post-breeding summer migration (20 October 2009 - 03 January 2010). Each seal track position is shown by a light grey circle, and these empty circles are 'filled in' wherever an associated satellite-derived ocean colour value is available. Values of Morel 8-day (a) and monthly (b) Z_{eu} are plotted in the first column. Values of Lee 8-day (c) and monthly (d) Z_{eu} are plotted in the second column. 34

Figure 11 Evaluating the relationship between 8-day MODIS Lee Z_{eu} and monthly MODIS Lee Z_{eu} using a Kruskal-Wallis test (a) indicates that there is no significant difference between them (the null hypothesis of "means are equal" cannot be rejected at the 5% significance level) and supports the hypothesis that monthly MODIS data can be used to fill in gaps in the 8-day data. A linear regression (b) shows good agreement between the two datasets (693 available data points) with a significant p-value well below 0.01. The R value, p-value and the number of points available for the combined product satellite coverage are reported in the top left-hand corner of each plot, and the linear equation with intercept and slope are reported in bold above. 35

Figure 12 Evaluating the relationship between 8-day MODIS Morel Z_{eu} and monthly MODIS Morel Z_{eu} using a Kruskal-Wallis test (a) indicates that there is no significant difference between them (the null hypothesis of "means are equal" cannot be rejected at the 5% significance level) and supports the hypothesis that monthly MODIS data can be used to fill in gaps in the 8-day data. A linear regression (b) between the two datasets (693 available data points) shows good agreement with a significant p-value well below 0.01. The R value, p-value and the number of points available for the combined product satellite coverage are reported in the top left-hand corner of each plot, and the linear equation with intercept and slope are reported in bold above. 36

- Figure 13 Comparison of monthly and 8-day estimates of the 1% light level using the Morel algorithm (a) and Lee algorithm (b) over time, from all seals tagged with TDR light meters between 2009-2014. In both cases, monthly products match maximum (deepest) values in the 8-day products, but values in the 8-day products show shallower (minimum) values not equalled by monthly values. Morel's monthly and 8-day Z_{eu} values are more conservative than Lee's. For both Morel and Lee, monthly data more than double the number of measurements available for comparison with *in situ* light data. 39
- Figure 14 Linear regression between 8-day Morel Z_{eu} and the *in situ* 1% light level grouped by year. The 1:1 line is in dashed red illustrating a perfect relationship, and the true linear fit is shown by the dashed grey line. The R value, p-value and the number of datasets collected by seal per year are reported in the top left-hand corner of each plot, and the linear equation with intercept and slope are reported in bold above 40
- Figure 15 Linear regression between 8-day Lee Z_{eu} and the *in situ* 1% light level grouped by year. The 1:1 line is in dashed red illustrating a perfect relationship, and the true linear fit is shown by the dashed grey line. The R value, p-value and the number of datasets collected by seal per year are reported in the top left-hand corner of each plot, and the linear equation with intercept and slope are reported in bold above 41
- Figure 16 Differences between fit of Lee Z_{eu} and Morel Z_{eu} to *in situ* measures of the 1% light level reported using slope from linear regressions grouped on a year-by-year basis 42

- Figure 17 Boxplot of 8-day and monthly Lee Z_{eu} and Morel Z_{eu} (a). The p-value reported from the Kruskal-Wallis test indicates that there is a significant difference between Morel and Lee Z_{eu} , and the null hypothesis of "means are equal" can be rejected at the 5% significance level. When evaluated using a linear regression (b), both the fit and slope suggest a good relationship between Morel and Lee Z_{eu} . The 1:1 line is in dashed red illustrating a perfect relationship, and the true linear fit is shown by the dashed grey line. The R value, p-value and the number of data points (n) are reported in the top left-hand corner of each plot. The linear equation with intercept and slope is reported in bold above. 43
- Figure 18 Correlating maximum, median and minimum values from all thirty of the smoothed *in situ* 1% light level datasets with the maximum, median and minimum values from the unsmoothed (a) and smoothed Morel Z_{eu} (b), and unsmoothed (c) and smoothed Lee Z_{eu} (d). The dashed grey line represents the 1:1 ratio line (perfect correlation) and the red line represents a second degree polynomial fit. 44
- Figure 19 Comparison of smoothed 1% light level depths and MODIS products. Plotted over time (Nov. 2009 – Jan. 2010) and per instrumented seal (tag number reported in bold above each plot), the smoothed *in situ* 1% light level depth is shown in blue-green, and 8-day-monthly Lee Z_{eu} is shown in dark grey. A linear regression of the smoothed *in situ* data and MODIS Z_{eu} is shown with R, P and number of data points (n) reported in the top left hand corner. Points are shaded by latitude, shown by the associated colourbar. The 1:1 fit line is shown by the dashed red line and the fit of *in situ* data to satellite data is shown by the dashed grey line. The linear equation with intercept and slope is reported in bold above the regression plot. Finally, for reference, seal tracks are shown with along-track points shaded by the depth of the *in situ* 1% light level, shown by the associated colourbar. 45

Figure 20 Comparison of smoothed 1% light level depths and MODIS products. Plotted over time (Nov. 2010 – Jan. 2011) and per instrumented seal (tag number reported in bold above each plot), the smoothed *in situ* 1% light level depth is shown in blue-green, and 8-day-monthly Lee Z_{eu} is shown in dark grey. A linear regression of the smoothed *in situ* data and MODIS Z_{eu} is shown with R, P and number of data points (n) reported in the top left hand corner. Points are shaded by latitude, shown by the associated colourbar. The 1:1 fit line is shown by the dashed red line and the fit of *in situ* data to satellite data is shown by the dashed grey line. The linear equation with intercept and slope is reported in bold above the regression plot. Finally, for reference, seal tracks are shown with along-track points shaded by the depth of the *in situ* 1% light level, shown by the associated colourbar. 46

Figure 21 Comparison of smoothed 1% light level depths and MODIS products. Plotted over time (Nov. 2011 – Jan. 2012) and per instrumented seal (tag number reported in bold above each plot), the smoothed *in situ* 1% light level depth is shown in blue-green, and 8-day-monthly Lee Z_{eu} is shown in dark grey. A linear regression of the smoothed *in situ* data and MODIS Z_{eu} is shown with R, P and number of data points (n) reported in the top left hand corner. Points are shaded by latitude, shown by the associated colourbar. The 1:1 fit line is shown by the dashed red line and the fit of *in situ* data to satellite data is shown by the dashed grey line. The linear equation with intercept and slope is reported in bold above the regression plot. Finally, for reference, seal tracks are shown with along-track points shaded by the depth of the *in situ* 1% light level, shown by the associated colourbar. 47

Figure 22 Comparison of smoothed 1% light level depths and MODIS products. Plotted over time (Nov. 2012 – Jan. 2013) and per instrumented seal (tag number reported in bold above each plot), the smoothed *in situ* 1% light level depth is shown in blue-green, and 8-day-monthly Lee Z_{eu} is shown in dark grey. A linear regression of the smoothed *in situ* data and MODIS Z_{eu} is shown with R, P and number of data points (n) reported in the top left hand corner. Points are shaded by latitude, shown by the associated colourbar. The 1:1 fit line is shown by the dashed red line and the fit of *in situ* data to satellite data is shown by the dashed grey line. The linear equation with intercept and slope is reported in bold above the regression plot. Finally, for reference, seal tracks are shown with along-track points shaded by the depth of the *in situ* 1% light level, shown by the associated colourbar. 48

Figure 23 Comparison of smoothed 1% light level depths and MODIS products. Plotted over time (Nov. 2014 – Jan. 2015) and per instrumented seal (tag number reported in bold above each plot), the smoothed *in situ* 1% light level depth is shown in blue-green, and 8-day-monthly Lee Z_{eu} is shown in dark grey. A linear regression of the smoothed *in situ* data and MODIS Z_{eu} is shown with R, P and number of data points (n) reported in the top left hand corner. Points are shaded by latitude, shown by the associated colourbar. The 1:1 fit line is shown by the dashed red line and the fit of *in situ* data to satellite data is shown by the dashed grey line. The linear equation with intercept and slope is reported in bold above the regression plot. Finally, for reference, seal tracks are shown with along-track points shaded by the depth of the *in situ* 1% light level, shown by the associated colourbar. 49

Figure 24 Correlating combined log-transformed MODIS [Chl-a] with smoothed *in situ* measures of the depth where light is attenuated to 1% of the surface value. 50

- Figure 25 Correlating combined log-transformed MODIS [Chl-a] with combined and smoothed Lee Z_{eu} . 50
- Figure 26 Unprocessed (quenched) vertical fluorescence yield retrieved by an animal-borne fluorometer over austral summer months November 2009 - January 2010. Fluorescence is measured in relative units rather than yield, and the colour bar represents relative fluorescence units (RFU). 57
- Figure 27 Tracks of 17 southern elephant seals (in black) tagged with FCTD-SRDLs over austral summers spanning 2009 to 2013. The general positions of the Subantarctic Front and the Polar Front are shown in green and blue, respectively (Orsi and Harris, 2014). 60
- Figure 28 Taken from Photopoulou et al. (2015): The iterative process of the broken stick algorithm is presented step-wise from (a) to (o). The red lines represent the true time?depth dive path, the solid black lines represent the abstracted dive path and the dashed lines represent the residuals for the abstracted dive path, at each iteration of the algorithm. The numbers represent the order in which points are added to the abstracted profile. Points 0 and 5 mark the beginning and end of the dive. The dashed black lines represent the residuals that are calculated at each time step between the true and abstracted dive. 62
- Figure 29 Two typical raw vertical fluorescence datasets collected by two southern elephant seals instrumented with FCTD tags. The grey lines show fluorescence yield before the offset (dark count added by manufacturers) is removed. Median yield at 175m is subtracted along each vertical fluorescence profile, resulting in a 'zeroed' dataset, shown in blue. 64
- Figure 30 Correlation between 8-day and monthly composites of MODIS Lee Z_{eu} ($n = 678$). 66
- Figure 31 Uncorrected surface fluorescence data (top 10m) collected over several summers, combined and plotted over local time (hours). Fitted second-degree polynomial is shown in red. 67

- Figure 32 Normalised vertical profiles of fluorescence (solid black line) corrected using either MLD (dashed red line) or Z_{eu} (dashed blue line). Fluorescence in (c) was measured at night and is thus unquenched (MLD in red but Z_{eu} absent at night). Profiles (a), (b) and (d) were collected at varying times during the day. 68
- Figure 33 Ratios of day to night surface fluorescence from data collected by 17 animal-borne fluorometers over 5 austral summers. Boxplots show the distribution of 'day' to 'night' ratios in (a), representing quenched to unquenched yield. Ratios decrease from 6h00 until 18h00, then recover to the 1:1 ratio (red line). Flanking grey sections represent times of the day where the sun is less than 6° below the horizon. Surface fluorescence corrected using MLD in (b) and corrected using Z_{eu} in (c) do not follow the same trend of deviation from the 1:1 ratio line. Indeed, at the surface specifically, correcting from MLD (b) or Z_{eu} (c) does not generate substantial differences. 70
- Figure 34 Density-derived MLD's calculated using CTD data collected from instrumented seals over 6 successive austral summers (2009 - 2014). The general positions of the Sub Antarctic Front and the Polar Front are shown by dashed light grey and dashed dark grey lines, respectively (Orsi and Harris, 2014). 81
- Figure 35 Vertical profiles of unquenched (night) normalised fluorescence (solid black line) with density-derived MLD (dashed red line). These profiles were selected from a number of different instruments over different years and at different times of the night (label above each plot). The top row of profiles show maximum fluorescence yield occurring within the mixed layer depth (a - c), while the bottom row of profiles show maximum fluorescence yield occurring below the density-derived limit (d - f). 82

- Figure 36 Discreet normalised vertical profiles of uncorrected (quenched) fluorescence (solid black line). Suppression of the fluorescence yield from quenching is evident within the surface waters, and the resulting profile thus exhibits maximum fluorescence yields below the depth of the 1% light level (MODIS Z_{eu}), shown by the dashed blue line. The depth of the density-derived mixed layer is shown by the dashed red line. 83
- Figure 37 Normalised vertical profiles of fluorescence (solid black line) corrected from MLD (dashed red line) or Z_{eu} (dashed blue line). Fluorescence in (c) was measured at night and is thus unquenched and uncorrected. For each daytime profile, quenched fluorescence is corrected using either Z_{eu} (depth and corresponding corrected fluorescence yield shown with dashed blue line) or MLD (depth and corresponding corrected fluorescence yield shown with dashed red line). 84
- Figure 38 Sections of fluorescence corrected using either the depth of the mixed layer or the depth of the 1% light level, Z_{eu} . The greyscale bar attached to the top of each plot illustrates when fluorescence data was collected relative to the time of day, with black for night and white for day. The top row of vertical profiles (a), (d) and (g) show sections of uncorrected fluorescence data. The fluorescence data in the second row (b), (e) and (h) have been corrected from MLD (dashed red line). The last row of fluorescence data (c), (f) and (i) have been corrected using Z_{eu} (dashed blue line). 86
- Figure 39 Spatial distribution of all FCTD-SRDL seal tracks (2009 ? 2015) shown in red, relative to a MODIS surface [Chl-a] climatology calculated for the same years over November ? December. 87

- Figure 40 Positions of DCM measured from all tracked seals (2009 ? 2015) shown in red, relative to a MODIS surface [Chl-a] climatology calculated for the same years over November ? December. DCM appear to be distributed along Chl-a edges or boundaries ? possibly related to fronts ? and downstream of islands. These small land masses include Kerguelen (49.3E, 69S) as well as East Island (52.2E, 46.44S). 88
- Figure 41 Histogram of all along-track log-transformed MODIS surface Chl-a concentrations shown in green. Histogram of log-transformed MODIS surface Chl-a concentrations that are only associated with DCM shown in blue. DCM show a largely normal distribution around -0.35 mg m^{-3} . All along-track surface Chl-a concentrations also show a largely normal distribution centred around -0.38 mg m^{-3} . 89
- Figure 42 Positions of the climatological fronts from Orsi et al. (2005) ? the circumpolar Sub Antarctic Front (SAF) is depicted in red and the circumpolar Polar Front (PF) is shown by the blue line. Background bathymetry in light grey was derived from the NOAA ETOPO2v2 database. 90
- Figure 43 Comparison of climatological fronts derived from Orsi et al. (2005) and the positions of the fronts calculated from *in situ* data collected around Kerguelen by tagged seals (2009 ? 2014). The climatological SAF is shown by the dashed red line and the PF by the dashed blue line. Background bathymetry in light grey was derived from the NOAA ETOPO2v2 database. Positions of the fronts calculated using *in situ* temperature and salinity data collected by the tagged seals (method from Boehme et al., 2008) are shown using red stars for the SAF and blue stars for the PF. 90

- Figure 44 All at-sea positions of southern elephant seals tagged on Kerguelen between 2009 and 2015 are shown by the black dots. Positions of deep chlorophyll maxima in the subtropical zone are shown by pink dots (proportion = 0.05), in the subantarctic zone by green dots (proportion = 0.15), and in the polar frontal zone with mauve dots (proportion = 0.25). Deep chlorophyll maxima found within the subantarctic front are shown by red stars (proportion = 0.33) and within the polar front by blue stars (proportion = 0.25). 92
- Figure 45 Relationships between the depth of the hydrographically defined mixed layer and surface Fluorescence (top 10m) from 2009-2014. Markers are coloured by the time of year over each summer season. The linear fit is shown by the dashed grey line. The R value, p-value and the number of datasets collected by seal per year are reported in the top left-hand corner of each plot, and the linear equation with intercept and slope are reported in bold above. 93
- Figure 46 Relationships between the depth of the hydrographically defined mixed layer (x-axis) and integrated Fluorescence (surface to 100m) from 2009-2014. Markers are coloured by the time of year over each summer season. The linear fit is shown by the dashed grey line. The R value, p-value and the number of datasets collected by seal per year are reported in the top right-hand corner of each plot, and the linear equation with intercept and slope are reported in bold above. 94
- Figure 47 Relationships between surface Fluorescence (top 10m) and time of year (November ? February). Markers are coloured by the depth of the mixed layer (m) with blue representing deepest MLD and yellow representing shallowest. Quadratic equation with numerical coefficients reported in bold above. 95

- Figure 48 Relationships between integrated Fluorescence (surface to 100m) and time of year (November ? February). Markers are coloured by the depth of the mixed layer (m) with blue representing deepest MLD and yellow representing shallowest. Quadratic equation with numerical coefficients reported in bold above. 96
- Figure 49 Global MODIS Aqua [Chl-a] seen with (a) a single overpass (b) merged into an 8-day composite and (c) a monthly composite. 103
- Figure 50 Tracks of southern elephant seals (in black) tagged with FCTD-SRDLs over austral summers spanning 2009 to 2013. The general positions of the Sub-Antarctic Front and the Polar Front are shown in green and blue, respectively (Orsi and Harris, 2014). 105
- Figure 51 Tagged seal Cy35-12 with track positions in space showing concurrently measured *in situ* fluorescence in time (a), associated log-transformed MODIS 8-day [Chl-a] (b) and the combined log-transformed 8-day-Monthly [Chl-a] products (c). Fluorescence is measured in relative fluorescence units (RFU). [Chl-a] is measured in mg m^{-3} . 106
- Figure 52 Evaluating the relationship between 8-day MODIS log Chl-a and monthly MODIS log Chl-a using a Kruskal-Wallis test (a) indicates that there is no significant difference between them. A linear regression (b) shows good agreement between the two datasets with a significant p-value well below 0.01. 108
- Figure 53 From all FCTD-SRDL seal positions, associated monthly and 8-day estimates of MODIS log [Chl-a]. Monthly products match minimum values in the 8-day product, but values in the 8-day products show higher (maximum) values not equalled by monthly values. The month of November, when seals are entering the water and moving swiftly away from Kerguelen, shows highest mismatch between monthly and 8-day products. The benefit of adding monthly data is that these data more than double the number of measurements available for comparison with fluorescence data collected by tagged seals. 109

- Figure 54 For each seal (tag labelled in bold in the bottom right hand corner of each plot), surface relative fluorescence values (top bin 10m) are correlated against 8-day MODIS surface Chl-a concentrations. The R value, p-value and the number of points available for the combined product satellite coverage are reported in the top left-hand corner of each plot, and the linear equation with intercept and slope are reported in bold above. 111
- Figure 55 For each seal (tag labelled in bold in the bottom right hand corner of each plot), surface relative fluorescence values (top bin 10m) are correlated against 8-day MODIS surface Chl-a concentrations. The R value, p-value and the number of points available for the combined product satellite coverage are reported in the top left-hand corner of each plot, and the linear equation with intercept and slope are reported in bold above. 112
- Figure 56 For each seal (tag labelled in bold in the bottom right hand corner of each plot), relative fluorescence values integrated from the surface to the depth of the 1% light level (Lee Z_{eu}) are correlated against 8-day MODIS surface Chl-a concentrations. The R value, p-value and the number of points available for the combined product satellite coverage are reported in the top left-hand corner of each plot, and the linear equation with intercept and slope are reported in bold above. 113
- Figure 57 For each seal (tag labelled in bold in the bottom right hand corner of each plot), relative fluorescence values integrated from the surface to the depth of the 1% light level (Lee Z_{eu}) are correlated against 8-day MODIS surface Chl-a concentrations. The R value, p-value and the number of points available for the combined product satellite coverage are reported in the top left-hand corner of each plot, and the linear equation with intercept and slope are reported in bold above. 114

- Figure 58 For each seal (tag labelled in bold in the bottom right hand corner of each plot), relative fluorescence values integrated from the surface to 100m depth are correlated against 8-day MODIS surface Chl-a concentrations. R value, p-value and the number of points available for 8-day satellite coverage are reported in the top left-hand corner of each plot, and the linear equation with intercept and slope are reported in bold above. 115
- Figure 59 For each seal (tag labelled in bold in the bottom right hand corner of each plot), relative fluorescence values integrated from the surface to 100m depth are correlated against 8-day MODIS surface Chl-a concentrations. R value, p-value and the number of points available for 8-day satellite coverage are reported in the top left-hand corner of each plot, and the linear equation with intercept and slope are reported in bold above. 116
- Figure 60 For each seal (tag labelled in bold in the bottom right hand corner of each plot), surface relative fluorescence values (top bin 10m) are correlated against combined 8-day-monthly MODIS surface Chl-a concentrations. The R value, p-value and the number of points available for the combined product satellite coverage are reported in the top left-hand corner of each plot, and the linear equation with intercept and slope are reported in bold above. 117
- Figure 61 For each seal (tag labelled in bold in the bottom right hand corner of each plot), surface relative fluorescence values (top bin 10m) are correlated against combined 8-day-monthly MODIS surface Chl-a concentrations. The R value, p-value and the number of points available for the combined product satellite coverage are reported in the top left-hand corner of each plot, and the linear equation with intercept and slope are reported in bold above. 118

- Figure 62 For each seal (tag labelled in bold in the bottom right hand corner of each plot), relative fluorescence values integrated from the surface to the depth of the 1% light level (Z_{eu}) are correlated against combined 8-day-monthly MODIS surface Chl-a concentrations. R value, p-value and the number of points available for 8-day satellite coverage are reported in the top left-hand corner of each plot, and the linear equation with intercept and slope are reported in bold above. 119
- Figure 63 For each seal (tag labelled in bold in the bottom right hand corner of each plot), relative fluorescence values integrated from the surface to the depth of the 1% light level (Z_{eu}) are correlated against combined 8-day-monthly MODIS surface Chl-a concentrations. R value, p-value and the number of points available for 8-day satellite coverage are reported in the top left-hand corner of each plot, and the linear equation with intercept and slope are reported in bold above. 120
- Figure 64 For each seal (tag labelled in bold in the bottom right hand corner of each plot), relative fluorescence values integrated from the surface to 100m depth are correlated against combined 8-day-monthly MODIS surface Chl-a concentrations. R value, p-value and the number of points available for 8-day satellite coverage are reported in the top left-hand corner of each plot, and the linear equation with intercept and slope are reported in bold above. 121
- Figure 65 For each seal (tag labelled in bold in the bottom right hand corner of each plot), relative fluorescence values integrated from the surface to 100m depth are correlated against combined 8-day-monthly MODIS surface Chl-a concentrations. R value, p-value and the number of points available for 8-day satellite coverage are reported in the top left-hand corner of each plot, and the linear equation with intercept and slope are reported in bold above. 122

- Figure 66 Relationship between *in situ* fluorescence data collected by 18 tagged seals between 2009 and 2015, and MODIS [Chl-a]. In terms of estimating phytoplankton abundance, remotely sensed surface measures appear to underestimate what fluorometers detect in the water column, from the surface to the depth of the 1% light level. Although it's not possible to determine if the poor relationship is due to the instrument or the satellite product, increasing latitude appears to play a role, with measurements taken further south appearing to be less representative of the *in situ* data. 124
- Figure 67 Per FCTD tag deployed in 2009, quenching corrected Z_{eu} -fluorescence shown by green markers and MODIS 8-day-monthly [Chl-a] shown by grey markers are plotted over time. Tag numbers are reported in bold. Tracks are shown for reference with values coloured by FCTD relative fluorescence units (RFU). This approach is qualitative rather than quantitative, but shows how the MODIS data mirrors the *in situ* values over time. Relationships between the two datasets appear to break down with increasing latitude. 125
- Figure 68 Per FCTD tag deployed in 2010, quenching corrected Z_{eu} -fluorescence shown by green markers and MODIS 8-day-monthly [Chl-a] shown by grey markers are plotted over time. Tag numbers are reported in bold. Tracks are shown for reference with values coloured by FCTD relative fluorescence units (RFU). This approach is qualitative rather than quantitative, but shows how the MODIS data mirrors the *in situ* values over time. Relationships between the two datasets appear to break down with increasing latitude. 126

- Figure 69 Per FCTD tag deployed in 2011, quenching corrected Z_{eu} -fluorescence shown by green markers and MODIS 8-day-monthly [Chl-a] shown by grey markers are plotted over time. Tag numbers are reported in bold. Tracks are shown for reference with values coloured by FCTD relative fluorescence units (RFU). This approach is qualitative rather than quantitative, but shows how the MODIS data mirrors the *in situ* values over time. Relationships between the two datasets appear to break down with increasing latitude. [127](#)
- Figure 70 Per FCTD tag deployed in 2012, quenching corrected Z_{eu} -fluorescence shown by green markers and MODIS 8-day-monthly [Chl-a] shown by grey markers are plotted over time. Tag numbers are reported in bold. Tracks are shown for reference with values coloured by FCTD relative fluorescence units (RFU). This approach is qualitative rather than quantitative, but shows how the MODIS data mirrors the *in situ* values over time. Relationships between the two datasets appear to break down with increasing latitude. [128](#)
- Figure 71 Per FCTD tag deployed in 2014, quenching corrected Z_{eu} -fluorescence shown by green markers and MODIS 8-day-monthly [Chl-a] shown by grey markers are plotted over time. Tag numbers are reported in bold. Tracks are shown for reference with values coloured by FCTD relative fluorescence units (RFU). This approach is qualitative rather than quantitative, but shows how the MODIS data mirrors the *in situ* values over time. Relationships between the two datasets appear to break down with increasing latitude. [129](#)
- Figure 72 FCTD tag deployed in 2015 with quenching corrected Z_{eu} -fluorescence shown by green markers and MODIS 8-day-monthly [Chl-a] shown by grey markers are plotted over time. Tag numbers are reported in bold. Tracks are shown for reference with values coloured by FCTD relative fluorescence units (RFU). This approach is qualitative rather than quantitative, but shows how the MODIS data mirrors the *in situ* values over time. [130](#)

- Figure 73 Proportion of our globe covered by cloud in December 2014, shown as a monthly mean of daytime values. Black represents little to no cloud cover, whereas white represents upwards of 80% cloud coverage. 138
- Figure 74 For reference and bearings, this labelled map of the Antarctic continent, ice shelves and Antarctic Seas provided was provided for free for paper integration by GEOATLAS® (2010). 143
- Figure 75 Mean log-transformed Chl-a (climatology) for each summer month, calculated using 12 years (January 2003 - December 2017) of MODIS Chl-a. Black contours represent the mean positions of the Sub Antarctic Front (SAF) and the Polar Front (PF), as calculated by Orsi and Harris (2014). 145
- Figure 76 Mean Z_{eu} (climatology) for each summer month, calculated using 12 years (January 2003 - December 2017) of MODIS Lee Z_{eu} . Black contours represent the mean positions of the Sub Antarctic Front (SAF) and the Polar Front (PF), as calculated by Orsi and Harris (2014). 146
- Figure 77 Mean cloud cover eye of Sauron (climatology) for each summer month, calculated using 12 years of MODIS cloud fraction data (January 2003 - December 2017). 147
- Figure 78 Changes to MODIS surface Chl-a concentration and vertical light attenuation for the month of October over the 13 year MODIS timeseries. Red represents increased Chl-a and an associated shallowing of Z_{eu} , Blue represents decreased Chl-a and an associated deepening of Z_{eu} . The ratio of increased Chl : decreased Chl-a and shallower Z_{eu} ; deeper Z_{eu} are reported in bold. Results point to an overall decrease in phytoplankton, but this is not matched by Z_{eu} , which shows an overall decrease in vertical light attenuation. 151

- Figure 79 Changes to MODIS surface Chl-a concentration and vertical light attenuation for the month of November over the 13 year MODIS timeseries. Red represents increased Chl-a and an associated shallowing of Z_{eu} , Blue represents decreased Chl-a and an associated deepening of Z_{eu} . The ratio of increased Chl : decreased Chl-a and shallower Z_{eu} ; deeper Z_{eu} are reported in bold. Results point to an overall decrease in phytoplankton, but this is not matched by Z_{eu} , which shows an overall decrease in vertical light attenuation. 152
- Figure 80 Changes to MODIS [Chl-a] and Lee Z_{eu} for the month of December over the 13 year MODIS timeseries. Red represents increase in Chl-a and an associated shallowing of vertical light attenuation, Blue represents decreased Chl-a and an associated deepening of Z_{eu} . The ratio of increased [Chl-a] : decreased [Chl-a], and shallower Z_{eu} ; deeper Z_{eu} are reported in bold. Spatially, patterns between [Chl-a] and Z_{eu} are similar, though results point to an overall decrease in phytoplankton (0.8) and overall shallowing of vertical light attenuation (1.6). 153
- Figure 81 Changes to MODIS [Chl-a] and Lee Z_{eu} for the month of January over the 13 year MODIS timeseries. Red represents increase in Chl-a and an associated shallowing of vertical light attenuation, Blue represents decreased Chl-a and an associated deepening of Z_{eu} . The ratio of increased [Chl-a] : decreased [Chl-a], and shallower Z_{eu} ; deeper Z_{eu} are reported in bold. Spatially, patterns between [Chl-a] and Z_{eu} are similar. 154
- Figure 82 Changes to MODIS surface Chl-a concentration and vertical light attenuation for the month of February over the 13 year MODIS timeseries. Red represents increased Chl-a and an associated shallowing Z_{eu} , Blue represents decreased Chl-a and an associated deeper Z_{eu} . Ratios of increased Chl : decreased Chl-a and shallower Z_{eu} ; deeper Z_{eu} are reported in bold. Results point to a sign change in surface concentrations of phytoplankton, with changes suggesting an increase. Z_{eu} shows a stronger decline in vertical light attenuation. 155

- Figure 83 Changes to MODIS surface Chl-a concentration and vertical light attenuation for the month of March over the 13 year MODIS timeseries. Red represents increased Chl-a and an associated shallowing of Z_{eu} , Blue represents decreased Chl-a and an associated deepening of Z_{eu} . The ratio of increased Chl : decreased Chl-a and shallower Z_{eu} ; deeper Z_{eu} are reported in bold. Results point to an overall decrease in phytoplankton, but this is not matched by Z_{eu} , which shows an overall decrease in vertical light attenuation. 156
- Figure 84 Trends in MODIS cloud fraction anomaly over 12 years (January 2003 - December 2017) for successive summer months. Positive trends (slope) in the anomaly are shown in black and suggest a possible increase in cloud cover. Conversely, negative trends (slope) in the anomaly are shown in green-blue and suggest a reduction in cloud fraction and a possible increase in light reaching the ocean surface. Landmasses are traced in black. 157
- Figure 85 Indian sector A (15E - 80E) changes to surface Chl-a concentration and vertical light attenuation for the month of December over the 13-year MODIS time-series. Red represents an increased Chl-a with an associated shallowing of Z_{eu} , Blue represents decreased Chl-a with an associated deepening Z_{eu} . Ratios of [gain : loss] are reported in bold above the colourbar as [increased Chl : decreased Chl-a] and [shallower Z_{eu} ; deeper Z_{eu}], respectively. Values above 1.0 indicate increased Chl and shallower Z_{eu} (more pixels are red), and values less than 1.0 indicate decreased Chl-a and deeper Z_{eu} (more pixels are blue). Results for the Indian ocean sector A point to increases in surface concentrations of phytoplankton and a strong shallowing of vertical light attenuation. 159

Figure 86 Indian sector A (15E - 80E) changes to surface Chl-a concentration and vertical light attenuation for the month of January over the 13-year MODIS time-series. Red represents an increased Chl-a with an associated shallowing of Z_{eu} , Blue represents decreased Chl-a with an associated deepening Z_{eu} . Ratios of [gain : loss] are reported in bold above the colourbar as [increased Chl : decreased Chl-a] and [shallower Z_{eu} ; deeper Z_{eu}], respectively. Values above 1.0 indicate increased Chl and shallower Z_{eu} (more pixels are red), and values less than 1.0 indicate decreased Chl-a and deeper Z_{eu} (more pixels are blue). Results for the Indian ocean sector A point to strong increases in surface concentrations of phytoplankton and a strong shallowing of vertical light attenuation. 160

Figure 87 Indian sector A (15E - 80E) changes to surface Chl-a concentration and vertical light attenuation for the month of February over the 13-year MODIS time-series. Red represents an increased Chl-a with an associated shallowing of Z_{eu} , Blue represents decreased Chl-a with an associated deepening Z_{eu} . Ratios of [gain : loss] are reported in bold above the colourbar as [increased Chl : decreased Chl-a] and [shallower Z_{eu} ; deeper Z_{eu}], respectively. Values above 1.0 indicate increased Chl and shallower Z_{eu} (more pixels are red), and values less than 1.0 indicate decreased Chl-a and deeper Z_{eu} (more pixels are blue). Results for the Indian ocean sector A point to very strong increases in surface concentrations of phytoplankton and a very strong shallowing of vertical light attenuation. 161

Figure 88 Indian sector B (80E - 160E) changes to surface Chl-a concentration and vertical light attenuation for the month of December over the 13-year MODIS time-series. Red represents an increased Chl-a with an associated shallowing of Z_{eu} , Blue represents decreased Chl-a with an associated deepening Z_{eu} . Ratios of [gain : loss] are reported in bold above the colourbar as [increased Chl : decreased Chl-a] and [shallower Z_{eu} ; deeper Z_{eu}], respectively. Values above 1.0 indicate increased Chl and shallower Z_{eu} (more pixels are red), and values less than 1.0 indicate decreased Chl-a and deeper Z_{eu} (more pixels are blue). Results here point to a decrease in surface concentrations of phytoplankton but a modest shallowing of vertical light attenuation for the Indian ocean sector B. 162

Figure 89 Indian sector B (80E - 160E) changes to surface Chl-a concentration and vertical light attenuation for the month of January over the 13-year MODIS time-series. Red represents an increased Chl-a with an associated shallowing of Z_{eu} , Blue represents decreased Chl-a with an associated deepening Z_{eu} . Ratios of [gain : loss] are reported in bold above the colourbar as [increased Chl : decreased Chl-a] and [shallower Z_{eu} ; deeper Z_{eu}], respectively. Values above 1.0 indicate increased Chl and shallower Z_{eu} (more pixels are red), and values less than 1.0 indicate decreased Chl-a and deeper Z_{eu} (more pixels are blue). Results here point to a substantial decrease in surface concentrations of phytoplankton and very little change in vertical light attenuation for the Indian ocean sector B. 163

Figure 90 Indian sector B (80E - 160E) changes to surface Chl-a concentration and vertical light attenuation for the month of February over the 13-year MODIS time-series. Red represents an increased Chl-a with an associated shallowing of Z_{eu} , Blue represents decreased Chl-a with an associated deepening Z_{eu} . Ratios of [gain : loss] are reported in bold above the colourbar as [increased Chl : decreased Chl-a] and [shallower Z_{eu} ; deeper Z_{eu}], respectively. Values above 1.0 indicate increased Chl and shallower Z_{eu} (more pixels are red), and values less than 1.0 indicate decreased Chl-a and deeper Z_{eu} (more pixels are blue). Results here point to a decline in surface concentrations of phytoplankton over this month, but a slight recovery from the strong loss seen in the month before. The associated shallowing of vertical light attenuation for the Indian ocean sector B appears to reflect this. 164

Figure 91 Ross Sea sector (160E - 150W) changes to surface Chl-a concentration and vertical light attenuation for the month of December over the 13-year MODIS time-series. Red represents an increased Chl-a with an associated shallowing of Z_{eu} , Blue represents decreased Chl-a with an associated deepening Z_{eu} . Ratios of [gain : loss] are reported in bold above the colourbar as [increased Chl : decreased Chl-a] and [shallower Z_{eu} ; deeper Z_{eu}], respectively. Values above 1.0 indicate increased Chl and shallower Z_{eu} (more pixels are red), and values less than 1.0 indicate decreased Chl-a and deeper Z_{eu} (more pixels are blue). Results here point to a decrease in surface concentrations of phytoplankton but a modest shallowing of vertical light attenuation over all Decembers in the timeseries. 165

- Figure 92 Ross Sea sector (160E - 150W) changes to surface Chl-a concentration and vertical light attenuation for the month of December over the 13-year MODIS time-series. Red represents an increased Chl-a with an associated shallowing of Z_{eu} , Blue represents decreased Chl-a with an associated deepening Z_{eu} . Ratios of [gain : loss] are reported in bold above the colourbar as [increased Chl : decreased Chl-a] and [shallower Z_{eu} ; deeper Z_{eu}], respectively. Values above 1.0 indicate increased Chl and shallower Z_{eu} (more pixels are red), and values less than 1.0 indicate decreased Chl-a and deeper Z_{eu} (more pixels are blue). Results here point to a very slight decline in surface concentrations of phytoplankton but a modest shallowing of vertical light attenuation over all Januaries in the timeseries. 166
- Figure 93 Ross Sea sector (160E - 150W) changes to surface Chl-a concentration and vertical light attenuation for the month of December over the 13-year MODIS time-series. Red represents an increased Chl-a with an associated shallowing of Z_{eu} , Blue represents decreased Chl-a with an associated deepening Z_{eu} . Ratios of [gain : loss] are reported in bold above the colourbar as [increased Chl : decreased Chl-a] and [shallower Z_{eu} ; deeper Z_{eu}], respectively. Values above 1.0 indicate increased Chl and shallower Z_{eu} (more pixels are red), and values less than 1.0 indicate decreased Chl-a and deeper Z_{eu} (more pixels are blue). Results here point to a recovery and slight increase in surface concentrations of phytoplankton, with an associated shallowing of vertical light attenuation over all Februaries in the timeseries. 167

Figure 94 East Pacific Sector (75W – 150W) changes to surface Chl-a concentration and vertical light attenuation for the month of December over the 13-year MODIS time-series. Red represents increased Chl-a with an associated shallowing of Z_{eu} , Blue represents decreased Chl-a with an associated deepening Z_{eu} . Ratios of [red : blue] are reported in bold above the colourbar as [Chl gain : Chl-a loss] and [shallower Z_{eu} ; deeper Z_{eu}], respectively. Values above 1.0 indicate increased Chl and shallower Z_{eu} (more pixels are red), and values less than 1.0 indicate decreased Chl-a and deeper Z_{eu} (more pixels are blue). Results for the East Pacific Sector over the last 13 years point to a reduction in surface concentrations of phytoplankton but a slight shallowing of vertical light attenuation. 168

Figure 95 East Pacific Sector (75W – 150W) changes to surface Chl-a concentration and vertical light attenuation for the month of January over the 13-year MODIS time-series. Red represents increased Chl-a with an associated shallowing of Z_{eu} , Blue represents decreased Chl-a with an associated deepening Z_{eu} . Ratios of [red : blue] are reported in bold above the colourbar as [Chl gain : Chl-a loss] and [shallower Z_{eu} ; deeper Z_{eu}], respectively. Values above 1.0 indicate increased Chl and shallower Z_{eu} (more pixels are red), and values less than 1.0 indicate decreased Chl-a and deeper Z_{eu} (more pixels are blue). Results for the East Pacific Sector over the last 13 years point to a small decrease in surface concentrations of phytoplankton, but increases to vertical light attenuation during the month of January. Although well north of the ACC, changes are very interesting along 40S, where moderate increases in [Chl-a] have generated a very strong shallowing of the 1% light level. 169

Figure 96 East Pacific Sector (75W – 150W) changes to surface Chl-a concentration and vertical light attenuation for the month of February over the 13-year MODIS time-series. Red represents increased Chl-a with an associated shallowing of Z_{eu} , Blue represents decreased Chl-a with an associated deepening Z_{eu} . Ratios of [red : blue] are reported in bold above the colourbar as [Chl gain : Chl-a loss] and [shallower Z_{eu} ; deeper Z_{eu}], respectively. Values above 1.0 indicate increased Chl and shallower Z_{eu} (more pixels are red), and values less than 1.0 indicate decreased Chl-a and deeper Z_{eu} (more pixels are blue). Results for the East Pacific Sector over the last 13 years point to a strong increase in surface concentrations of phytoplankton, with associated increases to vertical light attenuation during the month of February. Changes along 40S continue to be noteworthy, where increased [Chl-a] has generated a very strong shallowing of the 1% light level. 170

Figure 97 Drake Passage Sector (75W - 15E) changes to surface Chl-a concentration and vertical light attenuation for the month of December over the 13-year MODIS time-series. Red represents increased Chl-a with an associated shallowing of Z_{eu} , Blue represents decreased Chl-a with an associated deepening Z_{eu} . Ratios of [red : blue] are reported in bold above the colourbar as [Chl gain : Chl-a loss] and [shallower Z_{eu} ; deeper Z_{eu}], respectively. Values above 1.0 indicate increased Chl and shallower Z_{eu} (more pixels are red), and values less than 1.0 indicate decreased Chl-a and deeper Z_{eu} (more pixels are blue). Results for Atlantic Sector over the last 13 years point to decreases in surface concentrations of phytoplankton and a shallowing of vertical light attenuation during the month of December. 171

Figure 98 Drake Passage Sector (75W - 15E) changes to surface Chl-a concentration and vertical light attenuation for the month of January over the 13-year MODIS time-series. Red represents increased Chl-a with an associated shallowing of Z_{eu} , Blue represents decreased Chl-a with an associated deepening Z_{eu} . Ratios of [red : blue] are reported in bold above the colourbar as [Chl gain : Chl-a loss] and [shallower Z_{eu} ; deeper Z_{eu}], respectively. Values above 1.0 indicate increased Chl and shallower Z_{eu} (more pixels are red), and values less than 1.0 indicate decreased Chl-a and deeper Z_{eu} (more pixels are blue). Results for Atlantic Sector over the last 13 years point to a minor decrease in surface concentrations of phytoplankton and a shallowing of vertical light attenuation during the month of January. 172

Figure 99 Drake Passage Sector (75W - 15E) changes to surface Chl-a concentration and vertical light attenuation for the month of January over the 13-year MODIS time-series. Red represents increased Chl-a with an associated shallowing of Z_{eu} , Blue represents decreased Chl-a with an associated deepening Z_{eu} . Ratios of [red : blue] are reported in bold above the colourbar as [Chl gain : Chl-a loss] and [shallower Z_{eu} ; deeper Z_{eu}], respectively. Values above 1.0 indicate increased Chl and shallower Z_{eu} (more pixels are red), and values less than 1.0 indicate decreased Chl-a and deeper Z_{eu} (more pixels are blue). Results for Atlantic Sector over the last 13 years point to little overall change in surface concentrations of phytoplankton and vertical light attenuation during the month of February. 173

- Figure 100 For the months of December, areas where significant ($p < 0.05$) changes are evident in Chl-a, Lee Z_{eu} and Cloud Fraction relative to the SAM. For Chl-a and Z_{eu} , red suggests an increase in surface Chl-a concentration over the 12 consecutive years in the MODIS satellite record (2003 - 2017), while blue suggests a loss. For cloud fraction, black shows an increase in coverage over time, while blue-green shows a decrease in cloud and implies that more light may reach the ocean surface. 177
- Figure 101 For the months of January, areas where significant ($p < 0.05$) changes are evident in Chl-a, Lee Z_{eu} and Cloud Fraction relative to the SAM. For Chl-a and Z_{eu} , red suggests an increase in surface Chl-a concentration over the 12 consecutive years in the MODIS satellite record (2003 - 2017), while blue suggests a loss. For cloud fraction, black shows an increase in coverage over time, while blue-green shows a decrease in cloud and implies that more light may reach the ocean surface. 178
- Figure 102 For the months of February, areas where significant ($p < 0.05$) changes are evident in Chl-a, Lee Z_{eu} and Cloud Fraction relative to the SAM. For Chl-a and Z_{eu} , red suggests an increase in surface Chl-a concentration over the 12 consecutive years in the MODIS satellite record (2003 - 2017), while blue suggests a loss. For cloud fraction, black shows an increase in coverage over time, while blue-green shows a decrease in cloud and implies that more light may reach the ocean surface. 179
- Figure 103 Tracks of all 47 post-breeding adult female southern elephant seals tagged on Kerguelen and Marion Island and instrumented with FCTD tags and TDR light meters. Austral summers span from 2009 to 2014. 188
- Figure 104 Tracks of the five southern elephant seals not included for the cumulative sums analysis, where instrument failure has resulted in incomplete data collection. Tracks are coloured by day of the year, and larger marker sizes represent higher surface fluorescence yields, as measured by the FCTD-SRDL. 191

- Figure 105 Tracks of the remaining post-breeding adult female southern elephant seals tagged on Kerguelen and Marion Island from 2009 to 2014. Data from both FCTD tags and TDR light meters are shown in this figure. 192
- Figure 106 Cumulative sums CUSUM chart for all seals tagged with fluorometers. The blue line represents the cumulative speeds over time, with the Page Quality Number shown by the black horizontal line and phase changes shown by the vertical red dashed lines. Each plot is labelled by Tag, reported in bold. 195
- Figure 107 Cumulative sums CUSUM chart for all seals tagged with fluorometers. The blue line represents the cumulative speeds over time, with the Page Quality Number shown by the black horizontal line and phase changes shown by the vertical red dashed lines. Each plot is labelled by Tag, reported in bold. 196
- Figure 108 Cumulative sums CUSUM chart for all seals tagged with TDR light meters. The blue line represents the cumulative speeds over time, with the Page Quality Number shown by the black horizontal line and phase changes shown by the vertical red dashed lines. Each plot is labelled by Tag, reported in bold. 196
- Figure 109 Cumulative sums CUSUM chart for all seals tagged with TDR light meters. The blue line represents the cumulative speeds over time, with the Page Quality Number shown by the black horizontal line and phase changes shown by the vertical red dashed lines. Each plot is labelled by Tag, reported in bold. 197
- Figure 110 Cumulative sums CUSUM chart for all seals tagged with TDR light meters. The blue line represents the cumulative speeds over time, with the Page Quality Number shown by the black horizontal line and phase changes shown by the vertical red dashed lines. Each plot is labelled by Tag, reported in bold. 197
- Figure 111 Cumulative sums CUSUM chart for all seals tagged with TDR light meters. The blue line represents the cumulative speeds over time, with the Page Quality Number shown by the black horizontal line and phase changes shown by the vertical red dashed lines. Each plot is labelled by Tag, reported in bold. 198

- Figure 112 Cumulative sums CUSUM chart for all seals tagged with TDR light meters. The blue line represents the cumulative speeds over time, with the Page Quality Number shown by the black horizontal line and phase changes shown by the vertical red dashed lines. Each plot is labelled by Tag, reported in bold. 198
- Figure 113 Cumulative speeds from the three seals tagged with both FCTD-SRDLs and TDR Light Meters in 2009. The top panel shows cumulative speeds calculated using FCTD data only. With these tags, data are only collected from the deepest dive recorded over 6-hourly windows. The CUSUM chart shows cumulative speed around the Page Quality number (horizontal black line), and the corresponding tracks represent true speed (highest speeds represented by the smallest marker sizes, and visa versa). The bottom panel shows the same, but based on data collected by the TDR light meters. With these tags, data are collected every 2 seconds, however, all low light data (night or very overcast) have been filtered out. The CUSUM chart and tracks calculated using FCTD data matches the CUSUM chart and tracks calculated using TDR Light Meter data, despite differences in resolution. 199
- Figure 114 Histograms of fluorescence data collected by twelve southern elephant seals during three at-sea phases, namely: outbound (green), possible area-restricted search (ARS) foraging (red), and homebound (blue). Fluorescence values are lowest during the outbound phase and are highest during the homebound phase. Fluorescence data collected during the foraging phase are approximately normally distributed around a mean of 1. 200

Figure 115 Visualising speed and phase changes for FCTD tag 2009-1. In (a), the CUSUM chart shows cumulative speed relative to the Page Quality Number, represented by the black horizontal line. The two dashed, vertical red lines represent the phase changes from travel to foraging, and then to travel again. Phase changes were detected automatically using a Kruskal-Wallis test, with manual confirmation. The same phase change lines are plotted in (b), which shows the same track data over the same x-axis, but reported as m/s on the y-axis. The phase changes detected on the CUSUM chart are an exact match for when speeds drop below the mean (horizontal black line). Speed has been smoothed using a boxcar filter with window of 4, and is represented by the purple line. For comparison, vertically integrated fluorescence in green (c) has been smoothed using the same boxcar filter, and is plotted over the same x-axis with CUSUM phase change lines in red. Mean fluorescence is shown by the horizontal black line. For context, seal tracks are shown in (d). Larger marker sizes represent slower speeds, and visa-versa. The two black diamonds represent when in time the phase changes were detected on the CUSUM chart. 201

Figure 116 Visualising speed and phase changes for FCTD tag 2010-1. In (a), the CUSUM chart shows cumulative speed relative to the Page Quality Number, represented by the black horizontal line. The two dashed, vertical red lines represent the phase changes from travel to foraging, and then to travel again. Phase changes were detected automatically using a Kruskal-Wallis test, with manual confirmation. The same phase change lines are plotted in (b), which shows the same track data over the same x-axis, but reported as m/s on the y-axis. The phase changes detected on the CUSUM chart are an exact match for when speeds drop below the mean (horizontal black line). Speed has been smoothed using a boxcar filter with window of 4, and is represented by the purple line. For comparison, vertically integrated fluorescence in green (c) has been smoothed using the same boxcar filter, and is plotted over the same x-axis with CUSUM phase change lines in red. Mean fluorescence is shown by the horizontal black line. For context, seal tracks are shown in (d). Larger marker sizes represent slower speeds, and visa-versa. The two black diamonds represent when in time the phase changes were detected on the CUSUM chart. 202

Figure 117 Visualising speed and phase changes for FCTD tag 2011-1. In (a), the CUSUM chart shows cumulative speed relative to the Page Quality Number, represented by the black horizontal line. The two dashed, vertical red lines represent phase changes from travel to foraging, and to travel again. Phase changes were detected automatically using a Kruskal-Wallis test, with manual confirmation. The same phase change lines are plotted in (b), which shows the track data over the same x-axis, but reported as m/s on the y-axis. The phase changes detected on the CUSUM chart are a match for when speeds drop below the mean (horizontal black line). Speed has been smoothed using a boxcar filter with window of 4, and is represented by the purple line. For comparison, vertically integrated fluorescence in green (c) has been smoothed using the same boxcar filter, and is plotted over the same x-axis with CUSUM phase change lines in red. Mean fluorescence is shown by the horizontal black line. For context, seal tracks are shown in (d). Larger marker sizes represent slower speeds, and visa-versa. The two black diamonds represent when in time the phase changes were detected on the CUSUM chart. 203

Figure 118 Visualising speed and phase changes for FCTD tag 2012-2. In (a), the CUSUM chart shows cumulative speed relative to the Page Quality Number, represented by the black horizontal line. The two dashed, vertical red lines represent phase changes from travel to foraging, and to travel again. Phase changes were detected automatically using a Kruskal-Wallis test, with manual confirmation. The same phase change lines are plotted in (b), which shows the track data over the same x-axis, but reported as m/s on the y-axis. The phase changes detected on the CUSUM chart are a match for when speeds drop below the mean (horizontal black line). Speed has been smoothed using a boxcar filter with window of 4, and is represented by the purple line. For comparison, vertically integrated fluorescence in green (c) has been smoothed using the same boxcar filter, and is plotted over the same x-axis with CUSUM phase change lines in red. Mean fluorescence is shown by the horizontal black line. For context, seal tracks are shown in (d). Larger marker sizes represent slower speeds, and visa-versa. The two black diamonds represent when in time the phase changes were detected on the CUSUM chart. This is the clearest example of the inverse relationship speed may have to phytoplankton, and there are short foraging phases within travel phases that appear related to patches of increased fluorescence. 204

Figure 119 Visualising speed and phase changes for FCTD tag 2013-1. In (a), the CUSUM chart shows cumulative speed relative to the Page Quality Number, represented by the black horizontal line. The two dashed, vertical red lines represent phase changes from travel to foraging, and to travel again. Phase changes were detected automatically using a Kruskal-Wallis test, with manual confirmation. The same phase change lines are plotted in (b), which shows the track data over the same x-axis, but reported as m/s on the y-axis. The phase changes detected on the CUSUM chart are a match for when speeds drop below the mean (horizontal black line). Speed has been smoothed using a boxcar filter with window of 4, and is represented by the purple line. For comparison, vertically integrated fluorescence in green (c) has been smoothed using the same boxcar filter, and is plotted over the same x-axis with CUSUM phase change lines in red. Mean fluorescence is shown by the horizontal black line. For context, seal tracks are shown in (d). Larger marker sizes represent slower speeds, and visa-versa. The two black diamonds represent when in time the phase changes were detected on the CUSUM chart. 205

Figure 120 Visualising speed and phase changes for FCTD tag 2014-1. In (a), the CUSUM chart shows cumulative speed relative to the Page Quality Number, represented by the black horizontal line. The two dashed, vertical red lines represent phase changes from travel to foraging, and to travel again. Phase changes were detected automatically using a Kruskal-Wallis test, with manual confirmation. The same phase change lines are plotted in (b), which shows the track data over the same x-axis, but reported as m/s on the y-axis. The phase changes detected on the CUSUM chart are a match for when speeds drop below the mean (horizontal black line). Speed has been smoothed using a boxcar filter with window of 4, and is represented by the purple line. For comparison, vertically integrated fluorescence in green (c) has been smoothed using the same boxcar filter, and is plotted over the same x-axis with CUSUM phase change lines in red. Mean fluorescence is shown by the horizontal black line. For context, seal tracks are shown in (d). Larger marker sizes represent slower speeds, and visa-versa. The two black diamonds represent when in time the phase changes were detected on the CUSUM chart. This is the clearest example of the inverse relationship speed may have to phytoplankton, and there are short foraging phases within travel phases that appear related to patches of increased fluorescence. 206

Figure 121 Histograms of light level data collected by southern elephant seals tagged with TDR light meters during three at-sea phases: outbound (green), possible area-restricted search foraging (red), and homebound (blue). Lower 1% light level depths in meters (x-axis) are indicative of phytoplankton or other materials in surface waters. 207

Figure 122 Boxplot showing median, interquartile ranges and outliers of fluorescence (left) and the 1% light level (right) for three phases: outbound travel, potential foraging and homebound travel. 208

LIST OF TABLES

Table 1	Available time, depth and light intensity data used for this thesis, detailing year of deployment, and which chapters the data were used for. Additionally, the three seals that had a TDR light meter deployed alongside the FCTD data loggers are shown. All TDR light meters were deployed from Kerguelen Island. 14
Table 2	Available fluorescence, salinity and temperature data used for this thesis, detailing year of deployment, where animals were tagged, and which chapter the data were used for. Additionally, the three seals that had a TDR light meter deployed alongside the FCTD data loggers are shown. 15
Table 3	Part 1 - List of post-breeding female southern elephant seals tagged on Kerguelen between the summers of 2009-2015. TDRs measured light in an 'upward' and/or 'forward' and/or 'backward' and/or 'right' direction, depending on the type/s of TDR instrument deployed. 26
Table 4	Part 2 - List of post-breeding female southern elephant seals tagged on Kerguelen between the summers of 2009-2015. TDRs measured light in an 'upward' and/or 'forward' and/or 'backward' and/or 'right' direction, depending on the type/s of TDR instrument deployed. 27

ACRONYMS

ACC	Antarctic Circumpolar Current
ANOVA	Analysis of Variance

AOO	Antarctic Oscillation
ARS	Area Restricted Search
CDOM	Coloured Dissolved Organic Matter
Chl-a	Chlorophyll pigment associated with photosynthesising phytoplankton, measured through insitu processes
[Chl-a]	Remotely derived estimation of Chl-a concentration in surface waters
CO ₂	Carbon Dioxide
CUSUM	Cumulative Sums
CTD-SRDL	Conductivity, Temperature and Depth Satellite-Relayed Data Logger
CZCS	Coastal Zone Colour Scanner
DCM	Deep Chlorophyll Maxima
DIC	Dissolved Inorganic Carbon
ENSO	El Ni no-Southern Oscillation
EOF	Empirical Orthogonal Function
ESA	European Space Agency
FCTD-SRDL	Fluorescence, Conductivity, Temperature and Depth Satellite-Relayed Data Logger
HDF	High Definition Format
HNLC	High nutrient, low chlorophyll
HPLC	High Performance Liquid Chromatography
IOP	Inherent Optical Properties
K _d (490)	Diffuse attenuation coefficient for downwelling irradiance
L3	Level-3
MIZ	Marginal Ice Zone
MLD	Mixed Layer Depth

MODIS	The Moderate Resolution Imaging Spectroradiometer currently flying aboard the Aqua satellite.
NASA	National Aeronautics and Space Administration
NEODAAS	NERC Earth Observation Data Acquisition and Analysis Service
NOAA	National Oceanic and Atmospheric Administration
O₂	Oxygen
OBPG	Ocean Biology Processing Group
OC-CCI	Ocean Colour Climate Change Initiative
PAR	Photosynthetically Available Radiation
PCA	Principal Component Analysis
PF	Polar Front
RFU	Relative Fluorescence Units
SAF	Sub-Antarctic Front
SAM	The Southern Annular Mode
SMI	Standard Mapped Images
SST	Sea Surface Temperature
SWIR	Southwest Indian Ridge
TDR	Time Depth Recorder
WAP	Western Antarctic Peninsula
Z_{eu}	Depth that photosynthetically available radiation is attenuated to 1% of its surface value. For some studies, this is also referred to as euphotic depth.

INTRODUCTION

1.1 THE SOUTHERN OCEAN

The Southern Ocean is the world's most extensive ocean; unique from all other oceans because it stretches $\approx 24,000$ km around the globe with flow uninterrupted by land. This characteristic permits circumpolar circulation in the form of the Antarctic Circumpolar Current (ACC) (Thompson and Richards, 2011; Olbers et al., 2004). Thanks largely to the prevailing westerly winds that impart substantial kinetic energy into accelerating this zonal current (as well as mixing its surface waters), the ACC transports between 130 -140 Sv, where $1 \text{ Sv} = 10^6 \text{ m}^3 \text{ s}^{-1}$ (Nowlin and Klinck, 1986; Pollard et al., 2001).

The Southern Ocean is also the world's most distinctive ocean because, although it links the Atlantic, Indian and Pacific basins, it does not conform to their dynamics. In mid-latitude waters, flow can be balanced geostrophically across the permanent thermocline, limiting strong ocean currents to the surface layer (Tomczak and Godfrey, 1994). However, in the high southern latitudes, temperature differences between surface and deep waters are generally small (Sokolov and Rintoul, 2003) and the pressure gradient force is more evenly distributed over the water column. The ACC is thus deep-reaching; extending to depths of over 3,000 m (Gille et al., 2003; Olbers et al., 2004). As a consequence, this largely wind-driven current is topographically-steered with mean flow often funnelled, bifurcated, modified and/or displaced in/-downstream of areas of dominant bathymetry. Using mean kinetic energy at 250 m depth, the significance of this is illustrated in Fig. 1 (Thompson and Richards, 2011).

On a global scale, circulation of the Southern Ocean is fundamental to the thermohaline 'conveyor belt'. Surface waters from the high southern latitudes are continually replacing and overturning deep waters from the Atlantic, Indian and Pacific Ocean interiors (Toggweiler and Russell, 2008). This unique ocean is thus a key component of existing global circulation systems in terms of salt, heat and mass transport (Ganachaud and Wunsch, 2000). Furthermore, as the most significant sink of atmo-

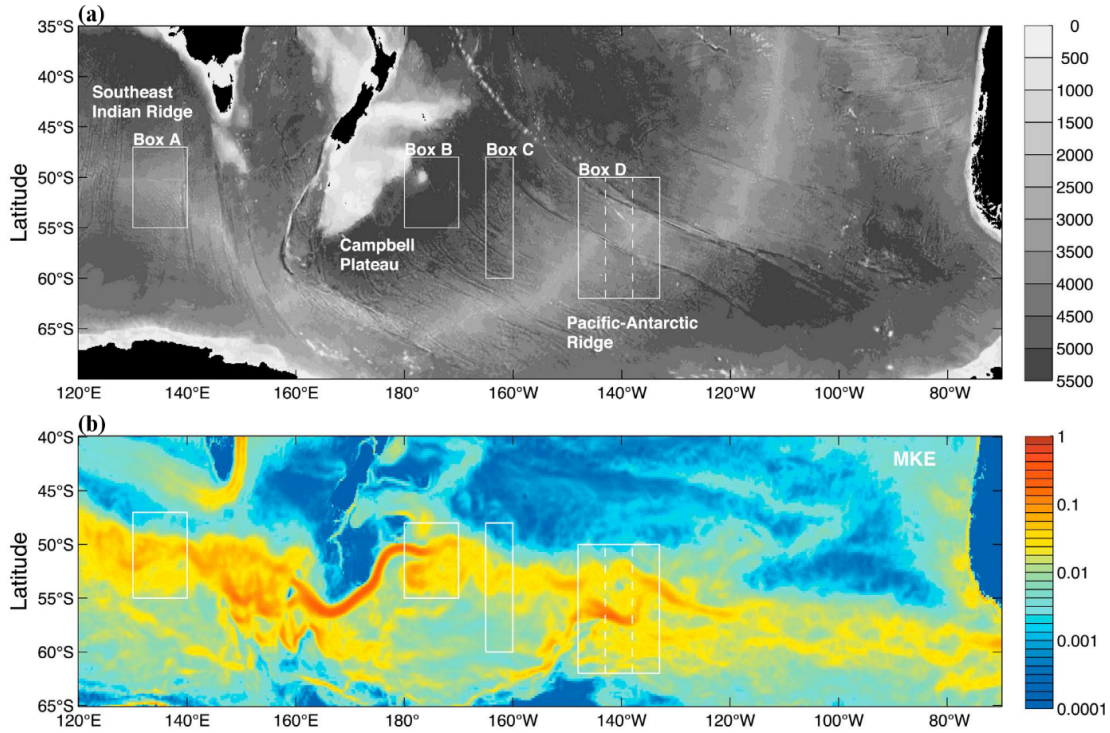


Figure 1: (a) Bathymetry of Indian and Pacific sectors of the Southern Ocean with depth in meters in greyscale, and land shown in black. (b) Mean kinetic energy ($\text{m}^2 \text{s}^{-2}$) of the ACC at a depth of 250m. Bathymetric features evident in (a), which present upstream and within boxes A-D generate the topographically-steered boundary currents, jets and eddies seen in (b). Figure from Thompson and Richards (2011).

spheric carbon, the Southern Ocean is also a key component of existing atmospheric systems (Gordon 2001; Toggweiler and Samuels 1993; Sabine et al. 2004; Watson et al., 2014), and appears to have a “disproportionate influence on the functioning of the global carbon cycle” (Boyd et al., 2010).

In response to global climate change, the Southern Ocean appears to be warming faster than the global ocean average (Gille, 2002). More specifically, these high latitude waters are responsive to effects of the Southern Annular Mode (SAM), a climate mode that is trending significantly toward its positive phase (Wang and Cai, 2013).

1.2 THE SOUTHERN ANNULAR MODE

Early studies by Rogers and van Loon (1982) and Thompson and Wallace (2000) identified the SAM as a zonally symmetric (annular) structure of circulation in the Southern Hemisphere. Centred at $\approx 50^\circ\text{S}$, it is characterised by alternating high to low pressure bands between the mid- to high latitudes polewards of 40°S (Rogers and

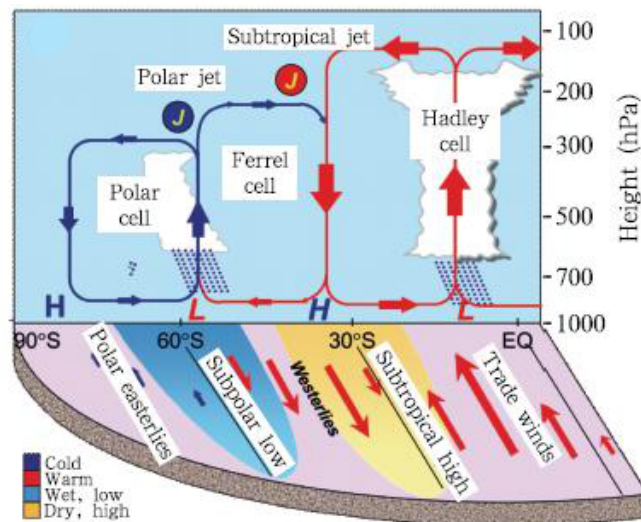


Figure 2: Atmospheric circulation in the Southern Hemisphere during the austral summer (December - February). Figure from Zheng et al. (2014).

van Loon, 1982; Ho et al., 2012). What makes the SAM so important is that it is the principal mode of variability in atmospheric circulation in the Southern Hemisphere (Thompson and Wallace, 2000; Lovenduski and Gruber, 2005; Sallée et al, 2010; Wang and Cai, 2013). Fundamentally, mechanisms driving the mode include the uneven heating of Earth's surface, and resultant energy transport and atmospheric circulation (King and Turner, 2007; Zheng, 2004) (Fig. 2).

The accumulation of heat and energy along the equator generates convergence at the surface and convection along the Inter-Tropical Convergence Zone (ITCZ) (Ho et al., 2012; Sturman and Tapper, 2006). Rising air moves poleward, slowly subsiding at the sub-tropics as heat is lost. In the Southern Hemisphere, this sinking air meets with air moving north from the South Pole, concurrently creating a region of high pressure at the sub-tropics (subsiding air from the equator at $\approx 20 - 30^\circ\text{S}$) as well as a circumpolar trough (air from South Pole rising above subsiding air from the equator at $\approx 60 - 70^\circ\text{S}$). Consequently, this process sets up longitudinally alternating regions of high and low pressure (Ho et al., 2012).

Historically, negative and positive phases of the SAM have been strongly associated with positive and negative phases of the El Niño-Southern Oscillation (ENSO), respectively. More recently, the relationship appears to have weakened due to strengthening anthropogenic global warming (Wang and Cai, 2004). Principally, ozone depletion and subsequent cooling of the Antarctic lower stratosphere is likely responsible for the SAM decoupling from ENSO forcing. Model projections suggest this will

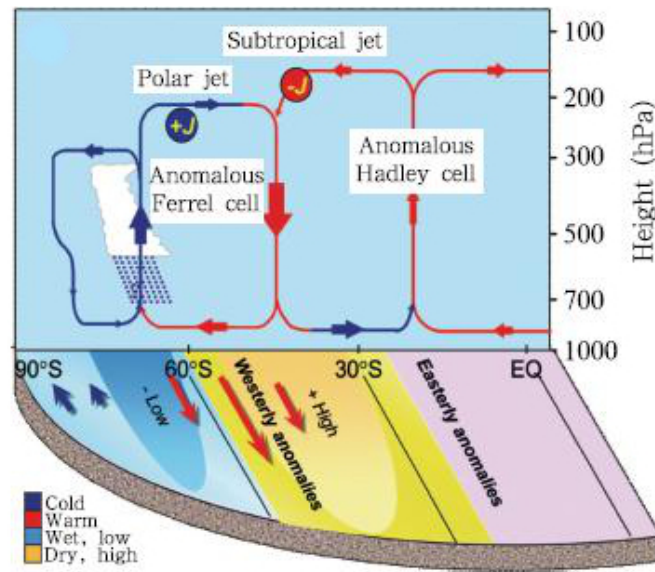


Figure 3: Circulation anomalies in the Southern Hemisphere when the SAM is positive over summer months (December - February). Figure from Zheng et al. (2014)

be reinforced by increases in greenhouse-gas forcing. Indeed, despite strong positive ENSO signals, the trend of the SAM since the mid-1970s has also been towards its positive phase (Shindell and Schmidt, 2004; Cai et al., 2005; Treguier et al., 2010; Turner et al., 2013) (Fig. 3).

A positive SAM is associated with anomalously low pressures over Antarctica, matched by anomalously high pressures at the mid-latitudes. Because the SAM is an atmospheric mode, changes in phase (positive or negative) tend to be associated with changes to atmospheric variables including air temperature, air pressure and geopotential height (Cai et al., 2005; Sallée et al., 2010; Wang and Cai, 2013). A positive SAM is also characterized by a strengthening circumpolar vortex and intensified winds contracting towards the Antarctic continent (Kidson and Sinclair, 1995; Marshall, 2003; Gille, 2014). Mediated by the mixed layer at the ocean surface, these changes in the atmosphere have appeared to affect circulation, biogeochemical cycling and physical mixing of Southern Ocean waters (Sallée et al., 2010). Based on Argo float data collected over six years, Sallée et al. (2010) showed that mixing depths in regions of the Southern Ocean differed by as much as $\pm 100\text{m}$ between positive and negative SAM events. These changes are likely to have profound impacts on the abundance and distribution of the photosynthesising phytoplankton composing the base of the marine food web (Hall and Visbeck, 2002; Oke and England, 2004; Watterson, 2000; Lovenduski et al., 2005).

1.3 PHYTOPLANKTON

Phytoplankton, from the Greek phyto (plant) and plankton (wander or drift), are predominantly single-celled, green microscopic organisms present at variable concentrations in every ocean (Falkowski and Kolber, 1995; Behrenfeld et al., 2009). Phytoplankton utilise their chlorophyll pigments to photosynthesise and, through this process of primary production, carbon is cycled between inorganic and living stocks (Behrenfeld et al., 2006). On a daily basis, more than a hundred million tons of atmospheric carbon (CO₂) are fixed into organic material by phytoplankton and then 'sunk' into the marine system (Behrenfeld et al., 2004).

The Southern Ocean is considered 'high nutrient, low chlorophyll' (HNLC) because, despite the availability of macro-nutrients such as phosphorus, nitrate and silica, standing stocks of phytoplankton remain low. Broadly, factors impacting the growth of these drifting plants can be divided into three categories, namely: physical (mixing and turbulence, stratification, solar irradiance), biological (grazing, growth rates) and chemical (nutrients, especially iron) (Sallee et al., 2015). However, interplays between physics, biology and chemistry are rarely straightforward. The dominant factors controlling phytoplankton growth in Southern Ocean HNLC waters are mixing and light, but critically iron (Boyd et al., 2010; Smetacek et al., 2004). Early analyses of satellite imagery collected by the Coastal Zone Colour Scanner (CZCS) showed an inverse relationship between ocean depth and surface chlorophyll-a concentration in the Southern Ocean (Comiso et al., 1993). More recent studies have illustrated that phytoplankton distribution is patchy - concentrated around all significant bathymetric features within the ACC (Sokolov and Rintoul, 2007; Sokolov, 2008).

In regions where the deep-reaching ACC interacts with 'significant bathymetry', non-zero bottom pressure torque is generated (Rintoul et al., 2001; Hughes, 2005). Relative vorticity of the entire water column is then affected, upwelling iron and other nutrients from the deep ocean (Moore et al., 1999; Sokolov and Rintoul, 2007). Around islands like Kerguelen, natural fertilisation of iron from the upwelled nutrient-rich water below supports large, persistent, seasonal blooms (Blain et al., 2007). In winter, light-limitation and intense mixing suppresses phytoplankton growth but low-level productivity is able to persist where the ACC encounters islands, ridges and plateaus (Moore and Abbott, 2002). In the spring, when wind-driven vertical mixing decreases

and light levels increase, the naturally iron enriched waters downstream of subantarctic islands, and along the melting ice edge and the Polar Front then bloom (Sullivan et al., 1993; Pollard et al., 2001).

Iron availability and increased phytoplankton abundance are also associated with enhanced primary productivity and carbon uptake over the Southern Ocean (De Baar et al., 1995; Watson et al., 2000). Around Kerguelen, Blain et al. (2007) found that the ratio of carbon export to iron concentration surpassed short blooms generated from iron-enriching experiments by a factor of ten. Iron is thus a key player in the carbon cycle, and changes in its availability in surface waters may have substantially impacted concentrations of atmospheric carbon dioxide over glacial–interglacial cycles (Blain et al., 2007; Watson et al., 2000).

One main projected climate-driven changes that will affect future phytoplankton patterns – and associated carbon uptake – is a shift in mixed layer depths (MLD) (Behrenfeld et al., 2006; Kemp and Villareal, 2013). The mixed layer itself is hydrographically defined; generated by previous mixing events such as turbulence from heat exchange and/or wind stress at the air-sea interface (Kara et al., 2003). It is one of the most important parameters of the upper ocean, acting as a gateway between the ocean and the atmosphere (Sallee et al., 2013) but also determining the volume over which primary productivity is distributed (Polovina, 1995; Kara et al., 2003). Despite the importance of the MLD, the methods used to determine it are relatively arbitrary. Depth is typically delineated as the shallowest point where a change in density or temperature reaches a pre-defined threshold (Kara et al., 2000; De Boyer Montégut et al., 2004; Franks 2014). However, the parameters (temperature, salinity or density) and thresholds used can vary significantly depending on the particular ocean being studied, time of year, or the preference of the author (Miller, 1976; Levitus 1982; Lewis et al., 1990, de Boyer Montégut et al., 2004).

Importantly, the mixed layer is distinct from the mixing layer, which is the zone where active mixing is currently taking place (Brainerd and Gregg, 1995).

As an air-sea interface, the properties of both mixed and mixing layers are strongly influenced by atmospheric processes such as mechanical stirring (wind stress) and buoyancy forcing (air-sea heat flux) (Sallee et al., 2010). Active mixing and high turbulence would be expected to impact phytoplankton growth by affecting light availability (physical) and access to iron or other limiting nutrients (chemical) (Sallee et al., 2010). Indeed, conditions most favourable for phytoplankton growth during the

austral summer include shallower mixed layers associated with elevated light levels (Krishnamurthy et al. 2008). The Southern Ocean iron-release experiment (SOIREE) (Boyd et al., 2010) was the first of thirteen *in situ* ocean iron fertilization (OIF) experiments to take place in the Southern Ocean (Yoon et al., 2016). Results illustrated that phytoplankton growth increased within iron-enriched zones during summer months when MLDs were at 45m and 65m. Conversely, over the same period, standing stocks showed no measurable improvement in zones with deep MLDs of 100m, suggesting light limitation or co-limitation with iron. These findings were supported by subsequent OIF cruises including the Southern Ocean iron experiment (SOFeX) (Coale et al., 2004; Krishnamurthy et al. 2008).

Over the austral summer months that are key for phytoplankton growth, the depth of the mixed layer is still sensitive to wind-driven vertical mixing. In open waters flanking the Polar and subantarctic Fronts, MLDs can exceed 100m over December and January. However, mixed-layers tend to decrease from north to south across the ACC, with concurrent increases in macro-nutrients and light (Boyd et al., 2010). By altering the prevailing westerly winds and perturbing physical mixing processes (through stirring), an increasingly positive SAM has the potential to also affect chemical cycling regimes (Lovenduski and Gruber, 2005; Sallee et al., 2010). The consequences for primary production and carbon cycling are unknown, though anomalies in MLDs have already been cited as drivers of change to phytoplankton abundance and distribution (Lovenduski and Gruber, 2005; Sallee et al., 2010).

To directly measure spatio-temporal phytoplankton patterns in our dynamic oceans is extremely challenging. Estimates are most often derived through measures of the photosynthetic pigment chlorophyll-a (Chl-a). Methods such as high-performance liquid chromatography (HPLC) are the most accurate at quantifying *in situ* Chl-a concentrations. However, these types of data collection tend to be limited to ship-based work along narrow transects. Alternatively, low-cost and non-invasive submersible fluorometers can be deployed on a range of platforms to approximate phytoplankton abundance and distribution in both the vertical and horizontal. For these reasons, fluorescence has been used widely as a proxy for phytoplankton abundance since the 1960's (Lorenzen, 1966; Cullen and Eppley, 1981; Falkowski and Kolber, 1995; Lavigne et al., 2012).

Despite the widespread use of fluorescence, this method still essentially generates point measurements in space and time. Thus, while fluorometer-derived *in situ*

datasets are enormously useful, they're rarely sufficient for studies seeking to examine 'bigger picture' spatial patterns. In these cases, remotely-sensed ocean colour observations generate the most comprehensive data for monitoring phytoplankton abundance on global, synoptic scales (Dierssen and Smith, 2000; McClain, 2009).

1.4 OCEAN COLOUR

As with fluorometers, ocean colour sensors are able to use the photosynthetic pigment Chl-a to estimate phytoplankton abundance and distribution. However, in this case, the information is collected remotely - from low earth orbit (Morel and Prieur, 1977; Gordon and Morel, 1983; Falkowski et al., 1998, Henson et al., 2010). Remote ocean colour sensors aboard different satellites are able to measure the small proportion of incident radiation not absorbed by the ocean and its constituent components. This is an average derived from the surface to 'one optical depth' - the depth to which satellites can 'see' (McClain, 2009). In the most optically non-complex (clear) waters, this depth rarely exceeds 20-25m (Kemp and Villareal, 2013).

The Moderate Resolution Imaging Spectroradiometers (MODIS) are sensors currently flying aboard the Terra and Aqua satellites. MODIS is what is known as a 'whisk-broom scanner' or spotlight sensor (across track scanner), and it uses optical cameras to obtain satellite images. This technology is used for passive remote sensing, where a mirror on the instrument in space is engaged to scan the earth across the satellite's path, reflecting light into a single detector. The mirror moves back and forth, collecting information one pixel at a time, resulting in relatively higher resolution data (King et al., 2013). There are 36 spectral bands on 4 focal plane assemblies that image the earth in a swath measuring 2330km across (cross-track) and 10km long (along-track) for each sweep of the mirror (King et al., 2013). The invaluable data returned by MODIS extends from global monitoring of terrestrial ecosystems to a vast range of ocean colour properties. The wide spectral range, frequent global coverage, and two high spatial resolution bands also allow for monitoring and measuring of atmospheric profiles, including air column water vapour and aerosol particles, and resulting cloud formation (King et al., 1992; King et al., 2003; King et al., 2013).

At Goddard Space Flight Centre (USA), MODIS data are received and processed into 5-minute granules (\approx 2000km long along the orbital track, and 2330km across the orbital track), generating approximately 244 granules (files) per day, per product

(King et al., 2013). Data are then processed into 3 levels and made freely available on the NASA Ocean Colour home page (<http://oceancolor.gsfc.nasa.gov/>). Level-1 data are measurements where radiances and brightness temperatures have been geolocated. Level-2 data are derived geophysical data products at the same resolution and location as the Level-1 data. Finally, Level-3 measurements are data that have been aggregated onto uniform space-time grid (1x1 latitude-longitude) scales (King et al., 2013).

For 'typical' end-users of ocean colour data, surface Chl-a concentration ([Chl-a]) can be freely accessed as a Level-3 standard product, and these data are widely used for monitoring and measuring the abundance and distribution of phytoplankton. However, NASA also provides a range of evaluative (under evaluation) Level-3 products. One such product is Z_{eu} - the depth of the 1% light level. This measure of light attenuation is often used as the approximate depth of the euphotic zone, or as a general measure of water clarity.

Remote sensing is an invaluable tool for measuring and monitoring our earth systems, however, satellite-derived measurements are not without caveats. In summer months, for example, sunlit waters populated by photosynthesising phytoplankton can extend 4 times deeper than one optical depth (Aksnes et al., 2007; Shang et al., 2011). This is a significant limitation because phytoplankton show complexity on vertical scales. On horizontal scales, accuracy in surface waters can also vary depending on the region being studied. This is true for optically complex waters with high concentrations of coloured dissolved organic material (CDOM or Gelbstoff). These waters tend to be coastal or near-coastal. Polar oceans are also a challenge due to low signal to noise ratios, sun angle, glint, cloud cover and sea-ice (Dierssen and Smith, 2000; McClain, 2009). Despite innovative improvements, these limitations at the ocean surface and at depth are not likely to be resolved with the new generation of ocean colour satellites (McCain et al., 2006). Continued collection of *in situ* data to qualify and quantify phytoplankton is thus essential (Johnson et al., 2009).

1.5 ELEPHANT SEALS AS SEMI-LAGRANGIAN SAMPLING PLATFORMS

At the very high latitudes where warming is rapid, both satellite coverage and *in situ* observations are hindered by the prevailing conditions, and are thus limited in availability (Gille, 2002). With regard to collecting *in situ* data in the Southern Ocean, con-

ventional methods rarely achieve measurements on extensive spatio-temporal scales. Shipboard observations and sampling are expensive and also confined to narrow transects, and autonomous instruments are vulnerable to damage from ice. Fortunately, recent adaptations to ARGO float technology include ice-avoidance software and hardened antennae (van Wijk et al., 2009). The addition of gliders to the sampling arsenal is showing promise (Johnson et al., 2009), as are 'less conventional' methods of ocean sampling, namely: the tagging of Southern elephant seals (*Mirounga leonina*) with instruments that measure oceanographic and behavioural data in near-real time (Fedak, 2004; Boehme et al., 2008a,b; Charrassin et al., 2010; Fedak, 2013). Advances in tag development have made it possible to track the extensive marine migrations of southern elephant seals for several months at a time, while simultaneously recording and relaying oceanographic data. Conductivity, temperature and depth satellite-relayed data loggers (CTD-SRDLs) developed at the Sea Mammal Research Unit (University of St. Andrews, Scotland) are capable of transmitting vertical profiles of salinity (conductivity resolution, 0.003 mS cm^{-1} ; accuracy 0.04 mS cm^{-1}), temperature (resolution 0.001°C ; accuracy 0.02°C) and pressure to depths of approximately 2000m (Boehme et al., 2008; Boehme et al., 2009).

Since 2004, southern elephant seals from a number of islands within the ACC have been tagged with CTD-SRDLs. Since 2008, adult females from Kerguelen and Marion Island have also been tagged with fluorometers and light meters. From an optical perspective, these fluorescence and light data are invaluable for ground-truthing of Level-3 [Chl-a] and Z_{eu} products, respectively. Particularly in the Southern Ocean, where *in situ* data is sparse and satellite coverage so patchy. As instrument platforms with wide-ranging foraging behaviour, these marine predators routinely collect data in regions inaccessible to other autonomous sampling technologies. Moreover, their shifting foraging patterns may also provide clues on the status of the underlying marine food web - from the bottom to the top (Sergio et al., 2008).

Elephant seals do not eat phytoplankton and their at-sea distributions may not be impacted on by the presence/absence of these microscopic cells. In other words, animals may coincidentally encounter patches of elevated phytoplankton during travelling and foraging phases. While evidence suggests that distributions of some marine animals at the top of the food chain are driven by primary productivity (Humphries et al, 2010, Kai et al, 2008; Ainley et al, 1991; Biuw et al, 2007; Sims et al, 2008;

Weimerskirch, 2007; Richardson and Schoeman, 2004), how likely is this to be true for southern elephant seals?

We cannot directly observe how southern elephant seals interact with their environment or their prey. As a result, proxies are used. Movement data from seals (on horizontal and vertical scales) can then be examined in relation to environmental parameters, and inferences made on the processes affecting behaviour. In order to better understand the foraging patterns of southern elephant seals, many studies have already tried to link their at-sea behaviour to the components of their environment, including:

- Temperature
- Salinity
- Mixed Layer Depth
- Light
- Bathymetry
- Sea surface height
- Eddies
- Front position
- Sea-ice

(Boyd and Arnborn, 1991; McConnell et al., 1992; Bradshaw et al., 2004; Bailleul et al., 2007; Biuw et al., 2007; Simmons et al., 2007; Biuw et al., 2010; Maxwell et al., 2011; Jaud et al., 2012; Vacquie-Garcia et al., 2012; Dragon et al., 2012; Costa et al., 2010).

As noted by Biuw et al. (2007), some studies show clear results while others are more ambiguous. Unless the physical data is retrieved by the seals themselves, there is typically a mismatch in spatial and/or temporal resolution. Adding to this is the fact that the Southern Ocean is not a heterogeneous environment and seals will forage in waters that are not spatially, chemically, physically or biologically alike. It's not surprising then that so many studies produce different answers to the same question: what drives southern elephant seal behaviour at sea?

Before we can answer this, we must consider why the question is relevant. Understanding how biogeochemical drivers impact free-ranging marine predators is useful if we are to predict the 'unseen' consequences of a warming world. Tertiary consumers in any given ecosystem are often the most sensitive and responsive to

ecosystem dysfunctions (Sergio et al., 2008). The success of southern elephant seal populations appears to mirror the health of their environment, with historical fluctuations coupled to changes in the marine environment (McMahon et al., 2005; Biuw et al., 2007). Information on these marine predators may thus also offer clues on the stability of the marine food web upon which they are dependant.

1.6 IN CONCLUSION

It appears certain that the SAM is already altering biogeochemical cycling through wind-driven changes to circulation and physical mixing. Via complex interplays between mixing, light and iron, perturbations initiated through the SAM will have implications for existing phytoplankton patterns (Hall and Visbeck, 2002; Oke and England, 2004; Watterson, 2000; Lovenduski et al., 2005). This is critical because changes to primary production will undoubtedly impact on energy flow and transport for the entire Antarctic ecosystem, and have consequences for larger ocean and atmospheric processes.

Satellite derived data are the most comprehensive measurements available for measuring phytoplankton patterns on useful spatial scales. Currently, however, the ocean colour time series is likely too short for differentiation of global climate change signals from interannual and decadal variability (Henson et al., 2010). Because the Southern Ocean is regionally influenced by the SAM on shorter timescales that are measurable (Thompson and Wallace, 2000; Lovenduski et al., 2005), this limitation may not apply. Improved understanding of the potential footprints of the SAM should provide valuable information on how Antarctic ecosystem dynamics are being/ will be affected. Furthermore, any new information may serve to improve our interpretations of historical atmospheric-ocean variability, as well as provide improved parameterization for regional biogeochemistry-ocean circulation models and global climate models.

For several years, tagged southern elephant seals have collected *in situ* data that is potentially useful for evaluating the accuracy of satellite products in the high southern latitudes. Moreover, their utility extends beyond their status as animal platforms and knowledge on elephant seal foraging behaviour may also be linked to the underlying food web as a whole (Sergio et al., 2008).

1.7 PHD OBJECTIVES

This body of work is composed of four themes, the first of which assesses the accuracy of *in situ* light data and fluorescence data collected by tagged southern elephant seals, and reviews the strengths and limitations of the data. Included in this thesis are the quality control methods that were developed to improve the accuracy and representability of these data, described within the context of comparison with remotely sensed data. For the second theme, because of the inherent limitations associated with remote sensing in the high latitudes, the quality-controlled *in situ* light data and fluorescence data are examined along-side remotely-sensed measures of MODIS Chl-a and the depth that sunlight is attenuated to 1% of its surface value, (MODIS Z_{eu}), respectively. Based on findings from this investigation, MODIS (Z_{eu}) is then introduced as a proxy for Chl-a. The third theme focuses on determining if changes to phytoplankton abundance and distribution in the Southern Ocean can already be measured in the MODIS Aqua satellite record. Climatologies, trends and anomaly maps are produced based on 12 years of ocean colour and cloud cover data, and any changes are examined for correlation with trends in the Southern Annular Mode. Finally, this thesis investigates whether the at-sea horizontal movement patterns of the tagged southern elephant seals are independent of the fluorescence and light data (as proxies of phytoplankton) that they collect. Seals exhibiting area restricted search (ARS) behaviour are specifically used for this study, and transit rates are input into a novel cumulative sums method for determining three behavioural phases, namely: outbound, foraging and homeward-bound.

Because of the different approaches and methods required for each dataset, chapters are divided by type of data (light, fluorescence, MODIS products, seal behaviour) rather than theme.

In the first data chapter, Chapter 2, two satellite-derived measures of the depth of the 1% light level, (Z_{eu}) are examined relative to light intensity data collected by a number of instrumented seals (Table ??). Because of self-shading and environmental factors such as cloud, waves, foam and bubbles, the *in situ* dataset is first processed to smooth out noise from signal. The resulting *in situ* measures of the depth of the 1% light level are then used to evaluate the accuracy of the two remotely sensed Z_{eu} products.

Instrument	Year	Tag Number	With Flouro	Chapters
Time-Depth Recorder (TDR) Light Meter	2009	TDR_2009-2	-	2 and 7
		TDR_2009-3	-	
		TDR_2009-5	Yes	
		TDR_2009-8	Yes	
		TDR_2009-10	-	
		TDR_2009-11	Yes	
	2010	TDR_2010-9	-	
		TDR_2010-11	-	
		TDR_2010-19	-	
		TDR_2010-20	-	
		TDR_2010-21	-	
	2011	TDR_2011-13	-	
		TDR_2011-18	-	
		TDR_2011-21	-	
		TDR_2011-27	-	
		TDR_2011-28	-	
	2012	TDR_2012-2	-	
		TDR_2012-4	-	
		TDR_2012-8	-	
		TDR_2012-9	-	
		TDR_2012-14	-	
	2013	TDR_2013-1	-	
		TDR_2013-2	-	
		TDR_2013-3	-	
		TDR_2013-4	-	
		TDR_2013-6	-	
	2014	TDR_2014-22	-	
		TDR_2014-23	-	
		TDR_2014-28	-	

Table 1: Available time, depth and light intensity data used for this thesis, detailing year of deployment, and which chapters the data were used for. Additionally, the three seals that had a TDR light meter deployed alongside the FCTD data loggers are shown. All TDR light meters were deployed from Kerguelen Island.

Instrument	Year	Tag Number	With TDR	Deployment	Chapters
Fluorometer, Conductivity, Temperature and Depth Satellite-Relayed Data Logger (FCTD-SRDL)	2009	ft03-Cy1-09	Yes	Kerguelen	2 and 7
		ft03-Cy2-09	Yes	Kerguelen	2 and 7
		ft03-Cy4-09	Yes	Kerguelen	2 and 7
		ft03-Cy5-09	-	Kerguelen	2
		Ft03-Cy11-09	-	Kerguelen	2
	2010	ft06-Cy14-10	-	Kerguelen	2 and 7
		ft06-Cy16-10	-	Kerguelen	2 and 7
		ft06-Cy20-10	-	Kerguelen	2 and 7
	2011	ft10-Cy31-11	-	Kerguelen	2
		ft10-Cy33-11	-	Kerguelen	2
		ft10-Cy35-11	-	Kerguelen	2 and 7
	2012	ft12-Cy35-12	-	Marion Island	2 and 7
		ft12-F1-12	-	Kerguelen	2 and 7
		ft12-F3-12	-	Kerguelen	2
		ft12-F4-12	-	Kerguelen	2 and 7
	2013	ft14-F4-13	-	Kerguelen	2 and 7
2014	ft18-F2-14	-	Kerguelen	2 and 7	
2015	ft19-15f-15	-	Kerguelen	2 and 7	

Table 2: Available fluorescence, salinity and temperature data used for this thesis, detailing year of deployment, where animals were tagged, and which chapter the data were used for. Additionally, the three seals that had a TDR light meter deployed alongside the FCTD data loggers are shown.

In Chapter 3, based on the results from Chapter 2 and using a novel processing method, *in situ* fluorescence data collected by seals tagged with FCTD-SRDLs are corrected for non-photochemical quenching (Table ??). This method successfully addresses the problem of quenching in surface waters, but the real strength of the method is that it also allows for conservation of deep chlorophyll maxima present between Z_{eu} and mixed layer depth. The presence of these deep features is presented in Chapter 4, and their relevance is discussed. In Chapter 5, the now quenching-corrected, vertically-integrated fluorescence dataset is used to evaluate the accuracy of remotely-sensed measures of [Chl-a].

Chapter 6 makes use of the MODIS Aqua products evaluated in the preceding chapters, with the addition of cloud data. For each product, climatologies are first built to show overall patterns of [Chl-a], Z_{eu} and cloud fraction. The anomalies are extracted by removing seasonal signals, and respective changes in depth, concen-

tration and percentage cover are evaluated over the 12-year record. Thereafter, any significant changes in trend are examined relative to the Southern Annular Mode, thus satisfying the primary objective of this thesis.

Previous studies examining relationships between foraging behaviour and remotely-derived measures of phytoplankton abundance have had limited success. Chapter 7 examines if this is due to a mismatch in scale/resolution by using concurrently collected *in situ* data instead. Applying a novel cumulative sums analysis of transit rates, slower swim speeds are used as a proxy for foraging behaviour. Quenching-corrected, vertically-integrated fluorescence and the 1% light level data are used as proxies of phytoplankton abundance, where prey species are more likely to be present.

EVALUATING THE ACCURACY OF MODIS Z_{EU} USING *IN SITU* LIGHT DATA RETRIEVED BY TAGGED SOUTHERN ELEPHANT SEALS.

2.1 BACKGROUND

Within the upper layers of our global oceans, light is a key factor; controlling everything from primary productivity to the distribution of marine predators and their prey within the water column. In pure water, light is diminished with depth by the complex and non-linear interactions between absorption and scattering (Kirk 1994). Despite the complexity of these processes, *in situ* measurements of underwater irradiance show an exponential decay of light with increasing depth. In 'impure' water, however, light penetration through the water column is controlled by the materials that are dissolved and suspended within. For this reason, for studies of water clarity (and quality), knowledge on the rate of light attenuation is considered an important parameter for monitoring the amount of dissolved, suspended, organic or inorganic material in surface waters (Zhao et al., 2013; Davies-Colley and Smith, 2001). Specifically, the depth where light is attenuated to 1% of the surface value can be applied broadly as a measure of water clarity (Lee et al., 2007).

The depth at which downward photosynthetically available radiation (PAR) is attenuated to $\approx 1\%$ of the near-surface value is also generally accepted as the depth of the euphotic zone. Biologically, the depth of the euphotic zone is relevant as the limit where light is still sufficient to support photosynthesis, and is thus important for primary productivity studies (Shang et al., 2011). For the next two chapters, knowledge on the depth of the 1% light level will be functional: used as the reference depth from which light is no longer sufficient to cause quenching and, therefore, the depth from which it can be corrected. This will be described in detail in Chapter 3 and 4, suffice to say here that measures of the 1% light level are useful for a number of reasons.

To my knowledge, only a couple of studies have applied *in situ* light level parameters to infer [Chl-a] (Teo et al., 2009; Jaud et al., 2012). This is possibly because the 1% light level is only measurably related to phytoplankton abundance under very specific circumstances, namely: Case-1 conditions.

Through a classification scheme introduced by Morel and Prieur (1977), oceanic waters are defined as either Case-1 or Case-2 (also Gordon and Morel, 1983). The former is true when phytoplankton are the primary drivers of variation in optical properties of the water. Associated biological materials (grazing debris and released dissolved organic matter, natural decay) plus organisms co-existing with phytoplankton (flagellates, bacteria and viruses) can also affect Case 1 optical properties (Morel and Ahn, 1991; Stramski and Kiefer, 1991; Ulloa et al., 1992). The key requirement is that variations stemming from other substances remain relatively small and remain relatable to phytoplankton concentration (IOCCG, 2000). The shift to Case-2 waters occurs when suspended inorganic particles (sediment, minerals) and yellow substances CDOM (coloured dissolved organic matter) significantly influence optical properties (Sathyendranath and Morel, 1983).

The open waters of the Southern Ocean are considered to be largely Case-1. Therefore, the main source of particles in the upper sunlit layer are expected to be phytoplankton, with vertical light attenuation primarily affected by phytoplankton and covarying concentrations of their associated detrital products.

The depth of the 1% light level is provided as a MODIS evaluative ocean colour product, Z_{eu} . Two algorithms are applied by the NASA Ocean Biology Processing Group (OBPG, Greenbelt, MD, USA), the outputs of which are provided freely as Level-3 (L3) data. The first is the Morel et al. (2007) Chl-approach, where Z_{eu} is calculated empirically from remotely derived surface Chl-a concentrations ([Chl-a]). This approach is inherently based on Case-1 assumptions, where Case-1 is defined as waters where phytoplankton (and their associated detrital elements) are the only optically active constituents (Morel et al., 2007). The second approach is the Lee et al. (2007) algorithm, which does not assume that the optical properties of the waters being measured (and, thus, subsurface light field) are affected 'only' by phytoplankton. Instead, Lee's measure of Z_{eu} is based on the principle that vertical variation of the light field is determined by underwater inherent optical properties (IOPs) (Lee et al. 2005; Lee et al., 2007). Using Lee's IOP-centered approach, the attenuation coefficient of visible light is modelled as an analytical function of water's absorption and

backscattering coefficients. Vertical attenuation of visible light is essentially identical to vertical attenuation of PAR (Lee et al., 2005; Morel and Gentili, 2004; Lee et al., 2007), thus when absorption and backscattering coefficients at a wavelength of 490 nm (in particular) are known, Lee's Z_{eu} can be calculated.

For simplicity, from this point, Z_{eu} calculated using the Lee et al. (2007) algorithm and Z_{eu} calculated using the Morel et al. (2007) algorithm are referred to as Lee Z_{eu} and Morel Z_{eu} , respectively.

Work done by Shang et al. (2011) on and off the shelf of the China Sea has shown that both algorithms produce reliably accurate Z_{eu} products. However, due to the uncertainty introduced by the empirical measure of [Chl-a], and the empirical relationship between [Chl-a] and Z_{eu} , Morel's estimation of the 1% light level proved to be significantly less accurate than Lee's (Shang et al., 2011). This is not unexpected as the China Sea waters from this study are subject to high suspended sediment load from major river system runoff and, thus, do not strictly conform to Case-1 assumptions.

The open waters of the Southern Ocean are thought to largely conform to Case-1 assumptions (Rasmus et al, 2004). However, in some studies, this assumption has been challenged (Tripathy et al, 2011). Presumably, if phytoplankton and their detrital components were the only actively complex materials in the Southern Ocean, Morel's measure of Z_{eu} would be sufficient for estimating the 1% light level. However, if circumstances exist where Case-1 assumptions are not true for these waters, the use of Lee's Z_{eu} would be the more robust approach. Either way, based on Shang's work in the China Sea, it should be possible to evaluate the accuracy of both Z_{eu} estimates in waters that are generally understood to be 'optically non-complex' using *in situ* measures of the 1% light level. For this study, however, the temporal retrieval of remotely sensed Z_{eu} and the method of *in situ* light collection are sufficiently different to prevent replication. Shang et al. (2011) utilised remotely derived Z_{eu} data at their most accurate - near daily. In our region of interest, however, this is not viable due to extensive and persistent cloud cover (Fig. 4).

Over the austral summer, when light is less limiting and satellite-derived ocean colour measures are most desirable, the fraction of ice cloud over the Southern Ocean tends to increase (King et al., 2013). Because ocean colour sensors are passive and cannot 'see' through clouds, this compounds the existing problems associated with monitoring of phytoplankton at these high latitudes. Temporal merging allows for the

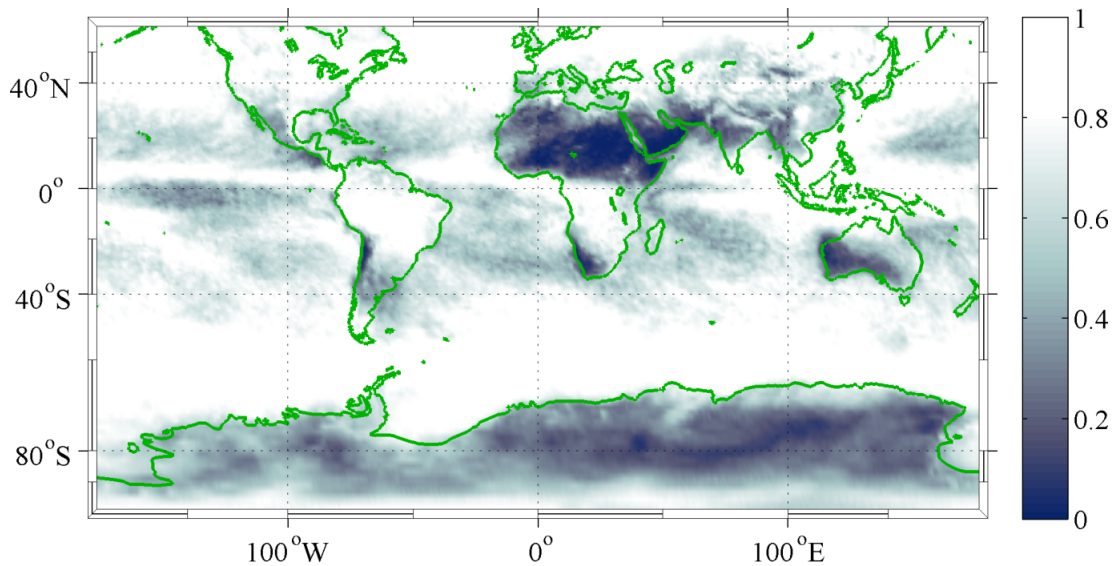


Figure 4: Mean MODIS daytime cloud fraction for December 2014. This map illustrates how the Southern Ocean is persistently blanketed by cloud over the austral summer, with white showing 100% mean cloud coverage and black representing little to none.

'filling in' of gaps in space, and 8-day and monthly products are available for both Lee and Morel Z_{eu} (Fig. 5). This improvement in spacial coverage understandably comes at a cost to temporal accuracy. Nonetheless, for a range of ocean colour data in the Southern Ocean, the use of monthly products is necessary and common (discussed in Takao et al., 2012). In this chapter, I will assess the use of 8-day data, which leaves gaps in the along-track seal data, compared with a combined 8-day-Monthly product, where temporal gaps are as filled as possible.

When combining such merged satellite products with *in situ* data, the latter is not necessarily less problematic than the former. This is perhaps especially true when the *in situ* data in question are collected by instrument 'platforms' with behavioural 'quirks'. Increasingly, a variety of novel animal-borne instruments have been facilitating the collection of a wide range of environmental data (Block et al. 2002, Costa et al. 2002, Polovina et al. 2004, Weng et al. 2005, Biuw et al. 2007, Teo et al. 2009). Since 2004, Conductivity, Temperature and Depth-Satellite Relay Data Loggers (CTD-SRDLs) deployed on free-ranging southern elephant seals have provided access to remote and under-sampled regions of the Southern Ocean (Roquet et al., 2014). Data collected by these animal-platforms is becoming increasingly accessible and well integrated through portals such as MEOP (Marine Mammals Exploring the Oceans Pole to Pole) and coordination bodies such as GOOS (Global Ocean Observing System). This is in part thanks to the accuracy and reliability of the hydrographic data

collected by CTD-SRDLs (Boehme et al., 2009). However, *in situ* data collected by instruments 'ancillary' to the main CTD tags require additional custom processing. This data includes fluorescence and light.

For this study, measures of light intensity through the water column were collected by instrumented female southern elephant seals.

Being aware of caveats and/or limitations associated with *in situ* information as well as remotely sensed data is important when attempting to compare them. Nonetheless, the pairing of the two is beneficial, and the usefulness extends both ways. For remotely-derived data, ground truthing with *in situ* data is valuable, especially in under-sampled and/ or cloudy regions. For the *in situ* data, even extensive sampling generates point collections in vast ocean systems. Coupling of satellite and *in situ* data thus serves to help ground-truth the former and enhance spatial relevance of the latter. The challenge is to make the two sources of data as equivalent as possible.

In this chapter, novel datasets of high resolution light measurements collected by tagged southern elephant seals are evaluated alongside remotely derived Z_{eu} at 4km (medium) resolution. The representability of the MODIS product relies on relative homogeneity within each pixel. In the open waters of the Southern Ocean, testing against *in situ* data allows for evaluation of the accuracy and relevance of the coarser resolution data. However, spatial caveats are not unique to the remotely sensed data. Positional estimates for the tagged seals relies on Doppler shift rather than GPS. The accuracy of each location thus depends on the number of uplinks received by an Argos satellite, the temporal pattern of these successful uplinks, as well as the position of the Argos satellite relative to the transmitting tag (Vincent et al., 2002). Locations are provided with a location class (LC) that estimates the radius of uncertainty associated with each positional estimate (Service Argos, 2010). These error radii encompass the 68th percentiles predictions (separately for latitude and longitude) rather than the full error (Costa et al. 2010). Studies on free-ranging animals reported larger errors than those indicated by Argos (Costa et al. 2010; Silva et al. 2014). To reduce error and uncertainty, the 'analysis-ready' data supplied by SMRU is normally quality controlled through application of a location filtering algorithm and a maximum speed cut-off of 2 m s^{-1} (McConnell et al. 1992). The filtered locations are then used to interpolate possible locations for future positions in space, based on time.

A second caveat associated with the light measurements collected by seals is how sensitive the data are to external variables. The *in situ* light data are used to calculate

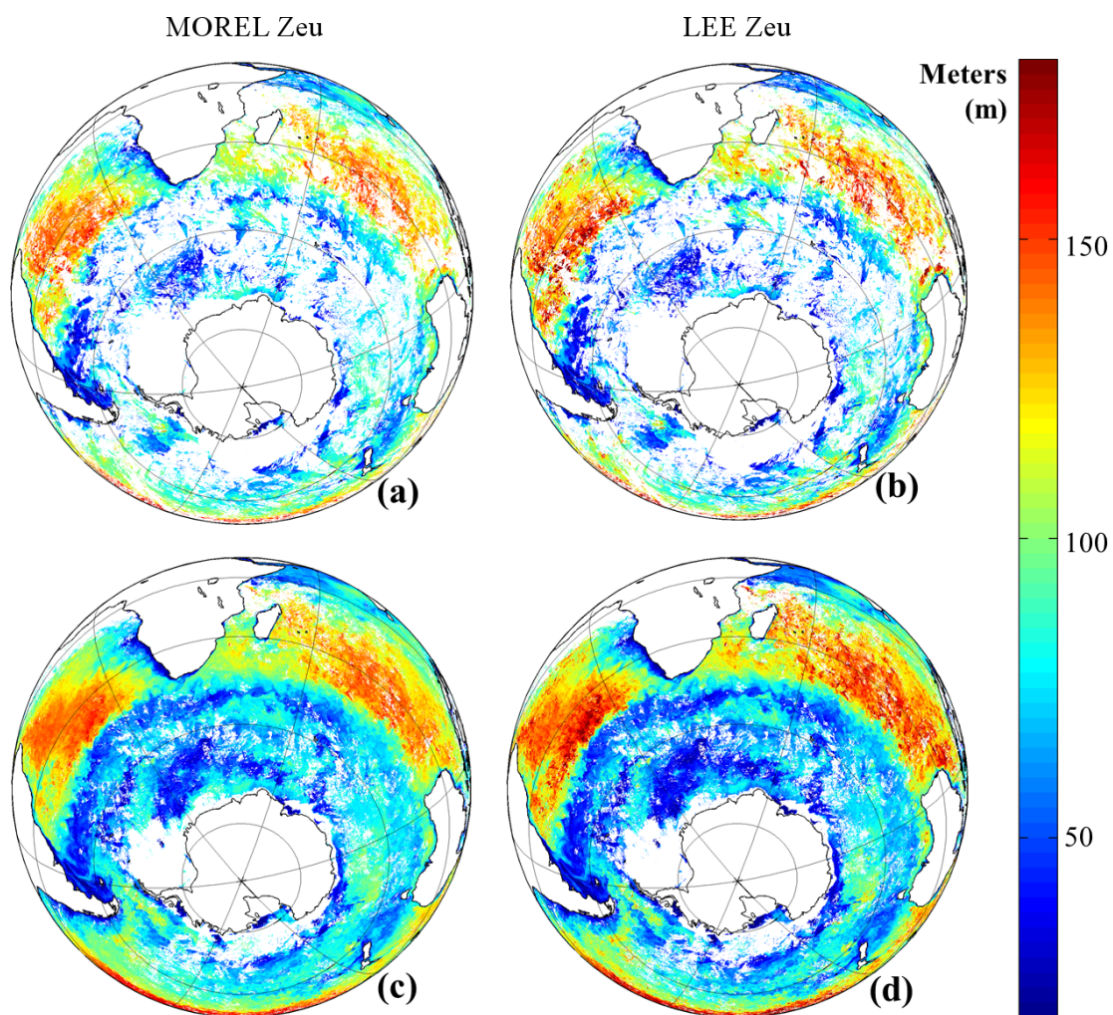


Figure 5: Merged composites of two MODIS Z_{eu} products, both measured in meters (m) and both 'representative' of the depth of the 1% light level. The depth of the 1% light level is shown as an 8-day merged product in the top row of figures (a) and (b). The bottom row of figures (c) and (d) represents the 1% light level for all of January 2015 (monthly product). These temporally-merged data are available as level 3 products, calculated using either the Morel et al. (2007) algorithm (first row) or the Lee et al. (2007) algorithm (second row).

the depth at which sunlight reaches 1% of its value at the surface - a relative value representing how light is interacting with the water column and its dissolved and/or suspended constituents. Results are thus meant to provide information on the properties of the water column. To account for fluctuations in light that are unrelated to the water column, data must first undergo quality control. Factors that contribute to fluctuations through shading or scattering include cloud, sun angle (time of day), waves and foam/ bubbles. The less conventional variable is self-shading of the TDR light sensor by the seal itself during diving/ surfacing/ swimming/ feeding behaviour. Instruments that are shaded at the surface will still provide a 1% light level with depth, but this will be a measure relative to shaded light rather than the 'true' ambient light field. Results will thus not provide reliable information on the properties of the water column, and the *in situ* data will not be suitable for assessing accuracy of remotely sensed data.

After accounting for fluctuations and calculating the depth at which light attenuates to 1% of its near-surface value, *in situ* measures of the 1% light level are compared with the two MODIS Z_{eu} products representing the depth at which PAR is reduced to 1% of the surface value (Shang et al., 2011; Soppa et al., 2013). To my knowledge, only one other study has tested the accuracy of Morel and Lee's estimations of Z_{eu} in the Southern Ocean. Soppa et al. (2013) based their evaluation of Z_{eu} on HPLC-derived Chl-a concentration, grouped together from various ship-based sampling studies between 1997 and 2008. The results from that study are ultimately compared with the work I have done as part of this chapter.

2.2 MATERIALS AND METHODS

2.2.1 *In-situ measures of the 1% light level*

Over the austral summer months spanning 2009 - 2015, a total of thirty-five post-breeding female southern elephant seals from Kerguelen Island were tagged (Fig. 6) with SPLASH₁₀-Fast-Loc GPS instruments; combining a time-depth recorder (TDR), a global positioning system (GPS) logger, an Argos satellite-relay instrument and a data storage logger (Wildlife Computers). These SPLASH₁₀ devices were programmed to archive the GPS location data (position recorded every 20 minutes, if the an-

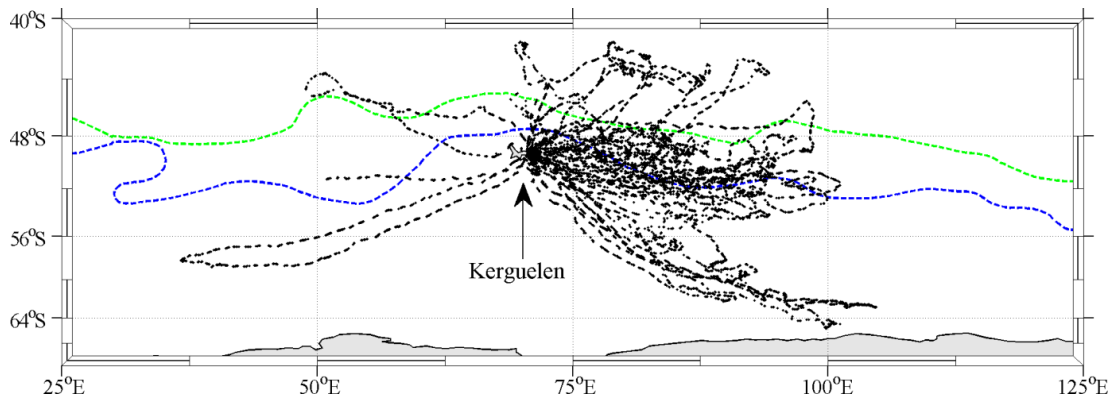


Figure 6: Tracks of 35 southern elephant seals (in black) tagged with light meters over the austral summers spanning 2009 to early 2015. The general positions of the Sub Antarctic Front and the Polar Front are shown in green and blue, respectively (Orsi and Harris, 2014).

imal was at the surface) and relay the Argos messages used to estimate positions (<http://www.argos-system.org>).

Four types of TDRs were deployed over the 6 years: MK9 with no addition to the TDR, MK10-fast_loc with the addition of GPS, MK10X with the addition of an accelerometer and MK10-DDT with a magnetometer (daily diary tag) (Tables 3-4). All versions of TDR loggers collected and stored measurements of pressure (surface to 1500m, ± 1 m), temperature (-40 to $+60^{\circ}\text{C}$, $\pm 0.1^{\circ}\text{C}$) and light intensity (from 5×10^{-2} to $5 \times 10^{-12} \text{ W cm}^{-2}$ in the blue spectrum) every 1 - 2 seconds (C. Guinet 2015, Pers. Comm., 01 April 2015). The main difference between TDRs was the orientation (and thus direction of capturing light) on the seal, with light either measured 'upwards', 'forwards', 'backwards' or to the 'right'. Most often, only one or two types of TDR loggers would be glued to the seal, but a few individuals had the maximum of four at a time (Tables 3-4).

Once measured, light level values were processed identically and were log-transformed onboard (compressed) into 3 digit values (Fig. 7 from Jaud et al., 2012).

All female seals selected for instrument deployment were anaesthetised with an intravenous injection of tiletamine and zolazepam 1:1 before being tagged. Patches of fur required for tag placement were cleaned with acetone and all instruments were then glued using a two component quick-setting epoxy (Jaud et al., 2012).

Post-foraging, once the tagged adult female seals returned to Kerguelen to moult, their general positions were established via satellite-relayed Argos information. They

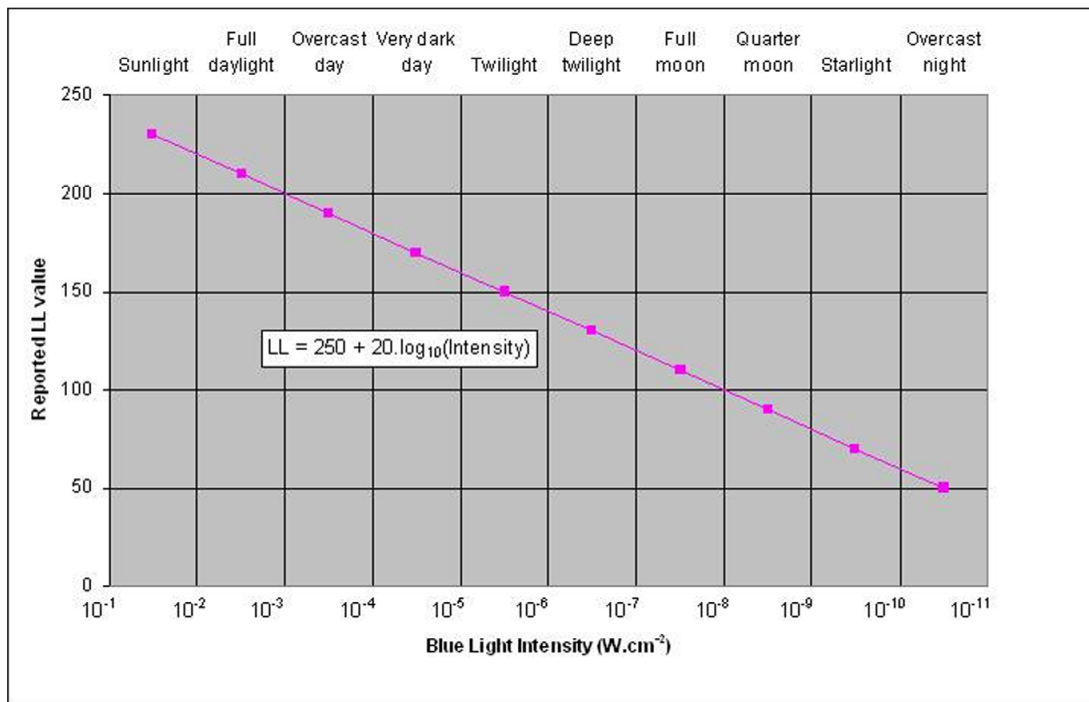


Figure 7: Logarithmic conversion of the light intensity measured by the TDR-MK loggers to light level values. Axes are delineated into 10 different classes of light intensity, which are representative of the range of different surface light conditions possibly experienced by the tagged seals. These range from full sunlight (highest possible light) to overcast night (lowest possible light). Figure from Jaud et al. (2012).

SealId	CTD	Mk10 fast_loc	Light direction	Mk9	Light direction	Mk10 accelerometer	Light direction	Acousonde	Daily Diary Tag (DDT)	Light direction	SPOT
2012-2		X	upward			X	forward	X			
2012-3		X	upward			X	forward	X			
2012-4		X	upward			X	forward	X			
2012-6		X	upward	X	backward	X	forward	X			
2012-9		X	upward	X	backward	X	forward		X	backward	
2013-1		X	upward	X	backward	X	forward	X			
2013-2		X	upward	X	forward	X	backward	X			
2013-4		X	upward	X	forward	X	backward	X			
2013-6		X	upward	X	forward	X	backward	X			
2013-7		X	upward	X	forward	X	backward	X			
2014-22		X	upward						X	backward	
2014-23		X	upward						X	backward	
2014-24	CTD								X	backward	X
2014-28	CTD	X	upward			X	night				
2014-29	CTD	X	upward			X	night				
2014-32	CTD					X	night				X
2014-33	CTD					X	night				X

Table 3: Part 1 - List of post-breeding female southern elephant seals tagged on Kerguelen between the summers of 2009-2015. TDRs measured light in an 'upward' and/or 'forward' and/or 'backward' and/or 'right' direction, depending on the type/s of TDR instrument deployed.

SealId	CTD	Mk10 fast_loc	Light direction	Mk9	Light direction	Mk10 accelerometer	Light direction	Acousonde	Daily Diary Tag (DDT)	Light direction	SPOT
2009-5		X	upward								
2009-6		X	upward								
2009-9		X	upward								
2009-10		X	upward								
2009-11		X	upward								
2010-15	CTD	X	upward	X	forward	X	backward				
2010-18		X	upward			X	backward				
2010-19		X	upward			X	backward				
2010-20		X	upward			X	backward				
2010-21		X	upward			X	backward		X	backward	
2011-16		X	upward			X	backward	X			
2011-18		X	upward			X	backward	X			
2011-21		X	upward			X	backward				
2011-26		X	upward			X	backward				
2011-27		X	upward			X	backward		X	backward	
2011-28		X	upward			X	backward				
2012-1		X	upward			X	backward	X			

Table 4: Part 2 - List of post-breeding female southern elephant seals tagged on Kerguelen between the summers of 2009-2015. TDRs measured light in an 'upward' and/or 'forward' and/or 'backward' and/or 'right' direction, depending on the type/s of TDR instrument deployed.

were then recaptured for weighing and retrieval of all the instruments. Archived light data were then recovered for processing.

(a) Processing of *in situ* data from tags In order to measure exponential light decay and attenuation, the untransformed light intensity in W cm^{-2} was more useful than the log-transformed light levels (LL). For this reason, the (compressed) log-transformed 3-digit values reported from the tag were reconverted to light intensity (I) in W cm^{-2} by:

$$I = 10^{\frac{(LL-250)}{20}} \quad (1)$$

For each dive, 'surface light intensity' (I_{surf}) was calculated. This surface light value was a near-surface rather than a strictly surface value, and was determined by calculating the mean light intensity (W cm^{-2}) within the top 2m. This step serves to reduce the effect of sun incidence angle in the very near-surface waters. Thereafter, to filter off 'very dark' (night/ fully overcast/ storm) data, only *in situ* surface values above a threshold of 0. W cm^{-2} (Fig. from Jaud et al. (2012)) were retained.

(b) Filtering the dataset The filtered data are still composed of highly variable values due to fluctuating cloud cover and other meteorological conditions, with absolute light at the surface ranging from between 0.001 W cm^{-2} (overcast) - 0.1 W cm^{-2} (full sunlight). Furthermore, light measurements for this study are retrieved by instrumented marine mammals with dive behaviours that may contribute to variability through shading of the TDR light meter. Visually inspecting the raw light data showed that measurements collected from up-facing sensors contained the most profiles where light intensity matched or exceeded 0.001 W cm^{-2} (equivalent to daylight from overcast sky) at the surface (top 2m). This suggests that sensors facing 'up' rather than forward, backward or to the right are possibly less vulnerable to self-shading from the animal as it surfaces or initiates a dive. However, if a tagged animal exhibits a tendency to roll upside down when surfacing or diving, the question on sensor placement and direction becomes moot. To accurately determine the depth that ambient light rather than shaded light reaches 1%, it is important to quality control light measurements made at the surface. Therefore, datasets from each TDR light meter were examined individually.

During the summer months when these tagged seals are collecting light data, the Southern Ocean receives surface irradiance values of 'full sunlight' (2000 $\text{mmol photons m}^{-2} \text{ s}^{-1}$) (Ross et al., 2008); equivalent to a tag reading of 1 W cm^{-2} . Of

the initial thirty-five datasets, thirty contained near-surface light measurements that matched or surpassed values of 0.001 W cm^{-2} (overcast to very dark day). Five datasets exhibited light intensities at the near-surface that rarely or never exceeded 0.001 W cm^{-2} , and these were removed. Persistently low surface light levels were attributed to sensor placement or seal behaviour, rather than meteorological variables such as cloud.

The majority of the thirty datasets retained for further analysis were from the light sensors that faced 'up'. In agreement with the study done by Jaud et al. (2012), this work used information from the ascent phase of each dive only. These 'upcasts' measured smoother profiles and showed less interference from bubbles, splashing or self-shading in surface waters.

(c) Calculating 1% light level depths and smoothing The depth of the 1% light level was approximated from the point at which light intensity was attenuated to 1% of I_{surf} ($I_{1\%}$) in W cm^{-2} :

$$I_{1\%} = \frac{I_{\text{surf}}}{100} \quad (2)$$

To minimize changeability of the light field introduced by meteorological and/or behavioural variables, the depths of the *in situ* 1% light level were smoothed. This was done by running a weighted mean on the time series. This step served to smooth out spikes in the depth of the 1% light level that could potentially be attributed to self-shading of the instrument, or factors such as passing cloud and/or sun angle. Depth values were smoothed with a Gaussian weighting scheme using a moving window size (filter width) from 1 to 4 time points (on each side). The results of each successively bigger smoothing window were then visually compared with the unsmoothed depth data (Fig. 8).

The danger of using a window that is too big is that small-scale spatial and temporal signals may be flattened. For this reason, it's important to find the smallest possible filter width that balances the smoothing out of data spikes (noise), without suppressing changes in depth of the 1% light level that may be attributed to changes in phytoplankton abundances (signal).

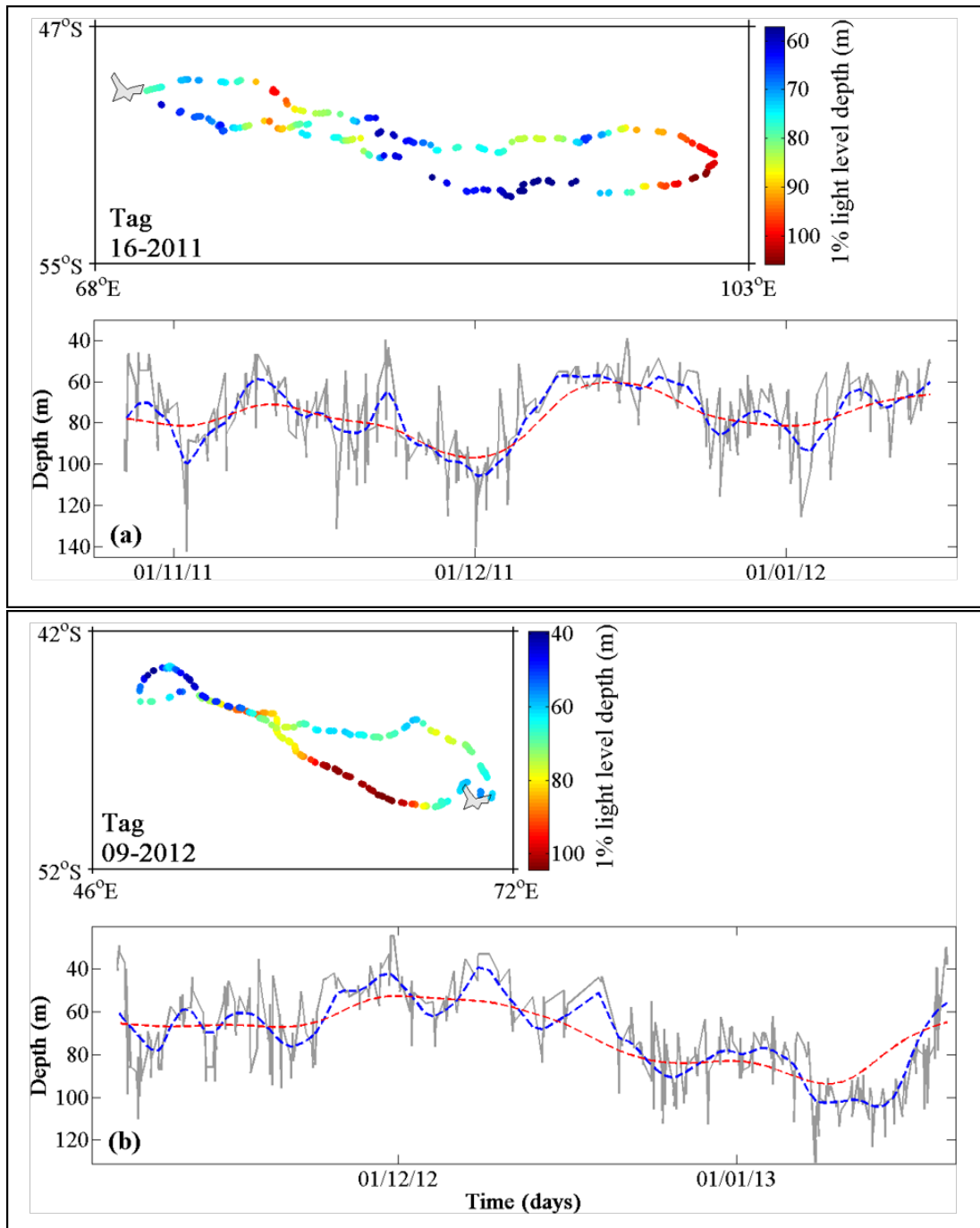


Figure 8: Examples of *in situ* 1% light level depths collected by two instrumented elephant seals from Kerguelen with tracks coloured by the depth of the 1% light level smoothed by a moving mean with widow size = 1. Corresponding plots (a) and (b) show the unsmoothed 1% light level depth data in grey, results when smoothed using the smallest moving mean (window = 1) in blue, and smoothed by a window of 4 in red.

2.2.2 MODIS Z_{eu}

All MODIS L3 products (data processed and calibrated by NASA) are freely available and were downloaded from the OceanColour website (<http://oceancolor.gsfc.nasa.gov>). Monthly and 8-day composites were downloaded as 4x4km resolution standard mapped images (SMI) in high definition format (HDF) (<http://oceancolor.gsfc.nasa.gov>), extracted using 7-zip and imported into Matlab for processing.

There is a limitation to the amount of ocean colour data collected over Southern Ocean waters because of persistent cloud cover. Daily data and even 8 day products are too rarely available, meaning that there is a requirement for the use of monthly composites. For Lee and Morel's algorithms, 8-day and monthly merged composites of Z_{eu} are available as evaluation products. Using seal positions as spatial reference points, satellite data were downloaded from the OceanColour website to cover the time period where tagged post-breeding female southern elephant seals from Kerguelen collected *in situ* light data (October 2009 - January 2015). The match ups were obtained when the latitude and longitude of the *in situ* observation fell within the MODIS 1×1 pixel window, and within the MODIS 8-day or monthly temporal window.

(a) Chl-a approach (Morel- Z_{eu} .) Based on the assumption of Case-1 conditions, the 1% light level can be estimated from remotely-sensed surface Chl-a concentrations (Lee et al., 2007; Morel and Berthon, 1989; Soppa et al., 2013).

$$\text{Morel } Z_{eu} = 34.0 ([\text{Chl}])^{-0.39} \quad (3)$$

(b) IOP approach (Lee- Z_{eu} .) An inversion algorithm was applied to analytically derive absorption (a_{490nm}) and backscattering (bb_{490}) coefficients from remote sensing reflectance (R_{rs}) (version 5, Lee, Lubak, Werdell and Arnone, 2009). This is described in detail in Lee et al. (2009) and explained comprehensively in Soppa et al. (2013). For the purposes of this study, it is suffice to say that a_{490nm} and bb_{490} are used to derive the vertical attenuation coefficient of PAR (K_{PAR}), allowing for Z_{eu} to be calculated as:

$$\text{Lee } Z_{eu} = \frac{4.605}{K_{PAR}(Z_{eu})} \quad (4)$$

To determine if any differences existed between the two algorithms in the Case-1 waters of the Southern Ocean, 8-day Lee Z_{eu} products were tested against 8-day Morel Z_{eu} products (Fig. 9).

(c) Creating the combined product and smoothing A total of 12,966 light profiles were collected by the thirty southern elephant seals over six successive austral summers. Products merged over 8-days have very large gaps in data cover, with even the monthly merged products showing missing data (Fig. 10).

Using only the 8-day products of either Lee or Morel resulted in 651 of the *in situ* datapoints being assigned an associated Z_{eu} value. Using monthly composites resulted in 1354 of the datapoints being assigned an associated Z_{eu} value. For both Lee and Morel algorithms, to determine if monthly Z_{eu} data are representative of 8-day Z_{eu} data, the products were examined using a Kruskal-Wallis test. Both Lee's monthly and 8-day Z_{eu} products, and Morel's monthly and 8-day Z_{eu} products show good agreement and were not significantly different (Fig. ??). We can thus be confident that monthly data are suitable for filling in the gaps in the 8-day data.

Because 8-day merged composites are understood to be the least temporally compromised, these Z_{eu} data were first used wherever available. Monthly Z_{eu} values were added thereafter to 'fill in' the missing data. The 2344 *in situ* data points without associated satellite values were left blank and filtered off. For simplicity, the resulting 8-day-monthly combination products will be referred to as 'combined Lee Z_{eu} .' and 'combined Morel Z_{eu} .' from this point.

For the purposes of plotting relationships between the *in situ* 1% light level and MODIS Lee Z_{eu} , the *in situ* values were smoothed using a boxcar filter of one-day width (moving average).

To determine if potential differences between the Z_{eu} products and the *in situ* measurements are most likely to occur in optically simple (clear) or complex waters, data subsets were built with only the minimum, maximum and median values extracted from each of the thirty (seal) datasets. This resulted in three subsets - smoothed *in situ* 1% light level depths, smoothed Lee Z_{eu} and smoothed Morel Z_{eu} - each containing 30 minimum, 30 median and 30 maximum values. The *in situ* 1% light level depths subset was then separately correlated against the Lee Z_{eu} subset, and the Morel Z_{eu} subset.

Finally, to evaluate the relationship between remotely derived phytoplankton concentration and light attenuation, MODIS [Chl-a] data were tested against Lee Z_{eu} and

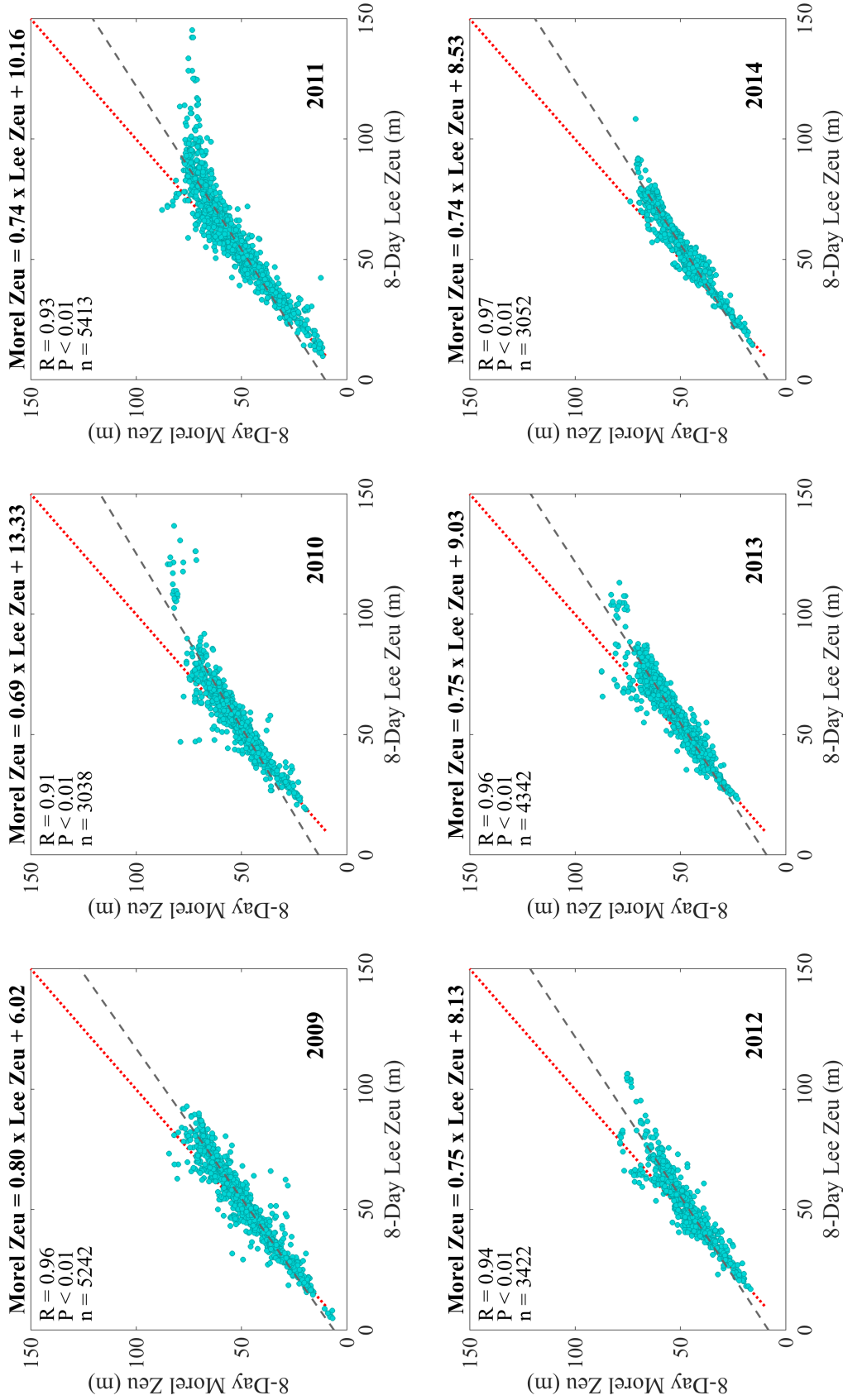


Figure 9: Linear regression between 8-day Morel Z_{eu} and 8-day Lee Z_{eu} grouped by year. The 1:1 line is in dashed red illustrating a perfect relationship, and the true linear fit is shown by the dashed grey line. The R value, p-value and the number of datasets collected by seal per year are reported in the top left-hand corner of each plot, and the linear equation with intercept and slope are reported in bold above.

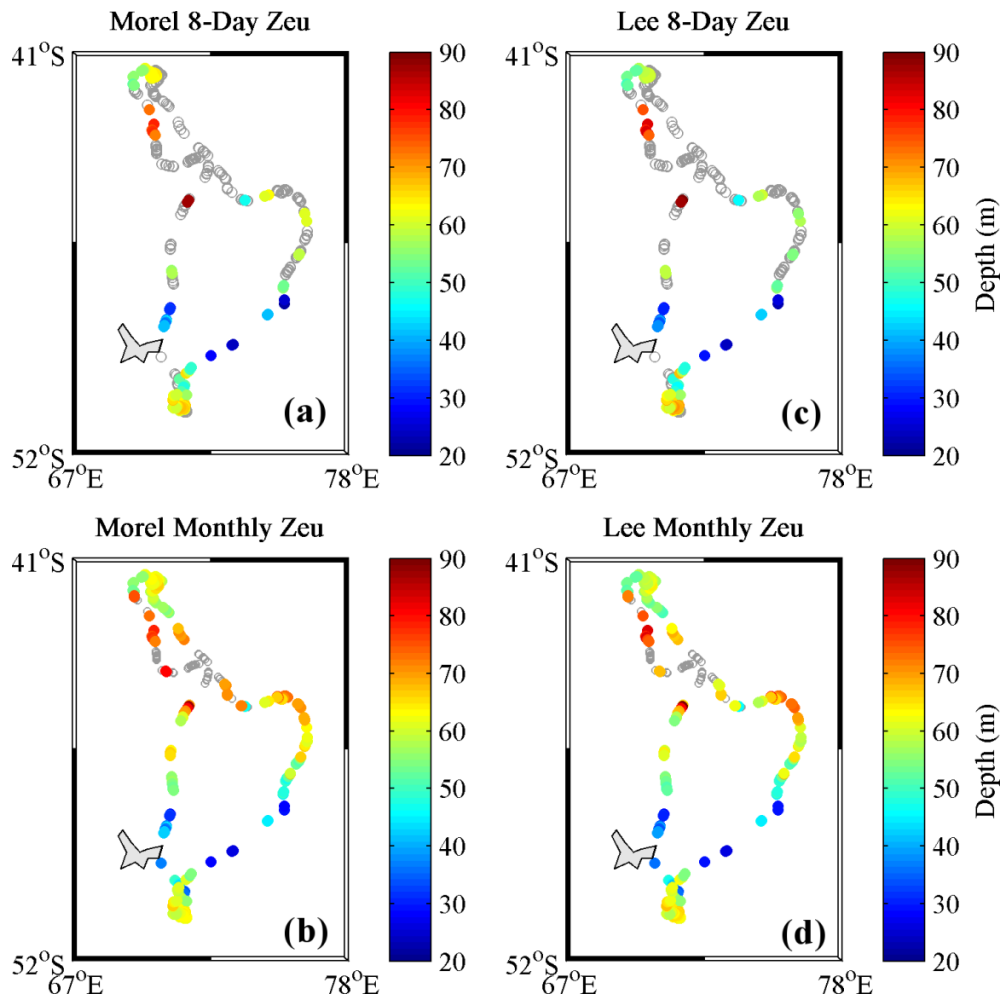


Figure 10: Elephant seal track for the duration of a post-breeding summer migration (20 October 2009 - 03 January 2010). Each seal track position is shown by a light grey circle, and these empty circles are 'filled in' wherever an associated satellite-derived ocean colour value is available. Values of Morel 8-day (a) and monthly (b) Z_{eu} are plotted in the first column. Values of Lee 8-day (c) and monthly (d) Z_{eu} are plotted in the second column.

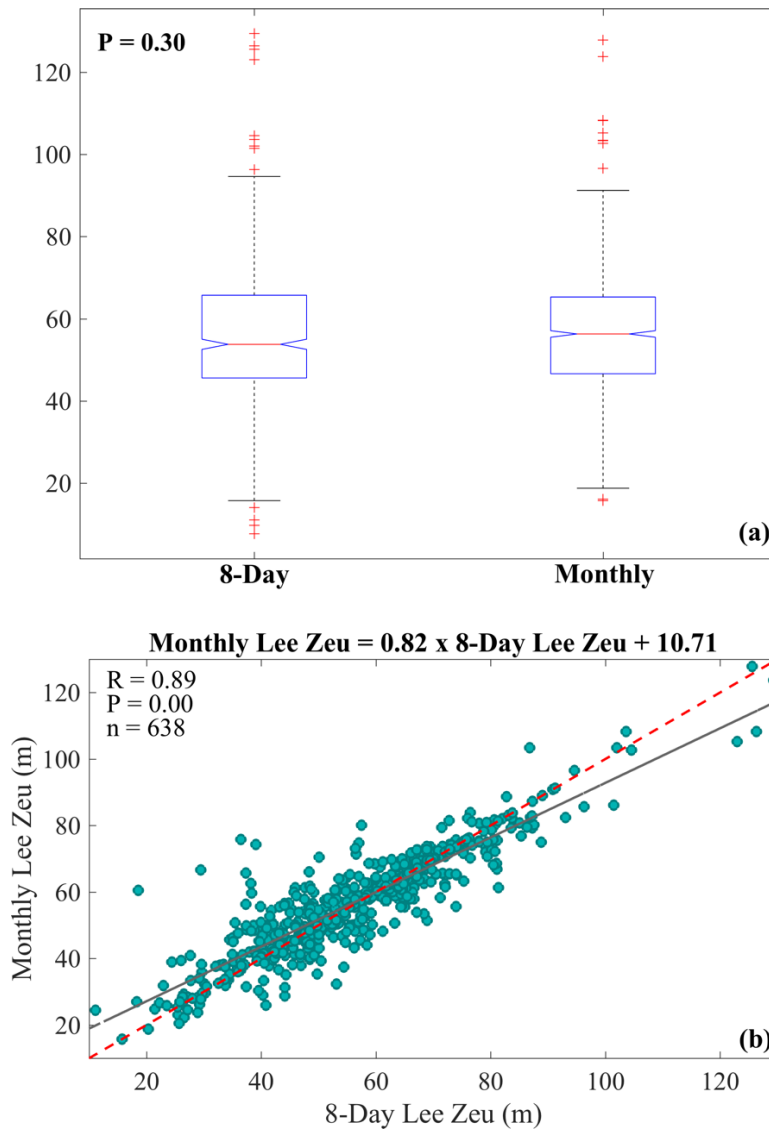


Figure 11: Evaluating the relationship between 8-day MODIS Lee Z_{eu} and monthly MODIS Lee Z_{eu} using a Kruskal-Wallis test (a) indicates that there is no significant difference between them (the null hypothesis of "means are equal" cannot be rejected at the 5% significance level) and supports the hypothesis that monthly MODIS data can be used to fill in gaps in the 8-day data. A linear regression (b) shows good agreement between the two datasets (693 available data points) with a significant p-value well below 0.01. The R value, p-value and the number of points available for the combined product satellite coverage are reported in the top left-hand corner of each plot, and the linear equation with intercept and slope are reported in bold above.

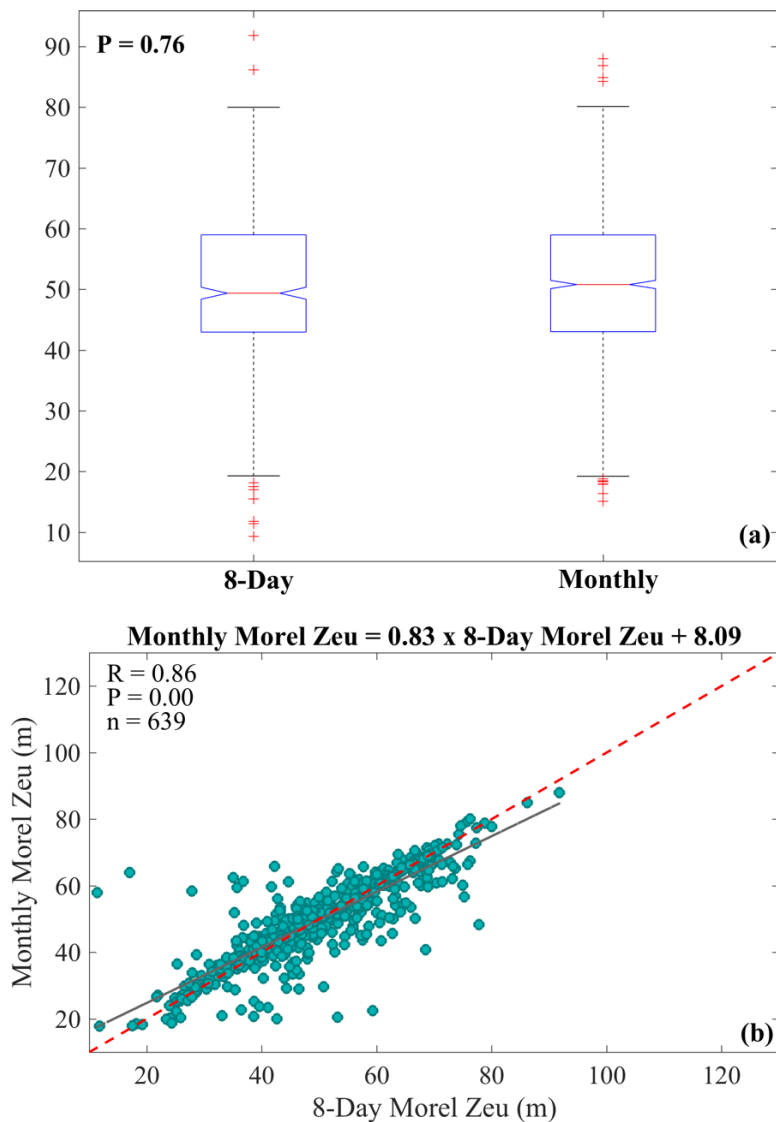


Figure 12: Evaluating the relationship between 8-day MODIS Morel Z_{eu} and monthly MODIS Morel Z_{eu} using a Kruskal-Wallis test (a) indicates that there is no significant difference between them (the null hypothesis of "means are equal" cannot be rejected at the 5% significance level) and supports the hypothesis that monthly MODIS data can be used to fill in gaps in the 8-day data. A linear regression (b) between the two datasets (693 available data points) shows good agreement with a significant p-value well below 0.01. The R value, p-value and the number of points available for the combined product satellite coverage are reported in the top left-hand corner of each plot, and the linear equation with intercept and slope are reported in bold above.

in situ 1% light level depths. The [Chl-a] data were combined and smoothed in the same way as the Z_{eu} values, generating an 8-day-monthly product. Chapter 5 details this step, suffice to say here that building the combined [Chl-a] product is beneficial for filling in spatial gaps.

2.3 RESULTS

Over the austral summers spanning 2009 - 2015, thirty-five post-breeding female southern elephant seals from Kerguelen Island were tagged with instruments to measure light in the water column. Information collected from up-facing sensors specifically contained the most profiles where light intensity matched or exceeded what would be received at the surface during a typically overcast day. This implies that instrument placement is important, and it's possible that sensors facing 'up' (rather than forward, backward or to the right) are less vulnerable to persistent self-shading from the animal. Indeed, there were five datasets where light intensities at the surface rarely/ never exceeded typically overcast conditions. These persistently low light levels were attributed to sensor placement and/or seal behaviour, rather than environmental conditions, and these five datasets were discarded.

Despite this step, it's unlikely that any variation of sensor placement would allow for sampling completely free of self-shading. Furthermore, variability from passing cloud, sun angle, waves, foam and even scattering layers would serve to add noise to the relationship between light attenuation with depth and phytoplankton concentration. Applying a moving mean to the 1% light level depths smoothed out data spikes. However, the depth of the 1% light level still showed changes in space, as the instrumented seal foraged and travelled. These remaining changes in depth may be potentially attributed to changes in phytoplankton concentration in surface waters.

Of the 12,966 light profiles collected by thirty southern elephant seals between 2009 and 2015, only $\approx 30\%$ of these had an associated temporal-spatial 8-day value. However, more than 80% of seal tracks had an associated monthly Z_{eu} value. The results from the correlation of monthly and 8-day Z_{eu} suggest that monthly products underestimate the depth of the 1% light level for both Morel and Lee's algorithm. However, a Kruskal-Wallis tests supports the similarities between the two datasets, and mean differences between 8-day and monthly data are small (Morel = 0.23; Lee

= 0.75). If we look at the 8-day and monthly products side-by-side where both y-axes are overlaid over time, match-ups are closer than the correlation suggested.

Filling in gaps from the 8-day product with monthly data served to retain the most temporally accurate values, while maintaining coverage in a way that was most spatially representative. Correlating *in situ* measures of the 1% light level with remotely sensed 8-day Z_{eu} resulted in similar slopes and correlation coefficients grouped per year (Fig. 14 and 15).

Year to year, differences in reported R values for correlations between Lee Z_{eu} and the 1% light level, and Morel Z_{eu} and the 1% light level are small. Nonetheless, the Lee Z_{eu} product marginally outperforms Morel's. The difference between the Z_{eu} algorithms is made clearer when we examine the slope reported for each correlation (table ??). Lee Z_{eu} appears to be consistently more representative of the *in situ* 1% light level, relative to Morel Z_{eu} .

These correlations also serve to illustrate that differences between the MODIS Z_{eu} algorithms appear small, relative to variability between years, conditions and possibly TDR light recorder instruments. Nonetheless, when Morel and Lee Z_{eu} measurements from the full timeseries are evaluated, the differences between the two products are significant.

By plotting the unsmoothed and smoothed subset data containing only minimum, median and maximum values from each of the 30 instruments, the small differences between Morel and Lee Z_{eu} are easier to see. Interestingly, Soppa et al. (2013) found that Morel Z_{eu} tended to be deeper than Lee Z_{eu} . Our results show the opposite to be true; with Lee Z_{eu} closely matching (only slightly underestimating) the deepest (> 90m) *in situ* values of the 1% light level, while Morel Z_{eu} tended to underestimate depths by up to ≈ 30 m.

Both Lee and Morel Z_{eu} appear to show a deviation from the 1:1 line after a 'threshold' depth of ≈ 60 m is reached. When the 1% light level is between 50 - 60m, our results show that Morel Z_{eu} marginally more closely aligns with the 1:1 line, relative to Lee Z_{eu} . Most of the time, however, the depth of the 1% light level in the smoothed *in situ* data tends to range between 40m - 100m.

Although the differences between Morel Z_{eu} and Lee Z_{eu} are small overall, the fact that Lee Z_{eu} more closely matches the *in situ* 1% light level depth suggests that the addition of IOP's is beneficial for the open waters of the Southern Ocean. Therefore, from this point, Lee Z_{eu} is the product used for further study.

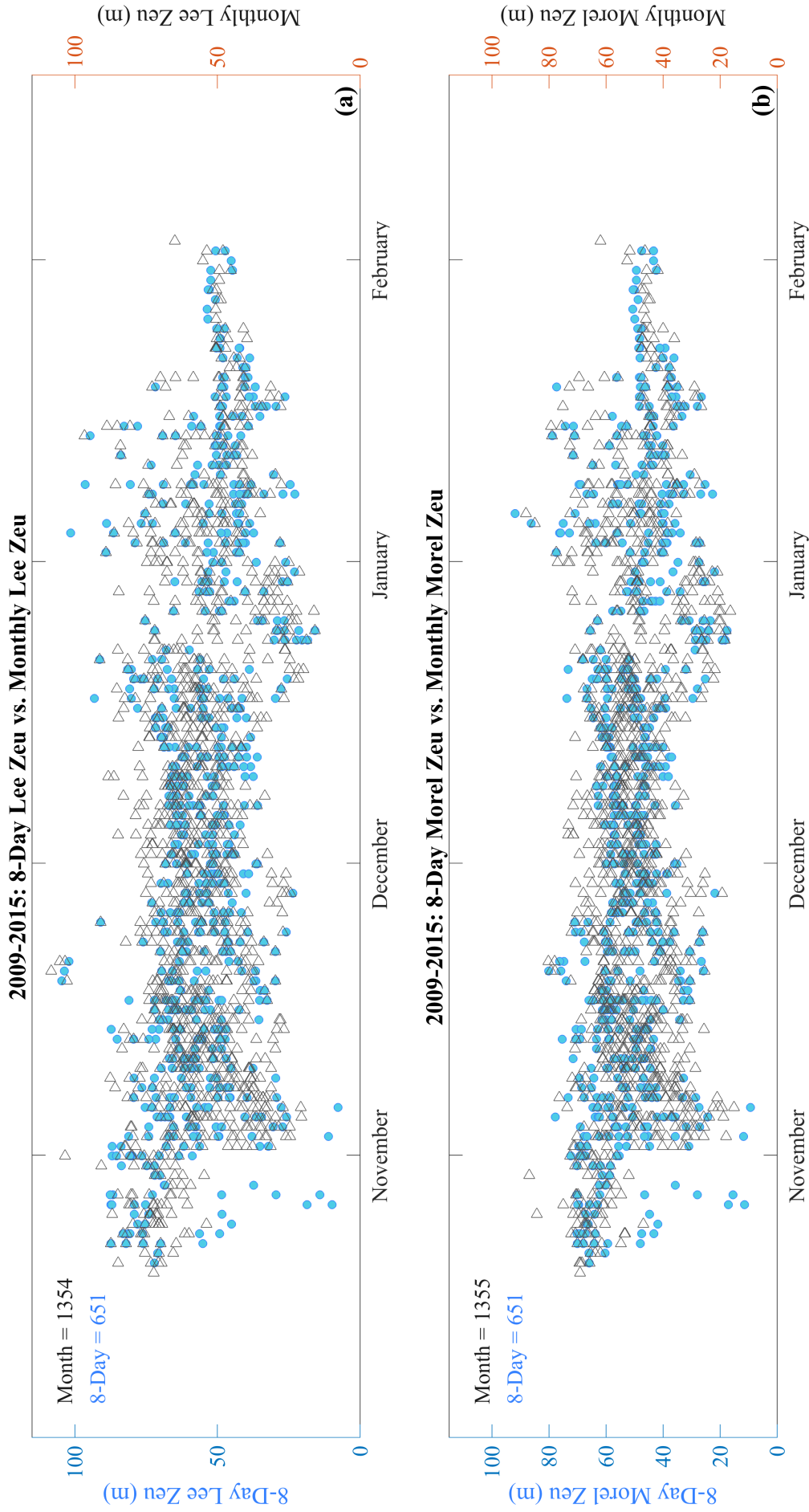


Figure 13: Comparison of monthly and 8-day estimates of the 1% light level using the Morel algorithm (a) and Lee algorithm (b) over time, from all seals tagged with TDR light meters between 2009-2014. In both cases, monthly products match maximum (deepest) values in the 8-day products, but values in the 8-day products show shallower (minimum) values not equalled by monthly values. Morel's monthly and 8-day Z_{eu} values are more conservative than Lee's. For both Morel and Lee, monthly data more than double the number of measurements available for comparison with *in situ* light data.

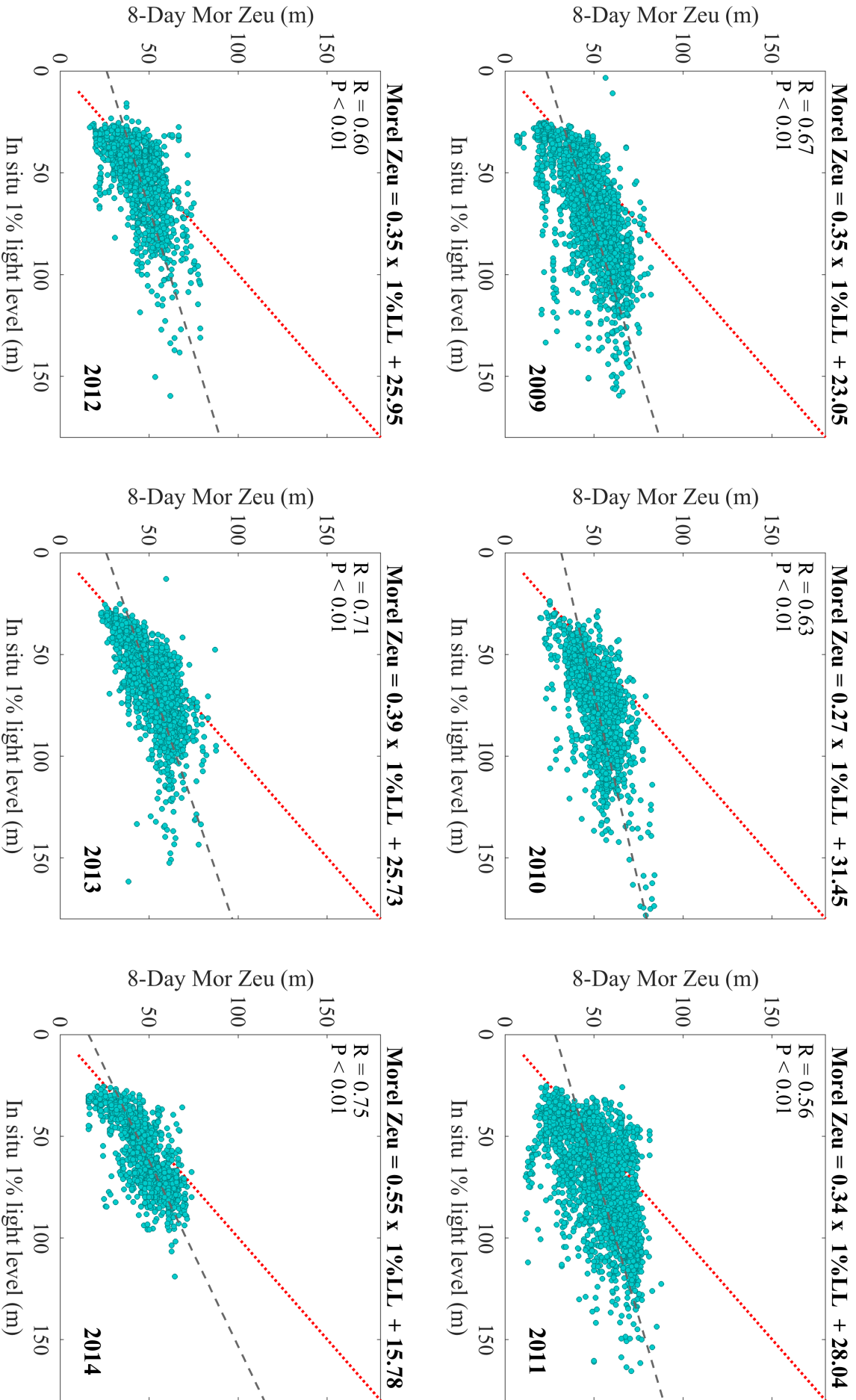


Figure 14: Linear regression between 8-day Morel Zeu and the *in situ* 1% light level grouped by year. The 1:1 line is in dashed red illustrating a perfect relationship, and the true linear fit is shown by the dashed grey line. The R value, p-value and the number of datasets collected by seal per year are reported in the top left-hand corner of each plot, and the linear equation with intercept and slope are reported in bold above

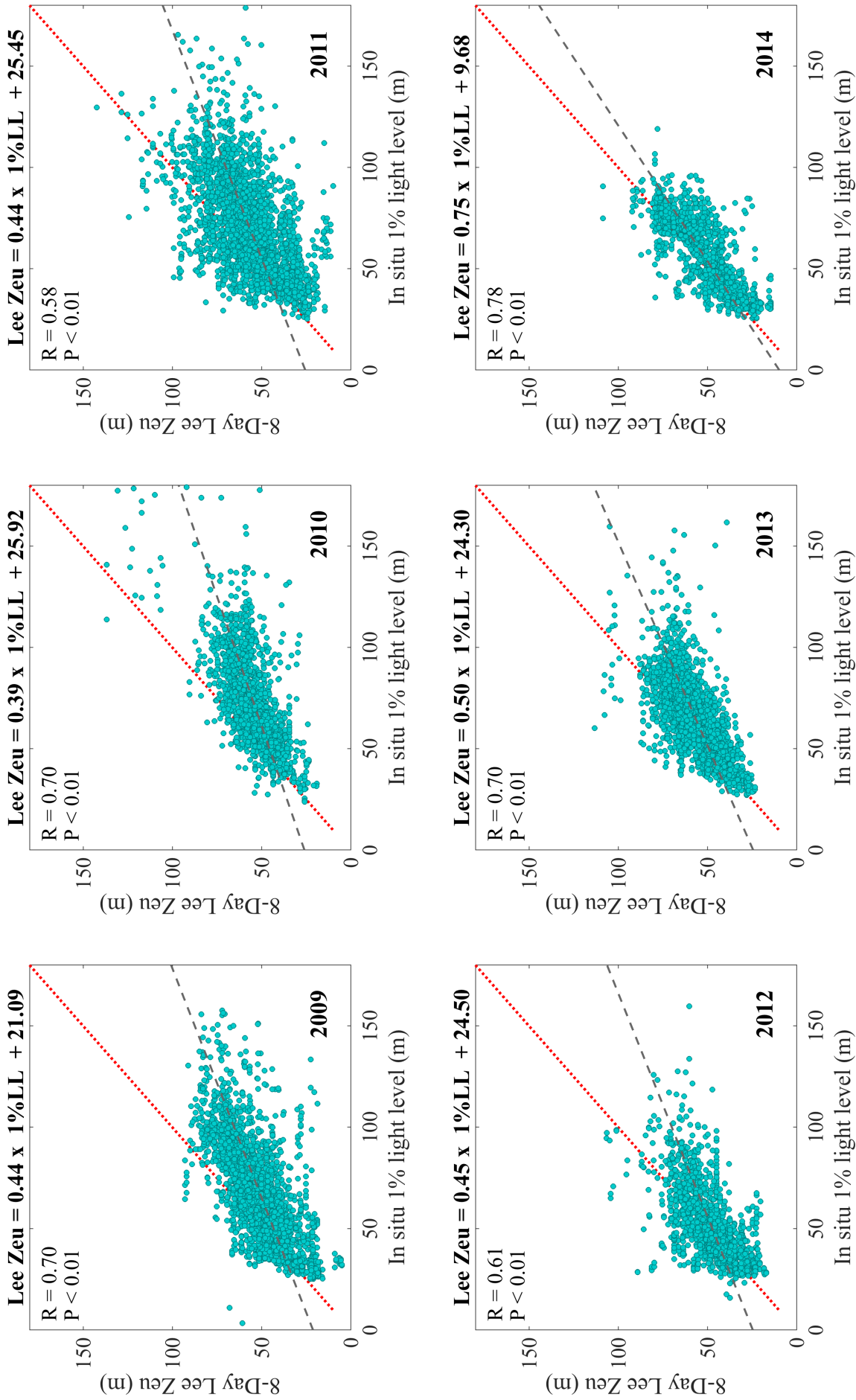


Figure 15: Linear regression between 8-day Lee Zeu and the *in situ* 1% light level grouped by year. The 1:1 line is in dashed red illustrating a perfect relationship, and the true linear fit is shown by the dashed grey line. The R value, p-value and the number of datasets collected by seal per year are reported in the top left-hand corner of each plot, and the linear equation with intercept and slope are reported in bold above

Year	Slope: Lee Z_{eu} vs 1% LL	Slope: Morel Z_{eu} vs 1% LL	Difference
2009	0.46	0.37	0.09
2010	0.36	0.25	0.11
2011	0.41	0.31	0.10
2012	0.33	0.26	0.07
2013	0.66	0.50	0.16
2014	0.72	0.54	0.10

Figure 16: Differences between fit of Lee Z_{eu} and Morel Z_{eu} to *in situ* measures of the 1% light level reported using slope from linear regressions grouped on a year-by-year basis

By plotting the 1% light level depths along-side the combined Lee Z_{eu} product, it becomes apparent that correlation, although useful for showing the MODIS data underestimates the depth of the 1% light level, may not be the best means of evaluating relationships. When plotted over time using a relative rather than quantitative approach, Lee Z_{eu} mirrors the trends in the *in situ* data over time.

Although I have shown that correlation is not the clearest method for determining relationships between these *in situ* data and MODIS measurements, the depth of the 1% light level does show a significant inverse relationship with combined [Chl-a]. Assuming that MODIS [Chl-a] is a sufficiently accurate measure of phytoplankton abundance in surface waters, the wide scatter suggests that Southern Ocean waters do not always conform to Case-1 assumptions. This finding supports the results of Tripathy et al (2011) and reinforces the importance of IOPs when calculating light attenuation, even in waters considered optically simple. With substantially less scatter, combined and smoothed Lee Z_{eu} shows a significant inverse relationship to combined and smoothed [Chl-a].

2.4 DISCUSSION

For this study, all *in situ* measures of light data were collected by adult female southern elephant seal 'autonomous platforms'. Tagging these wide-ranging and deep-diving marine predators ensured that instruments were transported vast distances over productive summer months, possibly to more biologically 'rich' waters. However, the caveats associated with such an approach included self-shading issues that varied between individuals and even between dives.

Understanding the impact that light sensor placement had on the collected data proved to be an essential part of the quality control process. To my knowledge, noth-

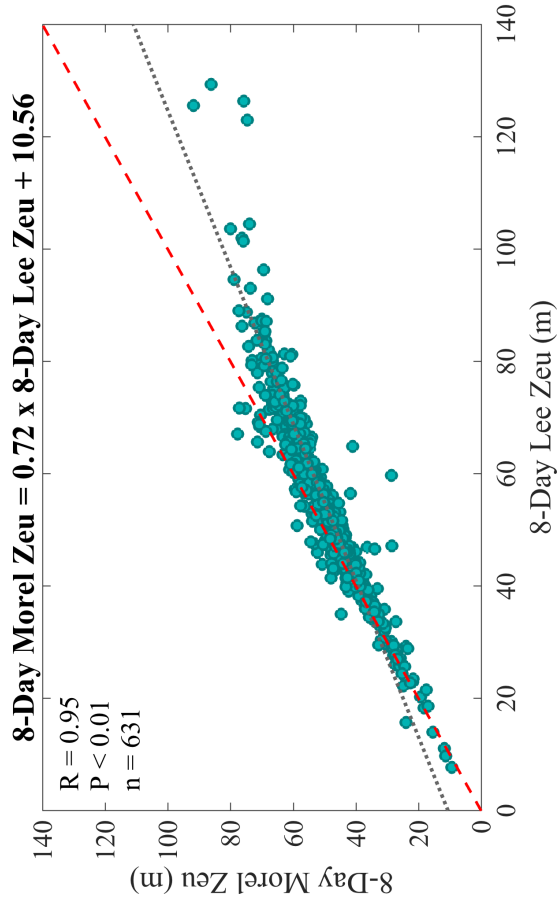
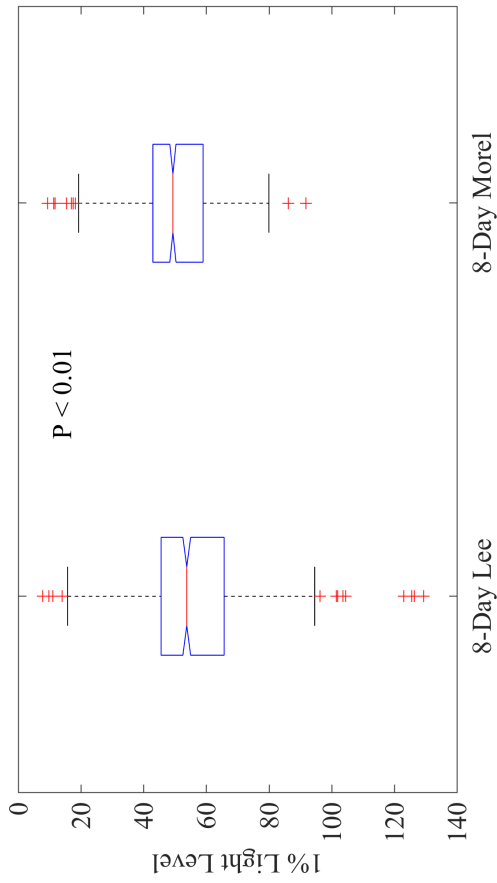
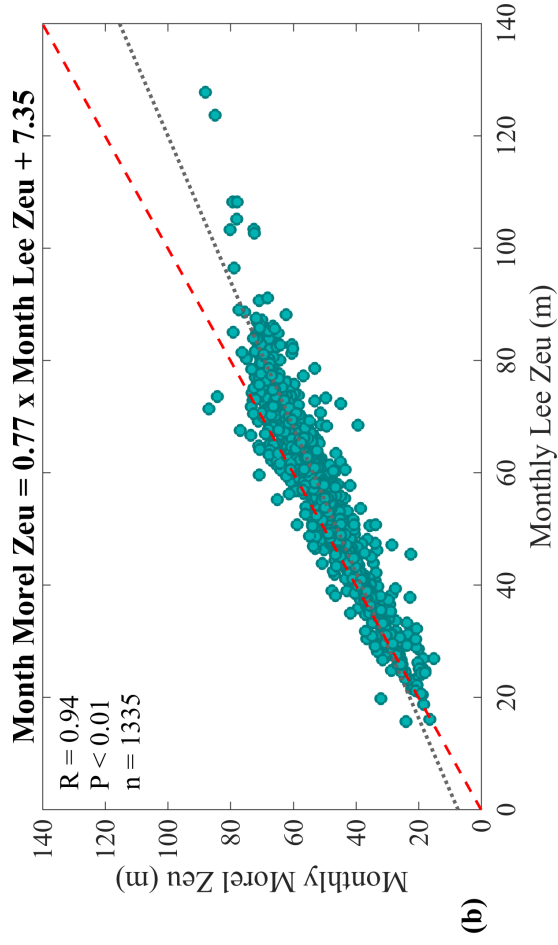
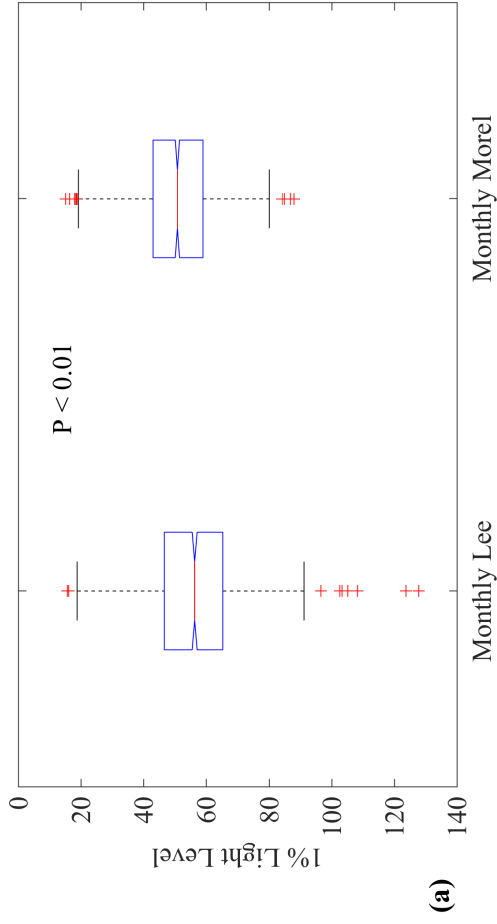


Figure 17: Boxplot of 8-day and monthly Lee Z_{eu} and Morel Z_{eu} (a). The p-value reported from the Kruskal-Wallis test indicates that there is a significant difference between Morel and Lee Z_{eu} , and the null hypothesis of "means are equal" can be rejected at the 5% significance level. When evaluated using a linear regression (b), both the fit and slope suggest a good relationship between Morel and Lee Z_{eu} . The 1:1 line is in dashed red illustrating a perfect relationship, and the true linear fit is shown by the dashed grey line. The R value, p-value and the number of data points (n) are reported in the top left-hand corner of each plot. The linear equation with intercept and slope is reported in bold above.

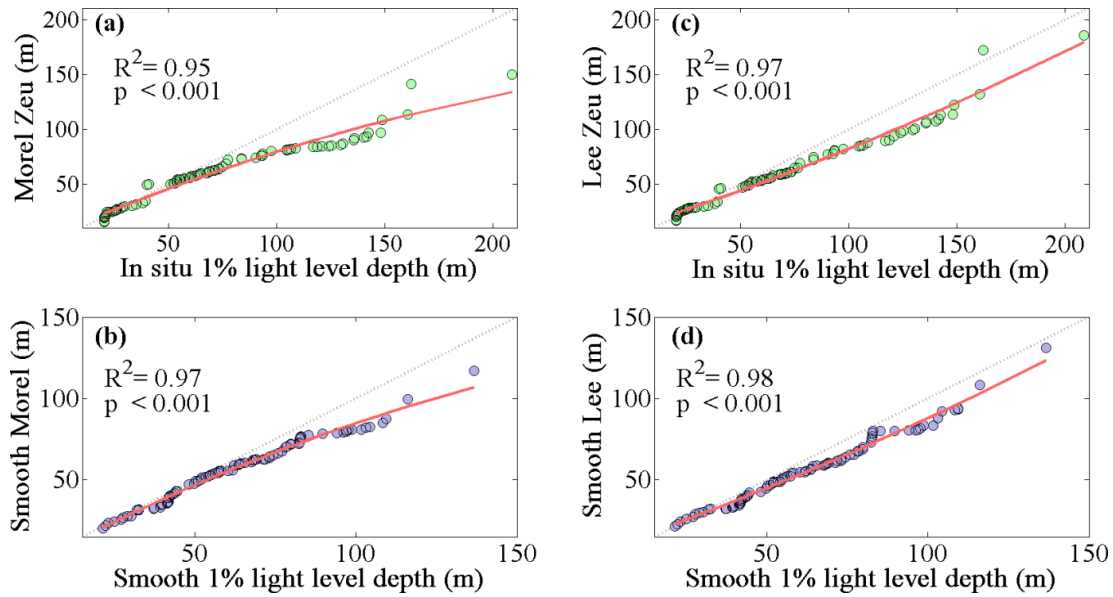


Figure 18: Correlating maximum, median and minimum values from all thirty of the smoothed *in situ* 1% light level datasets with the maximum, median and minimum values from the unsmoothed (a) and smoothed Morel Z_{EU} (b), and unsmoothed (c) and smoothed Lee Z_{EU} (d). The dashed grey line represents the 1:1 ratio line (perfect correlation) and the red line represents a second degree polynomial fit.

ing has been formally published on this, but my results may serve to improve or optimise tagging and subsequent data acquisition for future deployments. Of course, optimised instrument placement cannot prevent self-shading if tagged seals roll or turn upside-down when surfacing or diving. Fortunately, behavioural 'quirks' such as these were evident from vertical light data that were consistently darker at the surface, and these datasets could be filtered off. Two previous studies working with the same light data did not discuss or address self-shading (Jaud et al., 2012; Vacquie-Garcia et al., 2015), but these measurements of light were used for different purposes and were less sensitive to accuracy in surface waters.

Potential variability from self-shading deeper in the water column was impossible to discern from variability introduced by environmental sources, such as waves, passing/ persistent cloud or sun incidence angles. The combination of all these factors made the raw readings from up- and down-casts highly variable, but smoothing of these data allowed for signal to be teased out from the noise, and a robust calculation of the 1% light level. As an alternative to processing the data to determine the depth of the 1% light level, Jaud et al. (2012) used light intensities at 150m as an indicator of light availability at the mean "euphotic (phytoplankton) layer". The rationale being that this groups together all possible sources of light attenuation (sus-

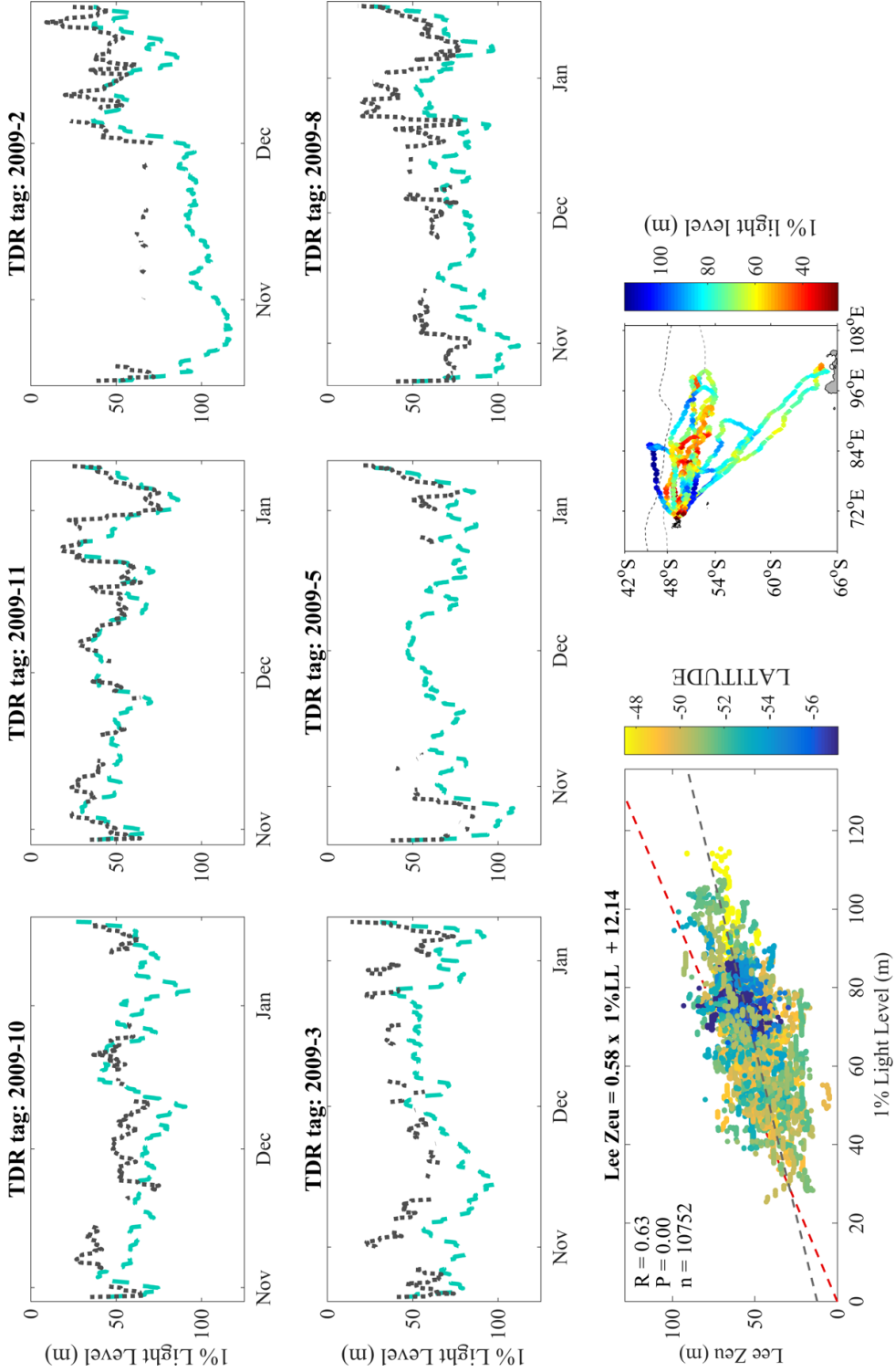


Figure 19: Comparison of smoothed 1% light level depths and MODIS products. Plotted over time (Nov. 2009 – Jan. 2010) and per instrumented seal (tag number reported in bold above each plot), the smoothed *in situ* 1% light level depth is shown in blue-green, and 8-day-monthly Lee Z_{eu} is shown in dark grey. A linear regression of the smoothed *in situ* data and MODIS Z_{eu} is shown with R, P and number of data points (n) reported in the top left hand corner. Points are shaded by latitude, shown by the associated colourbar. The 1:1 fit line is shown by the dashed red line and the fit of *in situ* data to satellite data is shown by the dashed grey line. The linear equation with intercept and slope is reported in bold above the regression plot. Finally, for reference, seal tracks are shown with along-track points shaded by the depth of the *in situ* 1% light level, shown by the associated colourbar.

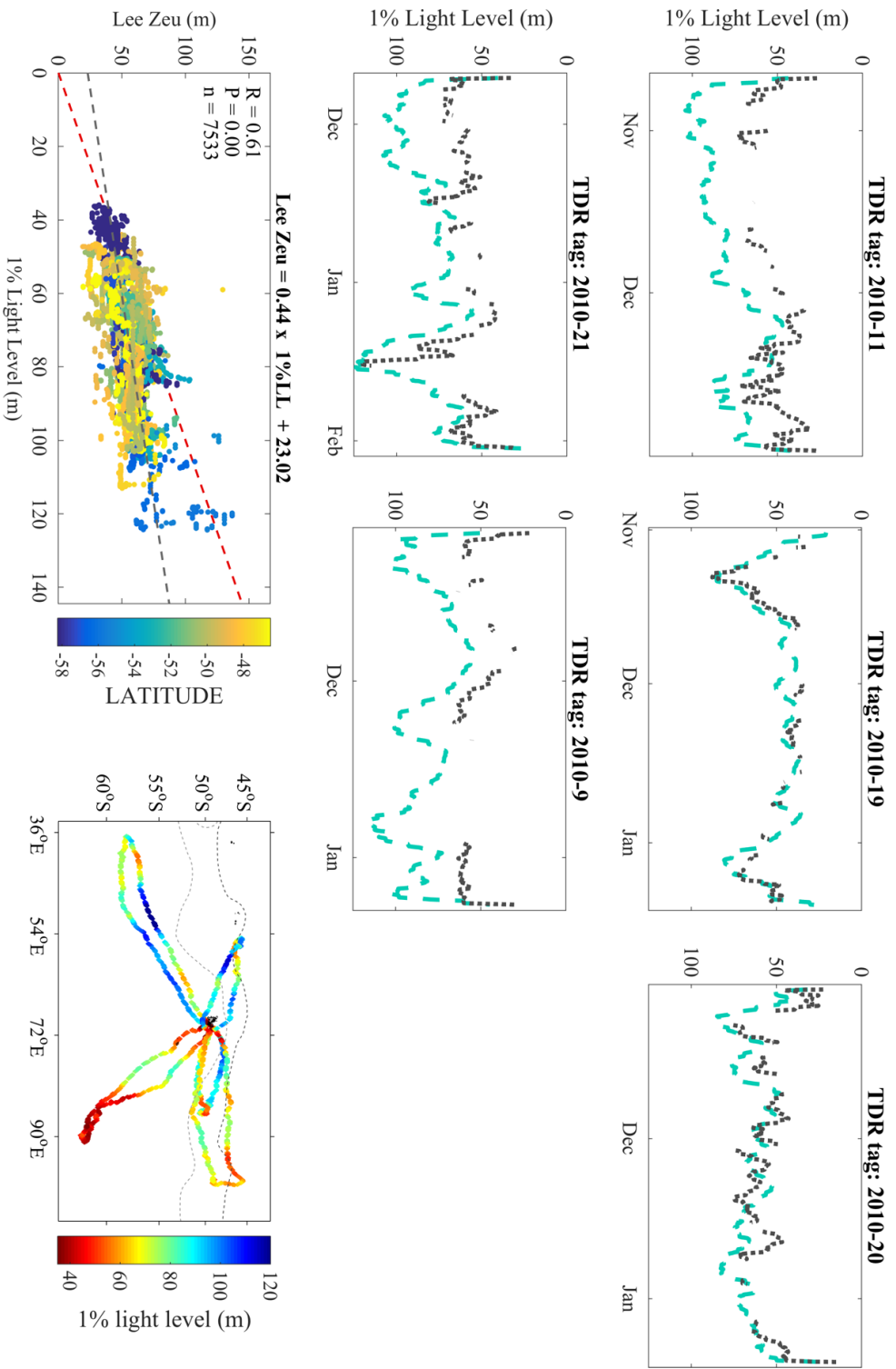


Figure 20: Comparison of smoothed 1% light level depths and MODIS products. Plotted over time (Nov. 2010 – Jan. 2011) and per instrumented seal (tag number reported in bold above each plot), the smoothed *in situ* 1% light level depth is shown in blue-green, and 8-day-monthly Lee Zeu is shown in dark grey. A linear regression of the smoothed *in situ* data and MODIS Z_{eu} is shown with R, P and number of data points (n) reported in the top left hand corner. Points are shaded by latitude, shown by the associated colourbar. The 1:1 fit line is shown by the dashed red line and the fit of *in situ* data to satellite data is shown by the associated colourbar. The linear equation with intercept and slope is reported in bold above the regression plot. Finally, for reference, seal tracks are shown with along-track points shaded by the depth of the *in situ* 1% light level, shown by the associated colourbar.

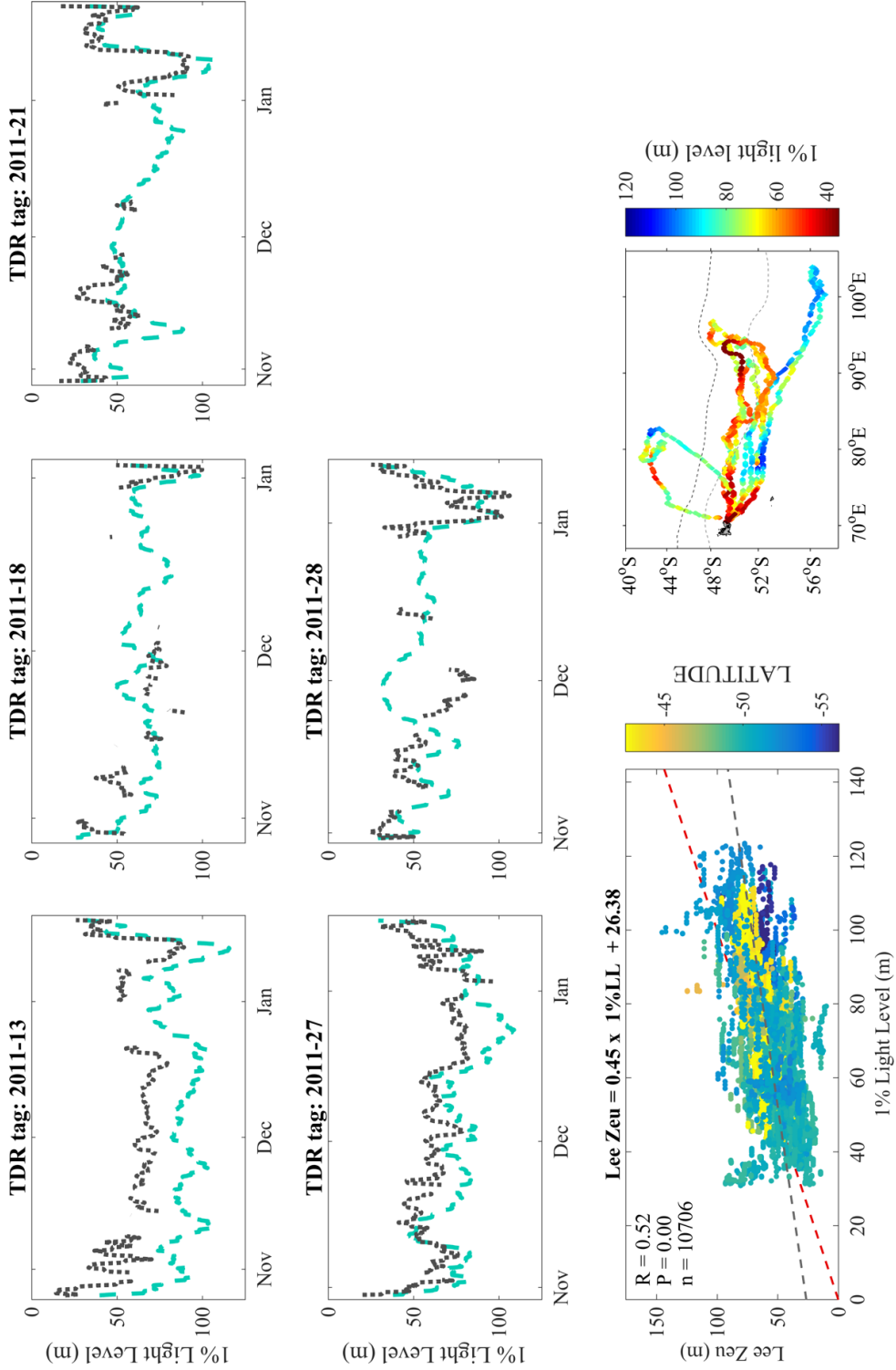


Figure 21: Comparison of smoothed 1% light level depths and MODIS products. Plotted over time (Nov. 2011 – Jan. 2012) and per instrumented seal (tag number reported in bold above each plot), the smoothed *in situ* 1% light level depth is shown in blue-green, and 8-day-monthly Lee Z_{eu} is shown in dark grey. A linear regression of the smoothed *in situ* data and MODIS Z_{eu} is shown with R, P and number of data points (n) reported in the top left hand corner. Points are shaded by latitude, shown by the associated colourbar. The 1:1 fit line is shown by the dashed red line and the fit of *in situ* data to satellite data is shown by the dashed grey line. The linear equation with intercept and slope is reported in bold above the regression plot. Finally, for reference, seal tracks are shown with along-track points shaded by the depth of the *in situ* 1% light level, shown by the associated colourbar.

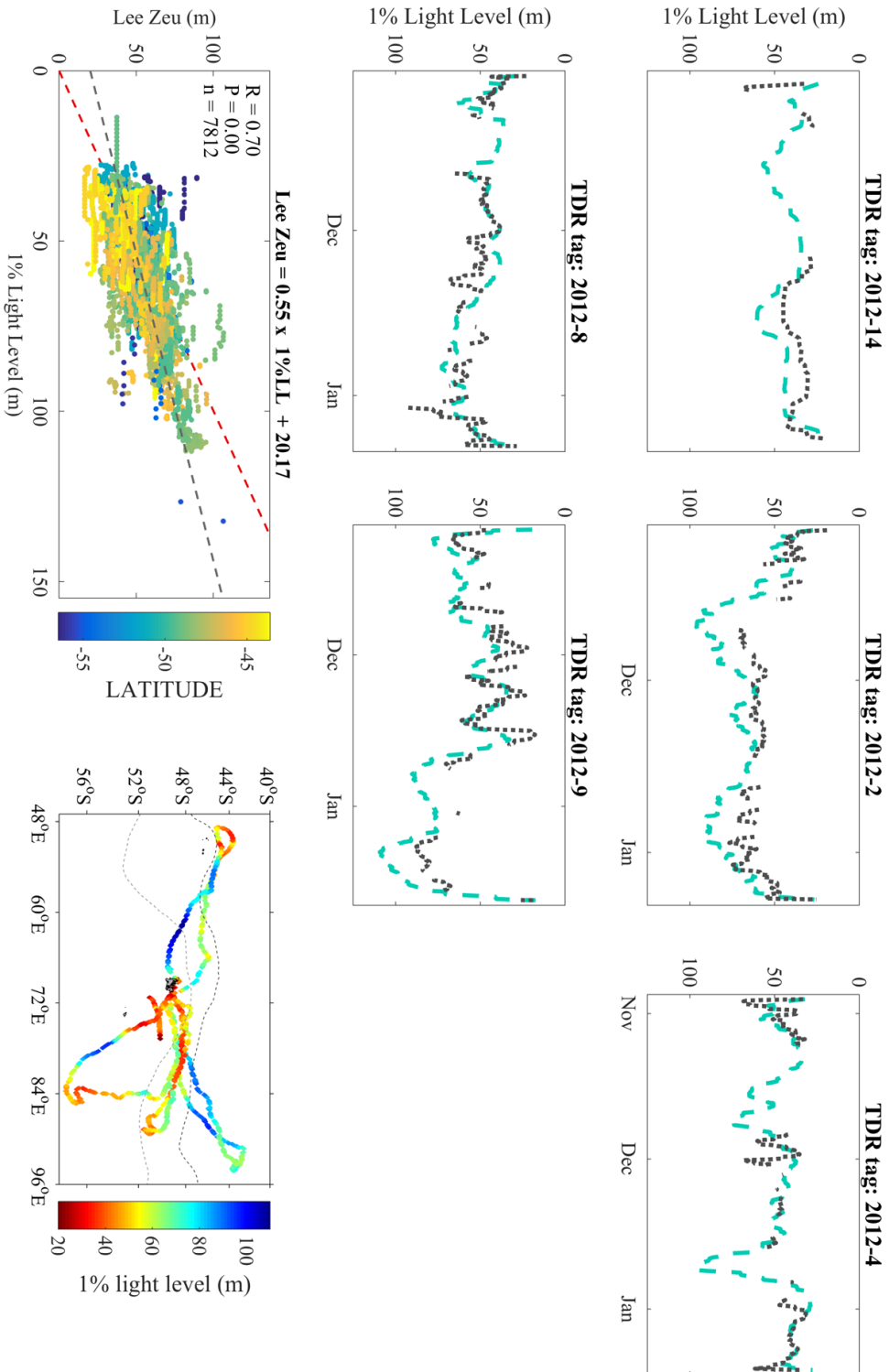


Figure 22: Comparison of smoothed 1% light level depths and MODIS products. Plotted over time (Nov. 2012 – Jan. 2013) and per instrumented seal (tag number reported in bold above each plot), the smoothed *in situ* 1% light level depth is shown in blue-green, and 8-day-monthly Lee Zeu is shown in dark grey. A linear regression of the smoothed *in situ* data and MODIS Z_{eu} is shown with R, P and number of data points (n) reported in the top left hand corner. Points are shaded by latitude, shown by the associated colourbar. The 1:1 fit line is shown by the dashed red line and the fit of *in situ* data to satellite data is shown by the associated colourbar. The linear equation with intercept and slope is reported in bold above the regression plot. Finally, for reference, seal tracks are shown with along-track points shaded by the depth of the *in situ* 1% light level, shown by the associated colourbar.

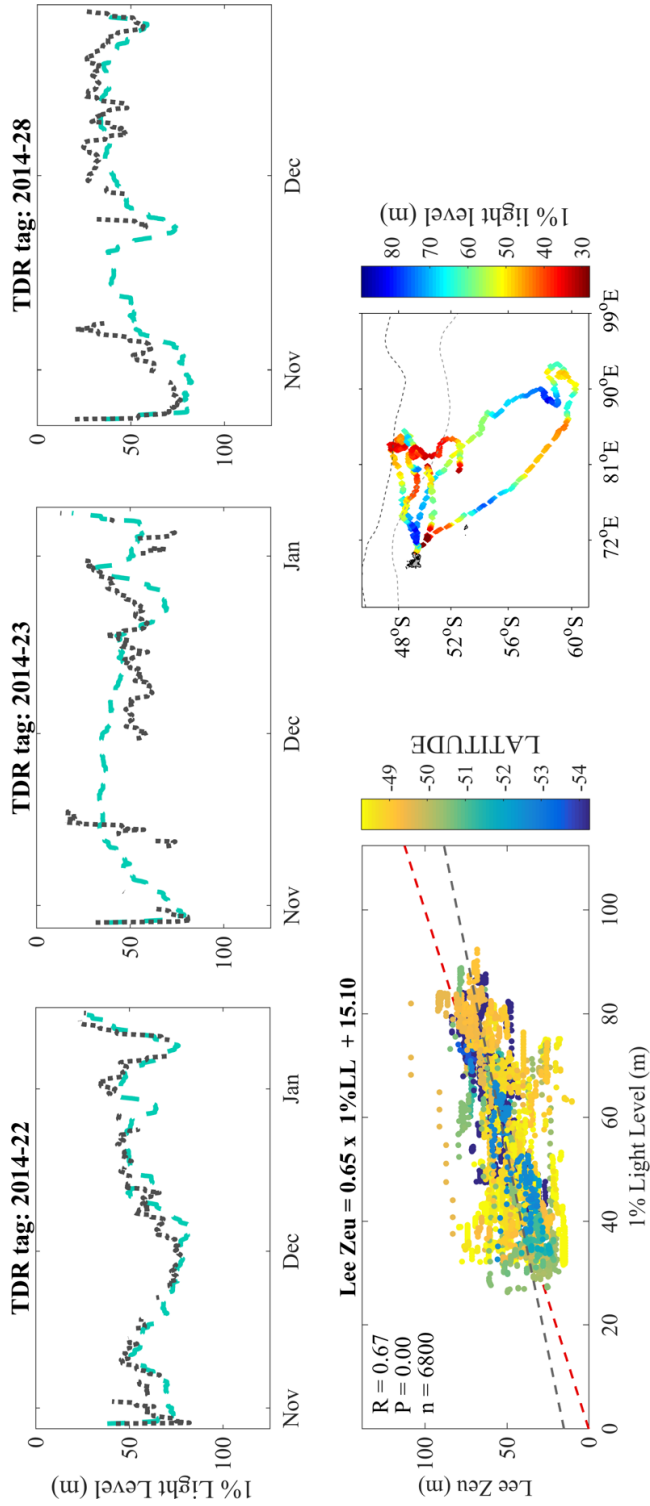


Figure 23: Comparison of smoothed 1% light level depths and MODIS products. Plotted over time (Nov. 2014 – Jan. 2015) and per instrumented seal (tag number reported in bold above each plot), the smoothed *in situ* 1% light level depth is shown in blue-green, and 8-day-monthly Lee Z_{eu} is shown in dark grey. A linear regression of the smoothed *in situ* data and MODIS Z_{eu} is shown with R, P and number of data points (n) reported in the top left hand corner. Points are shaded by latitude, shown by the associated colourbar. The 1:1 fit line is shown by the dashed red line and the fit of *in situ* data to satellite data is shown by the dashed grey line. The linear equation with intercept and slope is reported in bold above the regression plot. Finally, for reference, seal tracks are shown with along-track points shaded by the depth of the *in situ* 1% light level, shown by the associated colourbar.

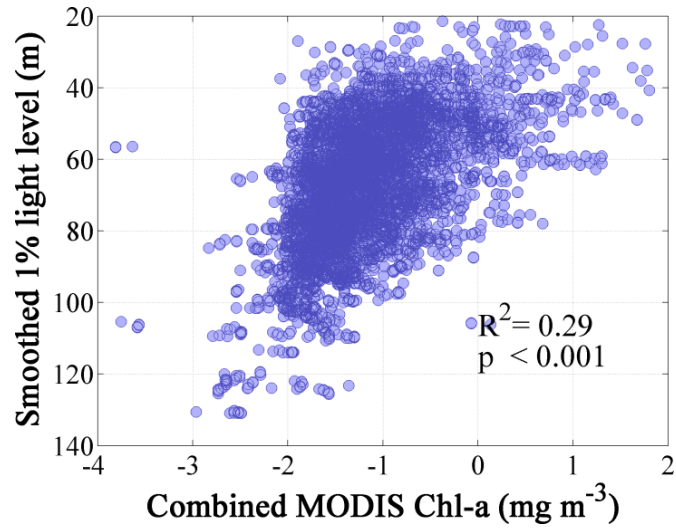


Figure 24: Correlating combined log-transformed MODIS [Chl-a] with smoothed *in situ* measures of the depth where light is attenuated to 1% of the surface value.

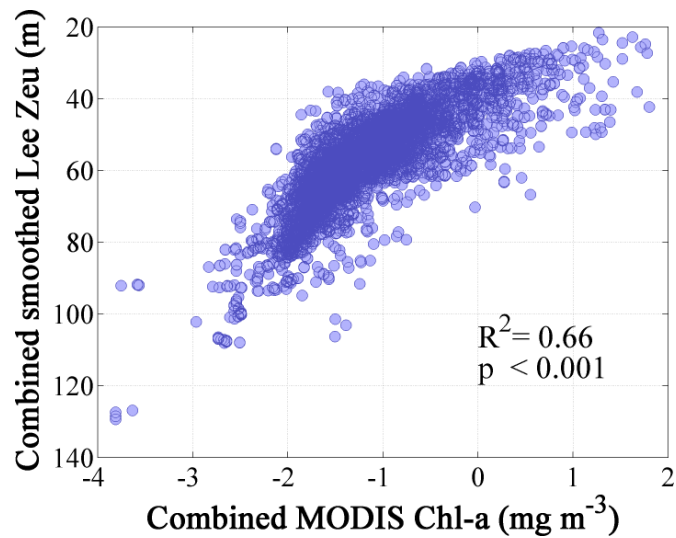


Figure 25: Correlating combined log-transformed MODIS [Chl-a] with combined and smoothed Lee Z_{eu}.

pended particle concentration, cloud cover and sun angle). My findings, however, do not support 150m as the mean depth of the euphotic zone. Instead, I suggest that the light attenuation in the Southern Ocean water column varies sufficiently to caution against such an approach.

Z_{eu} is essentially an estimation of light attenuation in the water column, and there are two approaches to calculating it. Firstly, from [Chl-a] retrieved using band reflectance ratios from remote sensing reflectance. This is the Morel et al. (2007) approach and estimations of Z_{eu} based on this algorithm rely heavily on Case-1 assumptions. In other words, for the product to be as accurate as possible, Morel Z_{eu} is constrained to waters that are not considered optically complex (Morel et al., 2009). The second approach to calculating Z_{eu} , however, relies on no such assumptions, and estimates the depth of the 1% light level with the addition of inherent optical properties near-analytically calculated from remote sensing reflectance. This is the Lee et al. (2007) algorithm.

Southern Ocean open waters have been thought to conform to Case-1 conditions. Thus, vertical light attenuation should be affected by phytoplankton primarily, with allowances for minor contributions from associated detrital products and/or co-existing organisms. Under these specific circumstances, Morel's measure of Z_{eu} is suitable for calculating the depth of the 1% light level. However, Case-1 assumptions for all Southern Ocean waters may not always hold. Recent ship-based and satellite remote sensing studies within the ACC suggest that understandings of a 'Southern Ocean optical water type' should be revised to more regional scales (Tripathy, 2015; Jena, 2016). In culture experiments, Ortega-Retuerta et al. (2009) found evidence that bacteria and krill (*Euphausia superba*) generate CDOM, and may significantly contribute to optical complexity in high latitude waters. Furthermore, possible shifts towards Case-2 conditions may only be part of the story. Coccolithophore blooms have also been shown to confound general models; supported by an extended water classification scheme introduced by Moore et al. (2011). Finally, work from this chapter shows that Morel's measure of Z_{eu} did not compare as consistently well as Lee's did, when evaluated alongside *in situ* measures of the 1% light level. Conditions where light attenuation is affected by other constituents are more explicitly accounted for in Lee's Z_{eu} . This may explain why values of Lee's Z_{eu} generally match the deep values in the *in situ* data, whereas Morel's Z_{eu} product tends to fall short.

In pure water, light is diminished with depth by complex interactions between absorption and scattering. Let us assume that when phytoplankton are present, the depth of the 1% light level is mainly affected by their abundance in surface waters. It is perhaps then not surprising that Lee and Morel's Z_{eu} are similarly accurate compared with the *in situ* data when higher concentrations of phytoplankton are present. However, at low quantities of phytoplankton biomass (regions where phytoplankton are evident in negligible quantities or where light attenuation is affected predominantly by other constituents), the majority of attenuation will be due to the IOPs, which are more explicitly accounted for in Lee's Z_{eu} . This may explain why values of Lee's Z_{eu} generally match the deep values in the *in situ* data, whereas Morel's Z_{eu} product tends to fall short.

Simple correlations between Z_{eu} and the *in situ* data are useful for showing these small differences between the Lee and Morel measurements. However, plotting the *in situ* 1% light level depths along-side the Z_{eu} products is perhaps more effective at illustrating similarities and differences. Indeed, correlation misses the fact that satellite-derived measures of the 1% light level closely mirror the *in situ* depths collected by the instrumented elephant seals.

At this point, it's worth noting how remarkable that relatively minor result is.

In this study, the Z_{eu} products evaluated against the *in situ* data are 8-day and monthly products that have been combined and then smoothed. Naturally, in order to remotely derive the depth of the 1% light level at its most accurate, it would be best to use daily or near-daily satellite data. As shown in Fig. 4 and Fig. 5, daily measurements at these high latitudes are unrealistic due to persistent cloud cover. Nonetheless, if daily remotely sensed Z_{eu} were available in the Southern Ocean, due to the nature of the *in situ* light data available for this study, we still would not be able to expect perfect match-ups. Indeed, it's important to keep in mind that the *in situ* component of this study was retrieved by instrumented marine predators.

Due to the unpredictable (and non-programmable) behaviour of the tagged elephant seals that collected the *in situ* data, it would be almost impossible to obtain simultaneous measurements between the satellite sensors and the tags. Furthermore, in the unlikely event that an instrumented seal measured the 1% light level at the moment of overpass on a perfectly clear day, data from the two measurements would still not 'match' unless the observation area (pixel) were completely homogeneous. MODIS provides a measurement of an averaged product within a 'pixel' of 4x4km or

9x9km resolution, while our *in situ* values (even once smoothed) represent fine-scale information. Such spatial and temporal mismatches are just a part of the inherent factors impacting the quality of *in situ* and satellite coherence. Studies attempting to compare the two sources of information are thus unlikely to achieve perfect relationships.

Of the two products available, the work in this chapter has shown that Lee's Z_{eu} is more accurate in the open waters of the Southern Ocean, relative to Morel's Z_{eu} . This is in accordance with results from a number of studies examining different Z_{eu} products (Shang et al., 2011) from different satellite sensors (Zhao et al., 2013). Thus, to maintain accuracy for further work in this thesis, Lee Z_{eu} will be applied as a reference depth in the next chapter, representing where light levels are sufficient for photosynthesis but too weak to generate light stress. However, Lee Z_{eu} is sufficiently accurate for it to be considered as a complimentary product to [Chl-a] in the Southern Ocean.

Currently, to remotely measure changes to abundance and distribution of phytoplankton, temporally-merged composites of MODIS [Chl-a] are used broadly. The addition of the Z_{eu} product as a measure of suspended phytoplankton (and potentially other materials) in open waters would be extremely useful. Indeed, it may prove to be superior. Where [Ch-a] is a measurement of phytoplankton abundance from the surface to one optical depth, Lee Z_{eu} contributes information on absorption and backscatter from other potential sources. Further, Z_{eu} provides clues on the vertical dimension.

Because Lee Z_{eu} proved sufficiently accurate relative to *in situ* measures of the 1% light level, and because both datasets showed a significant inverse relationship to MODIS [Chl-a], we can suggest that light attenuation in these waters is primarily related to suspended phytoplankton. Further, it may be possible that Lee Z_{eu} could provide an alternative means of estimating phytoplankton abundance (Teo et al., 2009), and stand as a complementary product to MODIS [Chl-a].

This study spans the summer months of November - January, and the study area is limited to between 40° - 60° S in latitude. Thus, over the time period measured, little measurable change in sun angle and associated irradiance is anticipated. However, the strength of Z_{eu} as a complementary measure of [Chl-a] would still be based on one central assumption: the amount of light reaching the ocean surface is not changing significantly. Potential changes to cloud cover over time will be addressed

in detail in chapter 6, suffice to say here that evaluation of a light-derived product should be considered in conjunction with light itself.

CORRECTING NON-PHOTOCHEMICAL QUENCHING OF FLUORESCENCE DATA RETRIEVED BY TAGGED SOUTHERN ELEPHANT SEALS, USING MODIS LEE Z_{EU} .

Parts of this chapter formed content included in the paper: Biermann, L., Guinet, C., Bester, M., Brierley, A. S., & Boehme, L. (2015). An alternative method for correcting fluorescence quenching. *Ocean Science*. DOI: doi:10.5194/os-11-83-2015. The paper and all methods therein were written, developed and conducted by the lead author, and have been expanded for inclusion in this thesis chapter.

3.1 INTRODUCTION

In the previous chapter, I introduced the satellite product Z_{eu} and evaluated its accuracy with *in situ* light data returned by tagged southern elephant seals. In this chapter, I now apply Lee Z_{eu} to improve the accuracy of a second set of *in situ* fluorescence data returned by tagged southern elephant seals.

Fluorescence is widely used as a relatively inexpensive, non-invasive method for measuring chlorophyll-a, the pigment that all oxygenic photosynthetic organisms contain (Lorenzen, 1966; Cullen and Eppley, 1981; Falkowski and Kolber, 1995; Lavigne et al., 2012). This is especially useful in the marine environment, where submersible fluorometers can be deployed on a range of platforms to approximate phytoplankton abundance and distribution in both the vertical and horizontal. Essentially, this process works because chlorophyll pigments packaged inside phytoplankton cells re-radiate $\approx 2\%$ of light energy as fluorescence. Active fluorescence can thus be measured by a fluorometer delivering output at 460nm (excitation in the blue) and measuring resultant fluorescence yield in the 620-715nm range (detection in the red). Assuming that the measured yield is proportional to the abundance of photosynthesising phytoplankton, relative values of fluorescence can then be used to quantify primary biomass. However, yield (and thus proportionality) can be profoundly af-

ected by several factors, including the intensity of sunlight each cell is exposed to (Behrenfeld and Boss, 2006).

Over the summer months in the Southern Ocean, phytoplankton in the well-mixed, well-lit fraction of the water column are exposed to highly variable amounts of light. When any given chlorophyll molecule packaged inside any given phytoplankton cell absorbs light, it shifts from a ground state to its excited state (Logan et al., 2014). At optimal illumination, light energy is used to drive the process of photosynthesis, where chemical energy and inorganic carbon are converted into organic carbon - biomass (Krause and Weis, 1991; Lee et al., 2014). Furthermore, under these optimal conditions, a photon of energy is also emitted in the form of fluorescence, which is measurable by a fluorometer instrument. Under high sunlight intensity (light stress), however, phytoplankton instead employ the mechanism of non-photochemical quenching to shift from the excited state into ground state. Simplistically, the process converts surplus excitation energy from excess light intensity into heat, which is then 'harmlessly' dissipated (Logan et al., 2014). In this way, non-photochemical quenching enhances protection against bleaching and cell death in environments where light energy absorption exceeds the capacity for light utilisation (Behrenfeld et al., 2009). Importantly, however, in this state of photo-protection, the process of photosynthesis is suppressed and measurable fluorescence yield drops (Müller et al., 2001).

This phenomenon of quenching is highly relevant for any studies relying on measures of fluorescence to quantify Chl-a in the marine environment. Across all oceans and over all seasons, during periods of high light stress, shallow-mixed phytoplankton in the euphotic zone will be protecting their photosystems by initiating non-photochemical quenching instead of photosynthesising (Milligan et al., 2012). If this process is unaccounted for during *in situ* evaluation of fluorescence, quenched yields at/near the surface will generate values under-representative of true Chl-a concentrations, with consequences for studies of phytoplankton abundance.

Avoiding such under-representation is particularly important when comparing satellite-derived [Chl-a] at the surface with *in situ* fluorescence-derived measures of Chl-a. It's important to note that the key concept here is 'surface'. Satellite sensors can only 'see' ocean colour from the surface to one optical depth; providing little to no information on the vertical structure of the water column. To illustrate, Fig. 26 shows a typical example of vertical fluorescence collected by a tagged southern elephant seal over a 3-month period. In this region of the Southern Ocean over this

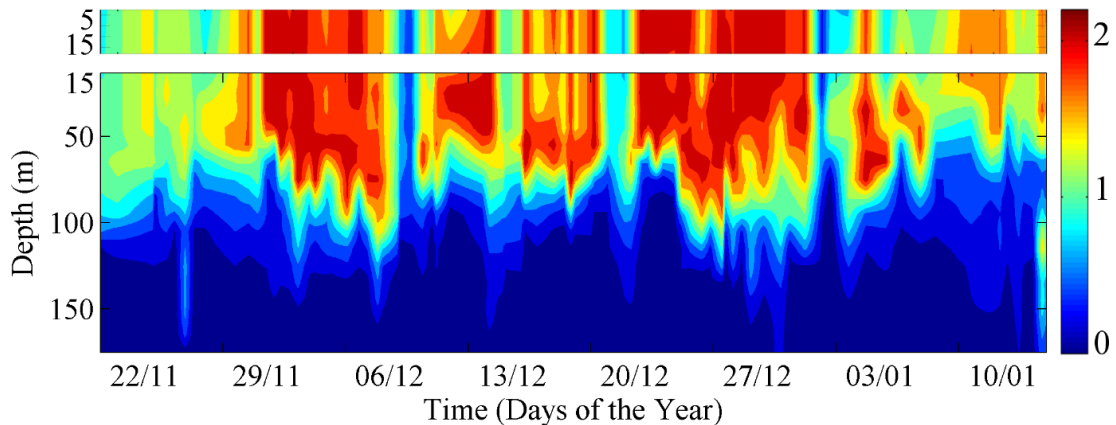


Figure 26: Unprocessed (quenched) vertical fluorescence yield retrieved by an animal-borne fluorometer over austral summer months November 2009 - January 2010. Fluorescence is measured in relative units rather than yield, and the colour bar represents relative fluorescence units (RFU).

period of time, mean optical depth ($1/K_d(490)$) that the MODIS sensor measured to was $\approx 15\text{m}$. The vertical *in situ* 'snapshot' collected by the tagged seal has thus been divided into what the satellite was able to 'see' (surface - 15m) and what remained 'hidden' (15m - 175m). Significant vertical complexity is clearly evident below the top panel representing mean optical depth.

Satellite-derived ocean colour images reveal seemingly chaotic distributions of [Chl-a] in space and time. This variability is further complicated by the fact that phytoplankton at the surface and phytoplankton in the vertical are often constrained or driven by entirely different processes (Behrenfeld, 2010; Chiswell, 2011; Chiswell et al., 2015). With this in mind, how reliable is remotely derived surface [Chl-a] at providing an approximation of true Chl-a and/or phytoplankton abundance? To answer this question, it is helpful to separate the 'skin' from what lies beneath. Therefore, this chapter focuses mainly on the ocean surface when processing fluorescence data collected by far-ranging marine predators in these high latitude waters.

Since 2008, instrumented southern elephant seals undertaking their post-breeding foraging migration have collected and relayed *in situ* fluorescence data over the productive austral summers. As discussed, however, in order to be representative of Chl-a, fluorescence data must be corrected for non-photochemical quenching at the surface. In previous work on glider data, correcting for quenching has involved using backscatter (Sackmann, 2008) or surface light intensity (Todd et al., 2009); each measured simultaneously to fluorescence. For autonomous platforms collecting 'only' fluorescence, salinity and temperature data in remote locations, this is not possible.

Thus, quenched fluorescence profiles collected by Argo floats (Xing et al., 2011) and tagged southern elephant seals (*Mirounga leonina*) (Xing et al., 2012; Guinet et al., 2013) have been corrected from a density-derived mixed layer depth (MLD).

The MLD defines a relatively homogeneous region of density at the surface; primarily driven by turbulent mixing from heat exchange and wind stress at the air-sea interface (Kara et al., 2003). It is one of the most important parameters of the upper ocean, acting as a gateway between the ocean and the atmosphere (Sallee et al., 2013). Despite the importance of the MLD, methods used to determine it are relatively arbitrary. It can be based on different parameters (temperature or density) and can vary significantly depending on the time of year, the preference of the author or the particular ocean being studied (Miller, 1976; Levitus 1982; Lewis et al., 1990, de Boyer Montégut et al., 2004). Xing et al. (2011) adopted a density-derived threshold of 0.03 kg m^{-3} to determine the depth of the mixed layer (de Boyer Montégut et al., 2004). To correct for quenching from the MLD, it must be assumed that the maximum fluorescence yield deeper within the mixed layer is representative of the quenched yield just above it. The deep fluorescence maximum can then be extrapolated to the surface, 'filling in' suppressed yield. The key assumption for this method is that turbulence is sufficient to maintain vertical homogeneity of phytoplankton, and the deep fluorescence maximum is not a distinct deep chlorophyll maximum (DCM) instead.

Turbulence and mixing layers are covered in detail in the discussion section of Chapter 4, which addresses the vertical dimension. Briefly: quenched fluorescence profiles often mimic the shape of DCM (Mignot et al., 2011). True DCM form in two ways: either due to differences in Chl-a packaging, or when the bulk of phytoplankton biomass settles to depths where both nutrients and light are sufficient (Cullen and Eppley, 1981; Holm-Hansen and Hewes, 2004; Mellard et al., 2011). Either way, because DCM are found below one optical depth, the abundance and distribution of such features cannot be measured by satellite (McClain, 2009; Charrassin et al., 2010). However, vertical distributions of phytoplankton play important roles in the organisation of pelagic trophic food webs (Mellard et al., 2011). DCM in particular play potentially under-reported roles in net primary production and carbon fixation (Fairbanks et al., 1982; Estrada et al., 1993; Claustre et al., 2008). It is therefore important to distinguish between quenched profiles mimicking the shape of DCM and true DCM features - correcting the former without masking the latter.

The upper layer of the Southern Ocean tends to be deeply mixed, even over austral summers, and DCM were previously thought to be rare (discussed in Holm-Hansen and Hewes, 2004). However, ship-based studies undertaken in different regions of the Southern Ocean have shown that mixing and settling patterns within and between functional types are dynamic (Holm-Hansen and Hewes, 2004; Mengesha et al., 1998; Quéguiner, 2013, Sangra et al., 2014). Indeed, phytoplankton can be heterogeneously distributed within the 'mixed' layer, especially if turbulence is weak to moderate. This is true for motile (flagellated) and seasonally successive (heavily silicified) species (Mengesha et al., 1998; Quéguiner, 2013). Furthermore, in response to a light gradient, the amount of chlorophyll pigment packaged per cell may vary with depth, generating DCM independent of biomass (Behrenfeld and Boss, 2006). The presence and potential significance of DCM will be discussed in detail in the next chapter, suffice to say here that reliance on the assumption of homogeneity within the mixing layer is possibly problematic.

In this chapter, I present an alternative method to account for quenching without relying on homogeneity in the density-derived upper layer. Instead of using MLD, quenching is corrected using the limit of the euphotic zone, defined as the depth at which downward photosynthetic available radiation (PAR) is at $\approx 1\%$ of the surface value (Shang et al., 2011; Soppa et al., 2013). As detailed in the previous chapter, light attenuation to 1% is an important parameter for monitoring water quality and measuring primary productivity (Lee et al., 2007). However, for the purposes of correcting quenching, what is most important is that at the 1% level, light is sufficient for photosynthesis (Ryther and Menzel, 1959; Morel and Berthon, 1989; Saulquin et al., 2013; Palmer et al., 2013) but too weak to cause quenching (Alderkamp et al., 2011, Ross et al., 2011). In Chapter 2, I was able to conclude that satellite-derived Z_{eu} calculated using the Lee et al. (2007) algorithm is sufficiently representative of *in situ* measures of the 1% light level. Thus, Lee Z_{eu} is used as the depth from which to correct for quenching.

This alternative method of correcting quenching from Z_{eu} is applied to fluorescence data collected by seventeen animal-borne fluorometer, conductivity, temperature and depth satellite-relayed data loggers (FCTD-SRDLs) deployed in the Southern Ocean over several austral summers (Table ??).

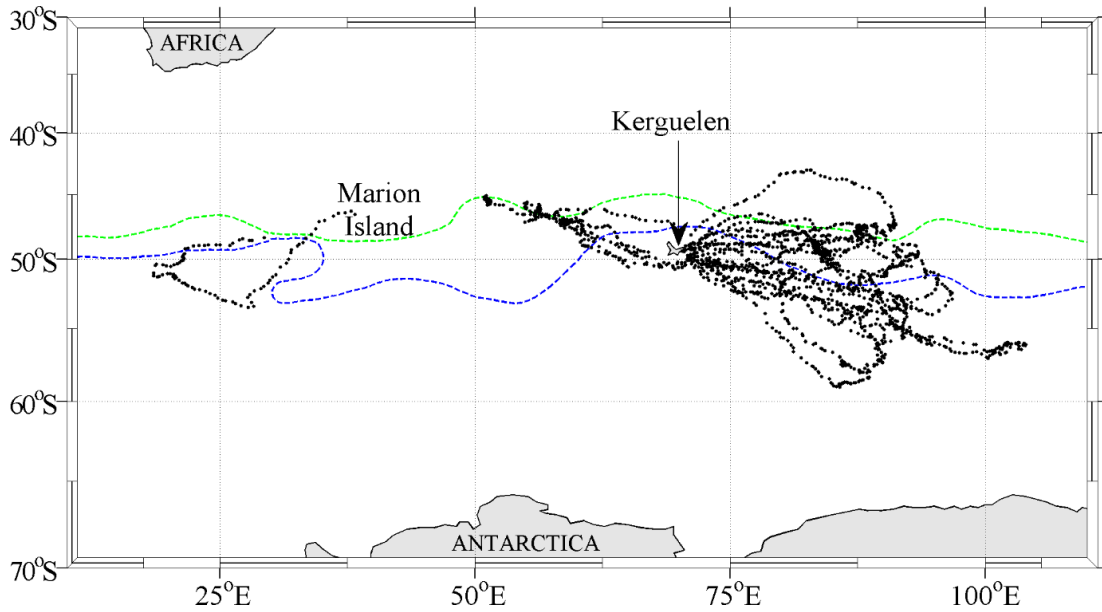


Figure 27: Tracks of 17 southern elephant seals (in black) tagged with FCTD-SRDLs over austral summers spanning 2009 to 2013. The general positions of the Subantarctic Front and the Polar Front are shown in green and blue, respectively (Orsi and Harris, 2014).

3.2 MATERIALS AND METHODS

3.2.1 Collection of *in-situ* data

Between 2009 and 2013, sixteen adult female southern elephant seals from Kerguelen and one from Marion Island were equipped with FCTD-SRDLs (Sea Mammal Research Unit, St Andrews University, Scotland) before the seals undertook their post-breeding foraging migration over the austral summer (Fig. 27).

Following established tagging protocols (Bester, 1988; McIntyre et al., 2010), the seal on Marion Island was immobilized with ketamine using a remote injection method and the tag was glued to the fur on the head with quick-setting epoxy resin. Seals on Kerguelen were anaesthetised with an intravenous injection of tiletamine and zolazepam 1:1 and tags were glued to the fur on the head using a two component industrial epoxy (Jaud et al., 2012).

After initial activation of a CTD-SRDL, the default state is 'idle' with automatic activation every 4 seconds to sample the pressure sensor and wet/dry sensors. Information from both is stored in a dedicated memory space called the samples buffer, and used to classify behavioural state: namely: hauled out, diving, at the surface or

cruising. The tag program (CTD-GEN-07B) attempts to detect what the seal is doing, and what further actions should be carried out. If the seal is classified as 'at the surface', for example, the tag is programmed to attempt data transmission to the nearest ARGOS satellite. If the animal is detected to be in a descending dive state, onboard instruments will record data on dive shape. On the other hand, if the tag detects that the seal has started the ascending phase of a dive, the hydrographic data will begin to be recorded (Boehme et al., 2009).

Once the wet/dry sensors have been wet for more than 8 seconds and the pressure sensors measure changes in dbar equivalent to depths below 6m, the tag will classify a behavioural state of 'diving'. Data on the dive shape is then collected and moved to the dive shape buffer. This dedicated space can hold up to 256 entries, and new data points are added every 4 seconds until criteria for the end of dive behaviour are met. If the dive lasts longer than 17 minutes, all the entries are filled. The tag deals with this by discarding every second data point as the dive continues, leaving 128 that are full, and then refilling. This process continues until dive-end criteria ('at surface') are met (Boehme et al., 2009).

Before data can be transmitted, they have to be compressed into 256 bits. At this stage, onboard processing is initiated and the broken stick model (BSM) is applied (Fedak et al., 2002). This reiterative algorithm acts to compress as much information as possible into a very small package of data by drawing a series of lines and generating break points and segments (Heerah et al., 2014). The BSM is best illustrated in the figure from Photopoulou et al. (2015). First, a line is drawn between the dive start point and the dive end point, joining them (b). Second, a line is drawn from this segment to the point furthest away from it (d). In this way, the BSM starts off with three points: (i) surface start point, (ii) maximum dive depth and (iii) surface end (e). This is the 'original dive profile' with two line segments and one break point. The next largest residual becomes the next break point, and this continues for the duration of each dive until there are four break points and five segments (f - o).

Hydrographic data are collected once the tag measures a steady decrease in pressure, indicating that the seal is ascending from depth to the surface. The CTD sensor measures conductivity, temperature and pressure every second between the deepest point in the dive and the surface, yielding an upcast. Typically, end-product CTD profiles are made up of 17 points, 9 of which are collected at fixed depths during the dive, and 8 extra which are selected at depths using the same BSM employed

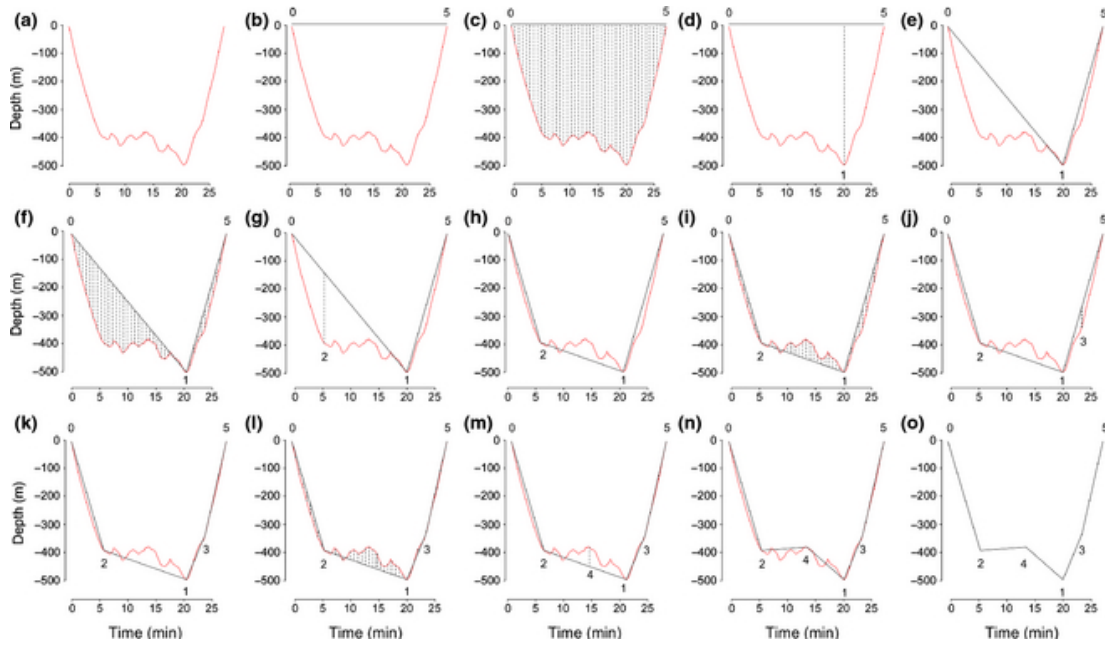


Figure 28: Taken from Photopoulou et al. (2015): The iterative process of the broken stick algorithm is presented step-wise from (a) to (o). The red lines represent the true time?depth dive path, the solid black lines represent the abstracted dive path and the dashed lines represent the residuals for the abstracted dive path, at each iteration of the algorithm. The numbers represent the order in which points are added to the abstracted profile. Points 0 and 5 mark the beginning and end of the dive. The dashed black lines represent the residuals that are calculated at each time step between the true and abstracted dive.

for dive shape profiles. 1000 temperature and 1000 salinity bins are made available in the hydrographic buffer during a given upcast, and they're added according to the relative pressure at which they are sampled. At least one CTD upcast is collected every 6 hours, provided the animal is diving. To ensure maximum coverage of the water column, only data from the deepest dive within that 6-hour period are retained in the hydrographic buffer.

Fluorescence is measured slightly differently. Yield is recorded by a Cyclops 7 fluorometer (Turner Designs, CA, USA), which delivers a voltage output proportional to the fluorescence detected in a wavelength between 620 and 715nm. The Cyclops instrument is programmed to measure fluorescence every 2 seconds during the ascent (upcast), from 180m to the surface. As with the dive and CTD data, fluorescence data have to be compressed for transfer through the Argos satellite system, (Boehme et al., 2009). Fluorescence yields are binned into 10m vertical intervals. The reading for '175m' is thus a weighted mean of all fluorescence readings taken between 180m and 170m. This is the deepest bin available - deep and dark enough to anticipate an absence of live, photosynthesising phytoplankton (Guinet et al., 2013). However, instruments do not return readings of zero at these depths. This 'dark count' is an offset value added by the manufacturers; useful because at very low signal, readings are indistinguishable from noise. The offset value increases the signal to noise ratio, which must be removed during data processing (Lavigne et al., 2012; Xing et al., 2011).

The median of readings at 175m was subtracted along each vertical profile from all measurements collected by the same tag (Fig. 29). This is not only useful for making the fluorescence values more representative, it also serves to reduce variability between tags (Xing et al., 2012). The resulting values are considered proportional to fluorescence, and are termed Relative Fluorescence Units (RFU).

All at-sea data were relayed via the Argos satellite system (<http://www.argos-system.org>). Locations were provided by Service Argos based on Doppler shift measurements and data were downloaded from the Sea Mammal Research Unit Instrumentation Group's website (<http://www.smru.st-andrews.ac.uk/>). Detailed information on the hardware and software of the CTD-SRDL is described by Boehme et al. (2009), and on-board data processing is described comprehensively by Fedak et al. (2002).

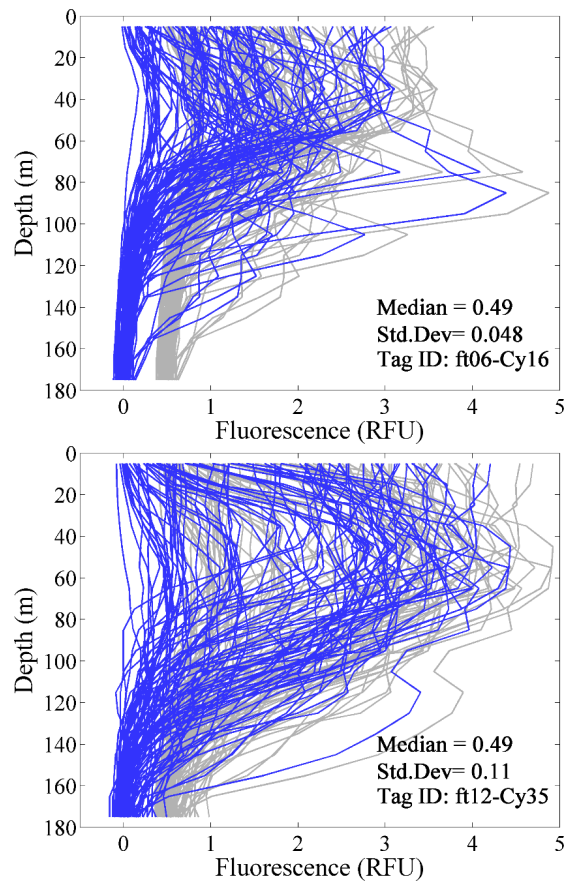


Figure 29: Two typical raw vertical fluorescence datasets collected by two southern elephant seals instrumented with FCTD tags. The grey lines show fluorescence yield before the offset (dark count added by manufacturers) is removed. Median yield at 175m is subtracted along each vertical fluorescence profile, resulting in a 'zeroed' dataset, shown in blue.

3.2.2 Satellite data

All MODIS L3 products (data processed and calibrated by NASA) are freely available and were downloaded from the OceanColour website (<http://oceancolor.gsfc.nasa.gov>). Monthly and 8-day composites were downloaded as 4x4km resolution standard mapped images (SMI) in high definition format (HDF), extracted using 7-zip and imported into Matlab for processing.

The evaluative product Z_{eu} reflects the limit where PAR has been attenuated to 1% of its surface value. To briefly recap the analysis done in Chapter 2: MODIS provides two products of Z_{eu} derived from remotely sensed ocean colour (Lee et al., 2007; Morel, 1988; Morel et al., 2007). Morel's Chl-approach is an empirical method centred on the assumption that the optical properties of the water are 'only' affected by phytoplankton (Case-1 waters). The calculation of Z_{eu} is thus solely based on remotely-sensed measurements of [Chl-a]. Lee's approach, on the other hand, is derived with the addition of inherent optical properties (IOPs) - the characteristics of water which depend entirely on its content. Knowledge of Z_{eu} thus requires information on backscattering and absorption coefficients at 490nm (Shang et al., 2011). When evaluated alongside *in situ* measures of the 1% light level, Lee's Z_{eu} appeared to be more accurate than Morel's, and is thus the product used for the rest of the work done in this thesis. For simplicity, Lee Z_{eu} is often referred to simply as Z_{eu} from this point, with the understanding that the selected algorithm is that of Lee et al (2007).

Based on the positions from the 17 elephant seals tagged with fluorometers, where each *in situ* position relates to an upcast (vertical fluorescence measured from 180m to the surface), 8-day Z_{eu} were used whenever available, and monthly values were added to 'fill in' the blanks. This method was applied in Chapter 2 and it served to balance spatial coverage with as little temporal compromise as possible. In this study, an even spread of variation and good agreement between the two products also supported the idea that monthly values are sufficiently representative of the missing 8-day values in these cloud-covered, open waters of the Southern Ocean (Fig. 30).

Despite combining 8-day data with monthly data, gaps in coverage were still present in space. For each fluorometer profile, the closest Z_{eu} value in space was extracted from the gridded dataset. If no value was available, Z_{eu} was interpolated linearly from the nearest seal position (upcast) with an associated Z_{eu} value.

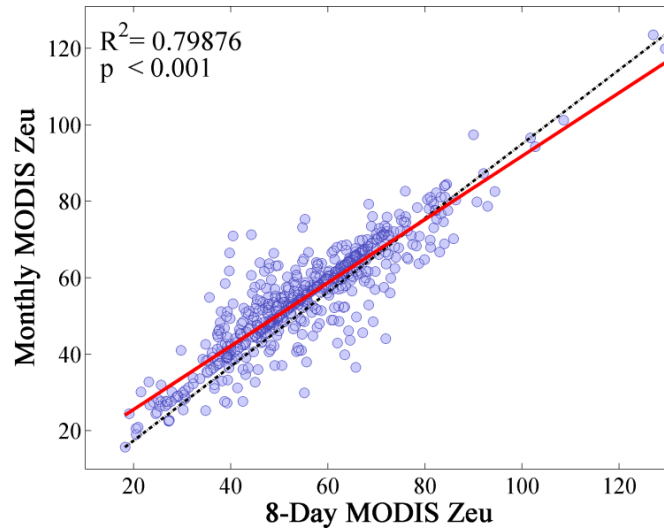


Figure 30: Correlation between 8-day and monthly composites of MODIS Lee Z_{eu} ($n = 678$).

3.2.3 Correcting for quenching

Quenching occurs in surface waters during daylight hours (Fig. 31). Data were thus categorised as 'day: quenched' (from sunrise to sunset; defined as when the sun is ≥ 6 degrees above the horizon) or 'night: unquenched'. Before proceeding, a small proportion of profiles with maximum fluorescence yields below 0.15 RFU were removed from the dataset. These low signals tend to fall within the noise, and the resulting vertical profiles cannot be meaningfully interpreted.

Despite daily variability attributed to cloud (variable light field), differences in phytoplankton assemblage, as well as abundance and distribution in time and space, suppression of fluorescence is ubiquitous (Fig. 31). Fitting a second order polynomial to surface fluorescence yield (top 10m) as a function of time of day (hours) showed that quenching around midday is also significant.

The fluorescence data were separated into 'night: unquenched' and 'day: quenched' datasets, delineated by when the sun was 6 degrees below or above the horizon, respectively. Night data did not exhibit quenching and was thus not processed for correction. For the day dataset, quenching was corrected from either the depth of the mixing layer (conventional method) or the depth of Z_{eu} . The density-derived MLD was calculated using salinity and temperature data collected concurrently to fluorescence by the CTD on the FCTD-SRDL. Here, MLD is defined as the depth where the vertical density gradient equals or exceeds a threshold value of 0.03 kg m^{-3} ; as employed by Xing et al. (2011, 2012) (de Boyer Montégut et al., 2004; Kara et al.,

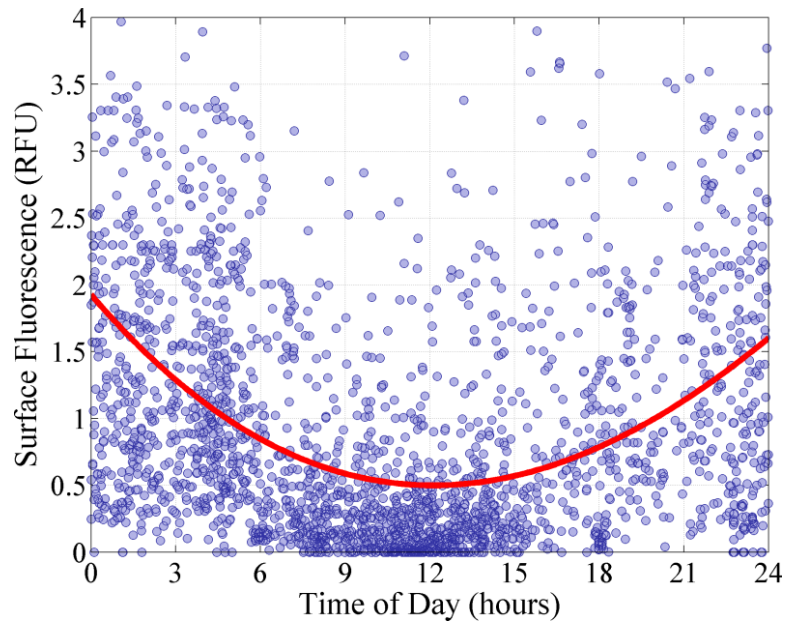


Figure 31: Uncorrected surface fluorescence data (top 10m) collected over several summers, combined and plotted over local time (hours). Fitted second-degree polynomial is shown in red.

2000). The MLD in the region of interest tends to remain deeper than 60m, even over the austral summer (Dong et al., 2008; this study). The second depth used to correct quenching is the remotely-derived Z_{eu} using Lee’s algorithm (2007). Separately, maximum fluorescence yield between MLD and the surface, or Z_{eu} and the surface, were then extended to fill in suppressed yield.

3.3 RESULTS

For over 80% of the day dataset, mixed layer depth was deeper than Z_{eu} . However, the small proportion ($\approx 20\%$) of waters with MLD shallower than Z_{eu} proved problematic for correcting quenching. In these instances, correcting from MLD generates still-quenched values. Conversely, correcting from Z_{eu} would mask shallow but potentially ‘true’ subsurface features. Where MLD shoaled above Z_{eu} , fluorescence data were thus flagged and removed from the dataset.

Where MLD exceeded Z_{eu} , quenching was corrected using both depths separately and the results were then examined side-by-side for any differences. Fig. 32 illustrates a few representative fluorescence profiles that were corrected for quenching. Suppressed surface values were ‘filled’ in with the maximum fluorescence value from Z_{eu} (shown in blue) or MLD (in red). In Fig. 32(a) and (b), correcting from Z_{eu} served

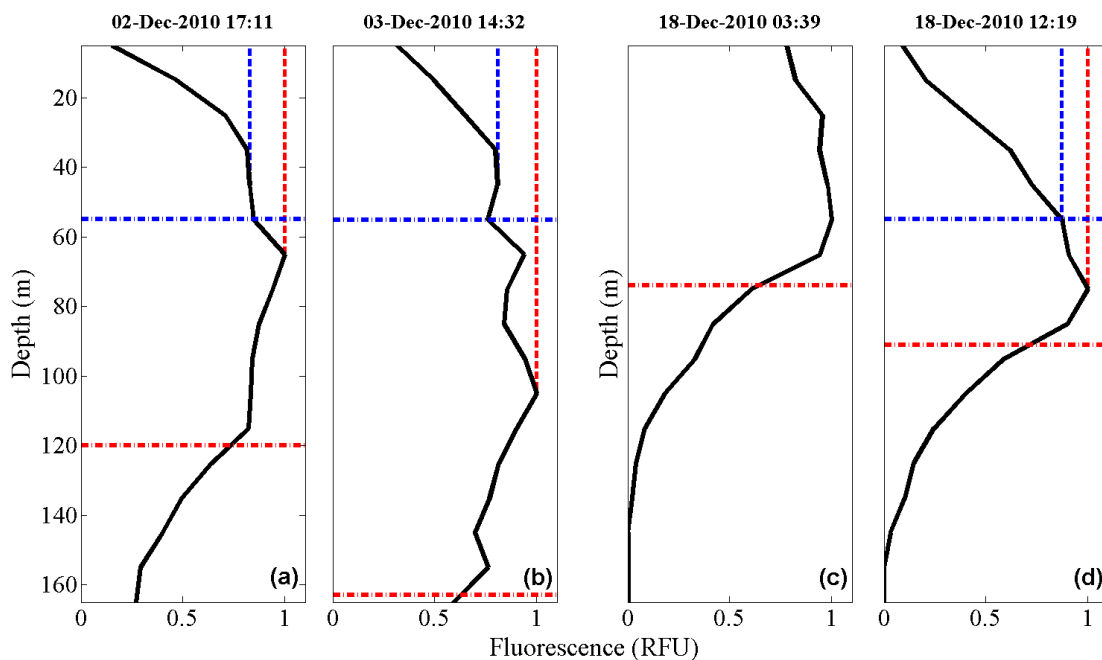


Figure 32: Normalised vertical profiles of fluorescence (solid black line) corrected using either MLD (dashed red line) or Z_{eu} (dashed blue line). Fluorescence in (c) was measured at night and is thus unquenched (MLD in red but Z_{eu} absent at night). Profiles (a), (b) and (d) were collected at varying times during the day.

to 'fill in' quenched surface yield while still conserving vertical complexity between the depth of the 1% light level and MLD. In these examples, the density-derived mixing layer was in excess of 100m and correcting from MLD relies heavily on the assumption of homogeneous mixing. This will be discussed in detail in Chapter 4, suffice to say here that any patterns of vertical heterogeneity would consistently be lost when correcting from MLD. Furthermore, if DCM are present below Z_{eu} but within MLD, correcting from the latter would mask the feature and cause possible overestimations of surface yield.

Although unquenched night data is often useful to serve as a reference, the fluorometer 'platforms' are top predators moving constantly in their search for food and surfacing at irregular intervals in-between. Thus, we cannot rely on night profiles to validate the day data, but when they are available they are highly useful. Fig. 32(c) is a night profile that was close in time and space to the quenched fluorescence profile in Fig. 32(d) and this helps validate the use of Z_{eu} over MLD. Indeed, correcting from Z_{eu} generates surface values that are similar to the surface yield measured in the unquenched night profile (c).

To illustrate the quenching effect without interannual and regional variability, 'day' yields were divided by the preceding 'night' yields to generate ratios. Data were then

binned by hour and plotted using boxplots (Fig. 33). Quenching was evident for a full 12-hour cycle, from approximately 6am until 6pm (Fig. 33a). However, once quenched surface values were 'filled in' with maximum fluorescence yield from the depth of the MLD, fluorescence largely recovered to the 1:1 ratio line (Fig 33b). Similarly, correcting quenching from the depth of Z_{eu} showed mean surface fluorescence recovering to the 1:1 ratio line (Fig. 33c).

As an alternative method to correct quenching in surface waters, Z_{eu} can thus be successfully used in place of MLD.

3.4 DISCUSSION

The phenomenon of non-photochemical quenching is well described and appears to be ubiquitous across oceans and seasons, as well as taxa of phytoplankton (Sackmann et al., 2008; Milligan et al., 2012). The depth at which attenuated light levels become too weak for quenching is key for correcting in-situ fluorescence data; ensuring yield is representative of vertical Chl-a concentrations. However, when fluorescence data is collected autonomously, this depth cannot always be measured in space and time.

When underwater gliders, bio-Argo floats or other autonomous platforms are collecting fluorescence data, other variables such as PAR and backscatter also tend to be collected. These additional data are more useful for quantifying quenching and correcting it (Sackmann et al., 2008). The Z_{eu} -correction method is only applied when no other data are available and, specifically, in waters where MLD surpasses the 1% light level. In less wind-mixed or seasonally stratified waters, where hydrographically defined mixed layers routinely shoal above Z_{eu} , this approach is impractical. In the Southern Ocean, where mixed layers are deeper than Z_{eu} more than 80% of the time, quenching can be corrected using the Z_{eu} approach when no other data are available.

For this study, removing quenched fluorescence would mean discarding 1221 of the 2034 profiles collected by seventeen animal-borne tags over several austral summers in the Southern Ocean. In order to evaluate satellites products in such an under-sampled ocean, losing over 60% of the *in situ* data is simply not viable. For this reason, being able to reliably correct fluorescence quenching in surface waters is vital. In the day (quenched) dataset, mixed layer depth surpassed the depth of Z_{eu} more than 80% of the time. The small proportion ($\approx 20\%$) of waters with MLD shallower

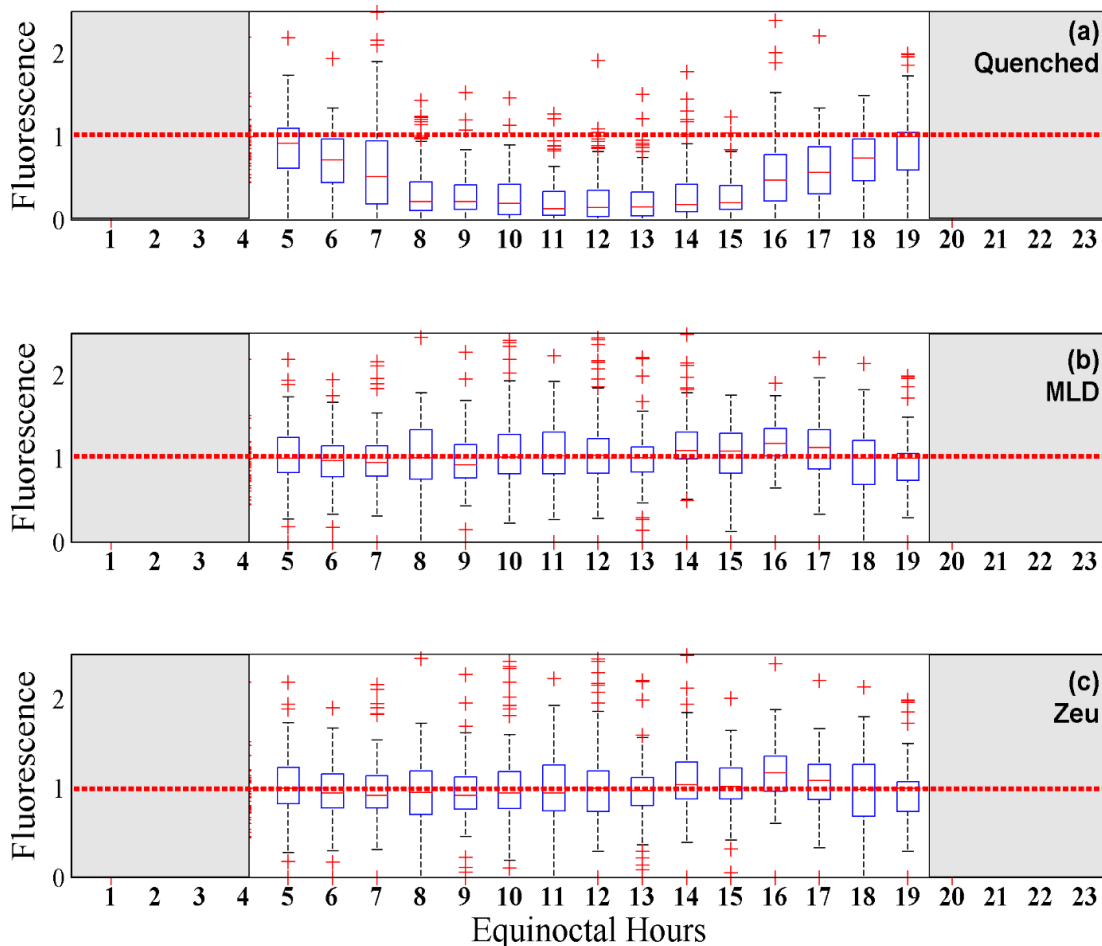


Figure 33: Ratios of day to night surface fluorescence from data collected by 17 animal-borne fluorimeters over 5 austral summers. Boxplots show the distribution of ‘day’ to ‘night’ ratios in (a), representing quenched to unquenched yield. Ratios decrease from 6h00 until 18h00, then recover to the 1:1 ratio (red line). Flanking grey sections represent times of the day where the sun is less than 6° below the horizon. Surface fluorescence corrected using MLD in (b) and corrected using Z_{eu} in (c) do not follow the same trend of deviation from the 1:1 ratio line. Indeed, at the surface specifically, correcting from MLD (b) or Z_{eu} (c) does not generate substantial differences.

than Z_{eu} proved problematic for correcting quenching. In these instances, phytoplankton in the shallow upper layer would not be mixed to deeper depths where light reaches less saturating intensities. Whether phytoplankton are heterogeneously or homogeneously distributed, this shallow mixed layer of phytoplankton is likely to be uniformly quenched. Without an unquenched maximum fluorescence measurement within the hydrographically defined mixed layer, the MLD approach fails. The Z_{eu} approach is also unable to correct quenching under these conditions, because the method would have to rely on phytoplankton being homogeneously distributed between the depth of the 1% light level and the surface. There is no physical, chemical or biological mechanism that would support this. Therefore, where MLD shoaled above Z_{eu} in this study, fluorescence data were flagged and removed from the dataset.

For profiles where MLD is deeper than the 1% light level, can we be confident that no quenching will be taking place at the limit of the euphotic zone? During daylight hours, a proportion of the euphotic zone (surface to the 1% light level) will be light-saturated relative to photosynthetic efficiency (Behrenfeld and Falkowski, 1997). Shallow-mixed phytoplankton are exposed to a range of super-saturating light intensities, while deep-mixed phytoplankton will be exposed to low-levels of light intensity that are suboptimal for photosynthesis in the absence of photoadaptation. Cells throughout any given euphotic zone adapt to variations in the light field through a range of physiological strategies (Arrigo et al., 2010; Kropuenske et al., 2009; Kropuenske et al., 2010). These include non-photochemical quenching for high light stress, and a range of dark adaptation strategies below a saturating light threshold. Photosynthesis typically saturates at light intensities of ≈ 200 mmol photons $m^{-2} s^{-1}$ and below ≈ 100 mmol photons $m^{-2} s^{-1}$ cells must initiate dark adaptation strategies (Garcia and Purdie, 1992). By definition, such 'dark-adapted' phytoplankton at the base of the euphotic zone are not experiencing high light stress. However, light is still sufficient for photosynthesis. Indeed, Hameedi (1978), Platt et al. (1982) and Lee et al. (2010) have shown that shade-acclimated phytoplankton from the 1% light level are largely free from cell damage associated with variable to high light stress, and are more productive overall than phytoplankton from the 50% light level (Alderkamp et al., 2011; Palmer et al., 2013).

At noon on a cloudless summer's day, the Southern Ocean can receive surface irradiance of up to 2000 mmol photons $m^{-2} s^{-1}$ (Ross et al., 2008). Under such super-saturating conditions, light saturation (stress) would still be anticipated at depths

where intensities have been attenuated to 10% of the surface value, and dark-adapting phytoplankton may be found at depths where light attenuation is at $\approx 5\%$. Therefore, at the depth of the 1% light level, phytoplankton are likely to be both dark-adapted (i.e. not exhibiting non-photochemical quenching) and actively photosynthesising.

Composites of MODIS Z_{eu} are provided as evaluative products and these were used to determine the depth where surface PAR would be attenuated to 1%. At this depth, light intensity would be too low to cause light stress and thus suppression of fluorescence yield. Lee's algorithm for Z_{eu} provided accurate and reliable estimates of Z_{eu} in open waters of the China Sea (Morel et al., 1988; Morel et al., 2007; Lee et al., 2007; Shang et al., 2011). In the previous chapter, I was able to show that Lee Z_{eu} also reliably estimate the depth of the 1% light level in the open waters of the Southern Ocean.

Combinations of 8-day and monthly Z_{eu} products were used to account for the holes in coverage, and remaining gaps were filled by interpolating. Despite the large temporal difference, 8-day and monthly products showed excellent agreement ($R_2 = 0.82$, $p < 0.0001$). This is less likely to be true for coastal or near-coastal regimes, where dynamics change on finer scales. For this reason, we would recommend using daily data combined with 8-day composites in these areas, or any region where cloud cover is less of a persistent problem.

For future deployments of FCTD-SRDLs in the Southern Ocean, it would be valuable to activate the fluorometer at depths surpassing 200m. During testing and tag calibration in the Mediterranean as part of the BOUSSOLE programme, 200m proved to be a robust 'dark count' depth (results not shown). Southern Ocean waters, however, experience more intense winds, frontal jets, mixing to greater depths and an entirely different community structure. Although no live phytoplankton capable of photosynthesis were expected to be present at this depth, in these high latitude, open waters, fluorescence readings at 200m suggest that this assumption is not always accurate. By turning instruments on at deeper depths ? between 300m-400m for example ? the deepest reading is more likely to be clear of fluorescence and allow for more confidence when calculating the offset (dark count) per instrument. The significance of this becomes more apparent when attempting to determine measurement error for each fluorometer, which is calculated by bootstrapping deepest values (Chapters 4 and 5).

In the next chapter, the benefits of correcting from Z_{eu} , which does not rely on homogeneity in the mixed layer, will be discussed in detail.

ON THE PRESENCE AND RELEVANCE OF DEEP CHLOROPHYLL MAXIMA IN DEEPLY MIXED INDIAN SECTOR WATERS OF THE SOUTHERN OCEAN

Parts of this chapter formed content included in the paper: Biermann, L., Guinet, C., Bester, M., Brierley, A. S., & Boehme, L. (2015). An alternative method for correcting fluorescence quenching. *Ocean Science*. doi:10.5194/os-11-83-2015. The paper and all methods therein were written, developed and conducted by the lead author, and have been expanded for inclusion in this thesis chapter.

4.1 INTRODUCTION

The Southern Ocean appears to be warming faster than the global average (Gille, 2002). Furthermore, this ocean regime is experiencing changes to its wind-driven circulation, with consequences for everything from heat and CO₂ exchange at the marine boundary layer, to mixing and upwelling processes (Son et al., 2008). Individually or cumulatively, these processes will undoubtedly influence primary producers composing the base of the marine food web - the phytoplankton. Whether climate forcing will cause an increase or decrease in net primary production (NPP) is a contentious question, with different answers (and drivers) for different regions. For example, Gregg et al. (2006), Behrenfeld et al. (2006) and Boyce et al. (2010) have reported decreases in global NPP, however, Saba et al. (2010), Kahru et al. (2009) and Arrigo and Van Dijken (2011) have found regional increases. Nonetheless, what does appear to be certain is that change is already happening, and understanding the potential impacts to primary production and carbon export is of vital importance.

At the low latitudes, mounting evidence from both *in situ* and ocean colour-based model studies unambiguously show that NPP has recently dropped (Gregg et al., 2003; Behrenfeld et al., 2006). Overall, ecosystem-biogeochemical and general circulation models project that NPP will continue decreasing in the subtropics due to increasing stratification and consequent reduction in nutrient availability (Finkel, 2014).

Indeed, one of the main projected changes to our global oceans is increased stratification and changes to mean MLD (Behrenfeld et al., 2006; Kemp and Villareal, 2013).

In temperate (cold and warm mid-latitude) waters, MLD tends to deepen from autumn into winter, shoaling again to shallower depths during spring and through summer (Franks, 2014). This process of deep mixing during autumn and winter is vital for injecting nutrients into the upper or surface waters that have become 'stripped' over the productive summer months; essentially recharging them. Model predictions and theoretical studies suggest that increases in temperature and stratification will cause decreases in such vertical mixing, consequently reducing primary production and carbon export (Bopp et al., 2005; Behrenfeld et al., 2006; Kemp and Villareal, 2013). Specifically, climate-driven warming and stratification will favour the smaller phytoplankton taxa not generally associated with high production or high rates of sinking (Kemp and Villareal, 2013). In the Southern Ocean, where diatoms are proposed to dominate mixed assemblages and also contribute the most to carbon draw-down (primary productivity) and export (sinking) (Timmermans et al., 2001), this is of major concern.

Southern Ocean (polar) waters largely conform to the same pattern of 'deep winter mixing layer followed by spring shoaling' seen in temperate oceans. However, the terms 'shallow' and 'stratified' have somewhat different meanings in this circumpolar ocean, where strong winds and extreme buoyancy fluxes generate some of the world's deepest mixed layers (Monterey and Levitus, 1997; Sallee et al., 2010). Even over the summer months, open waters of the Southern Ocean tend to be characterised by deep wind-mixed layers surpassing 60m (Dong et al., 2008; this study). Ecosystem-biogeochemical and general circulation models agree that increases in temperature at the high latitudes are expected to cause upregulation of NPP through increased ice retreat and decreased mixed layer depths (Arrigo et al., 2008; Finkel, 2014). This expectation may only be valid in certain regions of the Southern Ocean, as stronger winds associated with positive trends in the Southern Annular Mode (SAM) may drive mixed layers even deeper in the permanently open waters (Sallee et al., 2010). Changes to MLD have significant implications for conditions experienced by phytoplankton, changing everything from the irradiance regime (light limitation on the one extreme or saturation and light stress on the other) to nutrient availability (Sallee et al., 2010; Finkel, 2014). Using seven years of Argo float data, Sallee et al. (2010) were able to calculate MLD climatologies for the Southern Ocean. MLD anomalies were

compared with ocean colour data, and for much of these polar waters, an increase in MLD resulted in a significant decrease in satellite-derived [Chl-a]. Their results were largely consistent with the hypothesis that increases in MLD will impact on the amount of light available for phytoplankton growth in open waters (Sallee et al., 2010).

The relationship between phytoplankton abundance and MLD is not straightforward, but it is extremely important. For these and other reasons, resolving the vertical component of phytoplankton abundances these high latitude waters is a priority. However, this dimension is highly difficult to measure on broad spatial and temporal scales. As stressed in the previous chapter, satellite measures of [Chl-a] for estimating phytoplankton abundance are only able to resolve the near-surface component. To add the vertical dimension, fluorescence is one of the most practical and thus most widely used ways to measure Chl-a, and measures of Chl-a still stand as the best indicator of phytoplankton biomass (Cullen, 1982). This is not to say that these proxies or indicators are not without caveats. Indeed, the preceding chapter was specifically dedicated to addressing one of the problems associated with *in situ* surface fluorescence - quenching.

For autonomous platforms limited to collecting fluorescence, salinity and temperature data, the density-derived mixed layer (MLD) is currently used as the depth from which to correct for quenching (Xing et al., 2011; Guinet et al., 2013). In the waters south of the Sub-Antarctic Front (SAF), temperature and salinity approximately equally contribute to stratification (Pollard et al., 2012). For this reason, density (a combination of temperature and salinity) is a more appropriate measure of MLD than temperature alone. Thus, the MLD in the Southern Ocean is conventionally hydrographically defined as a region of quasi-homogeneous density at the surface; primarily driven by turbulent mixing from wind stress and heat exchange at the air-sea interface (Kara et al., 2003).

Xing et al. (2011) adopted a density-derived threshold of 0.03 kg m^{-3} to determine the depth of the mixed layer, from which quenching could be corrected (de Boyer Montégut et al., 2004). Subsequently, the MLD method works by finding the maximum fluorescence yield within a density-derived MLD, and 'filling in' the suppressed yields at the surface with this maximum value (Xing et al., 2011). To correct for quenching from the MLD, it must be assumed that the deep fluorescence maximum within a hydrographically defined mixing layer is representative of the

shallower 'invisible' (quenched) fluorescence yields. In other words, it assumes the mixing layer of homogeneous density is also a layer of homogeneous turbulence, and that the vertical phytoplankton pattern will thus be one of uniformity. However, if turbulence is low or presents as gradients within the hydrographically-defined density layer, fluorescence yields representative of Chl-a concentration may very well be heterogeneously distributed.

In the previous chapter, quenching was corrected from the depth of remotely-derived Z_{eu} and resulting fluorescence profiles were compared with quenching corrected from MLD. As detailed in the previous chapter, Z_{eu} is defined as the depth at which downward photosynthetic available radiation (PAR) is attenuated to $\approx 1\%$ of the surface value. At this level, light is still sufficient for photosynthesis but too weak to cause quenching. At the surface, the differences between resulting fluorescence yields were not substantially different. However, the operative word there is 'surface'. The previous chapter did not address the vertical dimension. However, Z_{eu} was ultimately selected as the reference depth to correct for quenching in deeply mixed waters to account for the possibility that Chl-a may not always be uniformly mixed within the hydrographically defined MLD.

DCM can form in two main ways. Firstly, due to differences in Chl-a packaging through photoacclimation processes, or floristic shifts. As a proportion of the dry weight, chlorophyll makes up only $\approx 1\%$ of any given phytoplankton cell (Cullen, 1982). Even within this fraction, the ratio between Chl-a and the organic carbon content per cell will vary considerably between and within phytoplankton types, as a function of nutrient stress, temperature and variations in irradiance (Cloern et al., 2003). With specific regards to a varying light field, even a homogeneous layer of phytoplankton cells will exhibit a gradient of increasing Chl-a with depth. Shallow-mixed cells at/near any given well-lit surface will require relatively little Chl-a to photosynthesise, due to exposure to high light or light-saturating conditions. As these cells become more abundant at the surface, deeper mixed phytoplankton will become increasingly shaded. Thus, due to the combination of shading and the exponential decay of light in water with depth (resulting in light limited conditions), deeper-mixed phytoplankton will package relatively high amounts of Chl-a per cell in order to photosynthesise. These light- and dark-adaptation strategies, resulting in differences in the amount of Chl-a packaged per cell, fall under the broader term photoacclimation.

Within a homogeneous layer of phytoplankton cells, there is a second scenario where Chl-a with depth may exhibit heterogeneity, and that is through community structure. For example, under controlled laboratory conditions, dinoflagellates have been shown to package more Chl-a per cell than diatoms, (Chan, 1980). For these reasons, even homogeneously mixed layers of biomass rarely result in homogeneous profiles of fluorescence or Chl-a. This situation is compounded when we consider the possibility of distinct heterogeneous layers of biomass in the vertical dimension.

The second main way in which DCM can form is when the bulk of phytoplankton biomass settles to depths where both nutrients and light are sufficient (Cullen and Eppley, 1981; Holm-Hansen and Hewes, 2004; Mellard et al., 2011). In terms of these nutrient and light levels, the definition of 'sufficient' is species-specific and challenging to predict (Yoshiyama et al., 2009). Nonetheless, because DCM are always found well below one optical depth, these features cannot be measured by satellite (McClain, 2009; Charrassin et al., 2010). However, the vertical distributions of phytoplankton may ultimately structure regional marine food webs (Mellard et al., 2011), and DCM reportedly play under-reported roles in primary production and carbon fixation on global scales (Fairbanks et al., 1982; Estrada et al., 1993; Claustre et al., 2008). In the high southern latitudes, having sufficient information on DCM formation and persistence on regional and seasonal timescales may thus be key to understanding everything from Southern Ocean ecosystems to net atmospheric carbon draw-down.

In the past, DCM were considered 'anecdotal', and their presence in datasets was attributed to under-sampling (Martin et al., 2010; Kemp and Villareal, 2013). Today, we recognise that these features are nearly ubiquitous in our global oceans and are often regionally and seasonally persistent. In the Mediterranean basin, it is well established that chlorophyll maxima are present almost exclusively as sub-surface to deep features (Macias et al., 2014). This appears to be less true in the late winter months, when mean mixed layer depth (MLD) is driven below 100m and phytoplankton become more homogeneously mixed within the upper density layer (Lavigne et al., 2015). Indeed, deep mixed layers are rarely considered environments suitable (sufficiently stable) for distinct deep chlorophyll maxima, based on the assumption that deep mixing translates to high and deeply homogeneous turbulence (Franks, 2015).

In this chapter, the fluorescence dataset that was corrected for quenching at the surface in Chapter 3 is now examined in the vertical dimension. This allows for evaluation of the relationship between phytoplankton abundance (using fluorescence)

and the depth of the hydrographically defined mixed layer (using density). Furthermore, examining the quenching-corrected vertical dimension allows for resolution of possible DCM and other heterogeneous patterns of phytoplankton within the 'mixed' layers of these open waters, and along fronts. Knowledge on these patterns is useful from a biological perspective to map DCM in space and time, with implications for how the marine food-web is structured. But information on DCM and vertical heterogeneity is also interesting from a physical perspective; providing clues on turbulence patterns or possible gradients.

4.2 METHODS

4.2.1 *Calculating mixed layer depth*

This study used temperature and conductivity (salinity) profiles collected by the satellite-relayed data loggers (FCTD-SRDL) (Sea Mammal Research Unit, St Andrews University, Scotland), deployed as animal-borne instruments in the Indian and Atlantic sectors of the Southern Ocean. MLD computation was based on direct salinity (accuracy of 0.03 - 0.05 practical salinity units) and temperature (accuracy of 0.02 - 0.03°C) measurements from individual profiles - a total of 1221 collected over 6 years - to compute density thresholds. Using a reference depth of 15m to avoid the diurnal cycle of the mixing layer, MLD was calculated with a surface-density-difference criterion of $\Delta\sigma \leq 0.03 \text{ kg m}^{-3}$. In other words, where the vertical density gradient equalled or exceeded a threshold value of 0.03 kg m^{-3} (Xing et al., 2011; de Boyer Montégut et al., 2004; Kara et al., 2000; Sallee et al., 2015).

4.2.2 *Resolving vertical fluorescence*

As discussed in detail in the previous chapter, concurrent to temperature and conductivity, the FCTD-SRDLs also measure summertime fluorescence yield. Because tags are deployed for the post-breeding season, the foraging trip is relatively 'short', spanning late October to late January. Fluorescence is, therefore, effectively measured over the height of the austral summer, when sunlight is at a maximum and light is no longer considered limiting. Indeed, the light intensity reaching surface ocean wa-

ters at this time of year may be more accurately considered a potential source of physiological stress.

To prevent cell damage caused by said light stress, significant quenching of fluorescence is evident in surface waters from around 06h00 to 18h00 (Fig. 33 in Chapter 3). In the previous chapter, fluorescence data collected during this period ('quenched day' dataset) were corrected using two different reference depths: *in situ* MLD (density gradient threshold of 0.03 kg m^{-3}) or remotely-sensed Lee Z_{eu} (depth of 1% light level). In this chapter, these 'MLD-corrected' and Z_{eu} -corrected' subsets were examined for presence of DCM, as were the remaining unquenched data collectively grouped as 'night'. To determine relative and comparative proportions of DCM and vertically heterogeneous features, the 3 datasets of 'unquenched night', 'MLD-corrected' and Z_{eu} -corrected' were processed separately but identically.

To ensure DCM were not within the measurement error, a 95% confidence interval for the error was calculated for each instrument by bootstrapping (1000 bootstrap samples) deepest fluorescence values. For automated detection of deep fluorescence maxima, the upper confidence limit was set as a threshold value. The algorithm subtracted the upper confidence value from the highest fluorescence yield detected below 20m and added the upper confidence value to the surface measurement (top 20m). If the maximum fluorescence value below 20m remained higher than the fluorescence value at the surface after this step, the profile was flagged as 'potential DCM?'. All deep fluorescence maxima that surpassed surface values outside of instrument error were then visually inspected for confirmation of DCM.

A typical deep chlorophyll maximum could be anticipated to resemble a vertical bell-curve in terms of shape. Instead, visual inspection of all potential DCM detected by the algorithm illustrated that fluorescence profiles indicative of deep maxima present in a variety of shapes. Nonetheless, all vertical profiles flagged by the automated process were confirmed to have maximum values deeper than 20m through manual inspection. For improved confidence with this method, collection of fluorescence data below 180m would improve calculation of the upper confidence limit.

Relative proportions of deep maxima features were then compared between the three data subsets.

4.2.3 *Test 1: Do DCM have surface Chl-a signatures?*

To understand the underlying shape of distributions, a histogram plot was used to display all along-track MODIS [Chl-a] and all DCM associated measures of MODIS [Chl-a]. Datasets were then compared for any significant differences using a student t-test.

4.2.4 *Are DCM associated with fronts or particular water masses?*

The Orsi fronts (Orsi et al., 2005) used in this thesis thus far are climatological ? illustrating the general positions of the fronts and useful for reference. However, general estimates are not necessarily sufficiently precise for determining positions of DCM relative to the SAF and PF. For this reason, I used the method of Boehme et al. (2008) to determine *in situ* positions of different water masses through which the tagged southern elephant seals swim. Namely: the subtropical zone (STZ) to the north of the SAF, the SAF itself, the subantarctic zone (SAZ) bounded to the north by the SAF and to the south by the PF, the PF itself, and the polar frontal zone, designated as all waters south of the PF.

4.2.5 *Is fluorescence abundance related to MLD?*

In situ fluorescence yields (as a proxy for Chl-a concentration and thus phytoplankton abundance) were examined relative to the concurrent *in situ* measures of density-derived MLD. Fluorescence yield was vertically integrated using a Trapezoidal numerical integration, which worked by approximating integration over a given depth (in this case, 180m) by breaking the area down into trapezoids with more easily computable areas (Mathworks, 2015). Integrated yield and MLD were first mapped side-by-side to visually examine possible similarities or differences in space. The two datasets were then correlated, as well as plotted over time (same x-axis) on 2-D line plots with their different y-axes conserved.

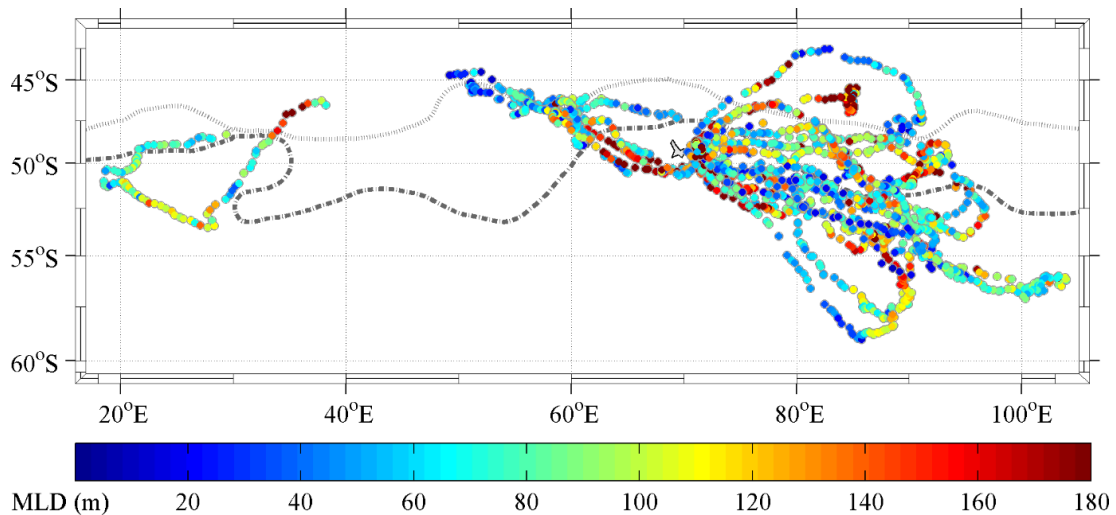


Figure 34: Density-derived MLD's calculated using CTD data collected from instrumented seals over 6 successive austral summers (2009 - 2014). The general positions of the Sub Antarctic Front and the Polar Front are shown by dashed light grey and dashed dark grey lines, respectively (Orsi and Harris, 2014).

4.3 RESULTS

The open waters of the Southern Ocean tend to be characterised by deep wind-mixed layers. This is true even over the height of the austral summer. In the dataset collected by nineteen tagged southern elephants seals over six consecutive summer seasons, density-derived MLDs exceeded 50m more than 80% of the time, and surpassed 100m more than 40% of the time (Fig. 34).

For these and other reasons, DCM were previously thought to be rare features in the Southern Ocean (discussed in Holm-Hansen and Hewes, 2004). However, increasingly, *in situ* data from this ocean regime are showing that DCM are persistent. Indeed, within this fluorescence dataset, 30% of the night (unquenched) data exhibited chlorophyll maxima at depth.

In the night dataset, distinct deep fluorescence maxima were measured both within and below the hydrographically defined MLD (Fig. 35). However, even when maximum fluorescence yields were found below MLD (Fig. 35d-f) there were only a few cases where vertical fluorescence yield was uniform from MLD to the surface (Fig. 35d as an example of homogeneity).

Due to the presence of distinct DCM in the unquenched night data, we can be reasonably confident that the day data will also contain DCM. However, quenched fluorescence profiles often mimic the shape of deep chlorophyll maxima (DCM) (Mignot

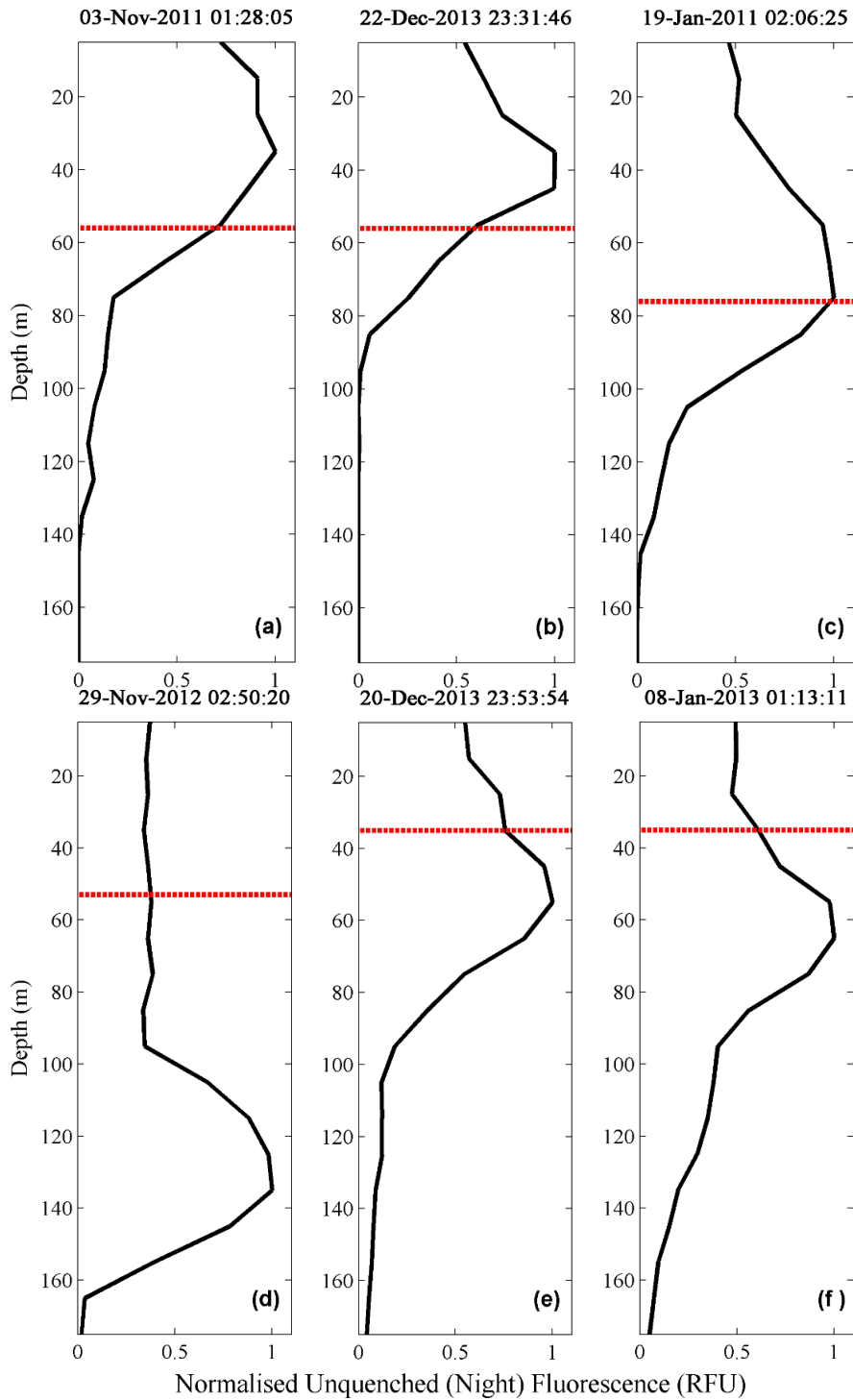


Figure 35: Vertical profiles of unquenched (night) normalised fluorescence (solid black line) with density-derived MLD (dashed red line). These profiles were selected from a number of different instruments over different years and at different times of the night (label above each plot). The top row of profiles show maximum fluorescence yield occurring within the mixed layer depth (a - c), while the bottom row of profiles show maximum fluorescence yield occurring below the density-derived limit (d - f).

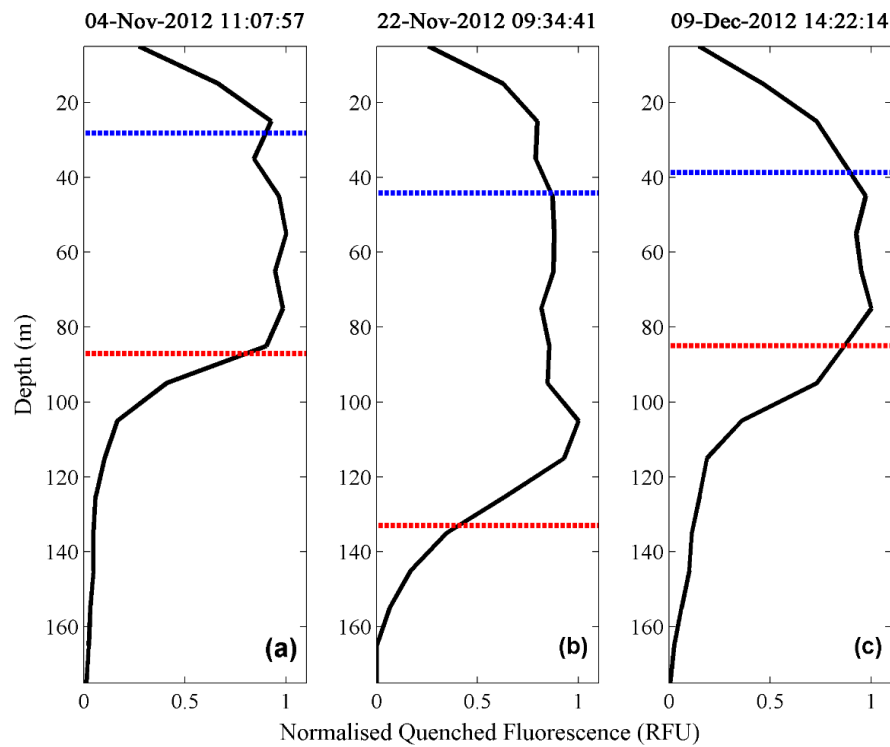


Figure 36: Discreet normalised vertical profiles of uncorrected (quenched) fluorescence (solid black line). Suppression of the fluorescence yield from quenching is evident within the surface waters, and the resulting profile thus exhibits maximum fluorescence yields below the depth of the 1% light level (MODIS Z_{eu}), shown by the dashed blue line. The depth of the density-derived mixed layer is shown by the dashed red line.

et al., 2011). This can be seen in the uncorrected quenched fluorescence data in Fig. 36, where the fluorescence at depth always exceeds yields at or near the surface (within the first 20m).

In the previous chapter, quenching at the surface was corrected using two reference depths, MLD and Z_{eu} . The resulting surface fluorescence yields were not significantly different, but the same is not true if we look beneath the surface. Indeed, differences are evident in Fig. 37, where individual fluorescence profiles have been corrected with MLD and Z_{eu} . Resultant surface fluorescence yields are slightly overestimated using MLD (shown in red); but perhaps more importantly, vertical complexity is lost. Correcting from Z_{eu} (shown in blue) serves to conserve heterogeneous dynamics on the vertical scale. This is perhaps best illustrated in Fig. 37(b), where phytoplankton may either be settling into different layers (floristic shifts), or where Chl-a packaging has become measurably different between deep-mixed and shallow-mixed layers (photoacclimation).

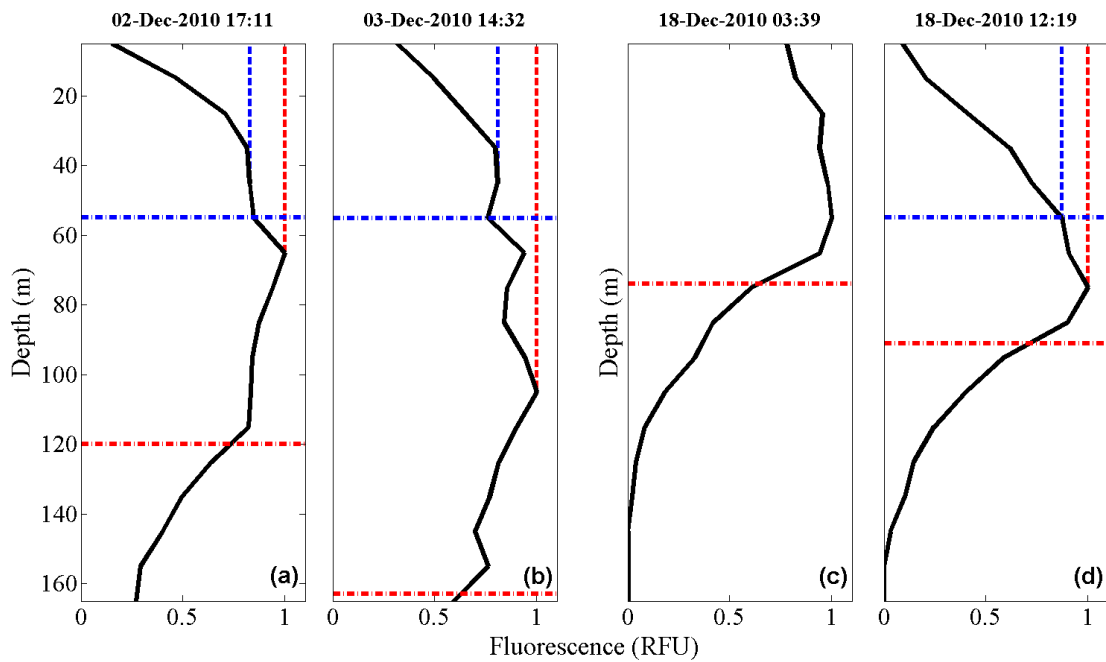


Figure 37: Normalised vertical profiles of fluorescence (solid black line) corrected from MLD (dashed red line) or Z_{eu} (dashed blue line). Fluorescence in (c) was measured at night and is thus unquenched and uncorrected. For each daytime profile, quenched fluorescence is corrected using either Z_{eu} (depth and corresponding corrected fluorescence yield shown with dashed blue line) or MLD (depth and corresponding corrected fluorescence yield shown with dashed red line).

The difference between the two methods is also evident in figure 38. Uncorrected vertical profiles in the top row (Fig. 38a, d and g) illustrate suppression of daytime fluorescence yield at the surface (grey-scale bar with daylight hours in white and black for night.). Quenching is corrected using MLD in the second row (Fig. 38b, e and h) and Z_{eu} in the third (Fig. 38c, f and i). The distinct subsurface fluorescence feature in (a) is within the mixed layer, and is thus masked when corrected from this depth (b). However, correcting from Z_{eu} conserves vertical complexity while still correcting quenching at the surface (c). The deep fluorescence feature in Fig. 38(d) also has a maximal yield below euphotic depth but within the mixed layer. This deep signal is masked when correcting from MLD (e) but remains distinct when using Z_{eu} (f). Finally, the dynamics in Fig. 38(g) are lost when correcting from the depth of the mixed layer (h) but conserved when correcting from Z_{eu} (i). The night data from this example in particular corroborates complex Chl-a dynamics with depth.

Recalling that 30% of the night (unquenched) data exhibited chlorophyll maxima at depth, DCM were evident in only 10% of the 'MLD-corrected' day data. Correcting from Z_{eu} doubled the number of DCM conserved in the day data (21%), more closely matching the 'night' (unquenched) dataset. Furthermore, correcting from Z_{eu} served to conserve vertically heterogeneous Chl-a features found between the 1% light level and mixed layer depth. A student t-test, which is robust to moderate violations of the assumption of normality, shows that MODIS [Chl-a] measurements only associated with positions of DCM are not significantly different from all along-track MODIS [Chl-a] measurements.

Is there perhaps a spatial component to DCM instead?

The core of ACC, which includes both the SAF and PF, is largely barotropic and thus constrained to the underlying bathymetry (Graham et al., 2012). However, results from this work support the literature suggesting a south-ward migration of the fronts over time (e.g.: Lenton and Matear, 2007; Sallee et al., 2008; Sokolov and Rintoul, 2009). In particular, results from this thesis support results from Sokolov and Rintoul (2009), which highlighted changes to the PF around Kerguelen as an 'extreme example?'. Their work found that the northern jet of the PF, which followed a path north of the Kerguelen plateau pre-1997, oscillated between northern and southern routes between 1997 - 2003, and moved south thereafter. As seen in Fig. (above), all *in situ* positions of the PF fall south of the climatological mean (Orsi et al., 2005) in this study. PF positions clustered closest to Kerguelen may suggest an oscillation between

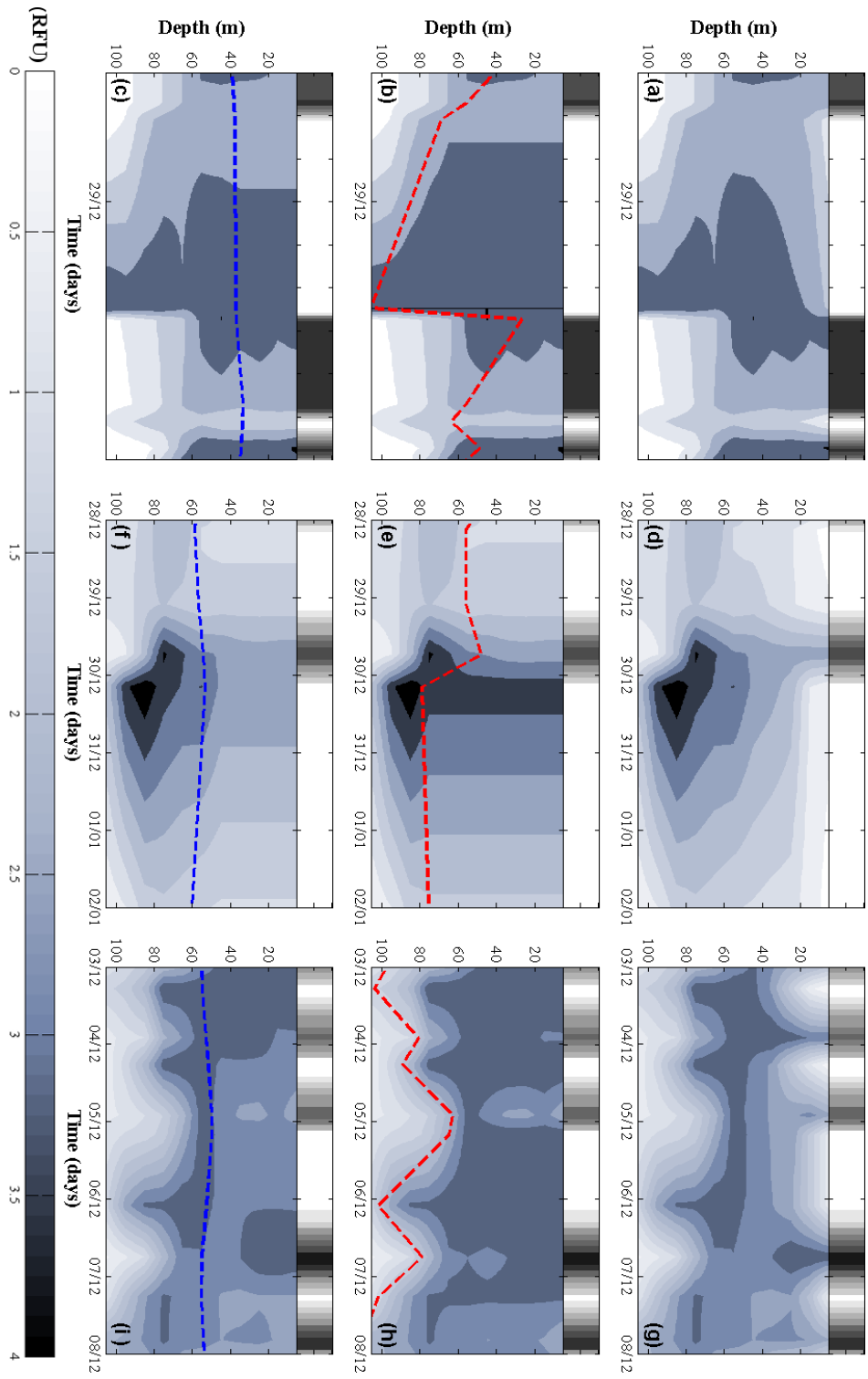


Figure 38: Sections of fluorescence corrected using either the depth of the mixed layer or the depth of the 1% light level, $Z_{1\%}$. The grayscale bar attached to the top of each plot illustrates when fluorescence data was collected relative to the time of day, with black for night and white for day. The top row of vertical profiles (a), (d) and (g) show sections of uncorrected fluorescence data. The fluorescence data in the second row (b), (e) and (h) have been corrected from MLD (dashed red line). The last row of fluorescence data (c), (f) and (i) have been corrected using $Z_{1\%}$ (dashed blue line).

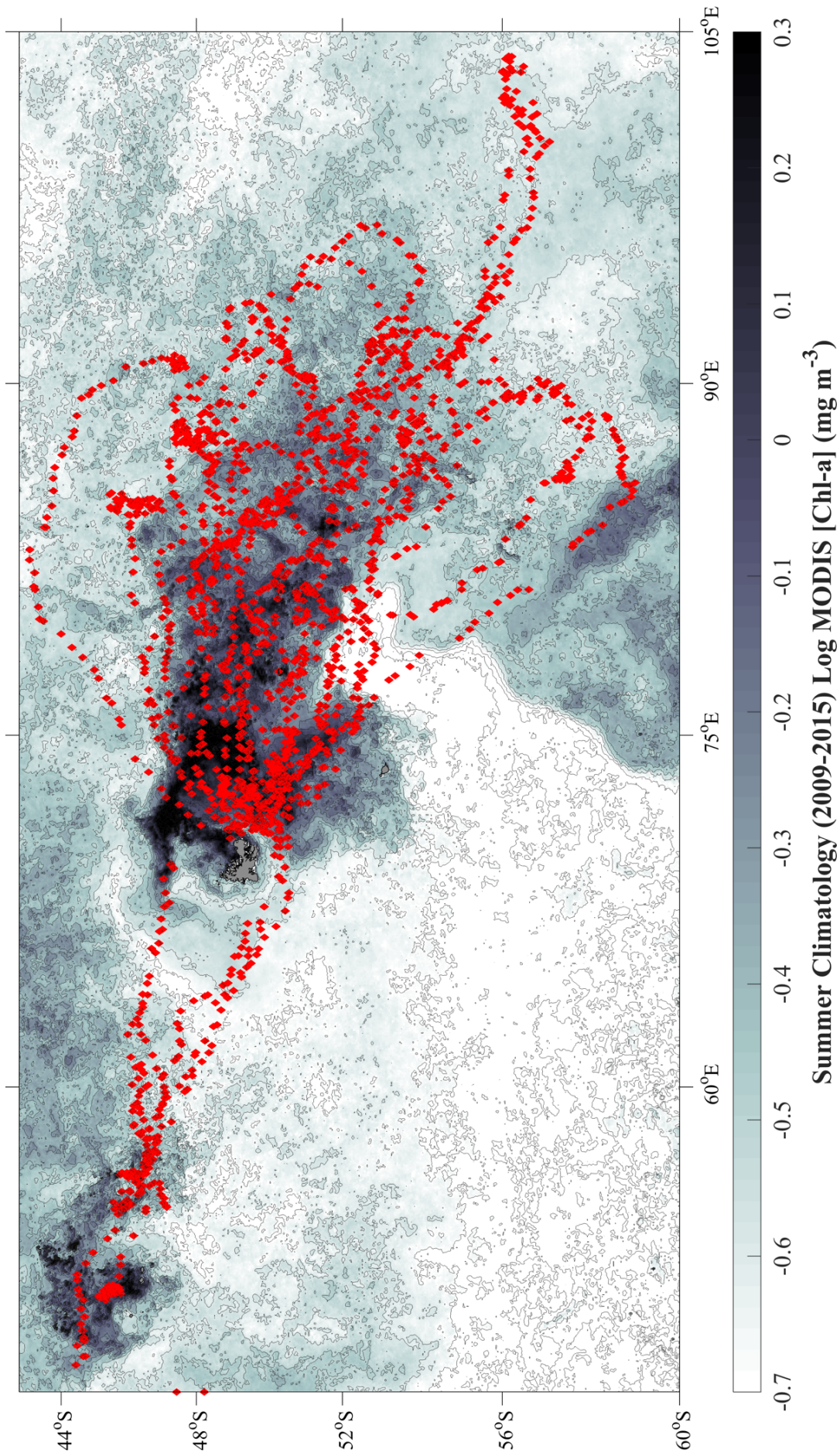


Figure 39: Spatial distribution of all FCTD-SRD L seal tracks (2009 ? 2015) shown in red, relative to a MODIS surface [Chl-a] climatology calculated for the same years over November ? December.

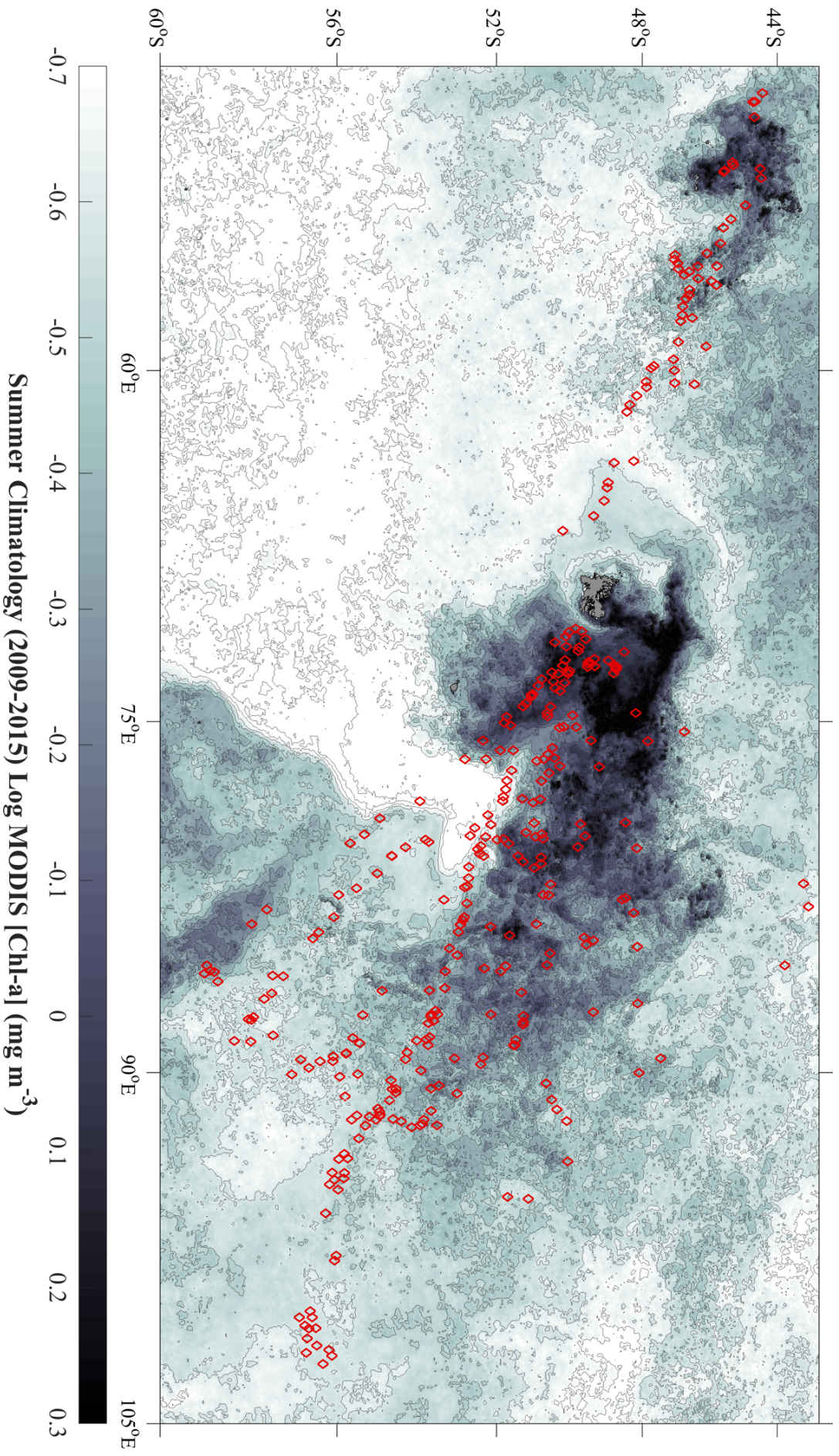


Figure 40: Positions of DCM measured from all tracked seals (2009 ? 2015) shown in red, relative to a MODIS surface [Chl-a] climatology calculated for the same years over November ? December. DCM appear to be distributed along Chl-a edges or boundaries ? possibly related to fronts ? and downstream of islands. These small land masses include Kerguelen (49.3E, 69S) as well as East Island (52.2E, 46.44S).

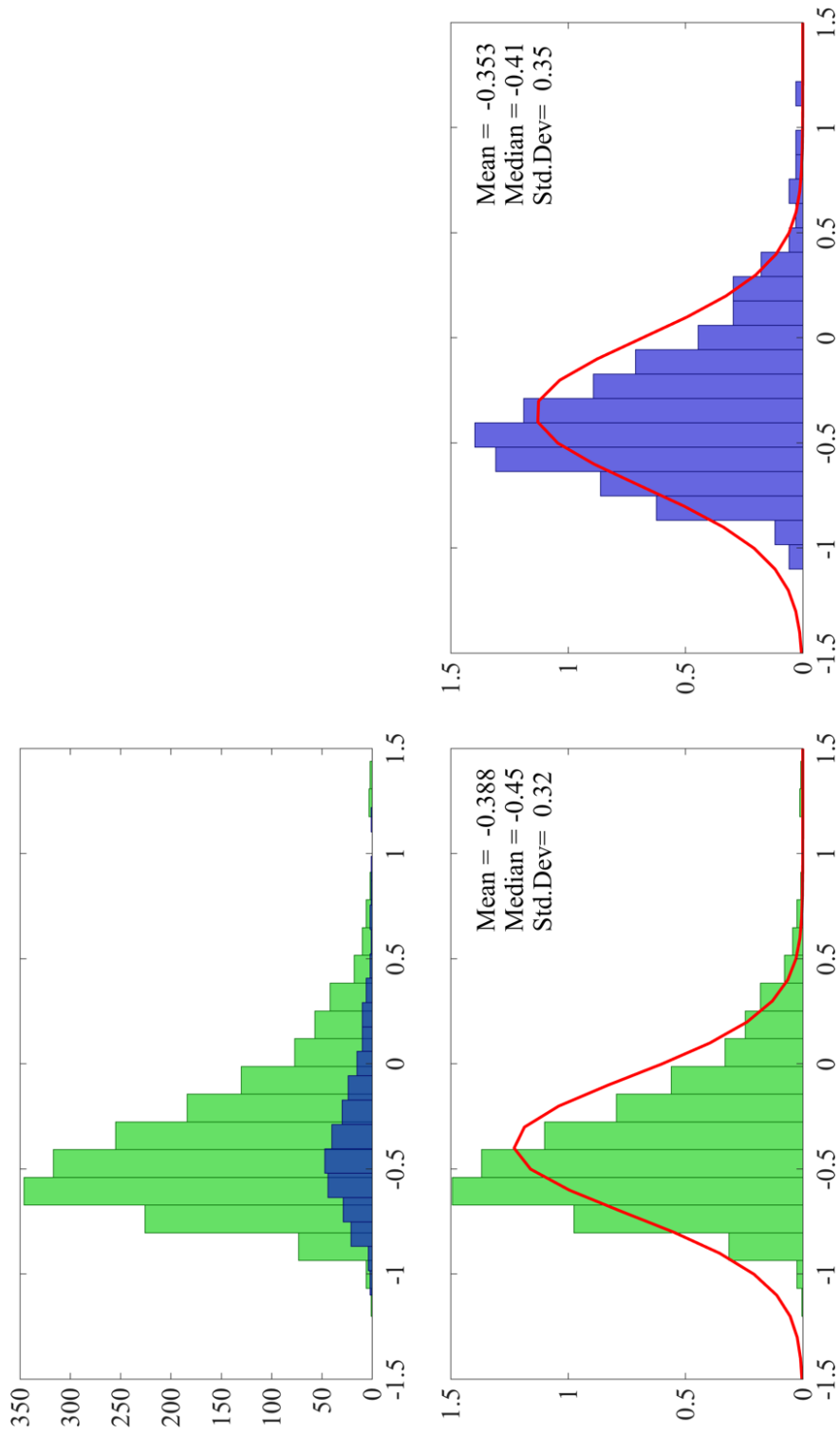


Figure 41: Histogram of all along-track log-transformed MODIS surface Chl-a concentrations shown in green. Histogram of log-transformed MODIS surface Chl-a concentrations that are only associated with DCM shown in blue. DCM show a largely normal distribution around -0.35 mg m^{-3} . All along-track surface Chl-a concentrations also show a largely normal distribution centred around -0.38 mg m^{-3} .

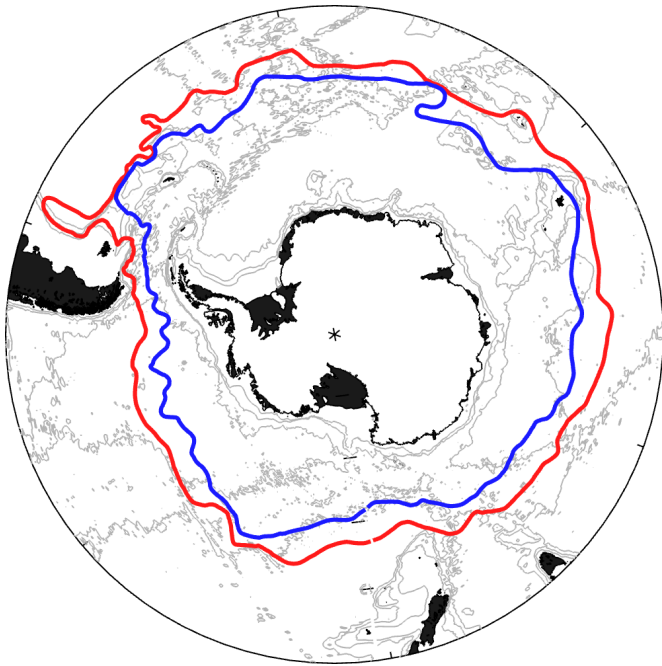


Figure 42: Positions of the climatological fronts from Orsi et al. (2005) ? the circumpolar Sub Antarctic Front (SAF) is depicted in red and the circumpolar Polar Front (PF) is shown by the blue line. Background bathymetry in light grey was derived from the NOAA ETOPO2v2 database.

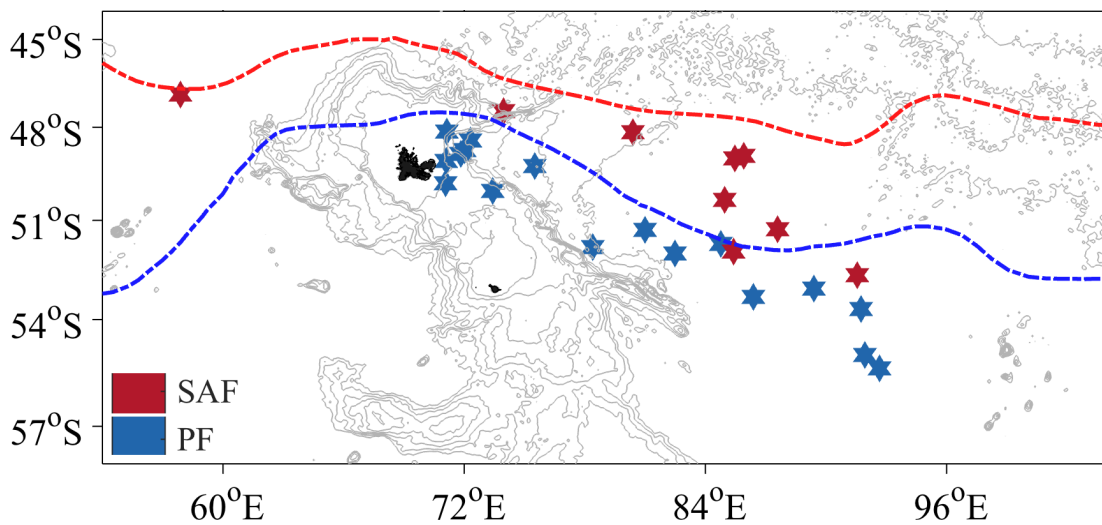


Figure 43: Comparison of climatological fronts derived from Orsi et al. (2005) and the positions of the fronts calculated from *in situ* data collected around Kerguelen by tagged seals (2009 ? 2014). The climatological SAF is shown by the dashed red line and the PF by the dashed blue line. Background bathymetry in light grey was derived from the NOAA ETOPO2v2 database. Positions of the fronts calculated using *in situ* temperature and salinity data collected by the tagged seals (method from Boehme at al., 2008) are shown using red stars for the SAF and blue stars for the PF.

paths north and south of the island itself. The SAF also shifts further south than the climatological position of the SAF derived from Orsi et al. (2005) and shows high spatial variability over the deep Kerguelen Plateau (+3500m).

A major part of the flow associated with the ACC is concentrated at deep fronts that separate zones of uniform water masses (Nowlin and Clifford, 1982; Nowlin and Klinck, 1986). The two fronts that define the classical zonation of the ACC are the subantarctic front (SAF) and the Polar Front (PF). However, closer inspection of their structures has suggested that each front is composed of bundled, eastward flowing jets which characteristically shed eddies (Sokolov and Rintoul, 2007). Indeed, the APF and SAF display strong temporal variability in latitude and structure (Olbers et al., 2004). DCM appear to be more likely to be associated with the SAF and PF. In terms of zones, the polar frontal zone appears to have a higher proportion of DCM than waters further north. On a temporal basis, DCM are found throughout the 3-month period the tagged seals are at sea, with proportions similar between night (0.30) and day (0.26).

Finally, water-column-integrated measures of fluorescence were compared against measures of the hydrographically defined MLD. Interestingly, shallow/deep MLD's do not appear to match areas of high/low fluorescence (Fig. 45 - Fig. 48). Fluorescence in the top 10m and integrated fluorescence from the surface to 100m does not appear to be robustly and repeatedly related to the depth of the mixed layer. From year to year, the relationship between MLD and fluorescence can change from weakly significant to not significant, and even changes sign in 2010 and 2014. Deep mixed layers between 150m to 200m do appear to be consistently associated with lowest fluorescence values.

Furthermore, fluorescence in the top 10m and integrated fluorescence from the surface to 100m does not appear to be related to time of year, beyond phytoplankton being more abundant when light limitation is not a factor. These data were collected only over austral summer months, between November to January.

Differences between MLD and surface fluorescence yield, and MLD and depth-integrated (100m) fluorescence yield, do not appear to be substantial. Grouping by year allows for an overview of the relationship between MLD and fluorescence, but it is important to keep in mind that each seal tag is slightly different in terms of gain and sensitivity. Most notably, the gain is adjusted after the first year of deployment.

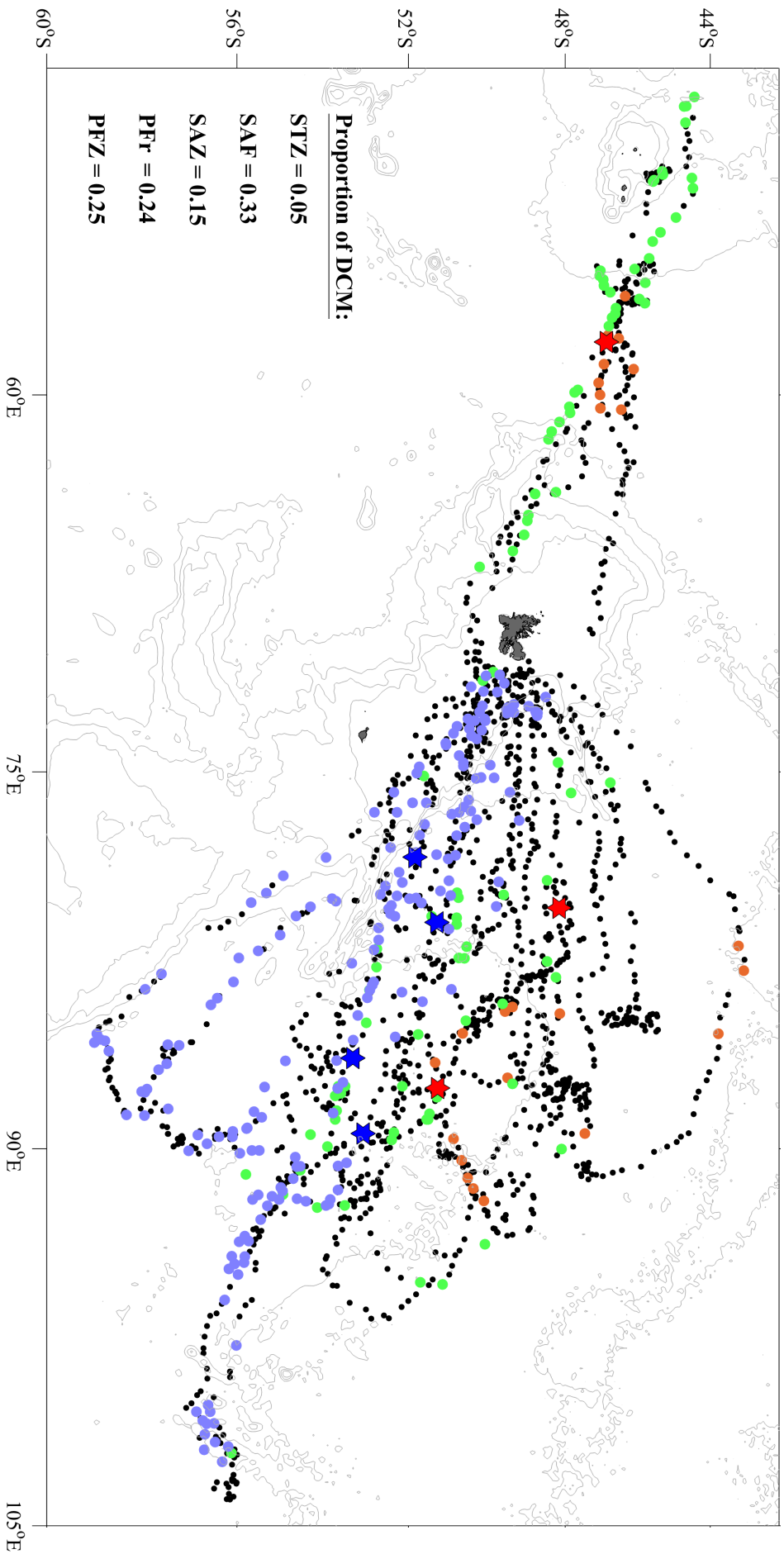


Figure 44: All at-sea positions of southern elephant seals tagged on Kerguelen between 2009 and 2015 are shown by the black dots. Positions of deep chlorophyll maxima in the subtropical zone are shown by pink dots (proportion = 0.05), in the subantarctic zone by green dots (proportion = 0.15), and in the polar frontal zone with mauve dots (proportion = 0.25). Deep chlorophyll maxima found within the subantarctic front are shown by red stars (proportion = 0.33) and within the polar front by blue stars (proportion = 0.25).

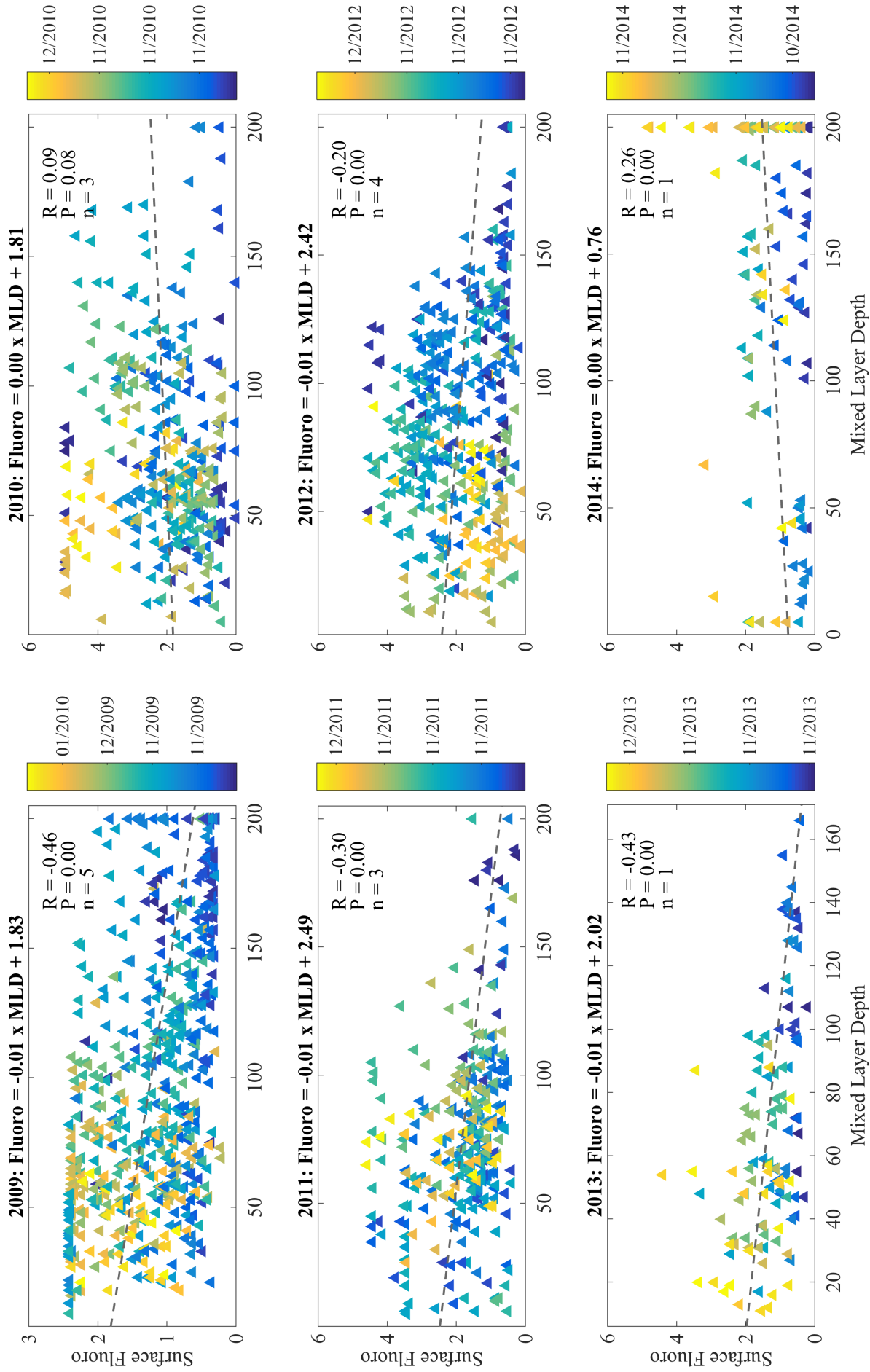


Figure 45: Relationships between the depth of the hydrographically defined mixed layer and surface Fluorescence (top 10m) from 2009-2014. Markers are coloured by the time of year over each summer season. The linear fit is shown by the dashed grey line. The R value, p-value and the number of datasets collected by seal per year are reported in the top left-hand corner of each plot, and the linear equation with intercept and slope are reported in bold above.

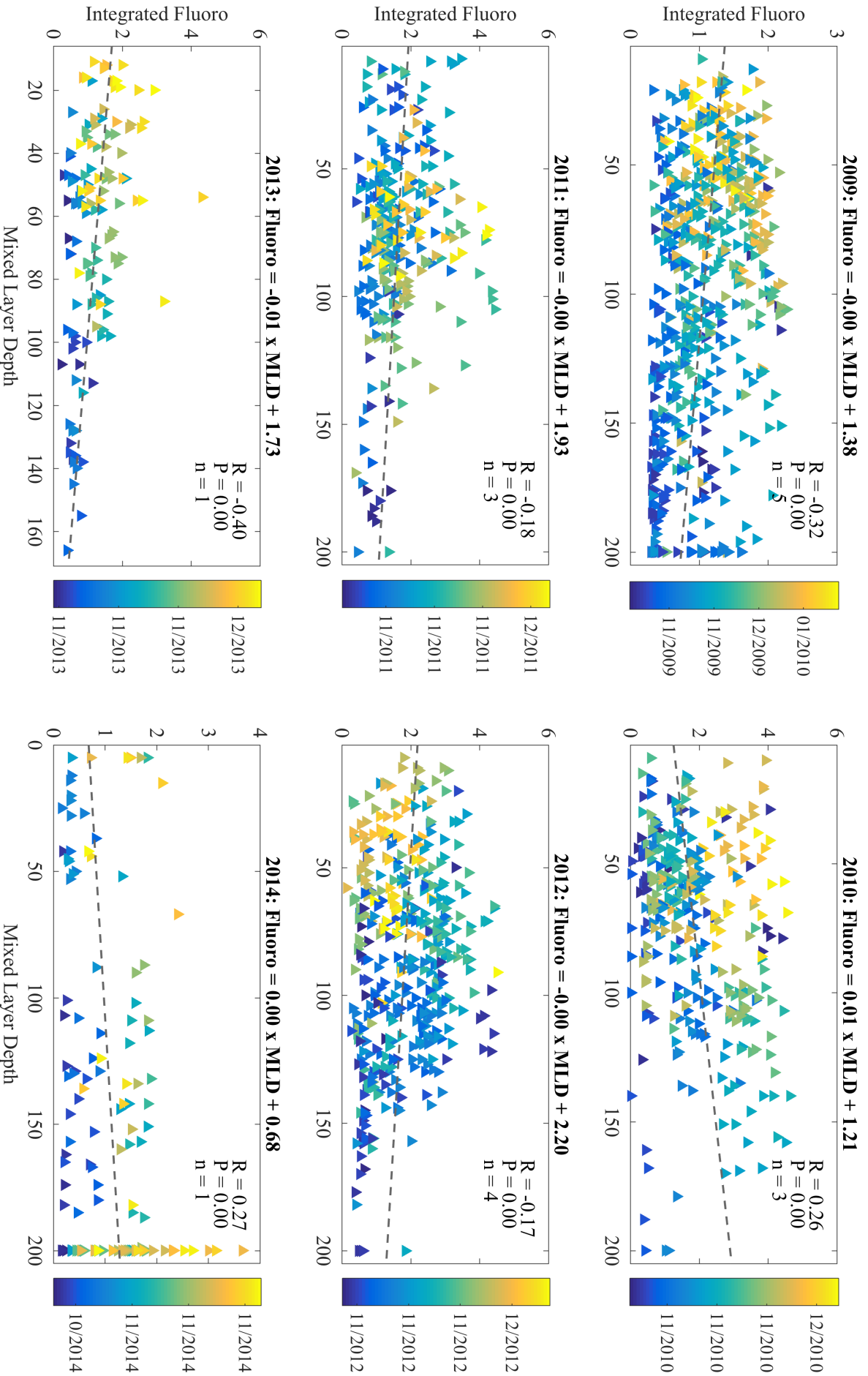


Figure 46: Relationships between the depth of the hydrographically defined mixed layer (x-axis) and integrated Fluorescence (surface to 100m) from 2009-2014.

Markers are coloured by the time of year over each summer season. The linear fit is shown by the dashed grey line. The R value, p-value and the number of datasets collected by sea per year are reported in the top right-hand corner of each plot, and the linear equation with intercept and slope are reported in bold above.

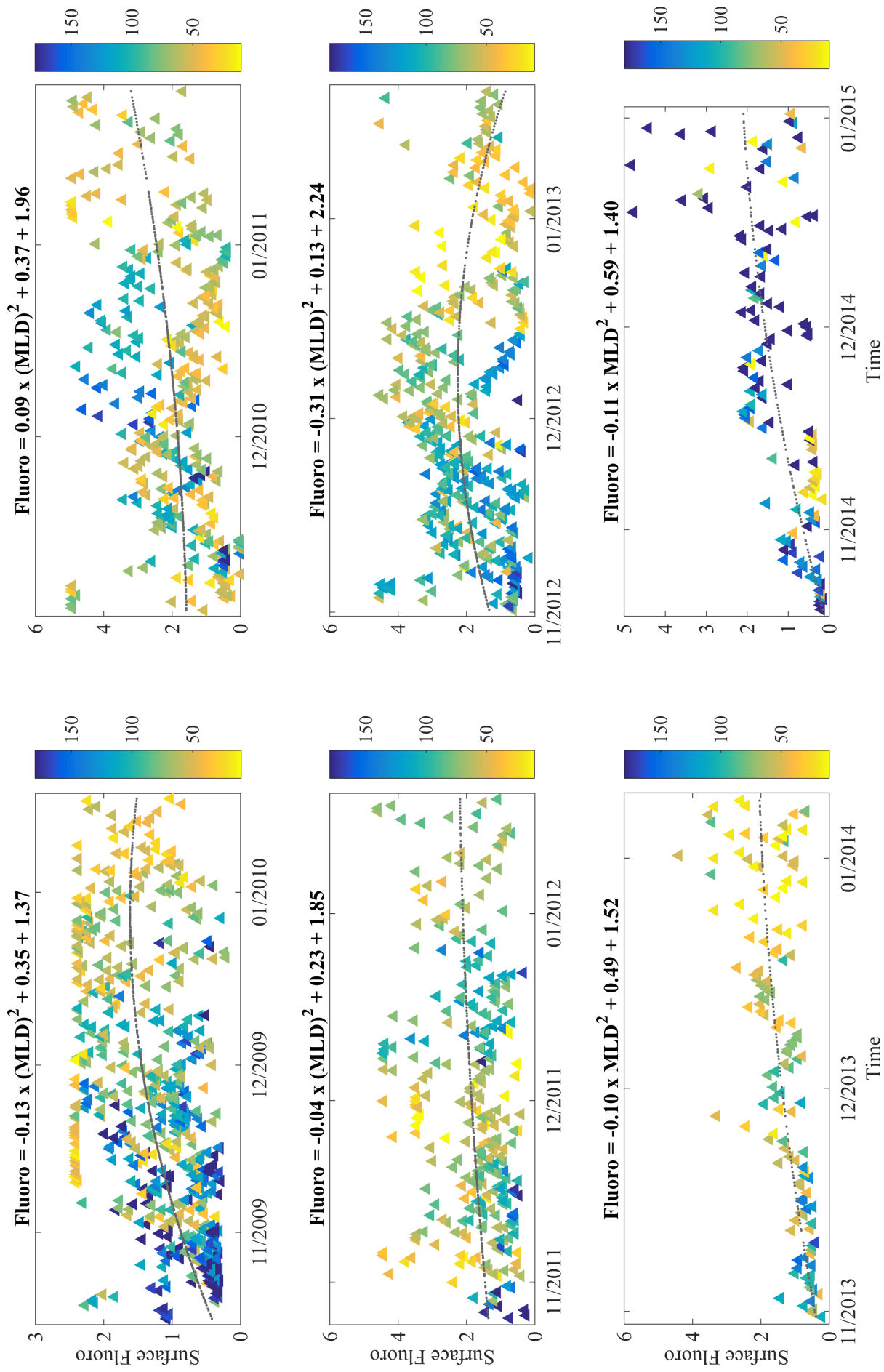


Figure 47: Relationships between surface Fluorescence (top 10m) and time of year (November ? February). Markers are coloured by the depth of the mixed layer (m) with blue representing deepest MLD and yellow representing shallowest. Quadratic equation with numerical coefficients reported in bold above.

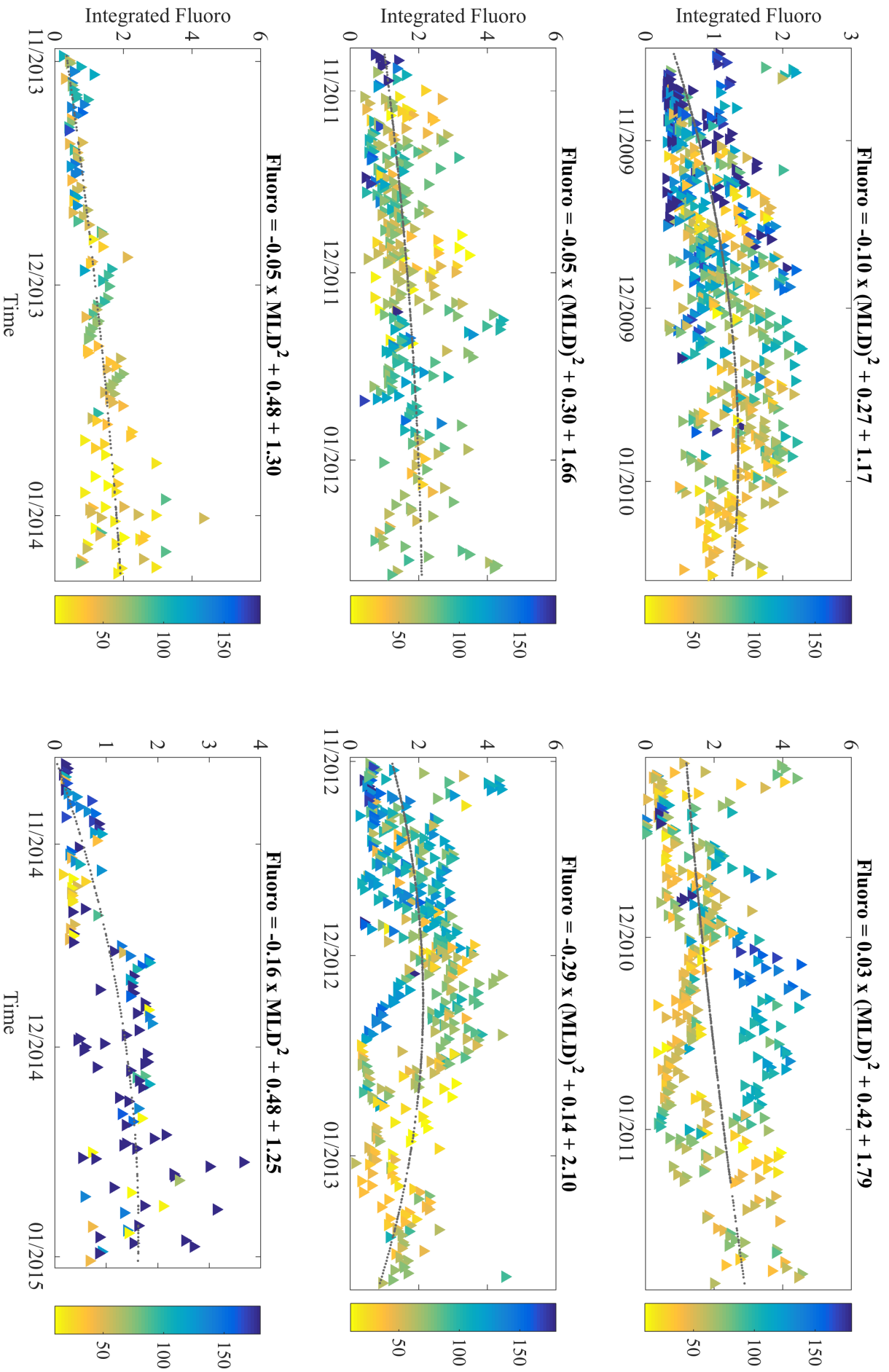


Figure 48: Relationships between integrated Fluorescence (surface to room) and time of year (November ? February). Markers are coloured by the depth of the mixed layer (m) with blue representing deepest MLD and yellow representing shallowest. Quadratic equation with numerical coefficients reported in bold above.

Differences between each instrument will introduce variability, but this assessment of MLD is to illustrate any relationship to fluorescence, rather than to quantify it.

If we were to examine the relationship between MLD and fluorescence by grouping all seal tag data together, normalising the fluorescence yield per instrument would account for the variation between instruments. However, I suggest that a year-by-year examination is more useful as it highlights how conditions change on interannual scales, and points to an interplay of factors influencing phytoplankton abundance. These factors will include spatial differences (seal positions around Kerguelen vary), as well as light and iron availability (physical and chemical factors).

Higher fluorescence does not appear associated with the time of year, other than it being the austral summer. The same appears to be true with regards to fluorescence and MLD, unless MLDs surpass 150m. It's possible that this depth represents a biological, chemical or physical threshold, possibly introducing factors such as light limitation and/or variability stresses. These results support findings from the Southern Ocean iron-release experiment (SOIREE), where phytoplankton growth increased when MLDs were at 45m and 65m but showed no measurable improvement where MLDs surpassed 100m.

4.4 DISCUSSION

Nineteen seals tagged with FCTD-SRDLs between 2009 and 2014 returned DCM in 30% of the night data. These features are unlikely to be residual artefacts of photoacclimation, and may instead point to differences in community structure with depth, or be evidence of biomass maxima. As explained previously, DCM can form in two main ways. Perhaps most commonly, DCM form through differences in Chl-a packaging from photoacclimation processes. Indeed, the amount of chlorophyll per cell can vary depending on nutrient history, light regime, depth and temperature (Steele, 1964; Cullen, 1982; Behrenfeld and Boss, 2006). Chl-a packaging can also vary between species of the same community. The consequence is that chlorophyll concentration and resulting fluorescence yield can vary with depth, even inside homogeneously mixed layers.

DCM form a second way, when phytoplankton settle to an optimal depth where both nutrients and light are deemed sufficient (Holm-Hansen and Hewes, 2004; Mel-lard et al., 2011). Just as Chl-a packaging varies between phytoplankton types, so too

does this 'optimal' depth, with dinoflagellates and diatoms of the same assemblage often 'preferring' different layers (Cullen and Eppley, 1981). In these cases, if different layers of biomass exist, vertical heterogeneity may be a more useful description than DCM.

Without concurrent laboratory analysis, we cannot confirm whether the vertical heterogeneity measured by these animal-borne fluorometers are biomass-driven features, or arise from differences in Chl-a packaging (photoacclimation or community structure). However, Holm-Hansen and Hewes (2004) found annually recurring deep phytoplankton biomass maxima on the nutricline at 60-90m in Drake Passage waters. Closer to Marion Island, results from the Antarktis XIII/2 'Frontendynamik und biologie' expedition (December 1995 - January 1996) confirmed that heavily silicated species of diatoms accumulated in deep layers as the summer season progressed (Quéguiner, 2013). Furthermore, a significant proportion of the open water community should be composed of non-diatom species by the mid- to late-summer months (around January). In the open waters south-west of Kerguelen, Mengesha et al., (1998) measured dinoflagellates and other motile species in greater abundances than diatoms. Dinoflagellates are mixotrophic and are able to switch between photosynthesis and predation upon other microorganisms. Indeed, studies on DCM composed of dinoflagellates in the Baltic Sea showed abundant biomass below euphotic depth (Carpenter et al., 1995).

With a basis in Sverdrup's critical depth hypothesis, the vertical distribution of phytoplankton has traditionally been understood to be controlled by mixing. Indeed, a 'thoroughly mixed top layer' is the first explicit assumption upon which Sverdrup's hypothesis is based. The second is that turbulence within this top layer is sufficiently strong enough to distribute phytoplankton uniformly (Sverdrup, 1953; Franks, 2014). There is, however, a clear need to distinguish between a mixed layer (as delineated by a density-defined threshold, in this case) and strength of the turbulence within that layer (Taylor and Ferrari, 2011). In other words, how intensely that mixed layer is mixing (Huisman et al., 1999; Franks, 2014).

Within this dataset, if we assume that the depth of the mixed layer is also the depth of the turbulence layer, DCM may still arise from photoadaptation (Chl-a packaging) processes. In this case, in response to light and nutrient gradients, the amount of chlorophyll pigment packaged per cell may measurably increase with depth, generating DCM independent of biomass. However, if vertical gradients of turbulence

do exist, this may permit different types of phytoplankton to select optimal depths at which to grow, based on species-specific nutrient and light requirements. Franks (2014) shows very clearly that vertical gradients of turbulence often exist even when turbulence is sufficient to homogenise the hydrography (in this case, density). Thus, the presence of a mixed, homogeneous, layer of density does not automatically indicate that turbulence is intense enough to move any given phytoplankton cell completely through the mixed layer. Indeed, even within highly turbulent flow, cell motility has been shown to prevail over dispersion by mixing (Durham et al., 2013).

The persistence of DCM within upper mixing layers either points to phytoplankton being able to overcome high turbulence, through active 'swimming' or by changing buoyancy. However, this may also suggest that turbulence strength changes with depth (vertical gradient) or is weak to moderate within the upper mixed layers of the Southern Ocean. This seems counter-intuitive because the Southern Ocean is largely wind-driven, and wind contributes significantly to turbulence. However, it is unclear how much kinetic energy the strong westerlies impart to horizontal acceleration of surface waters, and how much is imparted to generating turbulence. If the Southern Ocean waters experience a combination of weak stratification and strong vertical shear, even moderate wind-generated kinetic energy will be sufficient to generate vertical mixing of the density gradient (Franks, 2014).

In the North Atlantic, heterogeneous phytoplankton patterns within layers of homogeneous density are a common feature, resulting from slow mixing rates (relative to growth rates) during periods without deep convective mixing (Taylor and Ferrari, 2011). Although we have little to no information on turbulence in the Southern Ocean, the fact that phytoplankton heterogeneity within a hydrographically defined mixed layer appears to be the rule, rather than exception, points to interesting patterns of turbulence. This certainly warrants further investigation. Once sufficient *in situ* data is available on turbulent layers in the Southern Ocean, the potential usefulness of vertical fluorescence may be evaluated as an indicator of vertical variations in turbulence. As it stands, even without *in situ* data, the seasonal and regional persistence of deep maxima in 30% of the night data and 20% of the day data supports the premise that turbulence in the upper layers is not high or homogeneous. Thus, when 'ideal' levels of light and nutrients change with depth over time, we may understand that the vertical distribution of biomass in the water column may also change (evolutionary stable strategy depth) (Yoshiyama et al., 2009; Mellard et al., 2011).

These results on heterogeneous phytoplankton patterns and mixing within the hydrographically defined mixed layer are interesting from both biological and physical standpoints, but they are also relevant for topical studies. For example, very recent work by Sallee et al. (2015) continues to rely on the assumption that subsurface chlorophyll maxima are uncommon in the Southern Ocean, and that mixing processes (turbulence) are sufficient to generate homogeneous layers of Chl-a. However, the relevance of persistent DCM features can also be extended to 'bigger picture' work, namely: climate change at the high latitudes.

The prevailing westerly winds encircling Antarctica and driving the ACC appear to be strengthening and contracting as a result of an increasingly positive Southern Annular Mode (SAM). Waters now north of the contracted wind belt are likely to become stratified, with shallower turbulence layers or more pronounced gradients. This may allow for an increase in the presence of DCM. Indeed, any decreases in Chl-a over time, as seen from the satellite record, may point to an increase in abundances at depth rather than an overall loss. Conversely, waters within the contracted wind belt may become so deeply and persistently turbulent that phytoplankton remain light-limited throughout the summer months, resulting in net loss of biomass.

Around a quarter of all fluorescence profiles collected by tagged southern elephant seals showed evidence of deep chlorophyll maxima. This proportion does not make these features commonplace, but it adds to a growing body of evidence that DCM are persistent in Southern Ocean waters, and may play important roles in structuring the marine food web. For example, the primary foraging areas of northern elephant seals have been recently shown to correlate with positions of DCM in the eastern North Pacific (Saijo et al., 2016). Information on vertical phytoplankton dynamics is therefore useful, but they cannot be measured by satellite (McClain, 2009; Charrassin et al., 2010). Consequently, in order to ensure vertical heterogeneity and DCM in particular are not masked during quenching correction procedures, correcting from Z_{eu} is more effective than using MLD. The problem of reliance on homogeneity within MLD was commented on by Xing et al. (2012), but not addressed until now.

EVALUATING THE ACCURACY OF MODIS [CHL-A] USING VERTICALLY-INTEGRATED FLUORESCENCE DATA RETRIEVED BY TAGGED SOUTHERN ELEPHANT SEALS

5.1 INTRODUCTION

Phytoplankton are primary producers. Through the process of photosynthesis, these microscopic drifting (-plankton) plants (phyto) are able to transform chemical energy (sunlight and inorganic carbon) into biomass (organic carbon). As the foundation of the marine food web (Vargas et al., 2015), knowing where, and at what concentrations, phytoplankton are present provides insights into ecosystem dynamics. Phytoplankton are also responsible for removing carbon dioxide and other greenhouse gasses from the atmosphere, and information on their distribution and abundance is also important for carbon budget models. Indeed, in order to resolve our questions on ecosystem dynamics and biogeochemical cycles, an understanding of the distribution and concentration of phytoplankton species is essential (McClain, 2009).

From the Coastal Zone Colour Scanner (CZCS) to current sensors MODIS, Visible Infrared Imaging Radiometer Suite (VIIRS) and Sentinel-3, past and present ocean colour satellite sensors have made it possible to measure phytoplankton on the ocean surface by exploiting their photosynthetic pigment, Chl-a. All ocean colour studies are based quite literally on the fact that the colour of the oceans provides an enormous amount of information on the particulate and pigment content of the water (McClain, 2009).

Chl-a has well-defined absorption spectra with a primary peak at ≈ 440 nm. As mentioned in Chapter 2, water itself also has well-defined absorption spectra - it is transparent at blue to green wavelengths and absorbing at the longer wavelengths (towards red). In cases where water is not pure (i.e.: contains phytoplankton), a combination of particulate scattering at the longer wavelengths and absorption by Chl-a at around 440nm will shift the spectral reflectance of water out of the 'blue' (McClain, 2009). Specifically, the colour of the ocean water (spectrum of backscattered

sunlight) will progressively shift from blue to green to 'brownish' as the concentration of phytoplankton biomass increases (McClain, 2009; Yentsch, 1960; O'Reilly et al., 1998).

Since the early 1980's, remotely-derived surface Chl-a concentration ([Chl-a]) has been broadly used as indicator of phytoplankton biomass, and is subsequently used as the 'global indicator of the trophic state' (Morel, 2009). On temporal and spatial scales, ocean colour data provides the most practical means of measuring and monitoring phytoplankton variability for ecosystem dynamics and biogeochemical cycles. It is thus a basic requirement for ocean colour data to be as representative as possible of the 'true' state.

Throughout the 1980's, the work of Gordon and Clark (1981), Gordon et al. (1983) and Gorgon (1987) on oligotrophic waters helped set base-line accuracy requirements for satellite ocean colour data. Their results indicated that remotely-sensed [Chl-a] values were derived with a maximum uncertainty of 35% (Zibordi et al., 2015). Science requirement data product accuracy goals for all subsequent international ocean colour missions have thus been targeted to $\pm 5\%$ for water-leaving radiances (spectrally independent uncertainties of 5% with inter-band uncertainties of 1%) and $\pm 35\%$ for [Chl-a] in the open ocean waters. Unfortunately, regional differences can be problematically large (McClain, 2009). In Antarctic waters, Mitchell & Holm-Hansen (1991) found that concentrations of Chl-a were underestimated by as much 70%. However, later evidence from the Southern Ocean suggested that the differing methods to calculate *in situ* concentrations of Chl-a (range of fluorometric techniques vs. high-pressure liquid chromatography) contributed significantly to this mismatch, or at least impacted more than originally accounted for (Marrari et al., 2006). Indeed, as explained in previous chapters, any studies aiming to meaningfully compare *in situ* data with remotely sensed values have to take the caveats associated with both datasets into consideration. This is perhaps especially true for this chapter, where quenching-corrected *in situ* fluorescence is used to evaluate temporally merged satellite-derived [Chl-a].

Current measures of [Chl-a] are collected by the MODIS ocean colour sensor on the NASA Aqua Mission, and provided as a standard ocean colour product by the Ocean Colour Working group. Products are freely available through their website and are used extensively by the wider scientific community for a broad range of applied studies. In near-coastal regimes and the high latitudes, however, retrieval of Chl-a to within product accuracy goals (maximum uncertainty of 35%) is hindered by a

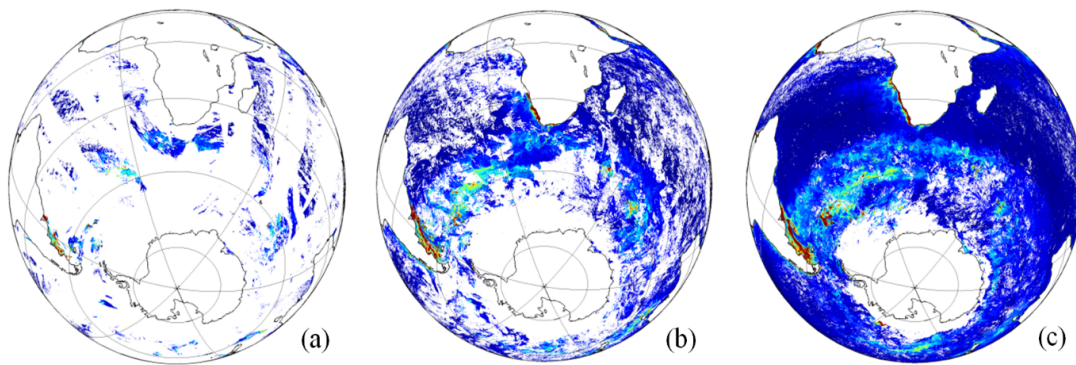


Figure 49: Global MODIS Aqua [Chl-a] seen with (a) a single overpass (b) merged into an 8-day composite and (c) a monthly composite.

series of challenges. As discussed in previous chapters, one of the problems ocean colour sensors face in the Southern Ocean is persistent cloud cover. This makes it very difficult to generate L3 daily data with coverage that is meaningful to synoptic studies. Merging of daily overpass data into 8-day and monthly composites go some way to correct spatial limitations (Fig. 49), but at what cost to accuracy?

In this chapter, I will assess the use of 8-day data, which leaves gaps in the along-track sea data, compared with a combined 8-day and Monthly product, where temporal gaps are as filled as possible.

To test if satellite measures of phytoplankton abundance in surface waters are 'accurate enough', *in situ* data are invaluable for ground-truthing. Although methods such as HPLC are deemed the most accurate at measuring *in situ* Chl-a concentrations, these types of data collection tend to be limited to ship-based work. For autonomous platforms such as gliders, floats and tagged marine animals, however, fluorescence is perhaps the best alternative for collecting *in situ* data on Chl-a concentrations. Thanks to the fact that fluorescence is low-cost, low power and non-invasive, it has been widely used since the 1960's (Lorenzen, 1966; Cullen and Eppley, 1981; Falkowski and Kolber, 1995; Lavigne et al., 2012). However, fluorescence is not without its caveats.

In Chapter 3, the problems associated with fluorescence were discussed in detail, and suppression of *in situ* yield (quenching) had to be accounted for and corrected in surface waters. This step is particularly important if the *in situ* data are to be applied for ground-truthing surface [Chl-a] measured by satellite. The operative word being 'surface'. Satellite sensors can only 'read' ocean colour to first penetration depth, commonly referred to as one optical depth (Gordon and McCluney, 1975). This depth

can be derived from the remotely-derived measures of $K_d(490)$, the diffuse attenuation coefficient for downwelling irradiance (Gordon and Morel, 2012). First optical depth varies widely in space and time, depending on factors such as water clarity and the amount of particulate material suspended in surface waters. Nonetheless it rarely exceeds 'near-surface' values. Consequently, values of remotely derived [Chl-a] provide little to no information on vertical phytoplankton distribution within the water column. The question arises: how reliable are temporally merged MODIS [Chl-a] products at providing an accurate approximation of vertically integrated phytoplankton abundance?

In this chapter, I also attempt to answer this question for Southern Ocean waters by comparing MODIS [Chl-a] with surface, Z_{eu} -integrated and vertically-integrated (0-100m) fluorescence data.

5.2 MATERIALS AND METHODS

5.2.1 *Collection of in-situ data*

Between 2009 and 2015, seventeen adult female southern elephant seals from Kerguelen and one from Marion Island were equipped with FCTD-SRDLs (Sea Mammal Research Unit, St Andrews University, Scotland) before they undertook their post-breeding foraging migration over the austral summer (Fig. 50).

Following established tagging protocols (Bester, 1988; McIntyre et al., 2010), the seal on Marion Island was immobilized with ketamine using a remote injection method and the tag was glued to the fur on the head with quick-setting epoxy resin. Seals on Kerguelen were anaesthetised with an intravenous injection of tiletamine and zolazepam 1:1 and tags were glued to the fur on the head using a two component industrial epoxy (Jaud et al., 2012).

All at-sea data were relayed via the Argos satellite system (<http://www.Argos-system.org>). Locations were provided by Service Argos based on Doppler shift measurements and data were downloaded from the Sea Mammal Research Unit Instrumentation Group's website (<http://www.smru.st-andrews.ac.uk/>). Detailed information on the hardware and software of the CTD-SRDL is described by Boehme et al. (2009), and on-board data processing is described comprehensively by Fedak et al. (2002). A summary is also provided in Chapter 3.

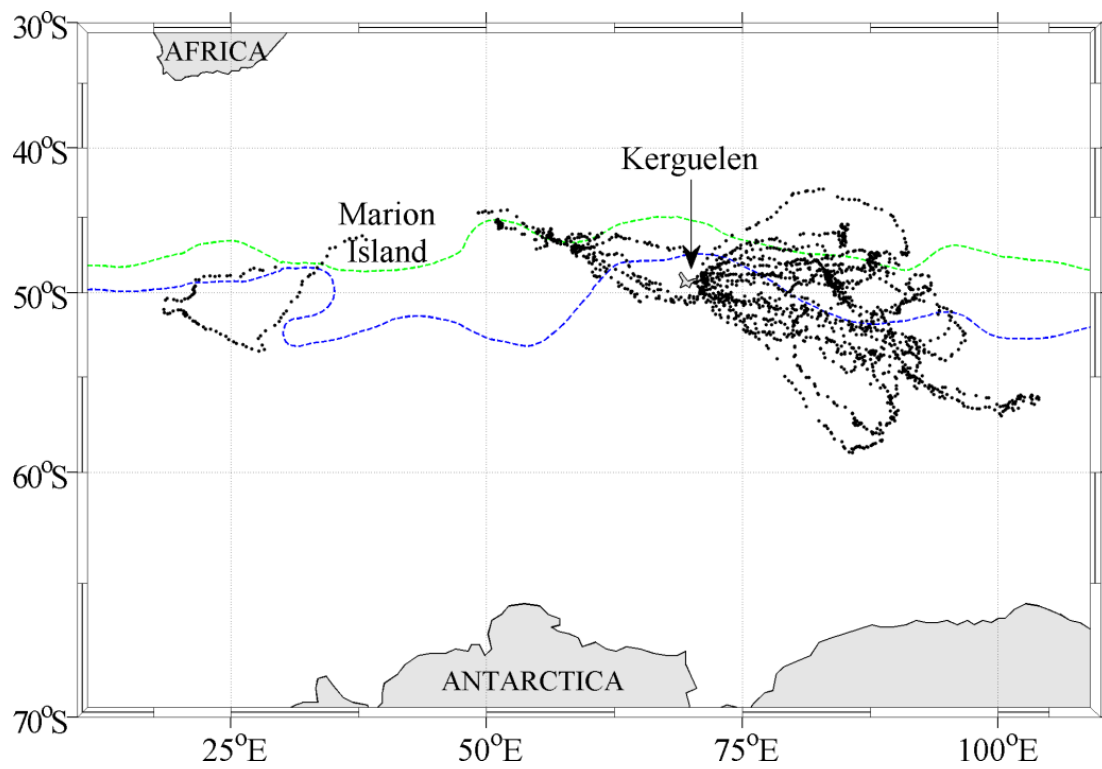


Figure 50: Tracks of southern elephant seals (in black) tagged with FCTD-SRDs over austral summers spanning 2009 to 2013. The general positions of the Sub-Antarctic Front and the Polar Front are shown in green and blue, respectively (Orsi and Harris, 2014).

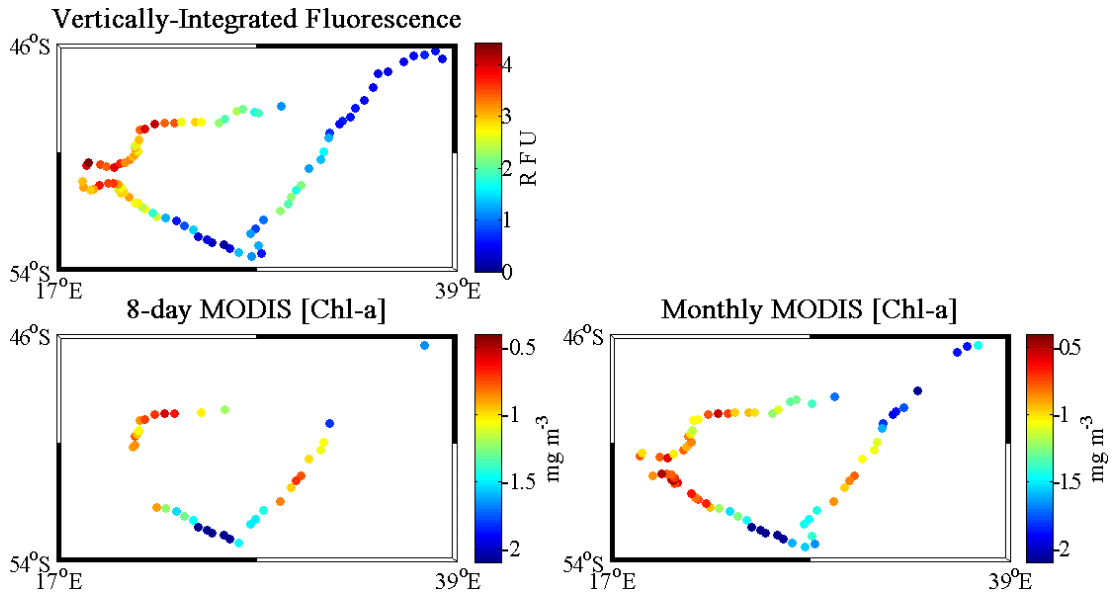


Figure 51: Tagged seal Cy35-12 with track positions in space showing concurrently measured *in situ* fluorescence in time (a), associated log-transformed MODIS 8-day [Chl-a] (b) and the combined log-transformed 8-day-Monthly [Chl-a] products (c). Fluorescence is measured in relative fluorescence units (RFU). [Chl-a] is measured in mg m^{-3} .

5.2.2 MODIS Chl-a data

All MODIS L3 products (data processed and calibrated by NASA) are freely available and were downloaded from the OceanColour website (Feldman and McClain, Ocean Color Web, MODIS, NASA Goddard Space Flight Center. <http://oceancolor.gsfc.nasa.gov>) for this study. Monthly and 8-day composites were downloaded as 4x4km resolution standard mapped images (SMI) in high definition format (HDF), extracted using the free software 7-zip (under GNU General Lesser Public License, version 9.20). All data processing was performed off-line using the commercial software package MATLAB (The MathWorks Inc., Natick, MA, 2000).

The southern elephant seals tagged between 2009 and 2015 generated a total of 1606 fluorescence profiles. In the previous chapter, all fluorescence profiles were processed to correct for quenching, ensuring that the $\approx 60\%$ of this data collected between the hours of 06h00 and 20h00 did not have to be discarded. However, less than 40% of these corrected fluorescence data had an associated MODIS 8-day [Chl-a] value. Applying the monthly composited MODIS data resulted in a substantial improvement in coverage, with 76% of the fluorescence data being assigned an associated [Chl-a] value (Fig. 51).

As with Z_{eu} , the use of daily MODIS [Chl-a] is not viable due to extensive cloud cover in the Southern Ocean. To determine if the monthly MODIS [Chl-a] product was significantly similar to the 8-day MODIS [Chl-a] product, a Kruskal Wallis test was applied. Good agreement between the 8-day and monthly MODIS [Chl-a] products suggests that monthly values are approximately representative of any missing 8-day values (Fig. 52 and Fig. 53).

The 8-day MODIS [Chl-a] data were used whenever available (30% of the time), and gaps in coverage were then 'filled in' with monthly MODIS Chl-a data. For simplicity, the resulting 8-day-monthly combination product will be referred to as 'Combined [Chl-a]' from this point. Where there are gaps in the satellite coverage, the associated sea data are filtered out of the dataset. Unlike earlier chapters, there is no interpolation to cover where the satellite data are missing. This was to ensure that only 'point values' of the MODIS [Chl-a] product would be measured against *in situ* fluorescence.

Surface concentrations of satellite-derived [Chl-a] are approximately log-normally distributed (Campbell, 1995; Lovenduski and Gruber, 2005). The MODIS 8-day and combined [Chl-a] products were thus log transformed before being correlated with the corresponding datasets of quenching-corrected *in situ* fluorescence.

5.2.3 Fluorescence data

Detailed descriptions of how the fluorescence data were processed is described in Chapter 3. For correlating with MODIS [Chl-a], three subsets of *in situ* fluorescence were generated, namely: 'surface yield', 'Zeu-integrated', and 'vertically integrated yield'. The subset of surface data was generated by extracting only the near-surface (top 5m bin) values. Zeu-integrated data were generated by calculating mean fluorescence from surface to the depth of Lee Zeu. The vertically integrated data were calculated per profile by finding the mean fluorescence yield from the surface to 100m. These Z_{eu} depth values were available from the quenching correction procedure detailed in Chapters 3 and 4.

The *in situ* fluorescence data were not converted to Chl-a concentrations. Although this is not conventional, there appeared to be no benefit to transforming relative fluorescence units to Chl-a concentration for this study. Basic tag calibration procedures were done in the Mediterranean as part of the BOUSSOLE programme, and not in the sector of the Southern Ocean where the tags were deployed. The results from the

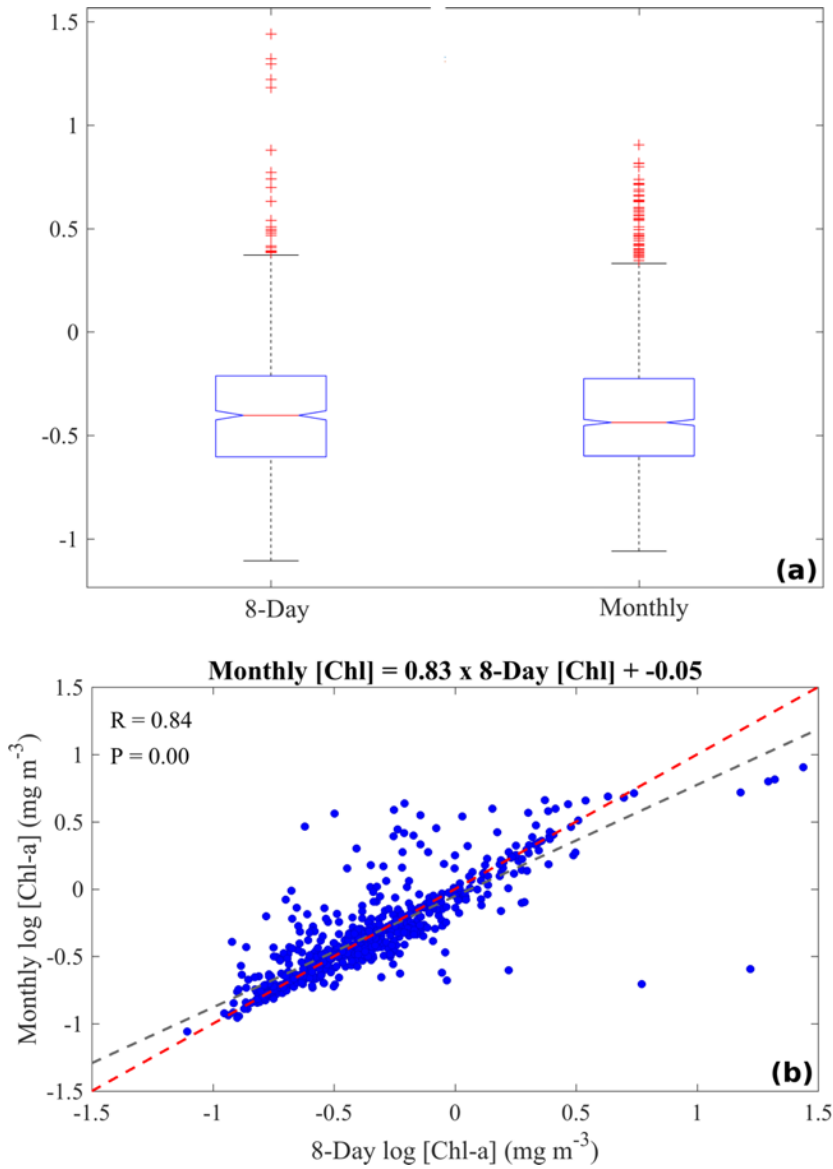


Figure 52: Evaluating the relationship between 8-day MODIS log Chl-a and monthly MODIS log Chl-a using a Kruskal-Wallis test (a) indicates that there is no significant difference between them. A linear regression (b) shows good agreement between the two datasets with a significant p-value well below 0.01.

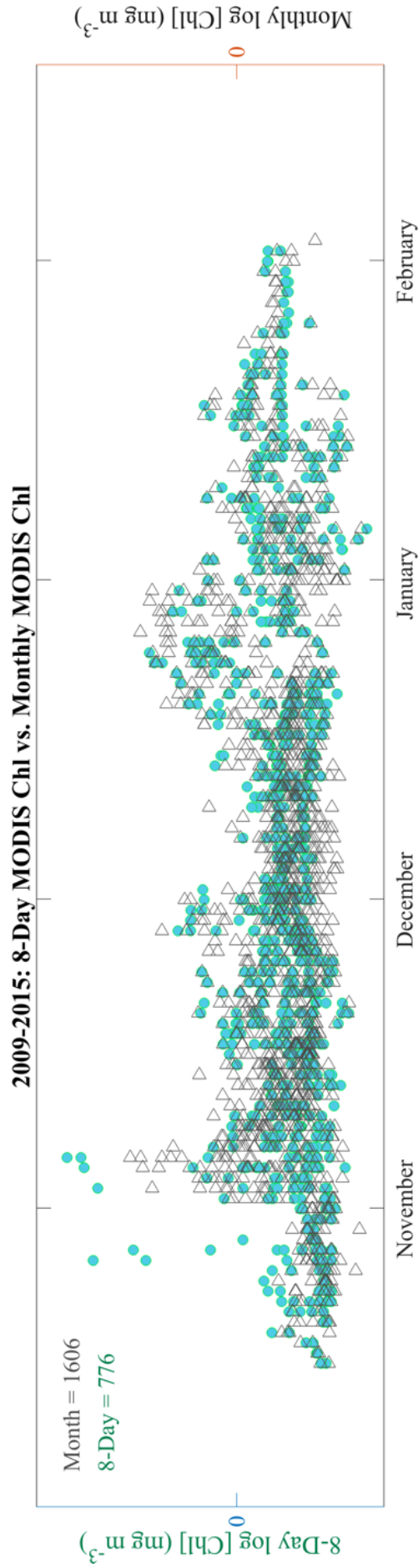


Figure 53: From all FCTD-SRD L seal positions, associated monthly and 8-day estimates of MODIS log [Chl-a]. Monthly products match minimum values in the 8-day product, but values in the 8-day products show higher (maximum) values not equalled by monthly values. The month of November, when seals are entering the water and moving swiftly away from Kerguelen, shows highest mismatch between monthly and 8-day products. The benefit of adding monthly data is that these data more than double the number of measurements available for comparison with fluorescence data collected by tagged seals.

calibrations in the Mediterranean proved useful for understanding the 'dark count' (offset value) as well as the extent of variability between tags. However, the Mediterranean and Southern Ocean are very different ocean regimes with unlike phytoplankton community structure and dynamics. Thus, the correlation coefficients and conversion factors calculated in the one are not specifically applicable to the other. Instead of converting fluorescence per tag, investigating instrument-to-instrument variability was prioritised to determine if values of fluorescence would be comparable between tags, and thus robust as a grouped dataset for comparison with MODIS data. For each fluorometer, the minimum and maximum vertically-integrated fluorescence yields and corresponding MODIS [Chl-a] values were tabulated and compared (Table ??).

5.2.4 Comparing Fluorescence and MODIS Chl-a

There appeared to be substantial discrepancies between fluorometer instruments. For this reason, fluorescence data were not grouped for comparison with MODIS [Chl-a]. Instead, each tag was treated as an individual dataset of quenching-corrected *in situ* fluorescence. Per fluorometer instrument, surface, Zeu-integrated and vertically integrated fluorescence were correlated against 8-day [Chl-a] and combined [Chl-a].

5.3 RESULTS

Evaluating the relationship between 8-day MODIS log Chl-a and monthly MODIS log Chl-a using a Kruskal-Wallis test indicated that there is no significant difference between them. A linear regression also showed good agreement between the two datasets with a significant p-value well below 0.01. The benefit of adding monthly data is that these data more than double the number of measurements available for comparison with fluorescence data collected by tagged seals.

With regards to the relationship between fluorescence and MODIS [Chl-a] per tag, differences in slope from each linear regression and correlation coefficients are substantial. There appears to be no discernible pattern between tags or within deployments (years), aside from the change in 'gain' of the fluorometer instruments between 2009 and all other years. Because the waters of the Southern Ocean are considered to conform to 'high nutrient, low chlorophyll' (HNLC) classifications, the sensitivity

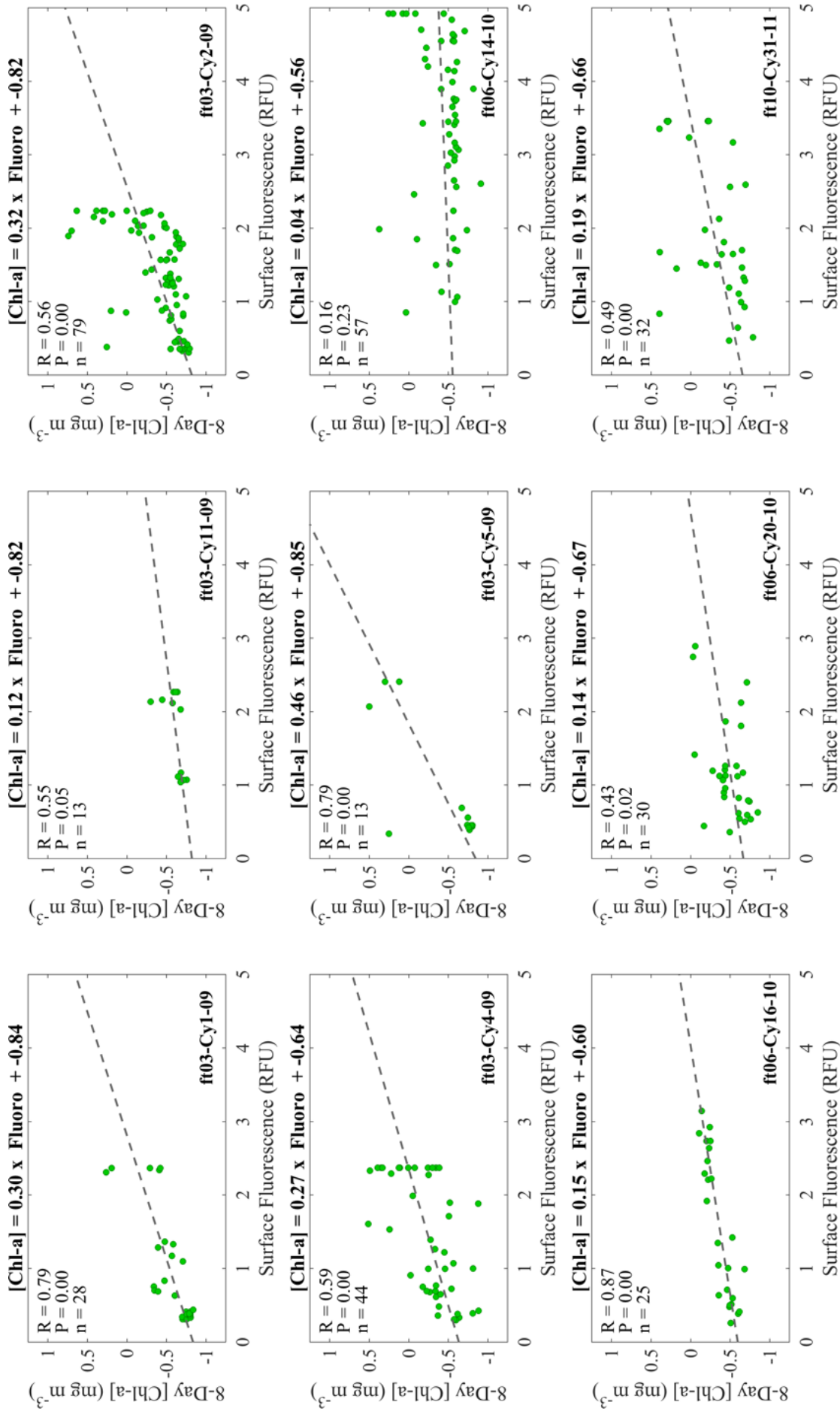


Figure 54: For each seal (tag labelled in bold in the bottom right hand corner of each plot), surface relative fluorescence values (top bin 10m) are correlated against 8-day MODIS surface Chl-a concentrations. The R value, p-value and the number of points available for the combined product satellite coverage are reported in the top left-hand corner of each plot, and the linear equation with intercept and slope are reported in bold above.

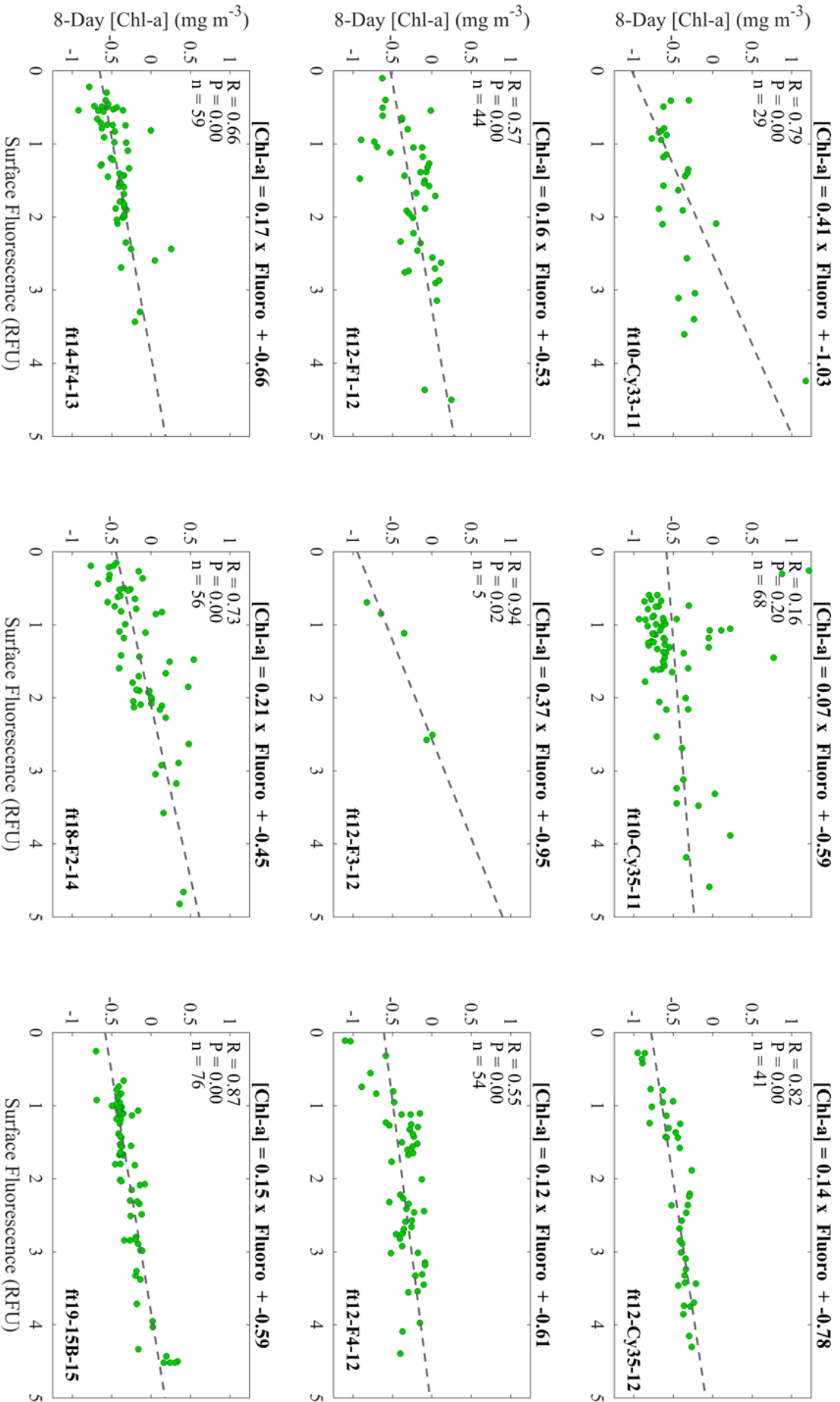


Figure 55: For each seal (tag labelled in bold in the bottom right hand corner of each plot), surface relative fluorescence values (top bin 10m) are correlated against 8-day MODIS surface Chl-a concentrations. The R value, p-value and the number of points available for the combined product satellite coverage are reported in the top left-hand corner of each plot, and the linear equation with intercept and slope are reported in bold above.

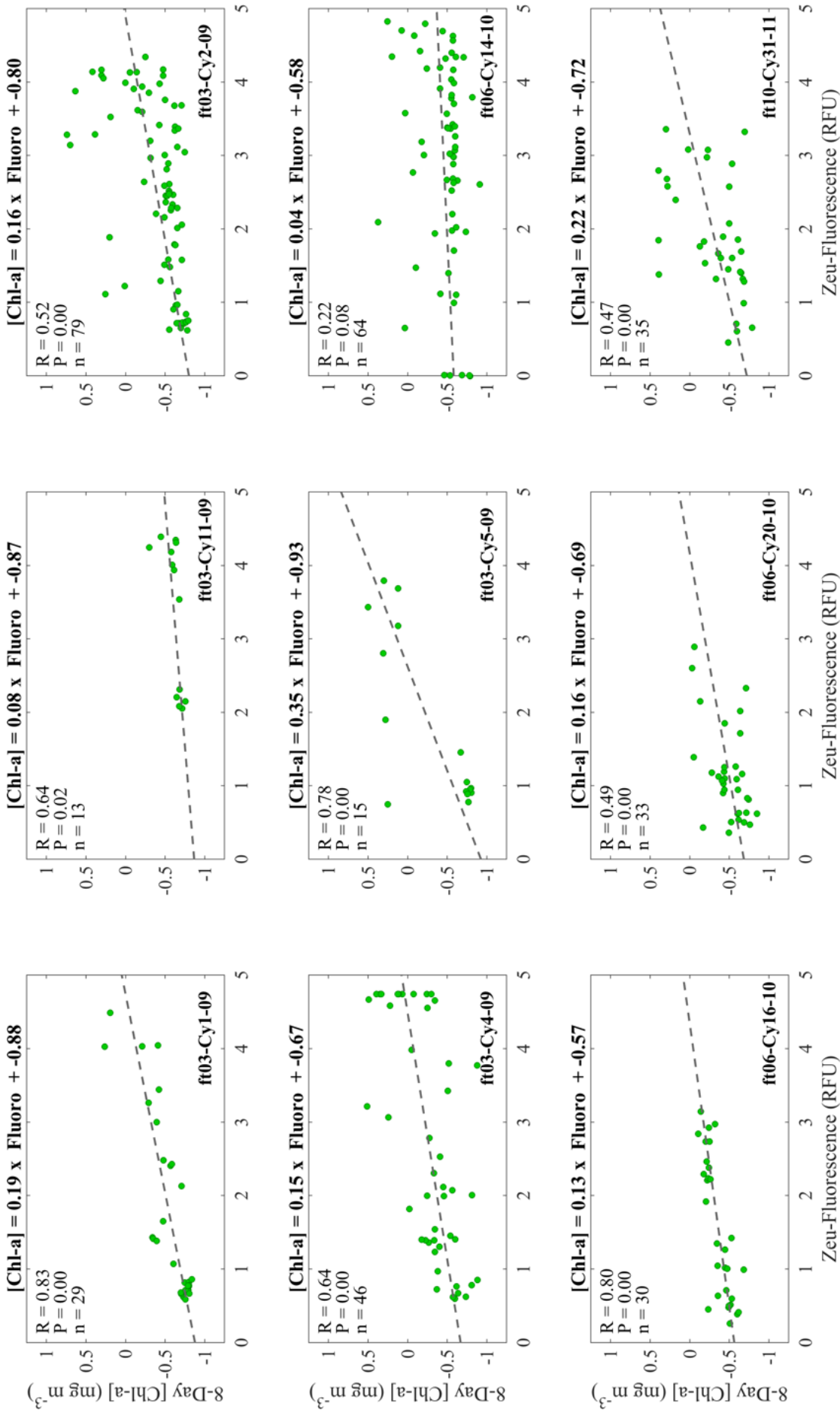


Figure 56: For each seal (tag labelled in bold in the bottom right hand corner of each plot), relative fluorescence values integrated from the surface to the depth of the 1% light level (Lee Z_{eul}) are correlated against 8-day MODIS surface Chl-a concentrations. The R value, p-value and the number of points available for the combined product satellite coverage are reported in the top left-hand corner of each plot, and the linear equation with intercept and slope are reported in bold above.

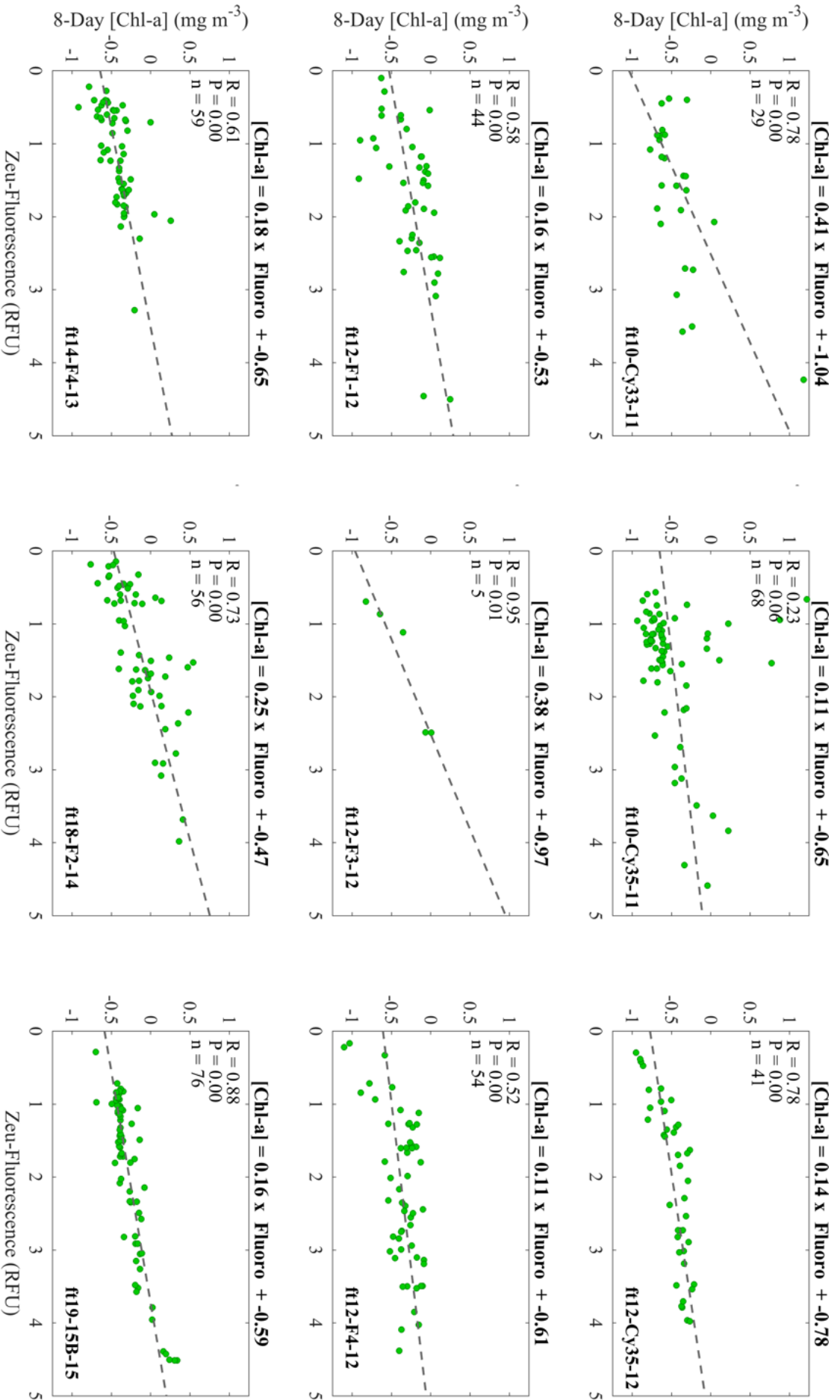


Figure 57: For each seal (tag labelled in bold in the bottom right hand corner of each plot), relative fluorescence values integrated from the surface to the depth of the 1% light level (Lee $Z_{0.01}$) are correlated against 8-day MODIS surface Chl-a concentrations. The R value, p-value and the number of points available for the combined product satellite coverage are reported in the top left-hand corner of each plot, and the linear equation with intercept and slope are reported in bold above.

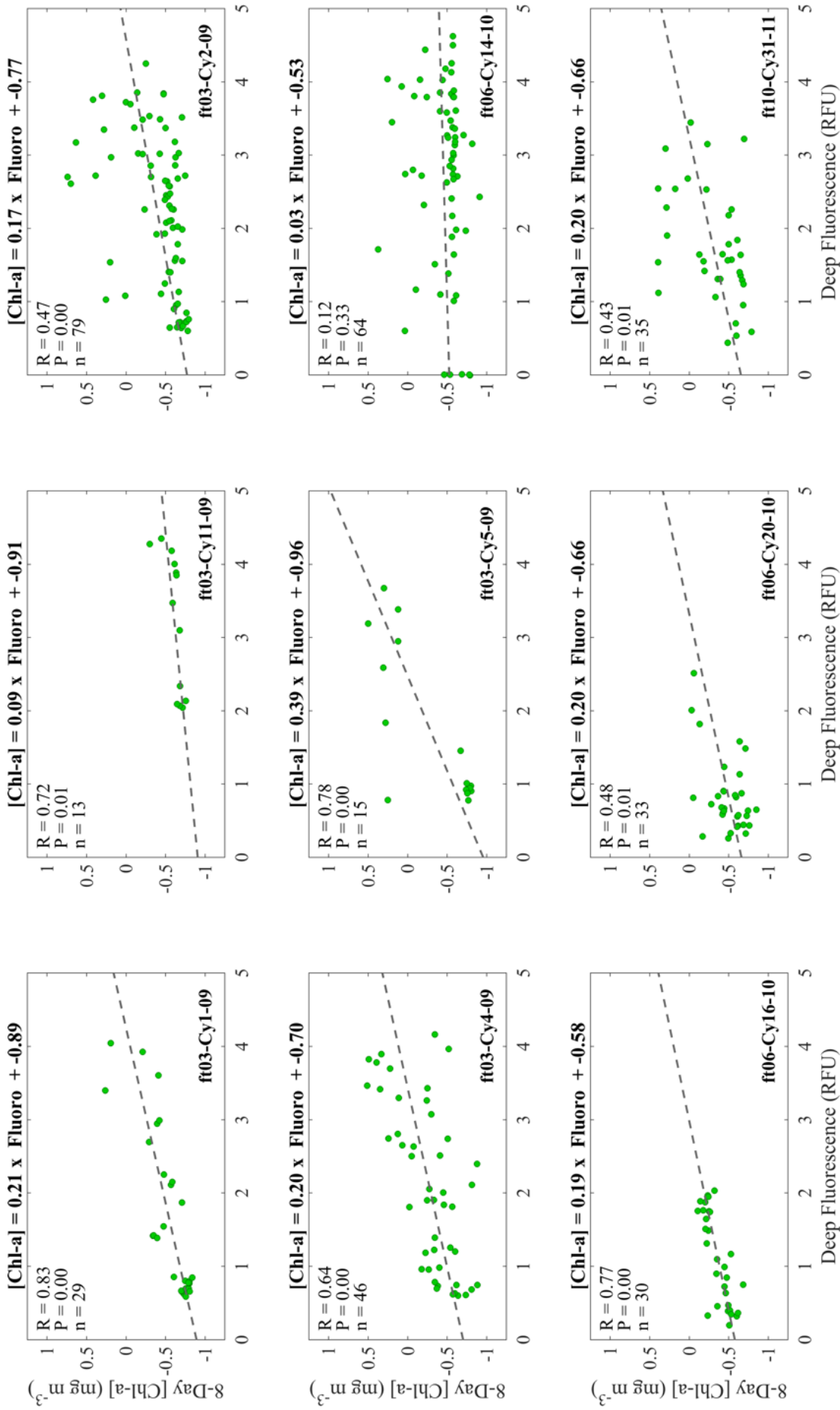


Figure 58: For each seal (tag labelled in bold in the bottom right hand corner of each plot), relative fluorescence values integrated from the surface to 100m depth are correlated against 8-day MODIS surface Chl-a concentrations. R value, p-value and the number of points available for 8-day satellite coverage are reported in the top left-hand corner of each plot, and the linear equation with intercept and slope are reported in bold above.

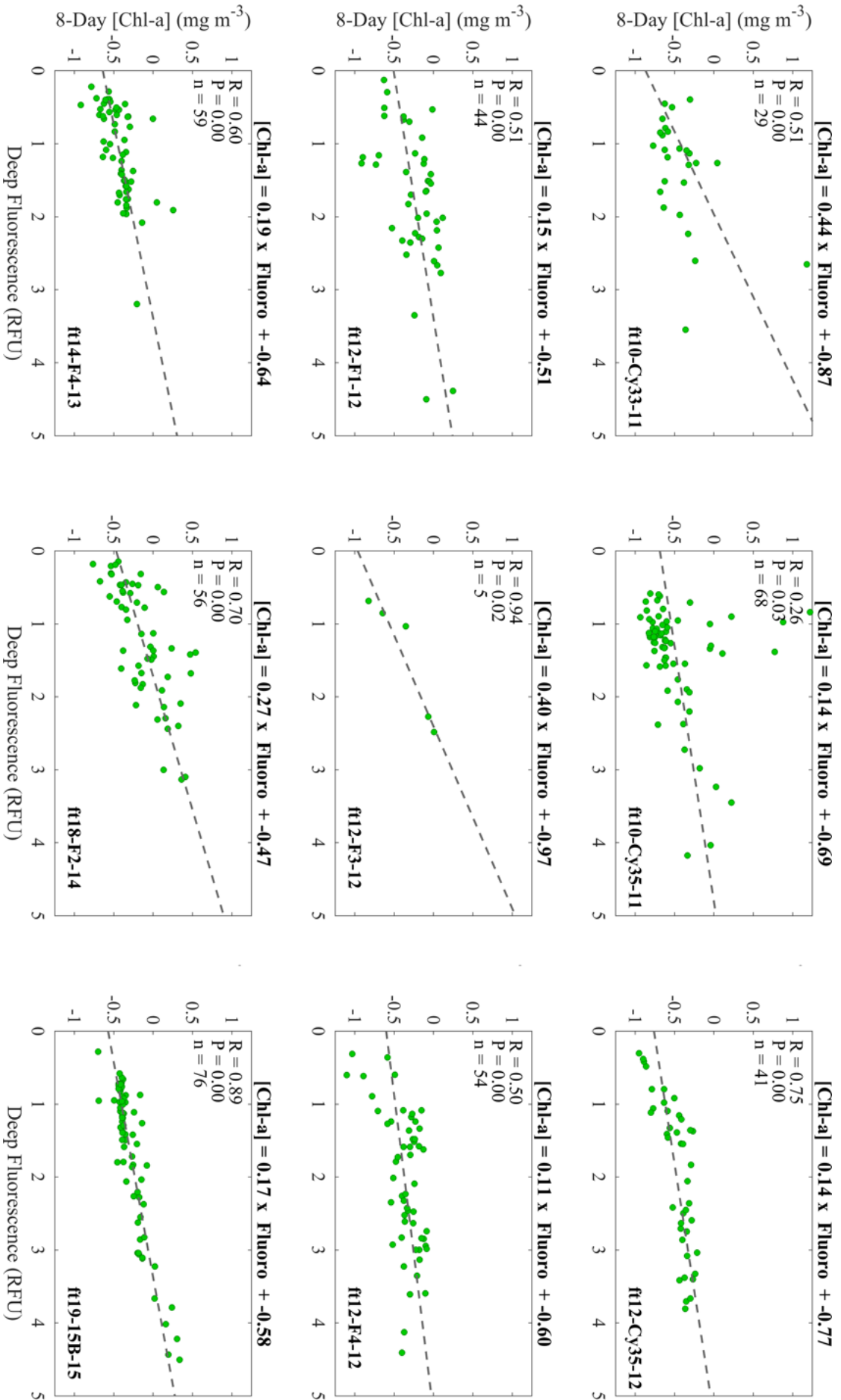


Figure 59: For each seal (tag labelled in bold in the bottom right hand corner of each plot), relative fluorescence values integrated from the surface to 100m depth are correlated against 8-day MODIS surface Chl-a concentrations. R value, p-value and the number of points available for 8-day satellite coverage are reported in the top left-hand corner of each plot, and the linear equation with intercept and slope are reported in bold above.

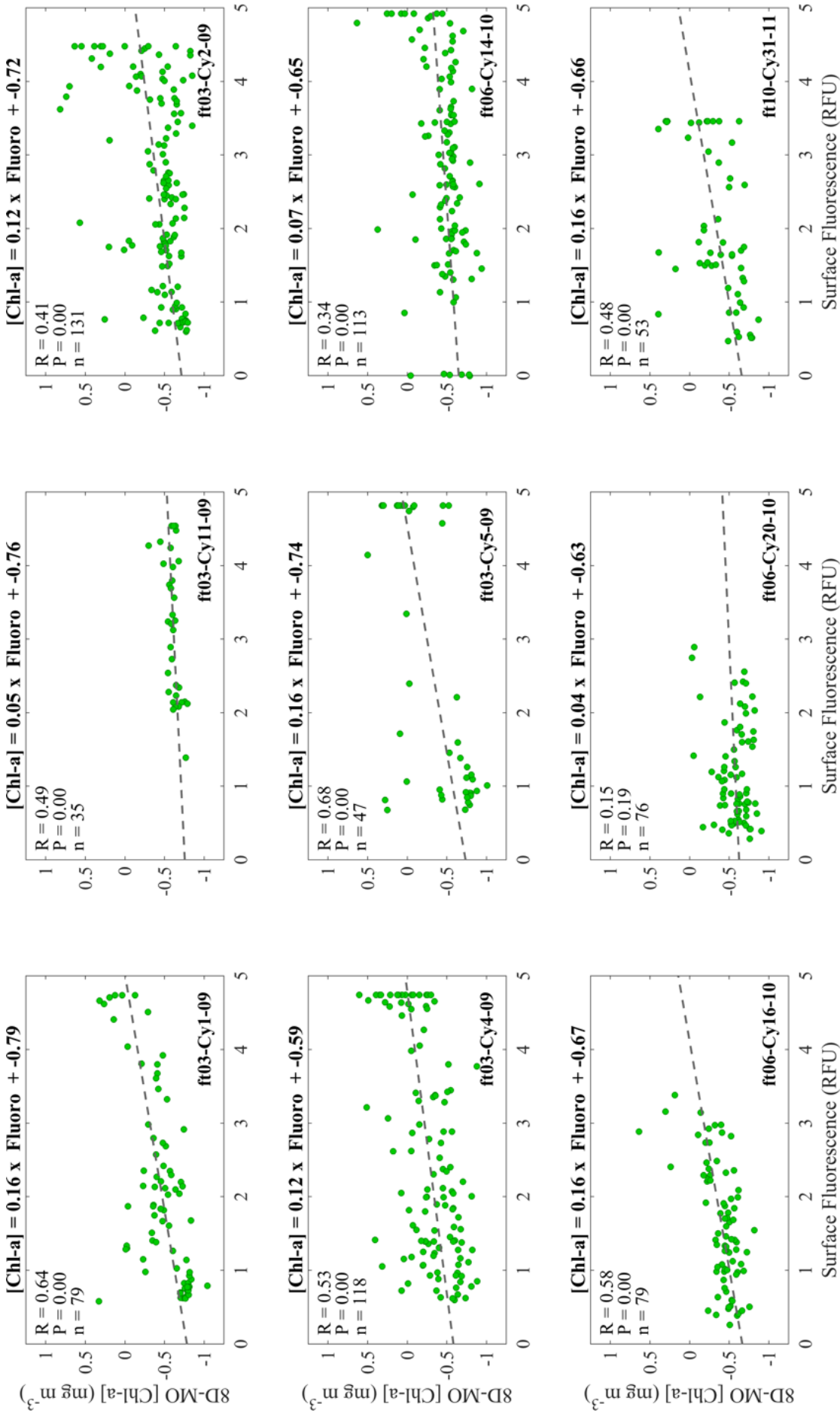


Figure 60: For each seal (tag labelled in bold in the bottom right hand corner of each plot), surface relative fluorescence values (top bin 10nm) are correlated against combined 8-day-monthly MODIS surface Chl-a concentrations. The R value, p-value and the number of points available for the combined product satellite coverage are reported in the top left-hand corner of each plot, and the linear equation with intercept and slope are reported in bold above.

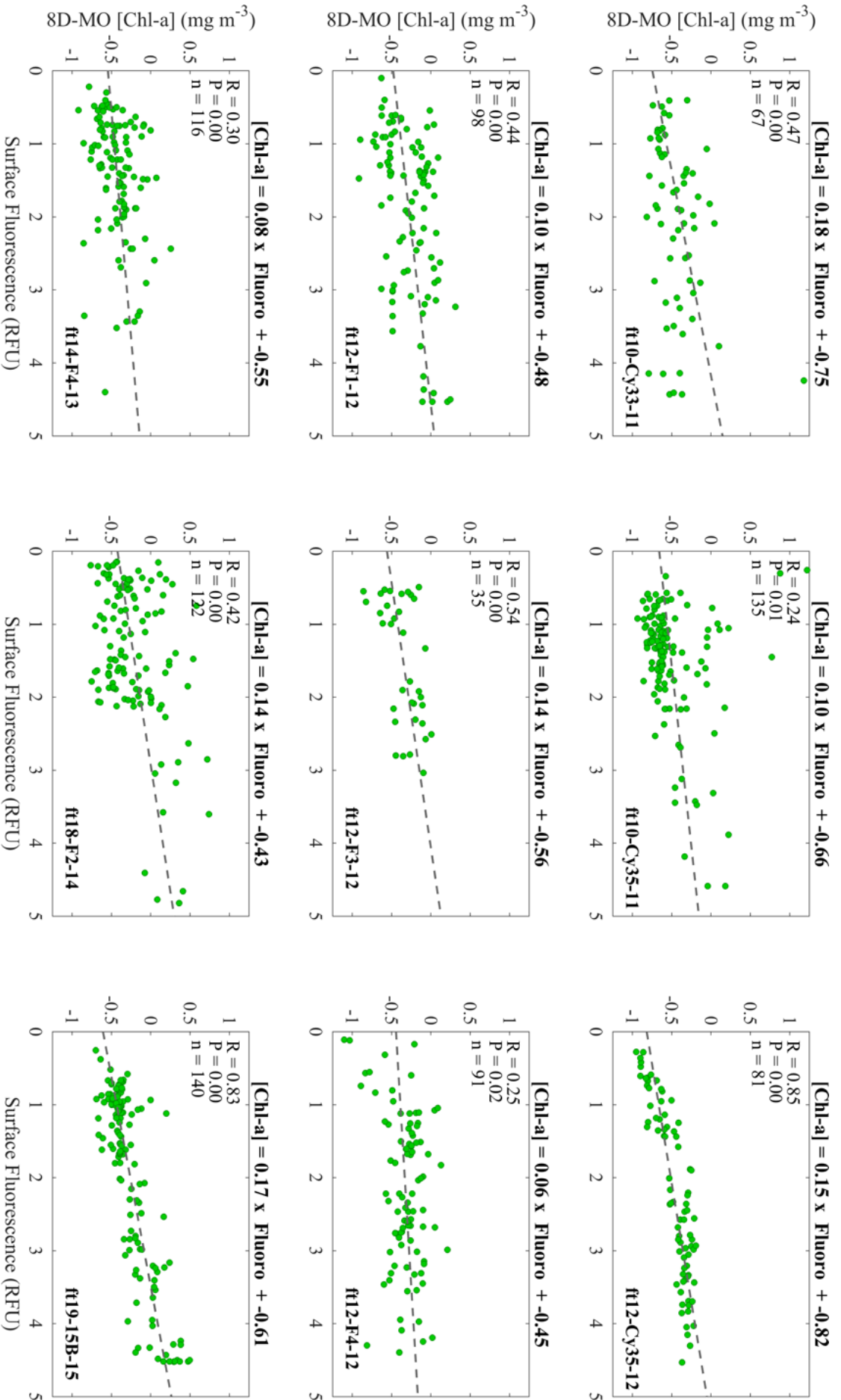


Figure 61: For each seal (tag labelled in bold in the bottom right hand corner of each plot), surface relative fluorescence values (top bin 10m) are correlated against combined 8-day-monthly MODIS surface Chl-a concentrations. The R value, p-value and the number of points available for the combined product satellite coverage are reported in the top left-hand corner of each plot, and the linear equation with intercept and slope are reported in bold above.

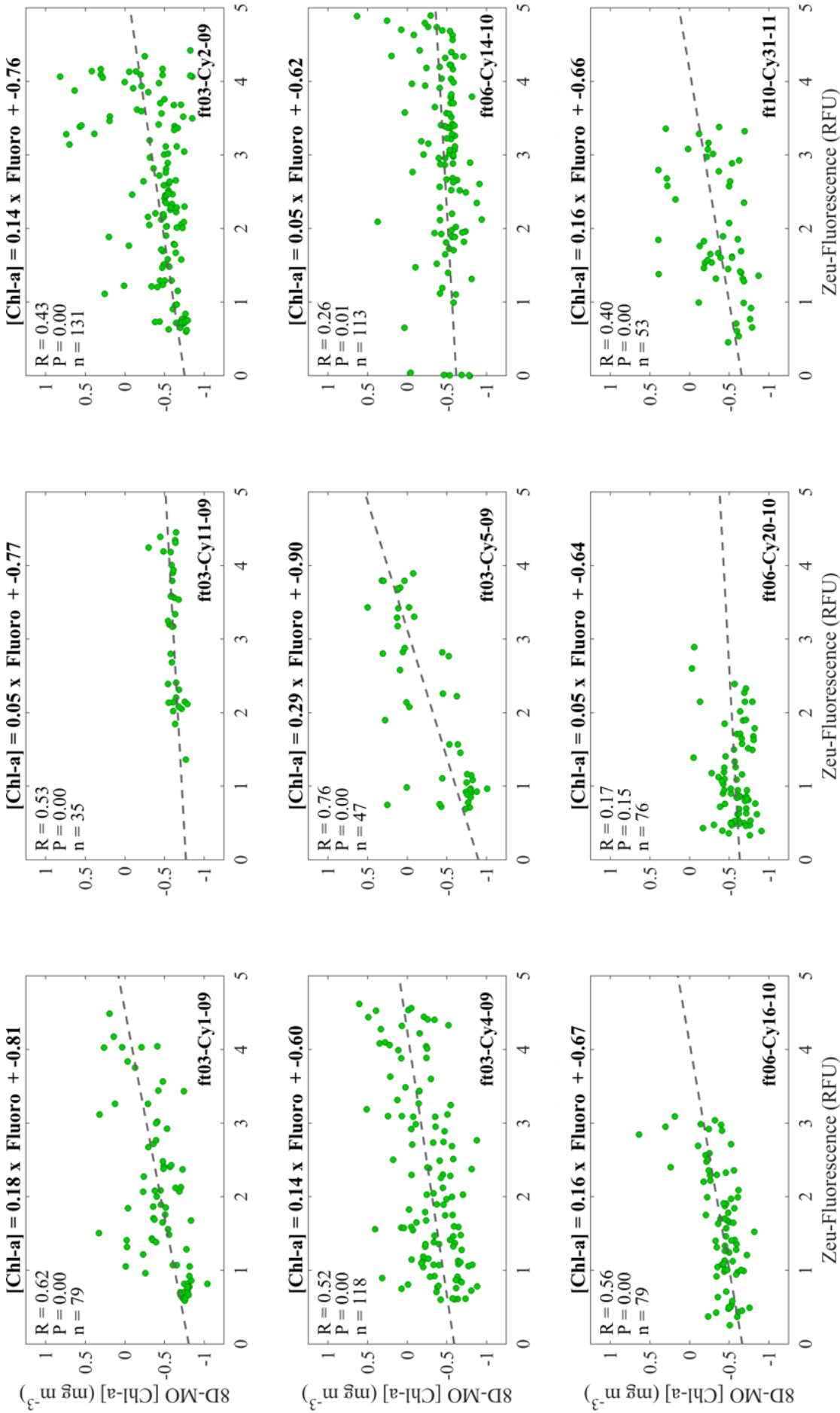


Figure 62: For each seal (tag labelled in bold in the bottom right hand corner of each plot), relative fluorescence values integrated from the surface to the depth of the 1% light level (Lee Z_{eul}) are correlated against combined 8-day-monthly MODIS surface Chl-a concentrations. R value, p-value and the number of points available for 8-day satellite coverage are reported in the top left-hand corner of each plot, and the linear equation with intercept and slope are reported in bold above.

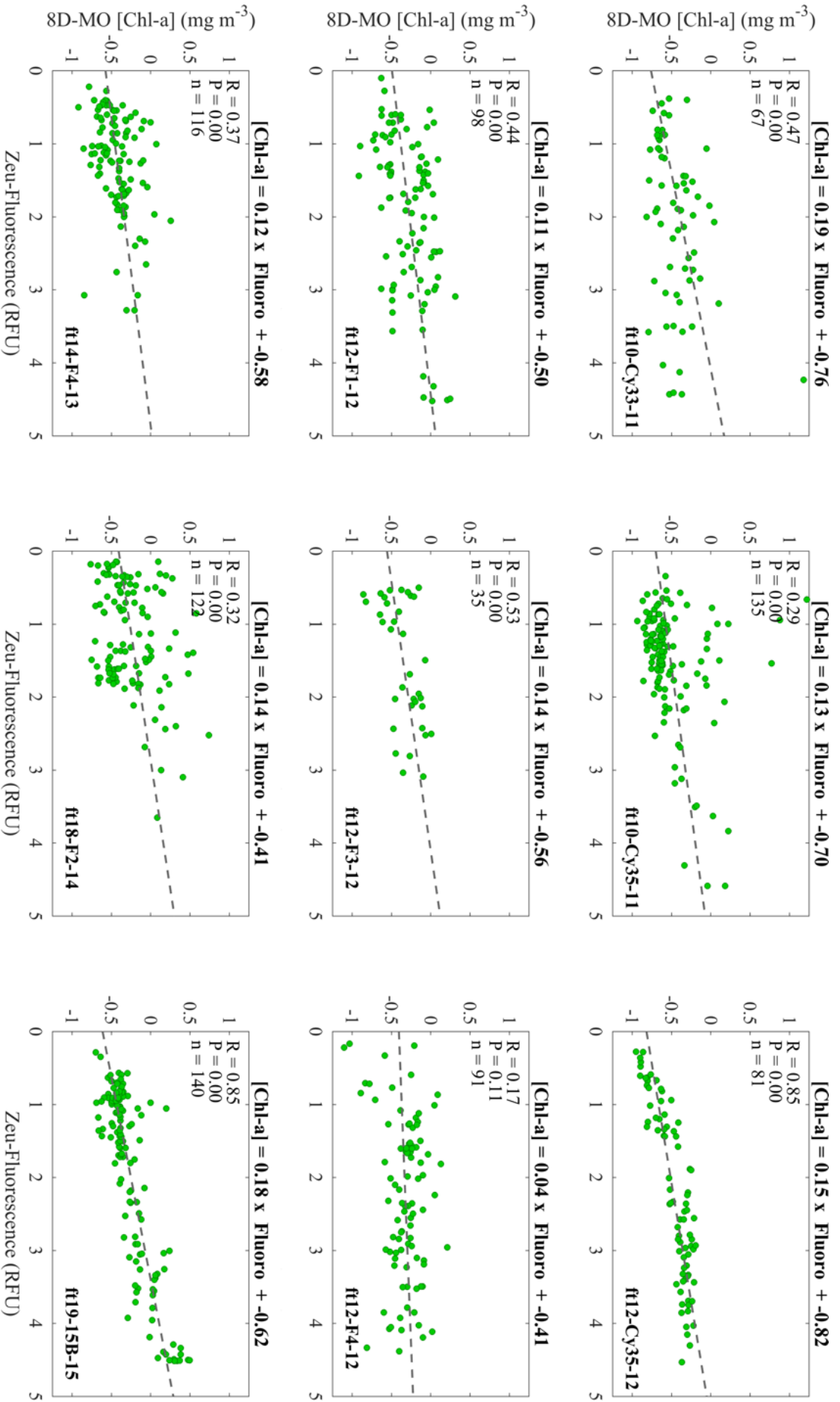


Figure 63: For each seal (tag labelled in bold in the bottom right hand corner of each plot), relative fluorescence values integrated from the surface to the depth of the 1% light level ($Z_{0.01}$) are correlated against combined 8-day-monthly MODIS surface Chl-a concentrations. R value, p-value and the number of points available for 8-day satellite coverage are reported in the top left-hand corner of each plot, and the linear equation with intercept and slope are reported in bold above.

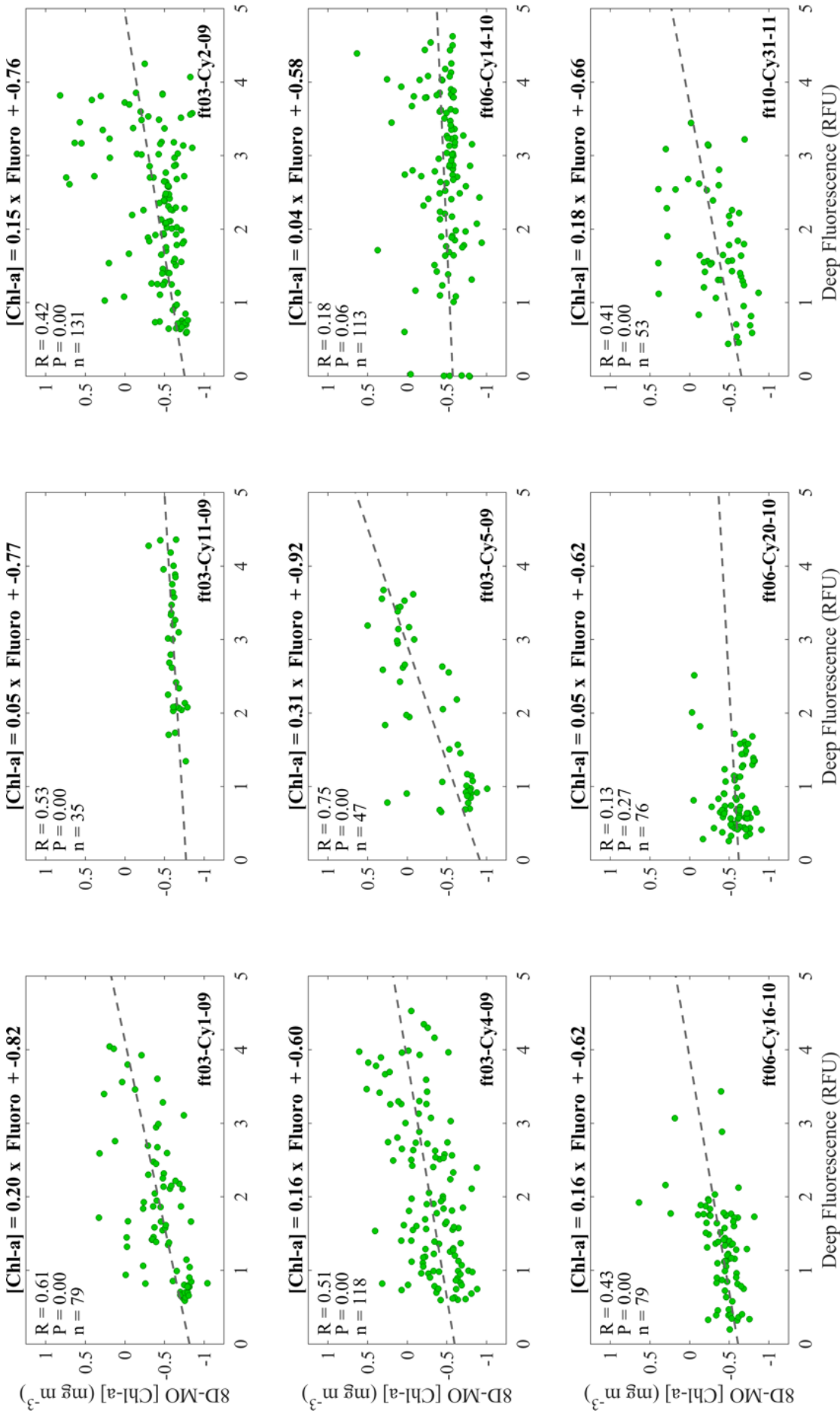


Figure 64: For each seal (tag labelled in bold in the bottom right hand corner of each plot), relative fluorescence values integrated from the surface to 100m depth are correlated against combined 8-day-monthly MODIS surface Chl-a concentrations. R value, p-value and the number of points available for 8-day satellite coverage are reported in the top left-hand corner of each plot, and the linear equation with intercept and slope are reported in bold above.

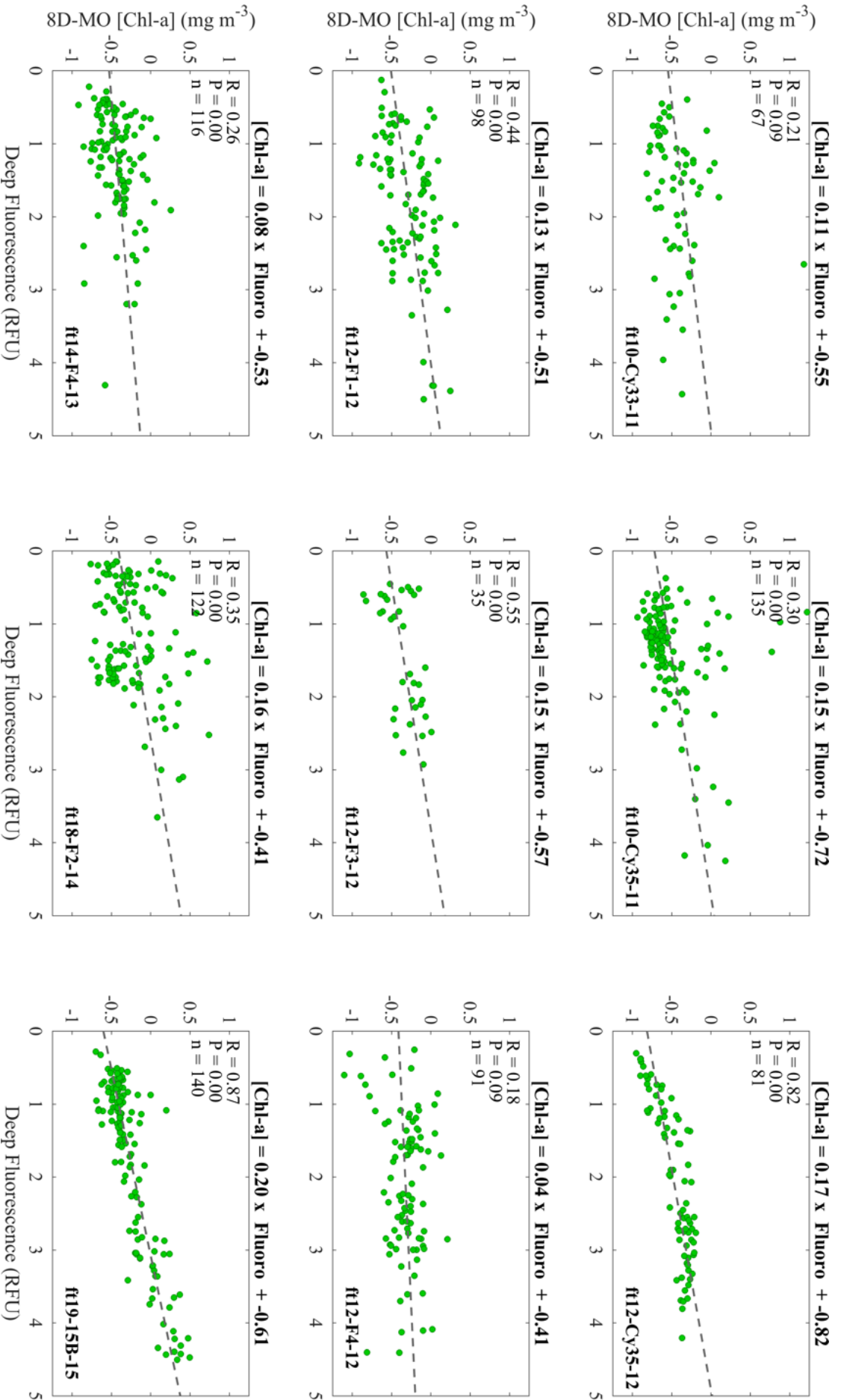


Figure 65: For each seal (tag labelled in bold in the bottom right hand corner of each plot), relative fluorescence values integrated from the surface to 100m depth are correlated against combined 8-day-monthly MODIS surface Chl-a concentrations. R value, p-value and the number of points available for 8-day satellite coverage are reported in the top left-hand corner of each plot, and the linear equation with intercept and slope are reported in bold above.

of the instrument would have been set to its highest (X_{100}) (Turner Design Manual, 2014). Under 'normal' conditions, this would serve to optimise the fluorometer when measuring concentrations of Chl-a that are not expected to exceed 5mg m^{-3} . However, it is likely that sensitivity settings were unavoidably altered during the potting process, where the fluorometer instrument is covered in a hardenable epoxy resin and added to the body of the CTD tag. After the first 'trial' deployment in 2009, the gain setting on all new instruments was set to a lower sensitivity to ensure the fluorometers would not go over scale (C Guinet 2015, Pers. Comm., 16 July). Thus, it is only in the first year (2009) that the maximum fluorescence yield is limited to ≈ 2.25 RFU. For all years thereafter (2010 - 2014), instruments show considerably higher values of relative fluorescence, with yields ranging from a minimum of 3 RFU to a maximum of 4.7 RFU. For the one correlation where all instruments are grouped and tested against combined [Chl-a], all fluorescence from 2009 datasets are transformed to match the adjusted gains from the following years.

To determine if vertically-integrating the fluorescence data and using monthly-merged MODIS data was contributing to the mismatch, all datasets of surface fluorescence were individually compared with their associated 8-day MODIS [Chl-a] data (Table ??). When correlated with 8-day MODIS [Chl-a] data, correlation coefficients from surface fluorescence data showed no substantial differences when compared with correlation coefficients from Zeu-integrated and vertically-integrated fluorescence data (Table ??). The same is true when the combined [Chl-a] product is tested against surface, Zeu-integrated and vertically-integrated fluorescence. These results point to two outcomes: values of fluorescence are not quantifiably comparable with values of MODIS [Chl-a], and correlation is not an ideal method to evaluate the relationship between the two.

Fig. ?? illustrates another way of evaluating the relationship between remotely sensed [Chl-a] and *in situ* fluorescence - over time rather than using correlation.

By plotting fluorescence and [Chl-a] over time (Fig. 67 - Fig. 72, it is apparent that the satellite product does conserve the 'shape of trend' seen in the *in situ* data.

Overall, although the relationship between MODIS [Chl-a] and *in situ* fluorescence does not appear related when the two datasets are correlated, it's uncertain how much of this is introduced by the *in situ* data and how much by the remotely sensed ocean colour data. Nonetheless, the temporally and spatially averaged MODIS [Chl-a] data does mirror the *in situ* point measurements of fluorescence yield.

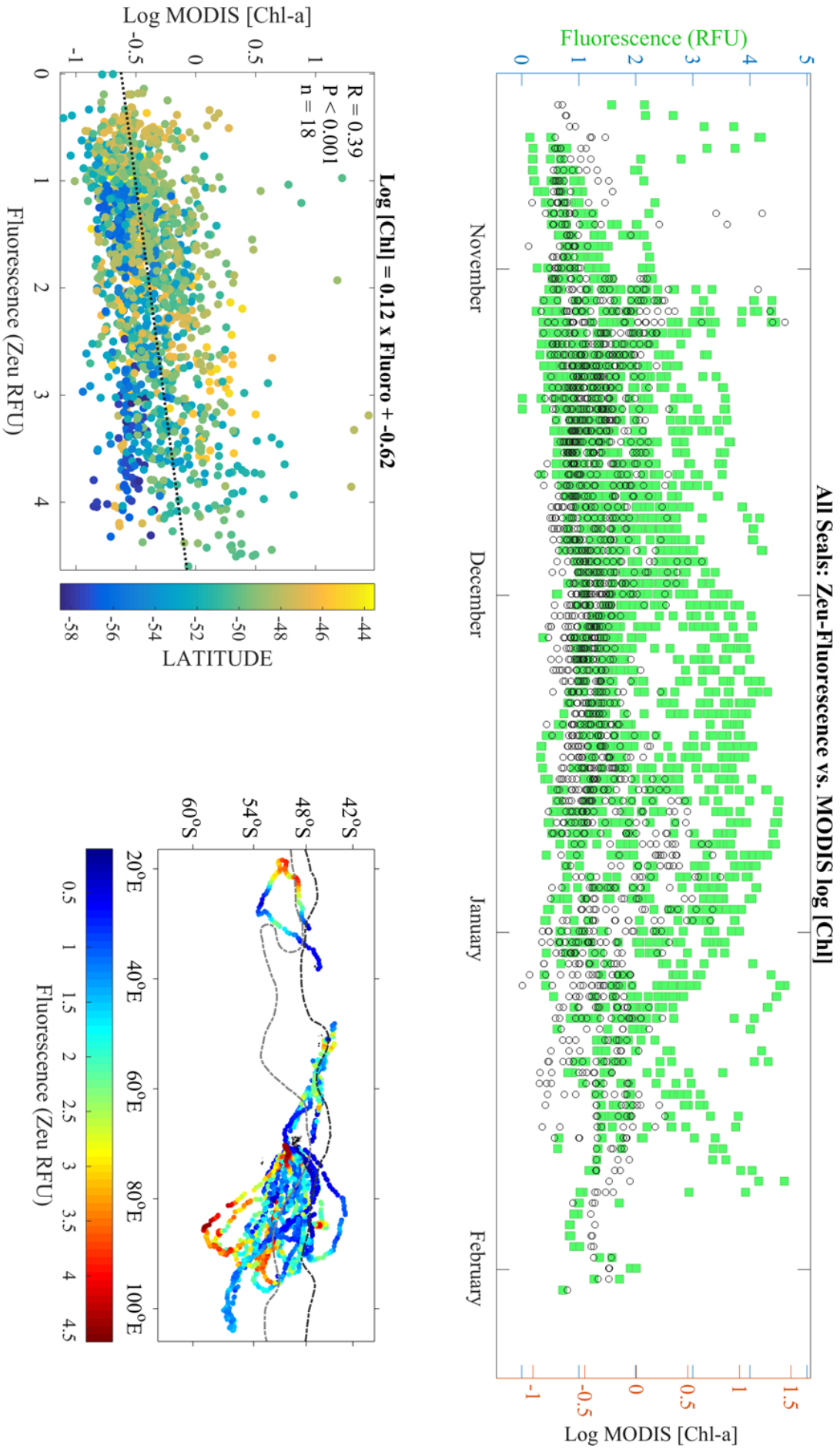


Figure 66: Relationship between *in situ* fluorescence data collected by 18 tagged seals between 2009 and 2015, and MODIS [Chl-a]. In terms of estimating phytoplankton abundance, remotely sensed surface fluorescence measures appear to underestimate what fluorometers detect in the water column, from the surface to the depth of the 1% light level. Although it's not possible to determine if the poor relationship is due to the instrument or the satellite product, increasing latitude appears to play a role, with measurements taken further south appearing to be less representative of the *in situ* data.

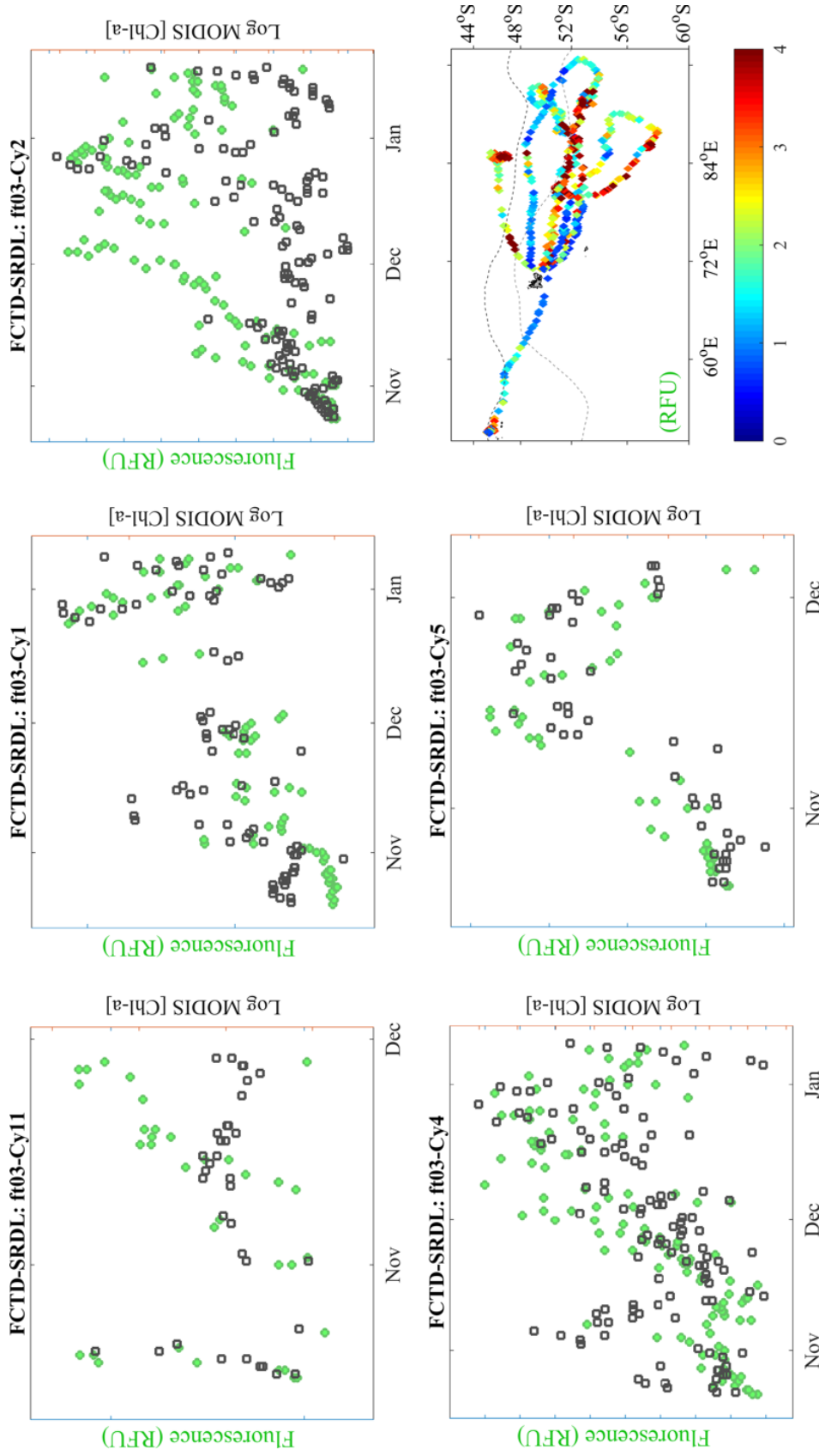


Figure 67: Per FCTD tag deployed in 2009, quenching corrected Z_{eu} -fluorescence shown by green markers and MODIS 8-day-monthly [Chl-a] shown by grey markers are plotted over time. Tag numbers are reported in bold. Tracks are shown for reference with values coloured by FCTD relative fluorescence units (RFU). This approach is qualitative rather than quantitative, but shows how the MODIS data mirrors the *in situ* values over time. Relationships between the two datasets appear to break down with increasing latitude.

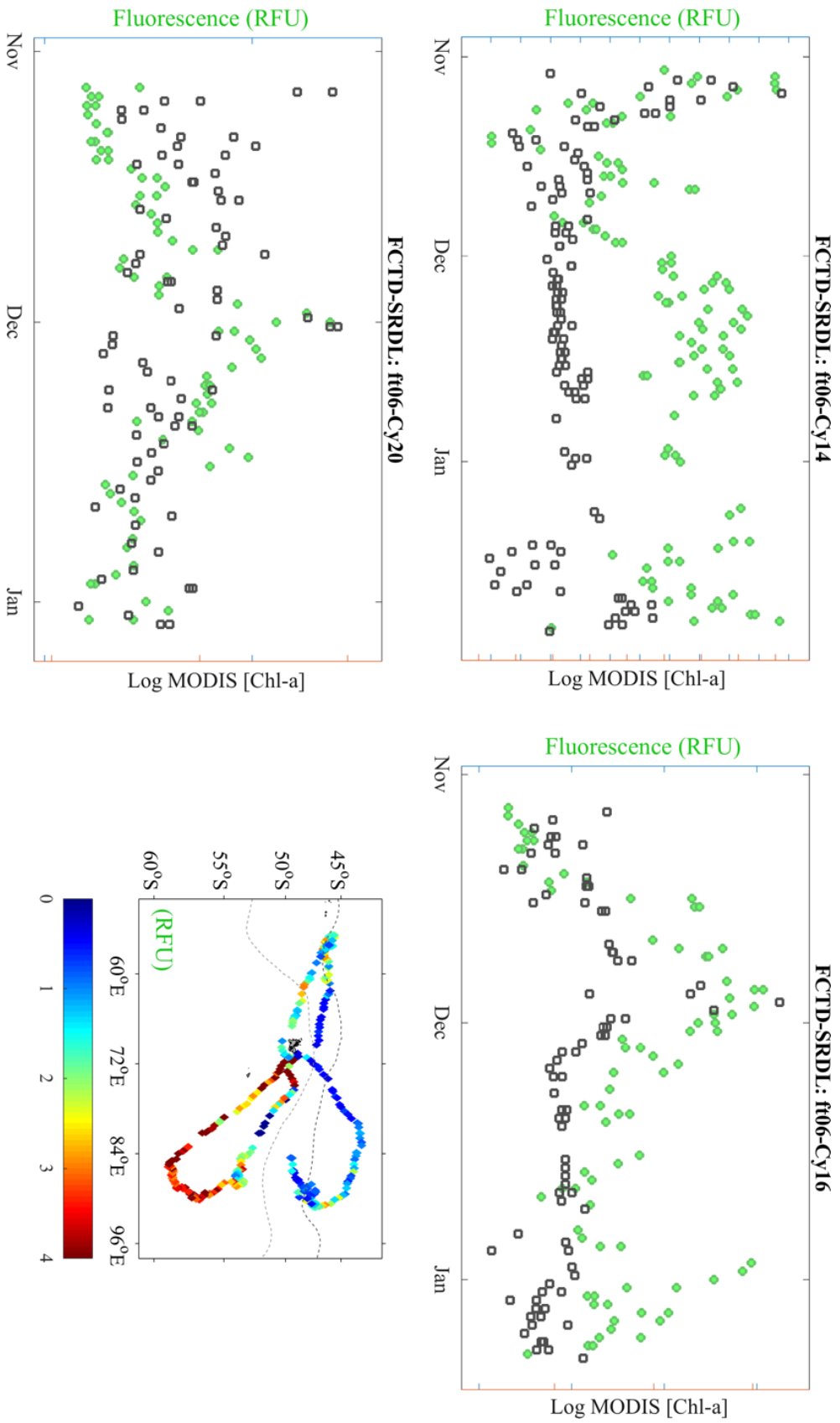


Figure 68: Per FCTD tag deployed in 2010, quenching corrected Z_{eu} -fluorescence shown by green markers and MODIS 8-day-monthly [Chl-a] shown by grey markers are plotted over time. Tag numbers are reported in bold. Tracks are shown for reference with values coloured by FCTD relative fluorescence units (RFU). This approach is qualitative rather than quantitative, but shows how the MODIS data mirrors the *in situ* values over time. Relationships between the two datasets appear to break down with increasing latitude.

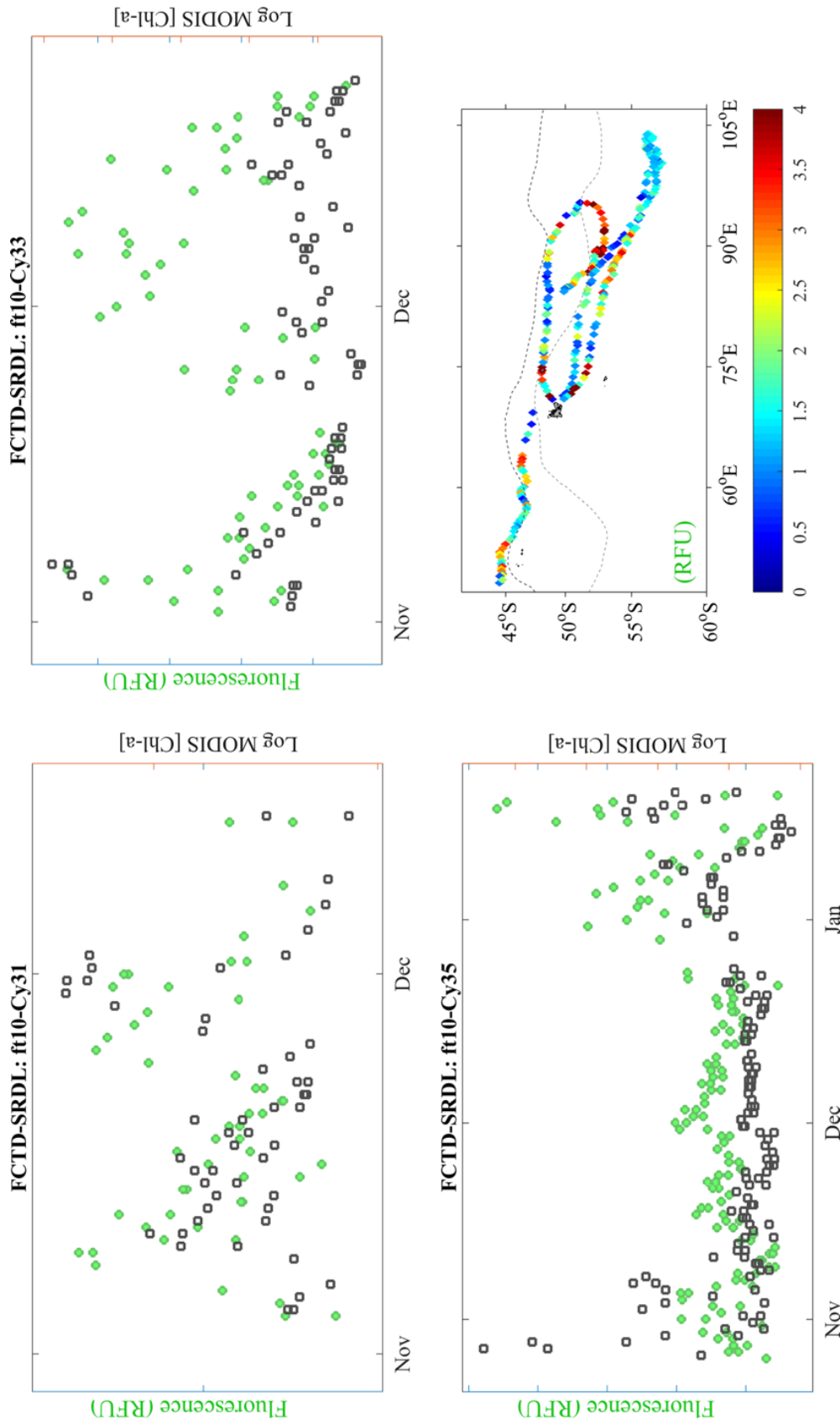


Figure 69: Per FCTD tag deployed in 2011, quenching corrected Z_{eu} -fluorescence shown by green markers and MODIS 8-day-monthly [Chl-a] shown by grey markers are plotted over time. Tag numbers are reported in bold. Tracks are shown for reference with values coloured by FCTD relative fluorescence units (RFU). This approach is qualitative rather than quantitative, but shows how the MODIS data mirrors the *in situ* values over time. Relationships between the two datasets appear to break down with increasing latitude.

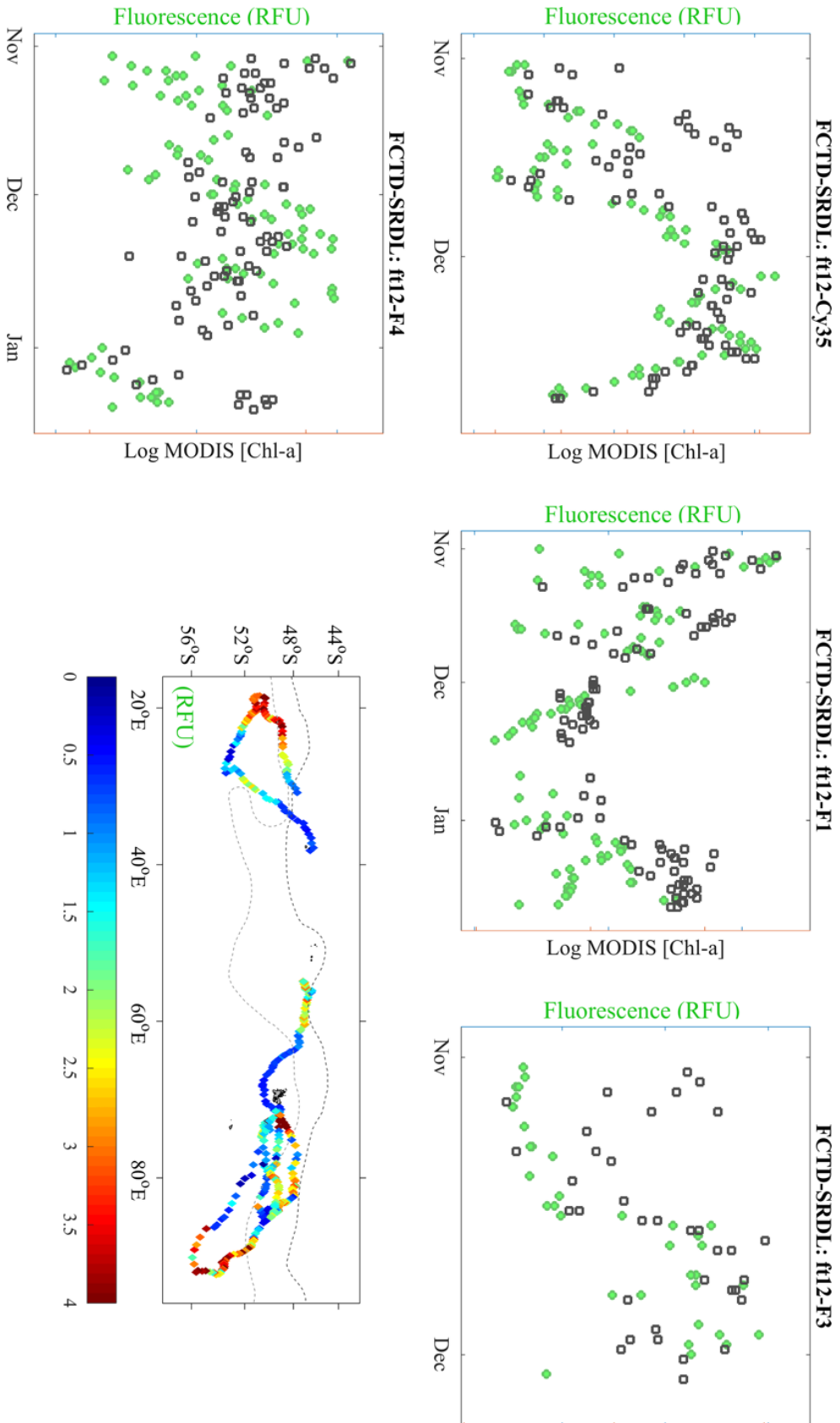


Figure 70: Per FCTD tag deployed in 2012, quenching corrected Z_{eu} -fluorescence shown by green markers and MODIS 8-day-monthly [Chl-a] shown by grey markers are plotted over time. Tag numbers are reported in bold. Tracks are shown for reference with values coloured by FCTD relative fluorescence units (RFU). This approach is qualitative rather than quantitative, but shows how the MODIS data mirrors the *in situ* values over time. Relationships between the two datasets appear to break down with increasing latitude.

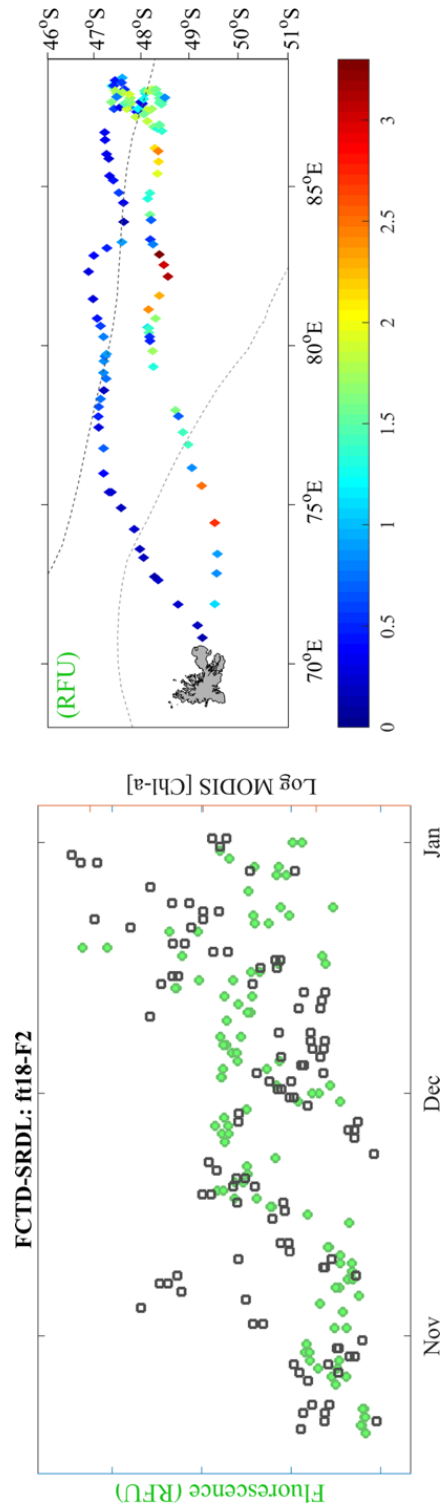


Figure 71: Per FCTD tag deployed in 2014, quenching corrected Z_{eu} -fluorescence shown by green markers and MODIS 8-day-monthly [Chl-a] shown by grey markers are plotted over time. Tag numbers are reported in bold. Tracks are shown for reference with values coloured by FCTD relative fluorescence units (RFU). This approach is qualitative rather than quantitative, but shows how the MODIS data mirrors the *in situ* values over time. Relationships between the two datasets appear to break down with increasing latitude.

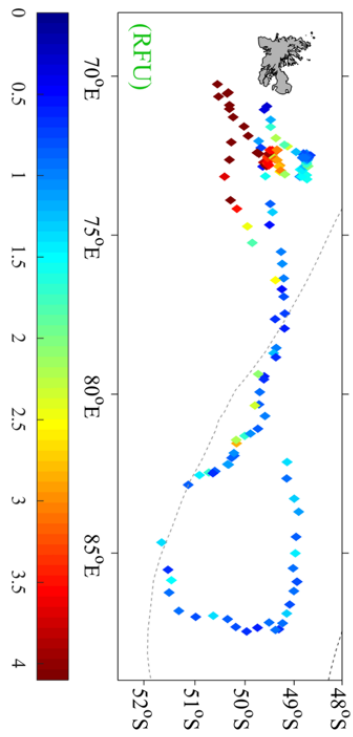
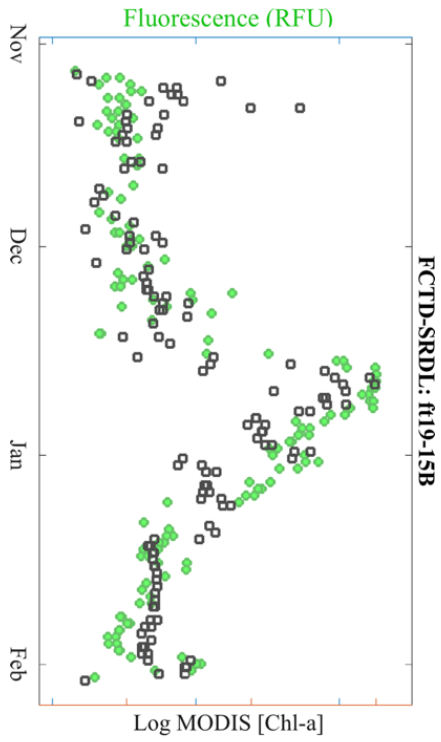


Figure 72: FCTD tag deployed in 2015 with quenching corrected Z_{eq} -fluorescence shown by green markers and MODIS 8-day-monthly [Chl-a] shown by grey markers are plotted over time. Tag numbers are reported in bold. Tracks are shown for reference with values coloured by FCTD relative fluorescence units (RFU). This approach is qualitative rather than quantitative, but shows how the MODIS data mirrors the *in situ* values over time.

5.4 DISCUSSION

Between 2009 and 2015, seventeen adult female southern elephant seals from Kerguelen and one from Marion Island were equipped with tags capable of collecting information on [Chl-a] via fluorometer instruments. These seals left the islands where they were tagged to undertake their post-breeding foraging migration over the austral summer, when light is no longer limiting in the Southern high latitudes and phytoplankton are at higher abundances. Indeed, light is strong enough to be a source of stress.

To account for light-induced suppression of fluorescence yield in well-lit surface waters, Z_{eu} was used as the reference depth from which to correct for quenching in previous Chapters. Conventionally, corrected fluorescence yield would then be converted to Chl-a concentration for comparison with MODIS [Chl-a]. For this study, a number of factors prevented this. Before being potted and added to the CTD tag, each Cyclops fluorometer is calibrated by the manufacturer (Turner Designs). This generates a crude calibration coefficient for each instrument. As discussed previously, potting affects instrument sensitivity. Furthermore, the relationship between fluorescence and Chl-a is affected by several factors, and calibration coefficients generated from controlled laboratory cultures are not generally representative of dynamic communities and variable conditions in open waters. The potted Cyclops fluorometers now part of the CTD tags thus undergo a second calibration. For the FCTD-SRDL instruments used in this study, the second round of testing took place as part of the BOUSSOLE programme in the Ligurian Sea (Xing et al., 2012, Guinet et al., 2013). These calibration procedures performed better than the first factory calibration (Xing et al., 2012); however, communities and conditions in the Mediterranean are still not representative of the Southern Ocean.

To date, it has not yet been possible to perform pre-deployment calibration of the tags off Kerguelen or in any sector of the Southern Ocean. Although proposals have been put forward for such work to be done in the future (L Boehme 2015, Pers. Comm. 28 May), for this study, the absence of instrument calibration and ship-based sampling of phytoplankton in waters around Kerguelen prevented a conversion of fluorescence to Chl-a. Moreover, there is a lack of a universal relationship between fluorescence and Chl-a (Sackmann et al. 2008). Formative studies and observations have shown that when fluorescence measurements are converted to Chl-a concentra-

tions, ratios can vary ten-fold over short spatial and temporal scales (Cullen, 1982). For these reasons, even if *in situ* suitable calibration coefficients had been available, transforming would have little apparent benefit.

In this chapter, I compare temporally merged satellite-derived measures of ocean colour with high resolution point measurements. The satellite data are collected from the cloudiest region on earth, where daily data are rarely available and 8-day composites cover less than 50 percent of the *in situ* data. Monthly data do not show a significant difference to the 8-day data, but do underestimate. This is only the temporal component. In terms of spatial resolution, the ocean colour data are provided as 4x4km pixels, and we must assume that this represents all the variability within that area. If we consider this using terrestrial landscapes, which change on scales of tens of meters, as a frame of reference, it seems impossible. However, the open waters of the Southern Ocean may not benefit from such fine-scale resolution. We see this in the *in situ* data, which shows a largely unvarying sea-scape with ‘hotspots’ and ‘deserts’ rather than highly variable changes between each point measurement.

In a study conducted by Clementson et al. (2001), surface Chl-a concentrations derived remotely were matched by concentrations of Chl-a within the upper 90m of the water column. This study also found little difference between surface (top 10m), integrated to depth of Z_{eu} or integrated through the water column to 100m when compared with MODIS measures of surface Chl. Instead, the relationship between *in situ* and remotely sensed data varied most widely from tag to tag. From work completed in this chapter, we cannot say how much of this observed variability is introduced by the MODIS satellite, and how much is from the potted, uncalibrated instrument itself. Interestingly one contributing factor appears to be increasing latitude. This reinforces the optical complexity of Southern Ocean waters but doesn’t resolve the poor relationship between MODIS [Chl-a] and *in situ* fluorescence.

For the purposes of this study, the results are disappointing, but not limiting. The overarching theme of this Ph.D. is to evaluate the usefulness of satellite products to trace long-term trends. Correlating MODIS [Chl-a] with fluorescence yield illustrates that fluorescence data collected by southern elephant seals is not directly relatable to remotely-sensed, medium-resolution estimates of surface Chl-a. However, when fluorescence and MODIS [Chl-a] are plotted on the same x-axis (over time) it becomes clear that the satellite data does do a reasonable job of following the same

trends/shape seen in the *in situ* data. In this regard, we can consider MODIS [Chl-a] sufficiently useful for mirroring *in situ* patterns of phytoplankton over time.

However, using a second MODIS ocean colour product in conjunction with [Chl-a] would be enormously useful.

In Chapter 2, I was able to show that Lee Z_{eu} mirrors the trend in depths of the 1% light level seen in the *in situ* data. Thus, MODIS [Chl-a] and Lee Z_{eu} could both be examined for changes over time, relative to climate forcing. In the next chapter, MODIS [Chl-a] and Lee Z_{eu} are simultaneously examined over time and relative to the Southern Annular Mode for possible shifts in phytoplankton abundance and distribution.

EVALUATING THE MODIS TIMESERIES FOR TRENDS OVER TIME, AND FOR CHANGES RELATIVE TO THE SOUTHERN ANNULAR MODE

6.1 INTRODUCTION

The Southern Ocean plays globally relevant roles in ocean circulation and transport, as well as in atmospheric dynamics (Gordon 2001; Karsten and Marshall 2002; Sarmento et al. 2004; Toggweiler and Samuels 1993; Murnane et al. 1999; Sabine et al. 2004; Mikaloff-Fletcher et al. 2006, 2007; Watson et al., 2014). This ocean is thus a key component of the climate system, but it also appears to be sensitive to the effects of an altering climate. Specifically, the Southern Ocean appears to be responsive to the increasingly positive Southern Annular Mode (SAM) (Gille, 2014).

The SAM is one of the strongest climate trends that can be directly attributed to human activities (Sallee et al., 2010). In the Southern Hemisphere, it is also the dominant mode of large-scale atmospheric variability (Ho et al., 2012; Wang and Cai, 2013). Shifts in phase (positive or negative) and strength have associated impacts on factors including air temperature, mean sea level pressure, and geopotential height (Thompson and Wallace, 2000; Sallee et al., 2010). When the SAM is in a positive phase, anomalously low pressures at/around Antarctica are matched by anomalously high pressures at the mid-latitudes. A positive SAM is also characterized by a strengthening circumpolar vortex. This is linked to intensification and contraction of the dominant westerly winds, with a measurable shift towards the Antarctic continent (Kidson and Sinclair, 1995; Marshall, 2003; Gille, 2014). A negative SAM is characterized by the opposite conditions, including weakening westerly winds and a northward shift in prevailing position.

The SAM has been exhibiting a significant trend to its positive phase since the mid-1970s. This appears to be driven by the cooling of the Antarctic lower stratosphere, principally through ozone loss - a theory previously proposed by modelling studies (Thompson et al., 2011). Levels of stratospheric ozone began declining in the early

1970's, driven by widespread release of chlorofluorocarbons (CFC's). The presence of CFC's and halons in the atmosphere lead to an almost complete depletion of ozone at 14 - 22km above Antarctica. Although there has been some recovery, the hole in the ozone layer re-forms every spring; cooling the stratosphere and increasing the strength of the polar vortex. Changes to the SAM thus appear to be most pronounced over the summer (Turner et al., 2013).

Climate models predict that increases in greenhouse-gas forcing will reinforce the positive trend in the SAM, but this is still uncertain (Treguier et al., 2010; Turner et al., 2013). What is clear is that in the last 30 years, the westerlies have strengthened by 15 - 20% (Korhonen et al., 2010; Turner and Marshall 2011) and contracted poleward by up to 2° in latitude (Turner et al., 2013). Coinciding with these changes to the westerlies, the largely wind-driven zonal ACC has strengthened and contracted around the Antarctic continent. Consequently, Sokolov and Rintoul (2009) found that the mean positions of the SAF and PF jets have moved further south. In chapter 3, I found the same in the in situ data collected by tagged seals. Furthermore, in response to changes in wind stress, ice cover and buoyancy (freshwater) fluxes, MLD has been shown to be significantly reactive to a positive SAM (Venables et al., 2013; Saltee et al., 2010). Any changes to vertical mixing and horizontal transport are likely to have impact on phytoplankton.

Through the process of photosynthesis, phytoplankton form the link by which carbon is cycled between inorganic and living stocks (Behrenfeld et al., 2006). I have discussed the importance of iron and light to phytoplankton in previous chapters, but availability of both can be limited (or enhanced) by changes to vertical mixing. This has consequences for primary production, the main driver of air-sea fluxes of CO₂. Photosynthetic processes consume vast amounts of Dissolved Inorganic Carbon (DIC) at the ocean surface, especially over the summer months (Dufour et al., 2013). On a global scale (and on a daily basis), excesses of a hundred million tons of atmospheric carbon are fixed into organic material by phytoplankton, and a similar amount of organic carbon is simultaneously shifted into the marine ecosystem through grazing (predation), and sinking (Behrenfeld et al., 2004). Majkut et al. (2014) calculated that as much as 50% of total oceanic uptake occurs south of 30°S. As the most significant sink of atmospheric carbon (Watson et al., 2014) and with the additional stresses on our earth system from anthropogenic sources, there is an

urgency to resolve our understanding of the processes that govern phytoplankton dynamics in the Southern Ocean.

Using a bio-optical algorithm based on monthly [Chl-a] data collected by the Coastal Zone Colour Scanner (CZCS) sensor aboard the Nimbus 7 satellite, Arrigo et al. (1998) calculated that total annual primary production in the Southern Ocean came to approximately 4414 g C yr^{-1} . On temporal scales, the summer month of December proved to be the most productive. Spatially, the permanently open ocean contributed almost 70% to the overall annual primary production of the Southern Ocean (Arrigo et al., 1998). Furthermore, all sectors including the marginal ice zone (MIZ) showed a seasonal pattern driven primarily by solar irradiance.

The amount of sunlight reaching the Southern Ocean is largely controlled by cloud. The skies above the open Southern Ocean are the cloudiest on earth (McCoy et al., 2015), while the Antarctic continent itself is rarely cloudy. This fits with the high pressure system over the South Pole, low pressure band at the mid-latitudes, with high mesoscale cyclone activity in the vicinity of the polar front (Irving et al., 2010). However, these longitudinally alternating cells of high and low pressure are potentially changing their mean positions with an increasingly positive SAM. Is it possible that cloud fraction - and thus the amount of light available to photosynthesising organisms in the upper ocean - is changing too?

Globally, cloud fraction over land is approximately 55%, with a distinct seasonal cycle (King et al., 2013). Cloud fraction over the oceans, on the other hand, exhibits relatively low seasonal variation but coverage has been shown to be as high as $\approx 72\%$ (Fig. 73).

Possible changes in cloud fraction over the Southern Ocean over time would have implications for increased or decreased light reaching surface waters. These changes to the light field may have positive or negative consequences for primary production, through either enhanced photosynthesis or increased photoinhibition (as described in chapters 2 and 3), respectively. As a function of vertical mixing, the amount light available to phytoplankton in Southern Ocean waters is a key factor regulating photosynthesis. Given the links between an increasingly positive SAM and perturbed mixing, there is a need to investigate if phytoplankton patterns have also changed (Ho et al., 2012). For the vast but chronically under-sampled Southern Ocean, the challenge is how best to measure and monitor these changes.

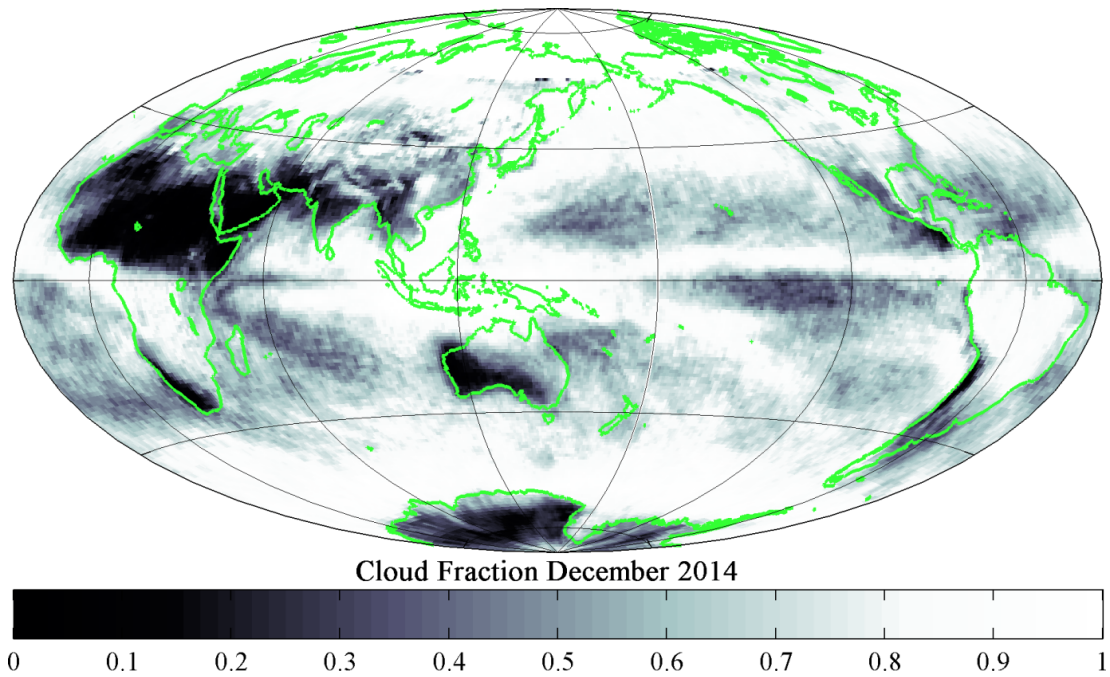


Figure 73: Proportion of our globe covered by cloud in December 2014, shown as a monthly mean of daytime values. Black represents little to no cloud cover, whereas white represents upwards of 80% cloud coverage.

The ocean colour satellite record is a powerful dataset for measuring spatio-temporal patterns of phytoplankton abundance. Although different missions and different sensors have had different strengths and weaknesses, the combined record goes back to 1979. This study focuses specifically on data collected by the MODIS sensor on the Aqua Mission (from July 2002), which has provided 13 years of ocean colour data, and continues to do so today. However, 13 years of ocean colour data is likely insufficient to be able to tell apart global warming signals from natural interannual or decadal variability. Henson et al. (2010) suggested that a time series of at least 40 years would be required before this is possible, especially at the high latitudes. Nonetheless, if the focus is shifted from global climate change to regional climate mode forcing, trends in phytoplankton abundance and distribution may become more evident (Martinez et al., 2009; Kemp and Villareal, 2013).

Martinez et al. (2009) showed that changes to Chl-a on interannual and decadal timescales correlate with the North Atlantic Oscillation index. More recently, Wernand et al. (2013) have shown there to be a slight increase in Chl-a concentration in the North Atlantic over the last century. However, as much as global trends in Chl-a show a robust correlation to sea surface temperature (SST), these changes do not express as uniform trends between oceans. Indeed, even within the same ocean regime,

changes and shifts to phytoplankton patterns can regionally specific or constrained (Hahn-Woernle et al., 2014).

On decadal timescales, regional variations to phytoplankton patterns may be measurable within the relatively short MODIS time series. Specifically: when examined relative to the climate modes that dominate in those regions (Behrenfeld et al., 2006). The SAM is not the only mode at work in the Southern Ocean (Hobbs and Raphael, 2010), with El Niño/Southern Oscillation (ENSO)-driven temperature variability in the central tropical Pacific appearing to correlate with mixed-layer depth in the Pacific sector of the Southern Ocean (Sallee et al., 2008). However, due to the MODIS satellite record being so short, studying ENSO-driven changes to ocean colour data is not within the scope of this study. Primarily, this chapter is dedicated to investigating potential trends and changes to MODIS [Chl-a] and MODIS Lee Z_{eu} in the Southern Ocean over the 13-year timeseries, and relative to trends in the SAM. In addition, MODIS cloud fraction is examined for potential changes over time, and relative to SAM forcing. The motivation to add cloud fraction to this chapter is that the amount of light reaching the ocean surface is key to the abundance and distribution of [Chl-a] on both vertical and horizontal scales. Furthermore, the combination of these two factors, light at the surface and [Chl], both fundamentally affect the depth to which light is attenuated to 1%.

6.2 METHODS AND MATERIALS

6.2.1 SAM Index

How the SAM is defined, the index used to represent it, the dataset used to calculate this index, and even how the various phases of SAM are classified tends to vary in the literature (Ho et al., 2012; Nan and Li, 2003; Reason and Rouault, 2005; Gillett et al., 2006). The two approaches that are more commonly used to approximate the SAM index are the Gong and Wang (1999) method, and Principal Component Analysis (PCA). Briefly, the former derives the SAM index by measuring the difference between the normalised mean zonal pressures at 40°S and at 65°S. This approach is not further addressed in this study, and the focus is on PCA instead. PCA is a procedure that is usually applied to reduce the dimensionality of a given dataset. It works by decomposing spatio-temporal data into its leading patterns in time (Prin-

Principal Component - PC) and space (Empirical Orthogonal Function - EOF) based on an orthogonal (at right angles; statistically independent) decomposition of the data covariance matrix (Björnsson and Venegas, 1997). In simpler terms, this method essentially replaces variables within a dataset with a weighted average of those variables. This new vector (PC₁) will explain the most variance in the original dataset. PC₁ will thus stand as the dominant pattern within the dataset. The remaining matrix of unexplained residuals can then be reduced to sequentially less dominant PCs explaining less and less of the variance (PC₂, PC₃, etc.) (McKittrick, 2005). With regards to calculating the SAM index, the PCA method finds the dominant pattern of variability (PC₁) of mid- to high latitude climate variables including temperature, geopotential height (GpH) and mean sea level pressure (MSLP) in the Southern Hemisphere (Thompson and Wallace, 2000).

Based on this PCA approach, the National Oceanic and Atmospheric Administration (NOAA) provides an index of the SAM, which is termed the Antarctic Oscillation Index (AAO). Data is freely available and provided as monthly means (1979 - present) in graphical, tabular and 7-bit binary American Standard Code for Information (ASCII) format, and can be downloaded from the National Centre for Environmental Prediction (NCEP) NOAA website. In terms of input data for the PCA, the AAO index is based on a numerical weather prediction model assimilating a combination of satellite data and *in situ* (station) observations. Ho et al. (2012) maintain that gridded data incorporating satellite information are less vulnerable to the spurious errors that have tended to influence previous reanalysis data (Marshall, 2003). Based on these assertions by Ho et al. (2012) and others (e.g.: Gong and Wang, 1999), I based this study on the NCEP-NOAA interpretation of the AAO index.

6.2.2 MODIS Data

Cloud Fraction Since 2003, MODIS Aqua and Terra have continuously retrieved physical and optical properties of cloud over both land and sea. The freely available archived products include global gridded Level-3 Cloud Fraction (Fig. 73). This cloud fraction product is derived by the MODIS cloud mask, and exists as a parameter within a significantly larger dataset called MODo8 (Terra) or MYDo8 (Aqua) (Pers. Comms, Kevin Ward, 2015). These datasets include cloud-top properties, cloud thermodynamics, as well as optical and microphysical parameters such as optical

thickness and effective particle radius, to name but a few (King et al., 2013). Studies undertaken by King et al. (2013) have shown that global cloud fraction is similar between night and day. Because cloud cover is relevant specifically to sunlight for this study, only mean day cloud fraction was used for this study.

Data were accessed from the Level 1 and Atmosphere Archive and Distribution System (LAADS) web interface <https://ladsweb.nascom.nasa.gov/data/>. The larger MYDo8_M3 product contained the 'Cloud_Fraction_Day_Mean_Mean' dataset required, and the monthly data were ordered for the summer months from the 'MODIS collection 5.1'.

Ocean Colour Data Based on results from the previous chapters, there is some confidence that MODIS [Chl-a] and MODIS Lee Z_{eu} products are sufficiently representative their equivalent *in situ* data over time. For this study, these ocean colour products are examined from 2003 to 2017, specifically looking at potential changes over the austral summers.

For every month from October to March in the dataset, 13 years of freely available level 3 MODIS [Chl-a] and MODIS Lee Z_{eu} were downloaded as 9 x 9km resolution standard mapped images (SMI) in high definition format (HDF) from the OceanColour website (<http://oceancolor.gsfc.nasa.gov>). The open source software 7zip (<http://www.7-zip.org>) was used to extract the compressed data into Matlab.

6.2.3 Processing MODIS Data

Surface concentrations of Chl-a are approximately log-normally distributed (Campbell, 1995; Lovenduski and Gruber, 2005). Thus, as described in previous chapters, the MODIS [Chl-a] product was log transformed before being processed further. After this point, [Chl-a] and Z_{eu} ocean colour products were processed identically, as were the MODIS cloud fraction data.

Firstly, for the [Chl-a], Z_{eu} and cloud fraction datasets, monthly climatologies were calculated. For this step, for each month over the period from 2003 to 2017, mean values of surface concentration (mg m^{-3}), depth (m) and coverage (%), were calculated for each dataset, respectively. To investigate the idea that some variability in Z_{eu} may be generated by shifts in cloud fraction, and thus light reaching the ocean, the depth (m) and coverage (%) climatology data were correlated and examined for a possible relationship.

Secondly, for the [Chl-a], Z_{eu} and cloud fraction datasets, the monthly anomaly was calculated. For this step, the monthly climatology (mean) was removed from each corresponding month. Using October as an example to illustrate this step: the climatology calculated for October was subtracted from all Octobers in the timeseries. This served to remove the mean values of surface concentration (mg m^{-3}), depth (m) and coverage (%), essentially subtracting the seasonal signal. Any signal remaining is thus a deviation from the 'standard', and may be considered the anomaly.

At this stage of the analysis, steps were taken to determine if any anomalies in the MODIS data are best represented as 'per month' composites, or as seasonal composites (summer months combined). In the anomaly dataset, MODIS [Chl-a], Z_{eu} and cloud fraction products were inspected on a month-by-month for any changes in concentration (mg m^{-3}), depth (m) and coverage (%), respectively. Months were sufficiently different from one another to warrant examining each individually, rather than combining months into seasonal subsets (December - February (DJF), for example).

Finally, for each month, [Chl-a], Z_{eu} and cloud fraction were examined for potential trends over time within the anomaly data. Thus, for each pixel over the Southern Ocean spanning from 30°S to 70°S , a least squares first-degree polynomial was fitted over the timeseries. Using month of October as an example again: for each point in space in the Southern Ocean for Octobers from 2003 to 2017, a polynomial was fitted to the 13 successive values in each dataset: [Chl-a], Z_{eu} and cloud fraction. For the output of 'October Anomaly Trend', if [Chl-a], Z_{eu} or cloud fraction had changed over the time period, each spatial position would yield a negative or positive coefficient. On the other hand, areas in space that yield neither a positive nor a positive coefficient would show no discernible change in sign over time, even if some variability existed between years.

For each month, trends were plotted and inspected for any evident spatial similarities or differences.

6.2.4 *Examining MODIS Data relative to the SAM*

For each month, a linear regression was fitted to each pixel in space over time for the [Chl-a], Z_{eu} and cloud fraction anomaly datasets, relative to the corresponding monthly SAM values. Within the bounds of the 95% confidence interval, only signi-

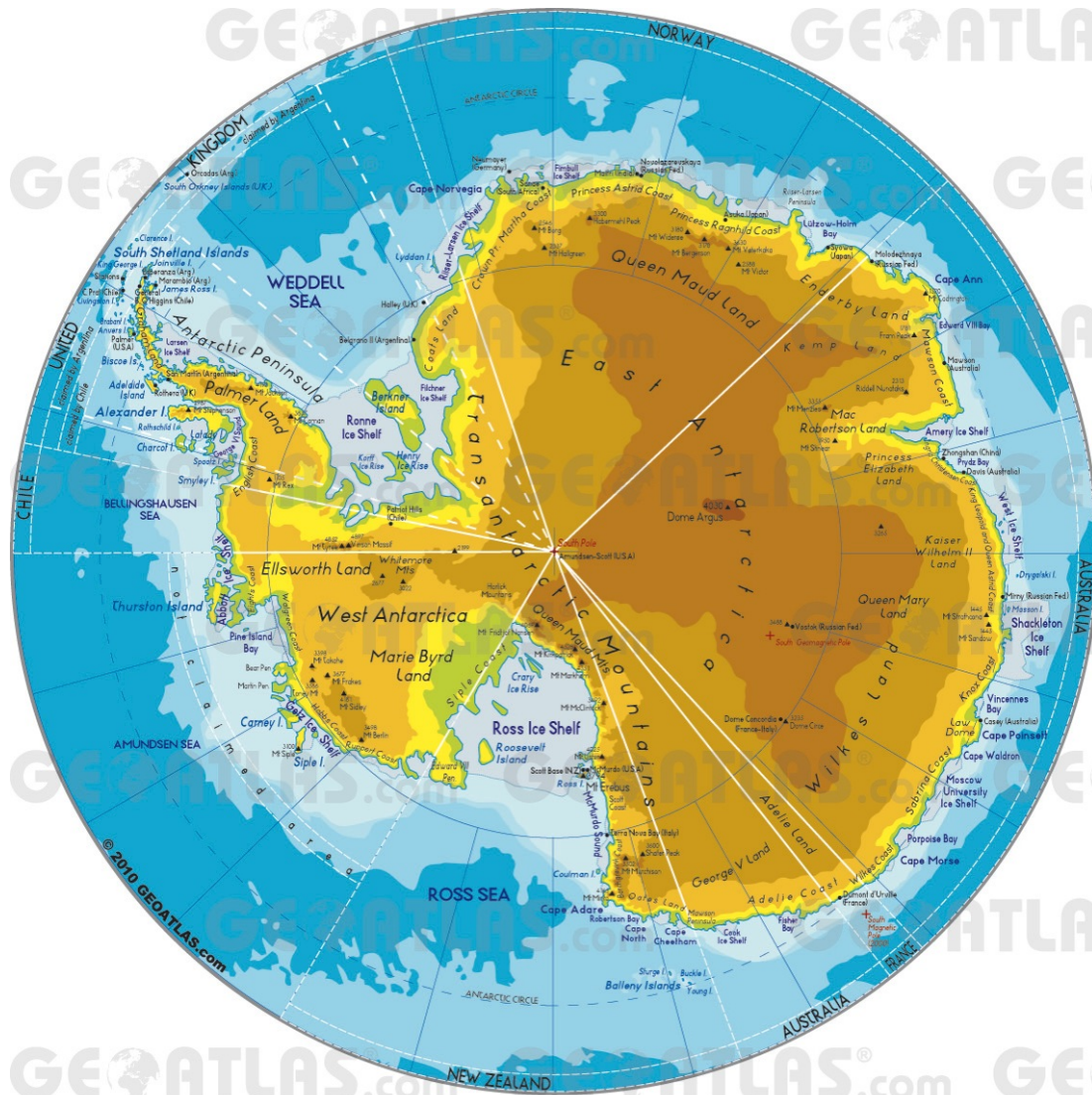


Figure 74: For reference and bearings, this labelled map of the Antarctic continent, ice shelves and Antarctic Seas provided was provided for free for paper integration by GEOATLAS® (2010).

ificant changes ($p < 0.05$) in trend in anomaly were retained and plotted to determine if changes relative to the SAM were zonal or regional.

6.3 RESULTS AND DISCUSSION

6.3.1 Climatologies

MODIS [Chl-a], Lee Z_{eu} and cloud fraction climatologies are shown in Fig. 75, Fig. 76 and Fig. 77, respectively. All months show differing patterns over time, which may be lost if monthly products were combined into a seasonal composite. For this reason,

MODIS products are investigated on a month-by-month and regional (Fig. 74) basis for changes in concentration (mg m^{-3}), depth (m) and coverage (%).

6.3.1.1 *October*

The pattern of Z_{eu} largely reinforces that of [Chl-a]. The clearest example is perhaps along the Malvinas/ Falkland Current to the east of South America and the Humboldt to the west, where the shallowest depths of the 1% light level coincide with the region of highest [Chl-a] (and lowest cloud cover). In general, south of the Sub Antarctic Front (SAF - dashed black line), [Chl-a] is low and Z_{eu} remains in excess of 50m. Downstream of the Drake Passage is perhaps the only clear exception, with elevated [Chl-a] and shallower measures of Z_{eu} (shoaling above 50m). There is also some evidence of slightly higher levels of [Chl-a] downstream of the South-west Indian Ridge (SWIR) and Kerguelen Island (Indian Ocean sector), extending along the continental ice-edge into the Pacific sector. These signals are very low in the [Chl-a] climatology, but are quite distinct in the Z_{eu} climatology.

The cloud fraction climatology appears to present maximum cloud cover ($\approx 100\%$) as a zonal band, generally seaward of the ice-edge and trailing the position of the polar front. Over the ocean, the region east of South America has the least cloud cover, which coincides with the region with highest [Chl-a] and shallowest Z_{eu} . This is also true for South Island of New Zealand and Tasmania, with the same combination of lowest cloud fraction, shallowest Z_{eu} and highest [Chl-a]. Within the ACC, The skies above South Georgia and Kerguelen also show lower cloud cover, higher [Chl-a] and shallower Z_{eu} (relative to the surrounding area), but to a substantially lesser degree. Interestingly, there appears to be a condensed region of high cloud cover over the Antarctic continent in the October climatology.

6.3.1.2 *November*

Specifically, along the Malvinas/ Falkland Current and around Kerguelen, South Georgia, New Zealand and Tasmania, climatological patterns of low cloud cover, high [Chl-a] and shallow Z_{eu} , remain largely unchanged between October and November. Along the Humboldt Current Large Marine Ecosystem, one of the most important upwelling regimes, signals in the [Chl-a] and Z_{eu} climatologies also reinforce one another, but cloud fraction remains as high as $\approx 90\%$.

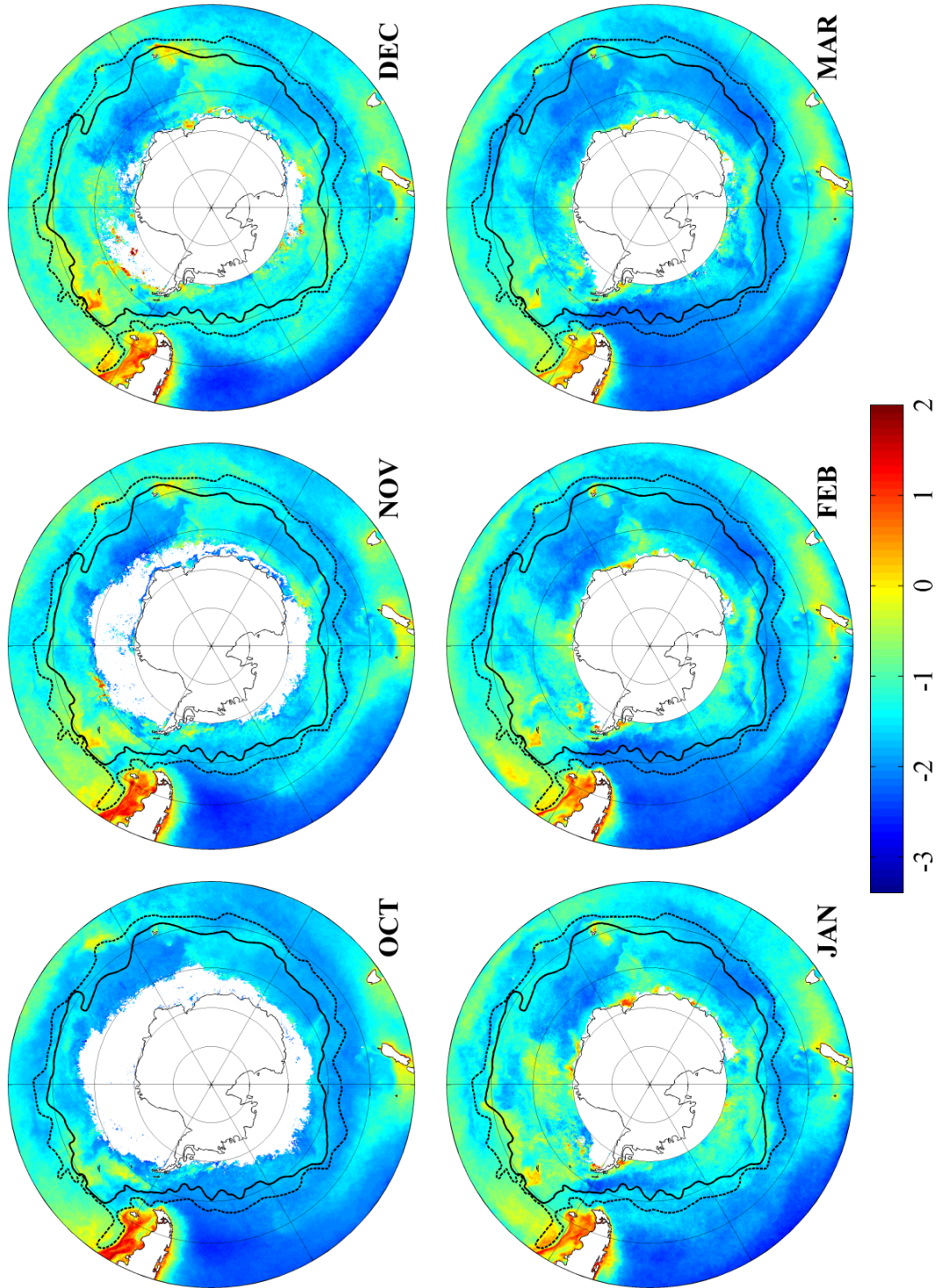


Figure 75: Mean log-transformed Chl-a (climatology) for each summer month, calculated using 12 years (January 2003 - December 2017) of MODIS Chl-a.

Black contours represent the mean positions of the Sub Antarctic Front (SAF) and the Polar Front (PF), as calculated by Orsi and Harris (2014).

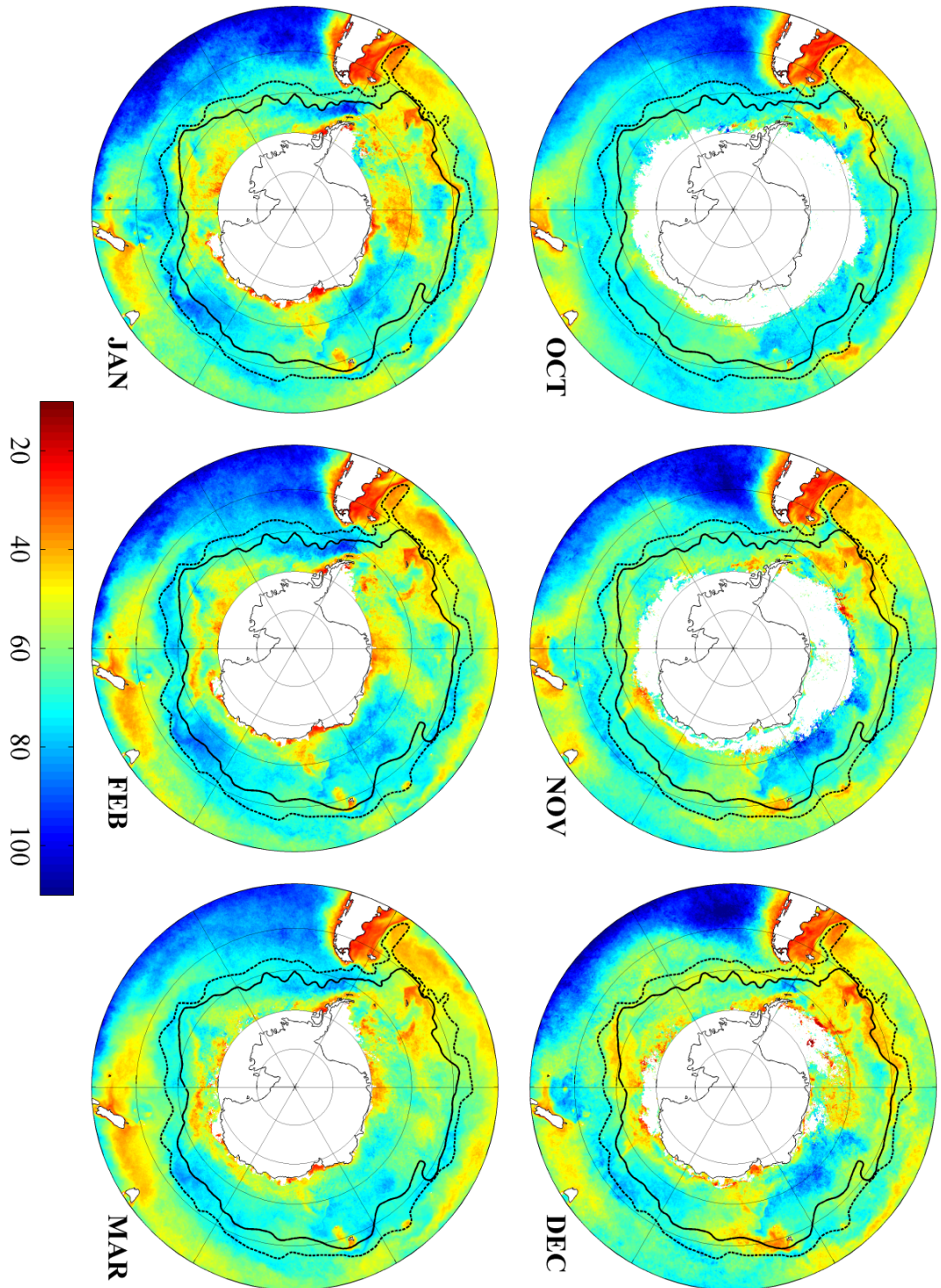


Figure 76: Mean Z_{eu} (climatology) for each summer month, calculated using 12 years (January 2003 - December 2017) of MODIS Lee Z_{eu} . Black contours represent the mean positions of the Sub Antarctic Front (SAF) and the Polar Front (PF), as calculated by Orsi and Harris (2014).

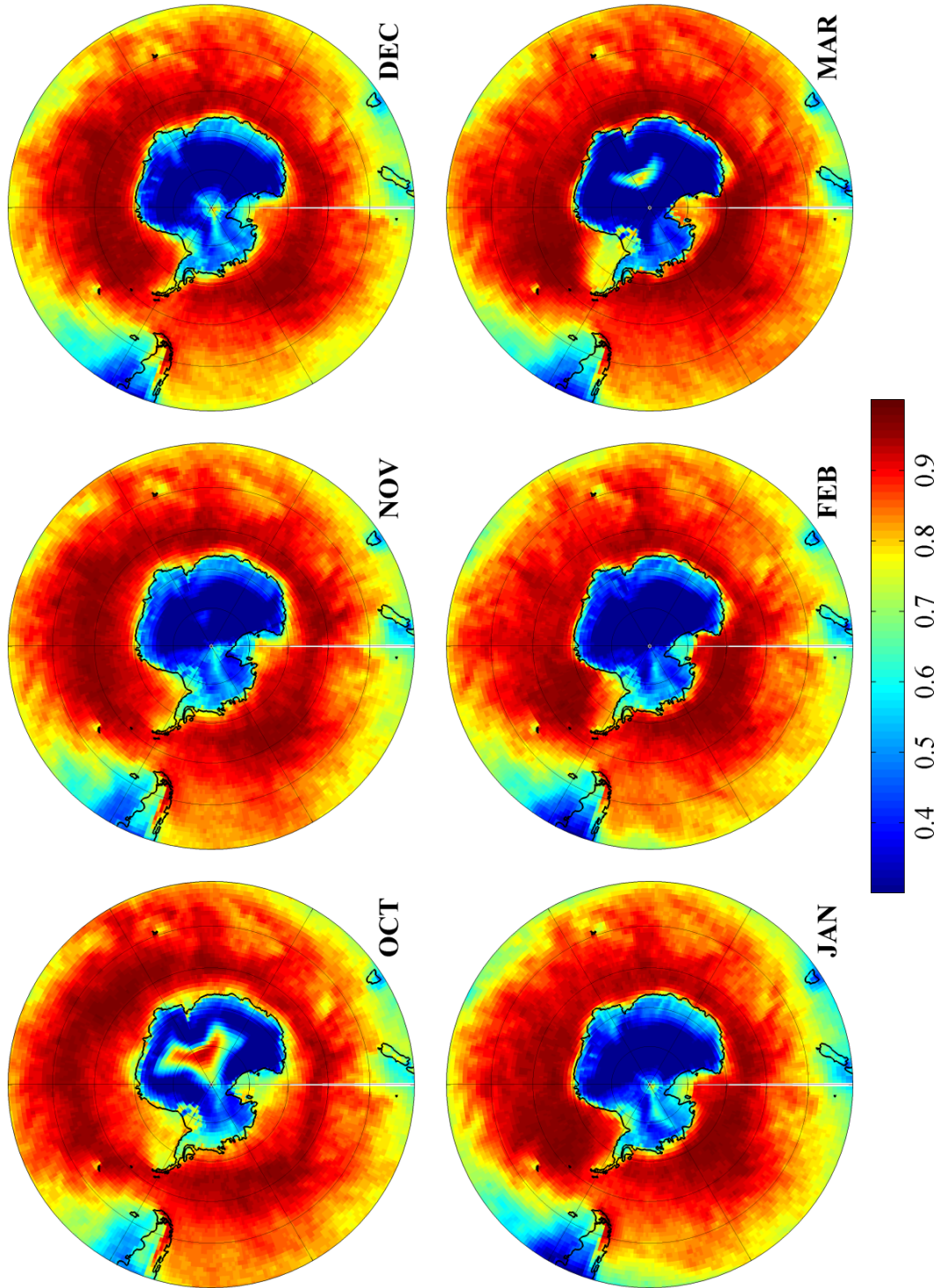


Figure 77: Mean cloud cover eye of Sauron (climatology) for each summer month, calculated using 12 years of MODIS cloud fraction data (January 2003 - December 2017).

In general, November sees relatively stronger signals of elevated [Chl-a] downstream of the South-west Indian Ridge (SWIR) and Kerguelen Island (Indian Ocean sector), extending along the continental ice-edge into the Pacific Ocean sector. These patterns are reinforced in the Z_{eu} climatology but with relatively stronger signals in some regions, particularly downstream of the Drake Passage and along the ice edge.

The climatology of cloud cover is noticeably different between October and November. Highest cloud fraction ($\approx 100\%$) has appeared to expand with the retreat and possible decay of the ice edge along the Bellingshausen side of the Western Antarctic Peninsula (WAP) and the Atlantic section bordering the Weddell Sea. The region of high cloud cover over the Antarctic continent seen in October is also absent from the November climatology.

6.3.1.3 December

Signals that were building in the October and November climatologies are now quite strong. For example, in the [Chl-a] data, elevated values that were seen around South Georgia in the October and November climatologies now appear as a distinct bloom. Furthermore, patches along the melting ice edge north of the Weddell Sea appear to be blooming, but a combination of (disintegrating) ice and extensive cloud cover prevents clear visualization. In the Z_{eu} data, the signals are stronger and clearer in both cases. This is especially useful along the Weddell Sea ice edge, where shoaling depths reinforce 'hints' that a substantial phytoplankton bloom has built up beneath and along the ice. Within both the [Chl-a] and Z_{eu} climatologies, these elevated signals extend downstream towards the ice-free open waters of the Atlantic and Indian sectors. In the November climatology, however, this vast 'downstream region' was still largely covered by ice.

For the rest of the continental ice edge, elevated [Chl-a] and shallow Z_{eu} are patchy but generally zonal. Strong signals persist around Kerguelen but the region of high [Chl-a] and shallow Z_{eu} downstream of the SWIR appears to have disappeared in the December climatology. Along the Polar Front (PF) at the Ross Sea, elevated [Chl-a] appears to be forming in a distinct band, which is reinforced by shallower measures of Z_{eu} in the same area.

Within the 'bud' of the SAF that bulges up and along the Malvinas/ Falkland Current, there now appears to be a region of slightly elevated [Chl-a] and shallower Z_{eu} . This area is also characterized by continually cloud-free skies. The combination

of low cloud cover, high [Chl-a] and shallow Z_{eu} also remains true for the Malvinas/ Falkland Current and South Georgia, as well as Kerguelen and the areas around Tasmania. However, while signals in the [Chl-a] and Z_{eu} climatologies are waning in these specific regions, the associated low cloud fractions appear to have dropped even further.

Overall, despite highest cloud fraction (coverage $\approx 100\%$) appearing to 'spread out' over the increasingly ice free waters around the Antarctic continent, higher cloud fraction values simultaneously appear to be 'contracting' towards higher latitudes. In other words, the latitudes north of $\approx 50^\circ\text{S}$ appear to be relatively less cloudy from around December (until around March).

6.3.1.4 *January*

In the [Chl-a] climatology for January, regions mostly show waning intensities. The exceptions to the overall drop in signal intensity include the vast open waters of the Atlantic and Indian sectors downstream of the Weddell Sea, the Amery Ice Shelf and the western WAP, as well as the section of the SAF that bulges up along the Malvinas/ Falkland Current. In these regions, [Chl-a] signals have intensified.

The overall drop in intensity in the [Chl-a] climatology for January is not perfectly reflected in the Z_{eu} climatology, which shows shoaling depths in a band extending around the Antarctic continent wherever there is data (southern limit of 70°S). However, the open waters of the Atlantic and Indian sectors downstream of the Weddell Sea, the western WAP, the Amery Ice Shelf and the SAF 'bulge' along the Malvinas/ Falkland Current are all highlighted by strong signals in the Z_{eu} climatology (depths shoal above $\approx 40\text{m}$), thereby reinforcing the [Chl-a] data.

Outside of the ACC, there are also divergences between the [Chl-a] and Z_{eu} climatologies. The former shows substantially lower levels along the Humboldt and Malvinas/ Falkland Currents, but the latter does not reflect such measurable changes. Cloud fraction remains low to the east of South America and very high to the west, with an overall continued contraction of highest coverage toward the highest latitudes. The most noticeable cumulative change in the cloud fraction climatology is that the zonal band of 100% coverage along the general position of the PF has gradually disintegrated. Indeed, by January, cloud fraction presents mostly as diffuse but high (between 80 - 90%) coverage over much of the Southern Ocean, with highest cloud cover over the Weddell Sea and Amundsen Sea.

At the Ross Sea along general positions of the PF, the band of elevated [Chl-a] and shallow Z_{eu} that was becoming noticeable in the December climatology is still apparent. From this region to the Antarctic continent, areas of elevated [Chl-a] and shallower Z_{eu} also extend towards the Amundsen Sea.

6.3.1.5 February

Overall, concentrations in the [Chl-a] climatology continue to show a drop in intensity. The region between Tasmania and New Zealand appears to be the exception outside of the ACC, and the band along the Ross Sea is the clear exception within the ACC. This band of elevated [Chl-a] is more distinct in the Z_{eu} climatology and appears to perhaps mirror the general position of the PF. With regards to cloud fraction, there is little apparent change between the January and February climatologies. Cloud cover is still highest over the Amundsen Sea and Weddell Sea, but there is some reduction along the WAP and over the Ronne Ice Shelf.

6.3.1.6 March

For March, waning intensities are evident in both the [Chl-a] and Z_{eu} climatologies. There are still regions proving to be exceptions to this; exhibiting relatively elevated [Chl-a] and shallow Z_{eu} . These regions include the open waters of the Atlantic and Indian sectors downstream of the Weddell Sea, the Amery Ice Shelf and the western WAP, as well as Kerguelen Island and South Georgia.

The cloud fraction climatology between the months of February to March is markedly different, with higher coverage again extending into the latitudes north of $\approx 50^\circ\text{S}$. For the first time in the six months of climatology data presented here, there appears to be substantially less cloud cover over the western side of the WAP and over the Ronne Ice Shelf. Lastly, a region of high cloud fraction ($\approx 60 - 70\%$) appears to have formed over the interior of the Antarctic continent itself, resembling land coverage last seen in the October climatology.

6.3.2 Trends in MODIS [Chl-a], Lee Z_{eu} and cloud fraction over time

On a summer month-by-month basis for the whole of the Southern Ocean, trends in [Chl-a] concentration, (mg m^{-3}), Z_{eu} (m) and coverage (%), are examined over the MODIS timeseries.

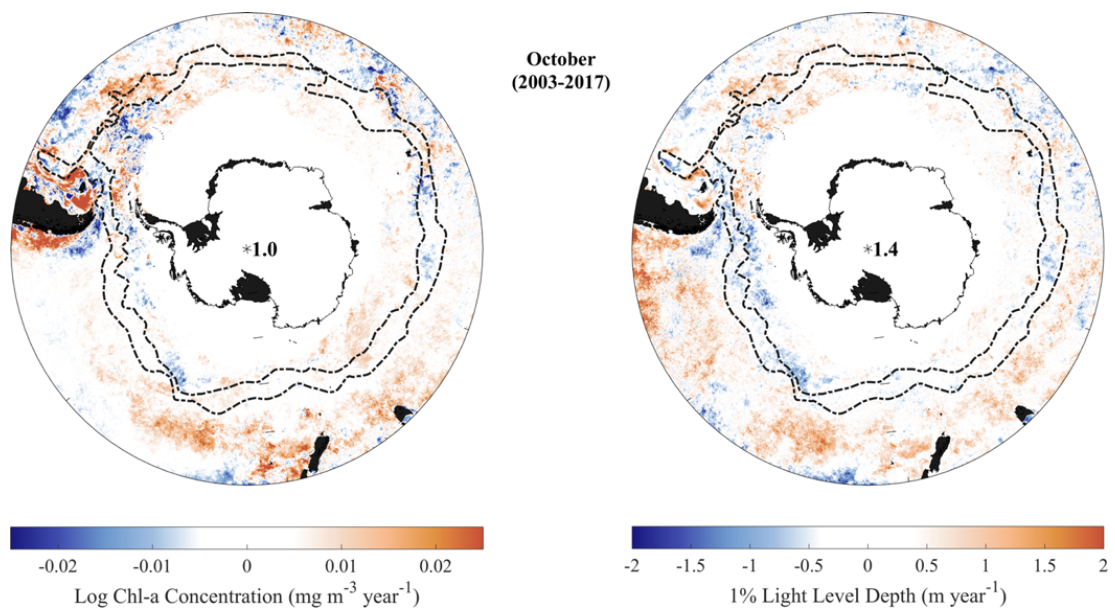


Figure 78: Changes to MODIS surface Chl-a concentration and vertical light attenuation for the month of October over the 13 year MODIS timeseries. Red represents increased Chl-a and an associated shallowing of Z_{eu} , Blue represents decreased Chl-a and an associated deepening of Z_{eu} . The ratio of increased Chl : decreased Chl-a and shallower Z_{eu} ; deeper Z_{eu} are reported in bold. Results point to an overall decrease in phytoplankton, but this is not matched by Z_{eu} , which shows an overall decrease in vertical light attenuation.

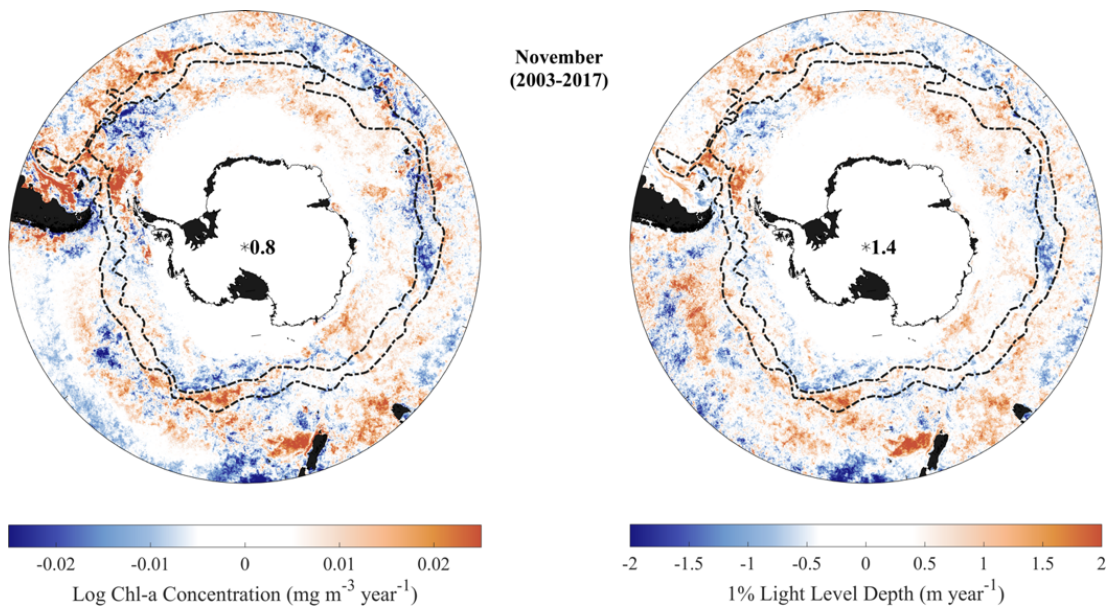


Figure 79: Changes to MODIS surface Chl-a concentration and vertical light attenuation for the month of November over the 13 year MODIS timeseries. Red represents increased Chl-a and an associated shallowing of Z_{eu} , Blue represents decreased Chl-a and an associated deepening of Z_{eu} . The ratio of increased Chl : decreased Chl-a and shallower Z_{eu} ; deeper Z_{eu} are reported in bold. Results point to an overall decrease in phytoplankton, but this is not matched by Z_{eu} , which shows an overall decrease in vertical light attenuation.

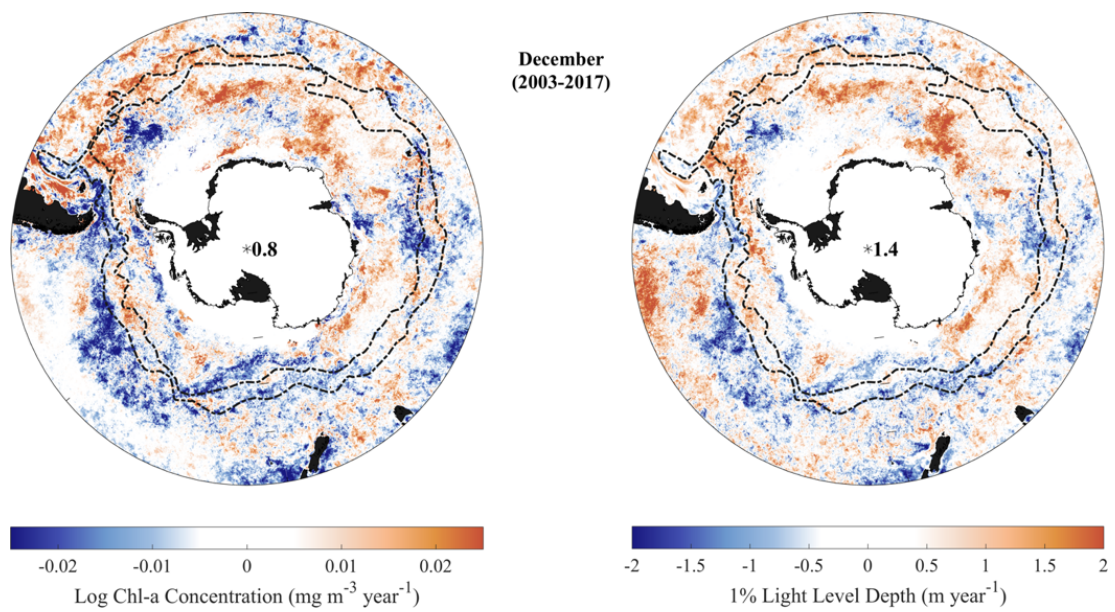


Figure 80: Changes to MODIS [Chl-a] and Lee Z_{eu} for the month of December over the 13 year MODIS timeseries. Red represents increase in Chl-a and an associated shallowing of vertical light attenuation, Blue represents decreased Chl-a and an associated deepening of Z_{eu} . The ratio of increased [Chl-a] : decreased [Chl-a], and shallower Z_{eu} ; deeper Z_{eu} are reported in bold. Spatially, patterns between [Chl-a] and Z_{eu} are similar, though results point to an overall decrease in phytoplankton (0.8) and overall shallowing of vertical light attenuation (1.6).

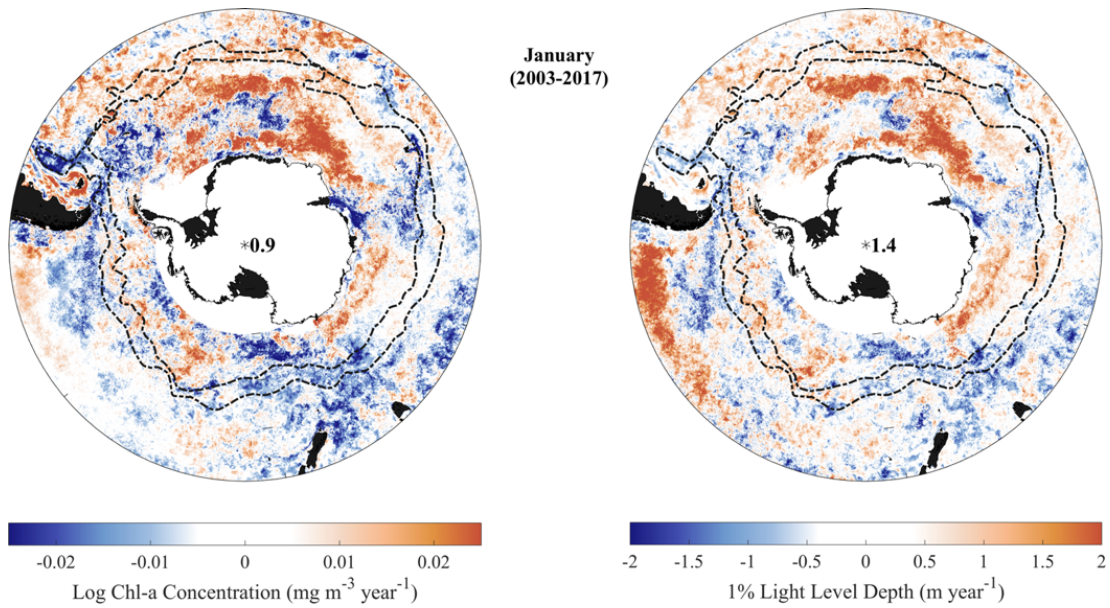


Figure 81: Changes to MODIS [Chl-a] and Lee Z_{eu} for the month of January over the 13 year MODIS timeseries. Red represents increase in Chl-a and an associated shallowing of vertical light attenuation, Blue represents decreased Chl-a and an associated deepening of Z_{eu} . The ratio of increased [Chl-a] : decreased [Chl-a], and shallower Z_{eu} ; deeper Z_{eu} are reported in bold. Spatially, patterns between [Chl-a] and Z_{eu} are similar.

Positive trends in [Chl-a] are shown in orange-red and suggest an increase in surface phytoplankton abundance over time. Negative trends in [Chl-a], which point to losses in surface phytoplankton abundance, are shown in blue. A negative trend in Z_{eu} suggests an increase in surface phytoplankton abundance (or an increase in suspended particles). For easier comparison with [Chl-a], the colorbar has been 'flipped' for Z_{eu} so that a negative trend here matches positive trends in [Chl-a]. In other words, for both ocean colour datasets, red points to increases in surface phytoplankton (or suspended materials) and blue suggests a loss (or clearer surface waters). Negative trends in cloud fraction are shown in blue-green and imply an overall reduction in mean cloud cover. A positive trend, which is shown in grey-black, suggests that there is an overall increase in mean cloud cover.

Overall, for trends to [Chl-a] and Z_{eu} , there appears to be little change over the month of October in the timeseries. Ratios of gain to loss are reported in bold in the centre of the plot. Cloud fraction appears to be in general decline over the Antarctic continent for this month of the timeseries but, interestingly, a trend of decrease in cloud fraction appears to match the trend of increased [Chl-a] and shallowing Z_{eu} upstream of Tasmania, as well as around South America and extending east to-

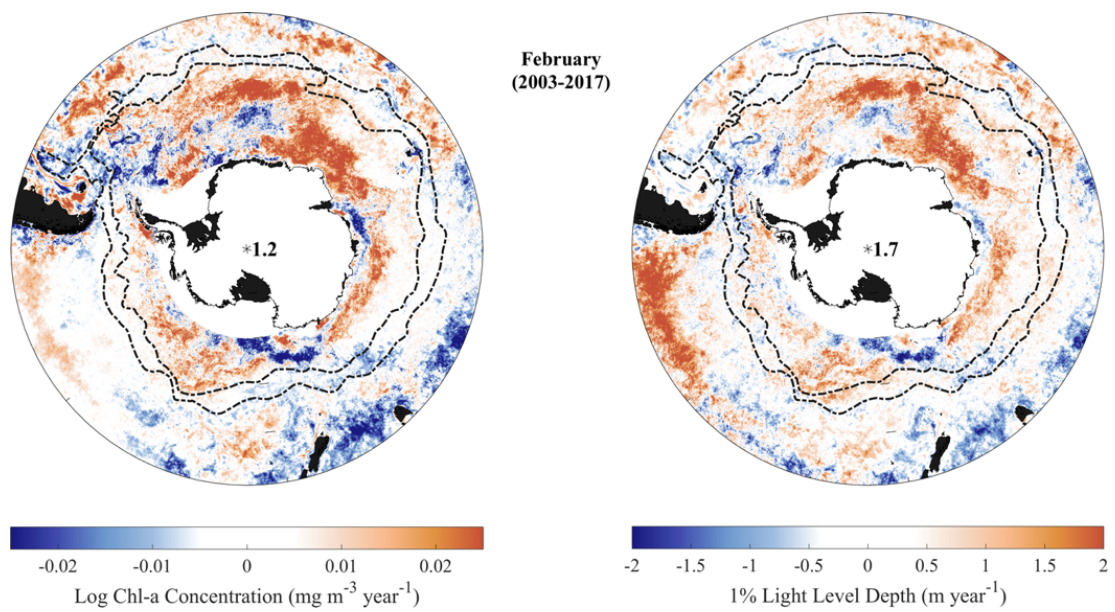


Figure 82: Changes to MODIS surface Chl-a concentration and vertical light attenuation for the month of February over the 13 year MODIS timeseries. Red represents increased Chl-a and an associated shallowing Z_{eu} , Blue represents decreased Chl-a and an associated deeper Z_{eu} . Ratios of increased Chl : decreased Chl-a and shallower Z_{eu} ; deeper Z_{eu} are reported in bold. Results point to a sign change in surface concentrations of phytoplankton, with changes suggesting an increase. Z_{eu} shows a stronger decline in vertical light attenuation.

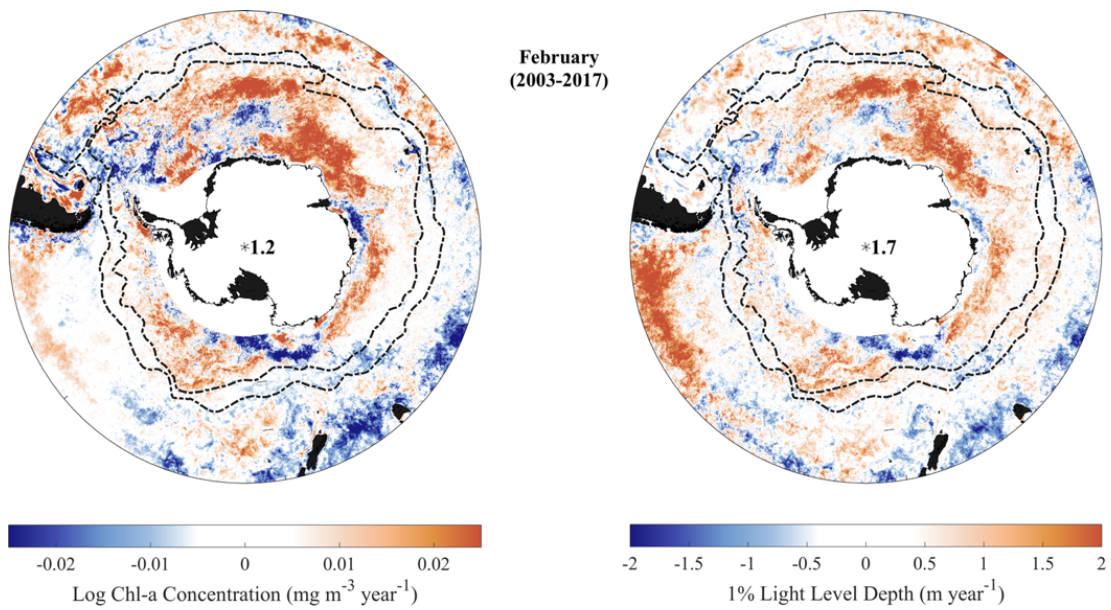


Figure 83: Changes to MODIS surface Chl-a concentration and vertical light attenuation for the month of March over the 13 year MODIS timeseries. Red represents increased Chl-a and an associated shallowing of Z_{eu} , Blue represents decreased Chl-a and an associated deepening of Z_{eu} . The ratio of increased Chl : decreased Chl-a and shallower Z_{eu} ; deeper Z_{eu} are reported in bold. Results point to an overall decrease in phytoplankton, but this is not matched by Z_{eu} , which shows an overall decrease in vertical light attenuation.

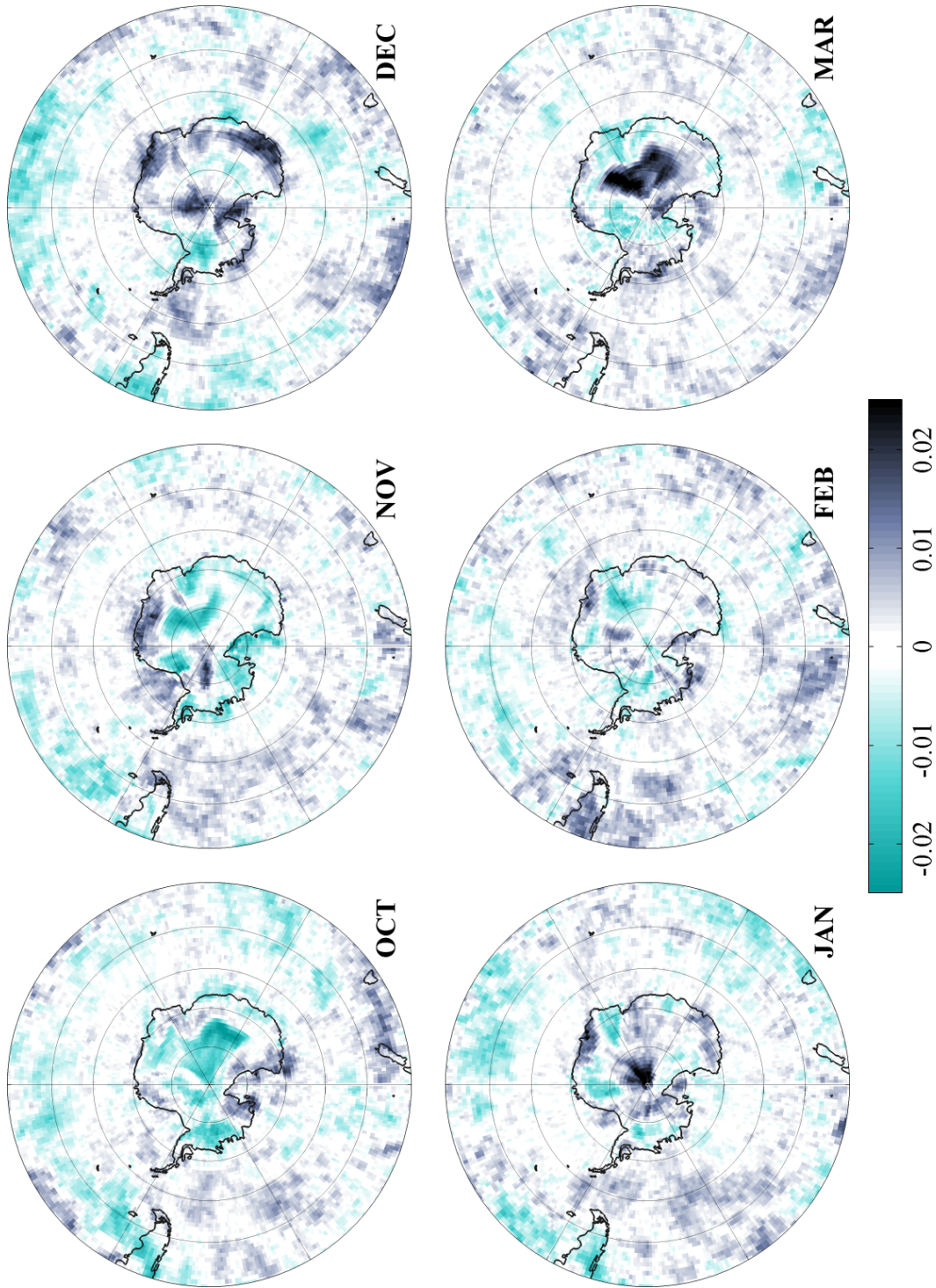


Figure 84: Trends in MODIS cloud fraction anomaly over 12 years (January 2003 - December 2017) for successive summer months. Positive trends (slope) in the anomaly are shown in black and suggest a possible increase in cloud cover. Conversely, negative trends (slope) in the anomaly are shown in green-blue and suggest a reduction in cloud fraction and a possible increase in light reaching the ocean surface. Landmasses are traced in black.

wards Kerguelen. For the month of November, there appears to be a slight decline in phytoplankton abundance and cloud. Z_{eu} remains unchanged from October, showing slight shallowing overall. By December, the ice has largely retreated to the continent but there is still a slight trend of decline in MODIS Chl-a, and Z_{eu} continues to show a slight shallowing in depth. Within the general positions of the PF, there appears to be increased cloud fraction at the Drake Passage and patches of coastal Antarctica, but decreased coverage over the Ronne and Shackleton Ice Shelves. The month of January in the timeseries shows more intense signals, but [Chl-a] and Z_{eu} remain largely unchanged from December. By February, however, [Chl-a] has changed sign to show moderate increases. Possibly in response, Z_{eu} is now exhibiting a strong change in depth. Shallowing is most pronounced at the ice edge south of the Polar Front, which matches strong signals in [Chl-a], but also upstream of Patagonia, Chile. Here, moderate changes to [Chl-a] have either had a disproportionate impact on light attenuation, or other factors are influencing optical properties of the water. Trends in cloud cover over the area upstream of Patagonia are quite pronounced, but are increasingly patchy otherwise.

For more regional analysis of changes to [Chl-a] and Z_{eu} over time, based largely on the Buiron et al. (2012) delineations, the Southern Ocean was divided into five sectors. Namely: the Drake Passage Sector (75W – 15E), Indian sector A (15E - 75E), Indian sector B (75E – 160E), a Ross Sea West Pacific sector (160E - 150W) and, lastly, the East Pacific sector (150W - 75W). Furthermore, because December, January and February exhibited the most intense trends in [Chl-a] and Z_{eu} over the timeseries, only these months are examined on regional scales.

6.3.3 *Anomalies in MODIS [Chl-a], Lee Z_{eu} and cloud fraction relative to the SAM*

Focusing specifically on anomalies in [Chl-a], Z_{eu} and cloud fraction over the 13-year period, only statistically significant ($p < 0.05$) results from the regression to the SAM are plotted (Figs. Fig. ??, Fig. ?? and Fig. 84 respectively). For [Chl-a] and Z_{eu} , red suggests an increase in phytoplankton abundance (or suspended particles) in surface waters, relative to the SAM. On the other hand, blue suggests a loss of phytoplankton (or clearer surface waters) relative to the SAM. For cloud fraction, grey-black shows an increase in coverage relative to the SAM, while blue-green shows a decrease.

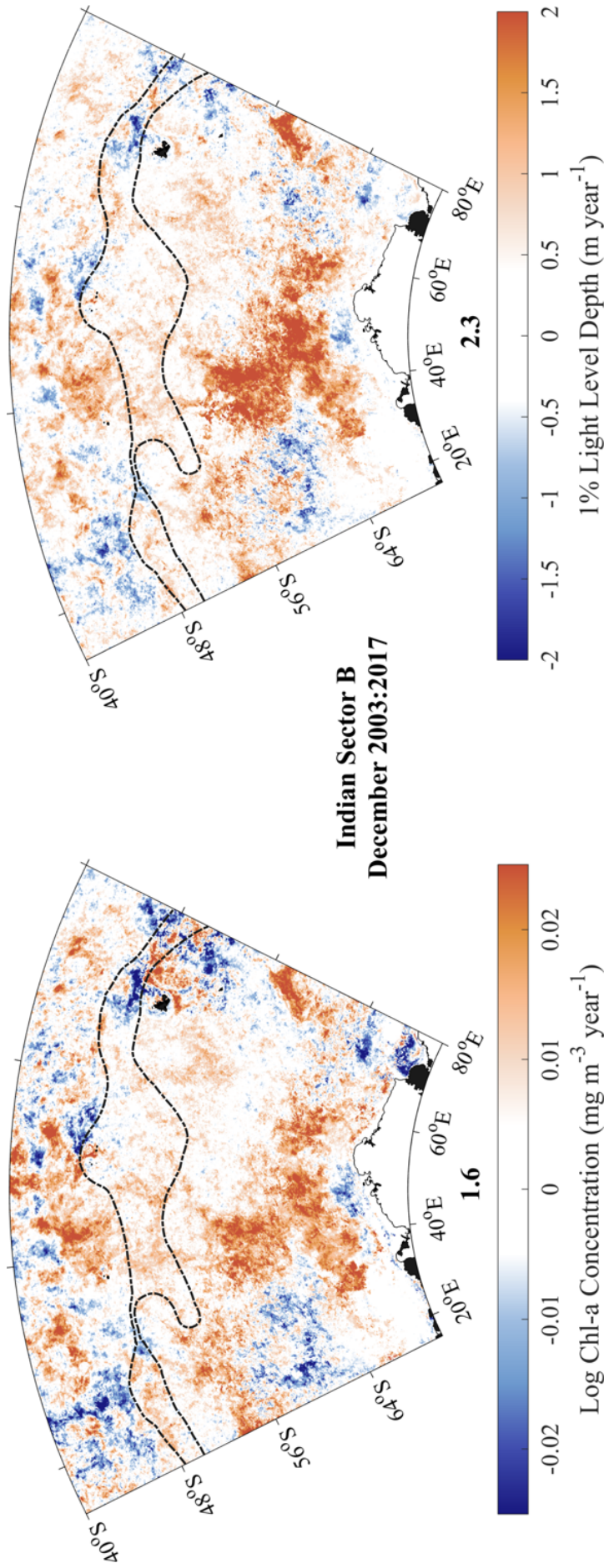


Figure 85: Indian sector A (15E - 80E) changes to surface Chl-a concentration and vertical light attenuation for the month of December over the 13-year MODIS time-series. Red represents an increased Chl-a with an associated shallowing of Z_{eu} . Blue represents decreased Chl-a with an associated deepening Z_{eu} . Ratios of [gain : loss] are reported in bold above the colourbar as [increased Chl : decreased Chl-a] and [shallower Z_{eu} ; deeper Z_{eu}], respectively. Values above 1.0 indicate increased Chl and shallower Z_{eu} (more pixels are red), and values less than 1.0 indicate decreased Chl-a and deeper Z_{eu} (more pixels are blue). Results for the Indian ocean sector A point to increases in surface concentrations of phytoplankton and a strong shallowing of vertical light attenuation.

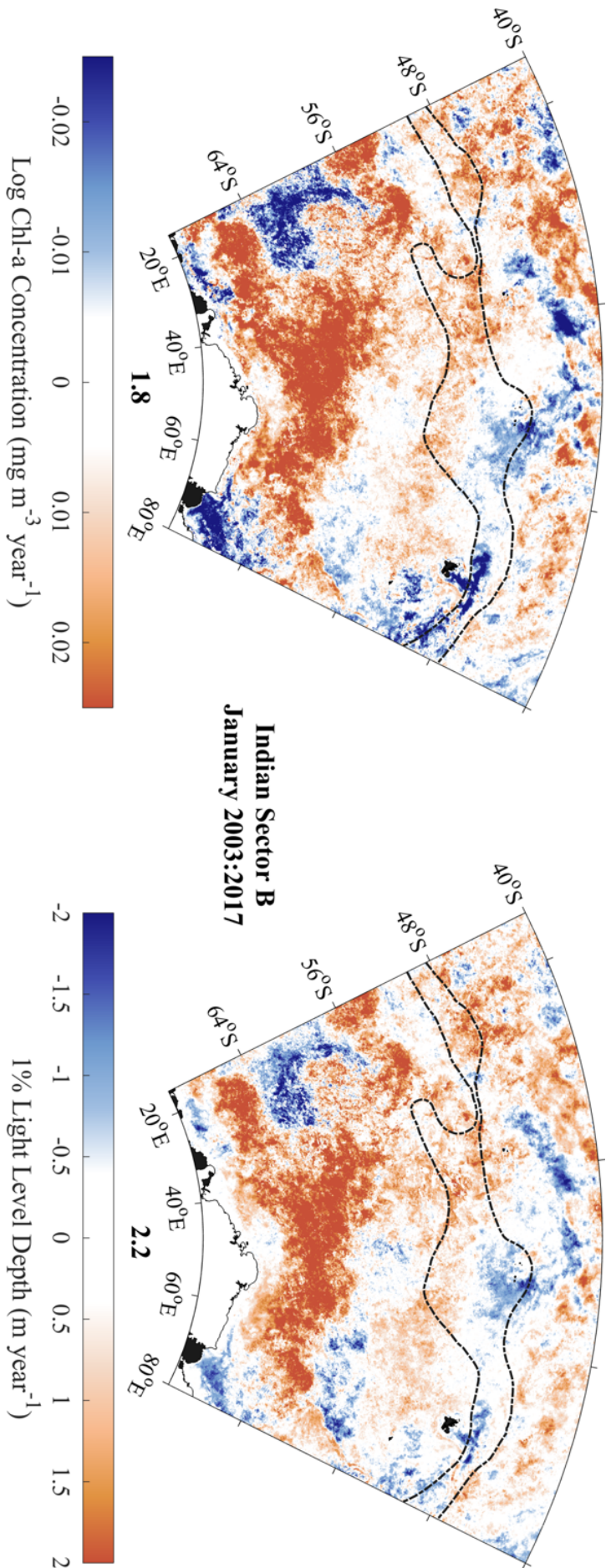


Figure 86: Indian sector A (15E - 80E) changes to surface Chl-a concentration and vertical light attenuation for the month of January over the 13-year MODIS time-series. Red represents an increased Chl-a with an associated shallowing of Z_{eu} . Blue represents decreased Chl-a with an associated deepening Z_{eu} . Ratios of [gain : loss] are reported in bold above the colourbar as [increased Chl : decreased Chl-a] and [shallower Z_{eu} ; deeper Z_{eu}], respectively. Values above 1.0 indicate increased Chl and shallower Z_{eu} (more pixels are red), and values less than 1.0 indicate decreased Chl-a and deeper Z_{eu} (more pixels are blue). Results for the Indian ocean sector A point to strong increases in surface concentrations of phytoplankton and a strong shallowing of vertical light attenuation.

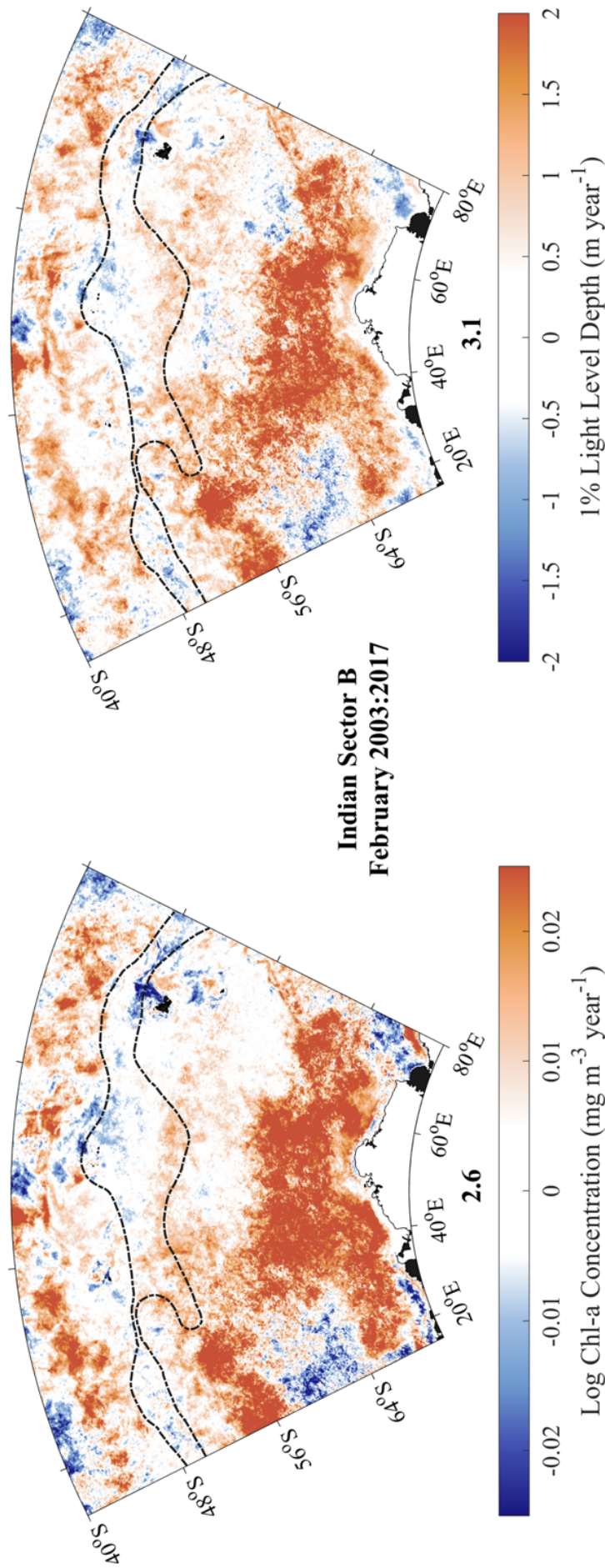


Figure 87: Indian sector A (15E - 80E) changes to surface Chl-a concentration and vertical light attenuation for the month of February over the 13-year MODIS time-series. Red represents an increased Chl-a with an associated shallowing of Z_{eu} . Blue represents decreased Chl-a with an associated deepening Z_{eu} . Ratios of [gain : loss] are reported in bold above the colourbar as [increased Chl : decreased Chl-a] and [shallower Z_{eu} ; deeper Z_{eu}], respectively. Values above 1.0 indicate increased Chl and shallower Z_{eu} (more pixels are red), and values less than 1.0 indicate decreased Chl-a and deeper Z_{eu} (more pixels are blue). Results for the Indian ocean sector A point to very strong increases in surface concentrations of phytoplankton and a very strong shallowing of vertical light attenuation.

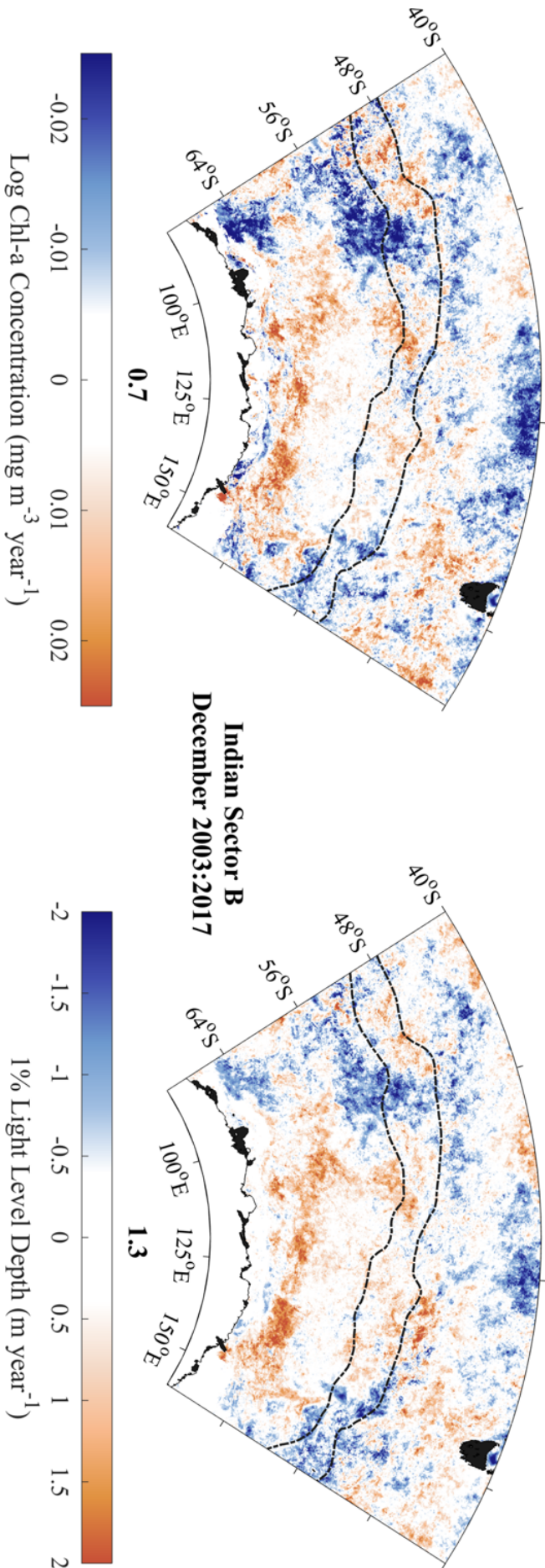


Figure 88: Indian sector B (80E - 160E) changes to surface Chl-a concentration and vertical light attenuation for the month of December over the 13-year MODIS time-series. Red represents an increased Chl-a with an associated shallowing of Z_{eu} . Blue represents decreased Chl-a with an associated deepening Z_{eu} . Ratios of [gain : loss] are reported in bold above the colourbar as [increased Chl : decreased Chl-a] and [shallower Z_{eu} : deeper Z_{eu}], respectively. Values above 1.0 indicate increased Chl and shallower Z_{eu} (more pixels are red), and values less than 1.0 indicate decreased Chl-a and deeper Z_{eu} (more pixels are blue). Results here point to a decrease in surface concentrations of phytoplankton but a modest shallowing of vertical light attenuation for the Indian ocean sector B.

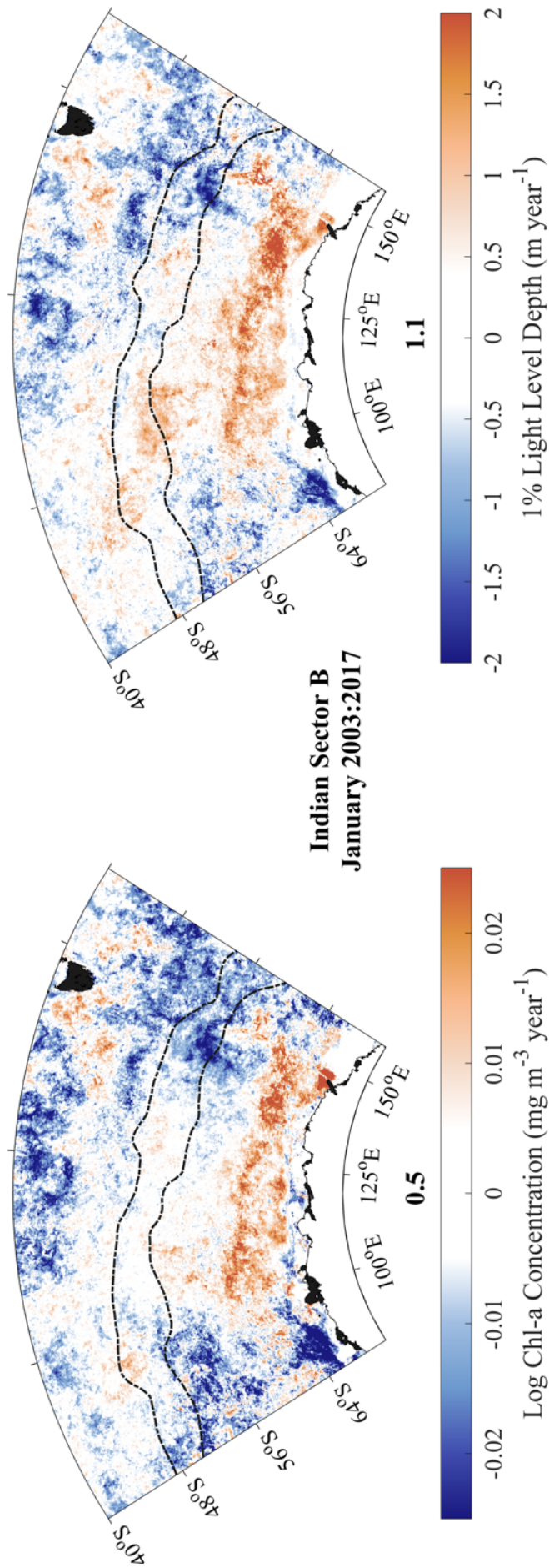


Figure 89: Indian sector B (80E - 160E) changes to surface Chl-a concentration and vertical light attenuation for the month of January over the 13-year MODIS time-series. Red represents an increased shallowing of Z_{eu} . Blue represents decreased Chl-a with an associated deepening Z_{eu} . Ratios of [gain : loss] are reported in bold above the colourbar as [increased Chl-a] and [shallower Z_{eu} ; deeper Z_{eu}], respectively. Values above 1.0 indicate increased Chl and shallower Z_{eu} (more pixels are red), and values less than 1.0 indicate decreased Chl-a and deeper Z_{eu} (more pixels are blue). Results here point to a substantial decrease in surface concentrations of phytoplankton and very little change in vertical light attenuation for the Indian ocean sector B.

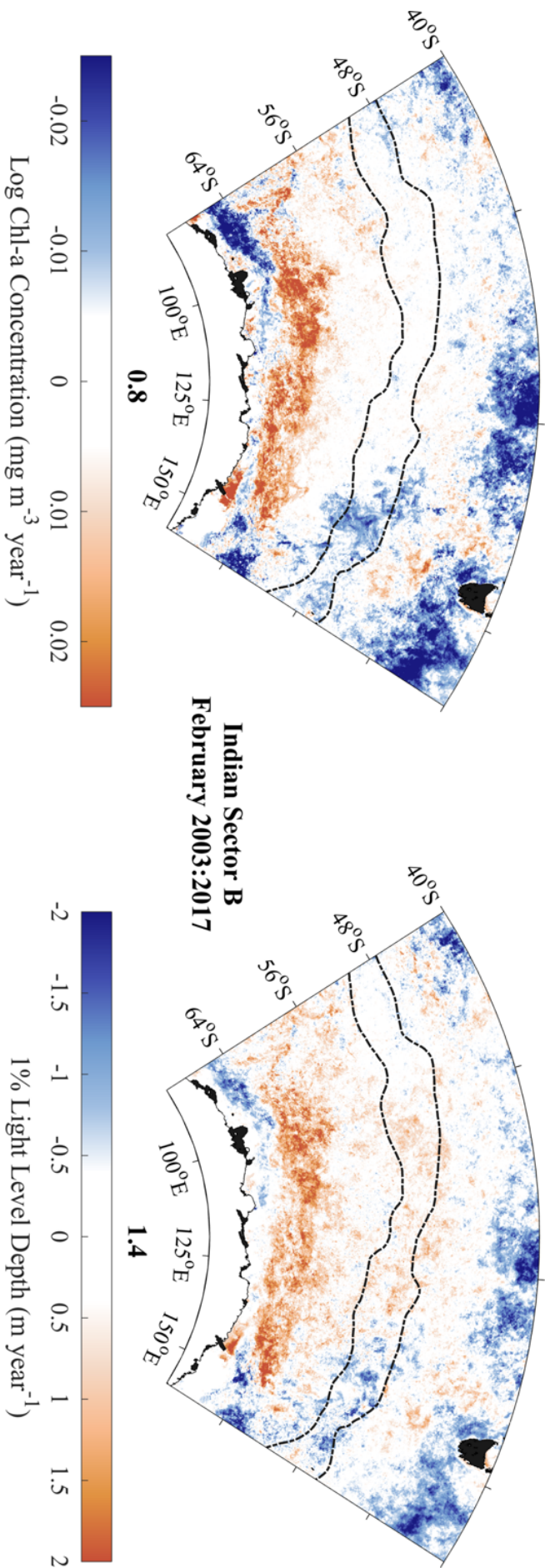


Figure 90: Indian sector B (80E - 160E) changes to surface Chl-a concentration and vertical light attenuation for the month of February over the 13-year MODIS time-series. Red represents an increased Chl-a with an associated shallowing of Z_{eu} , Blue represents decreased Chl-a with an associated deepening Z_{eu} . Ratios of [gain : loss] are reported in bold above the colourbar as [increased Chl : decreased Chl-a] and [shallower Z_{eu} : deeper Z_{eu}], respectively. Values above 1.0 indicate increased Chl and shallower Z_{eu} (more pixels are red), and values less than 1.0 indicate decreased Chl-a and deeper Z_{eu} (more pixels are blue). Results here point to a decline in surface concentrations of phytoplankton over this month, but a slight recovery from the strong loss seen in the month before. The associated shallowing of vertical light attenuation for the Indian ocean sector B appears to reflect this.

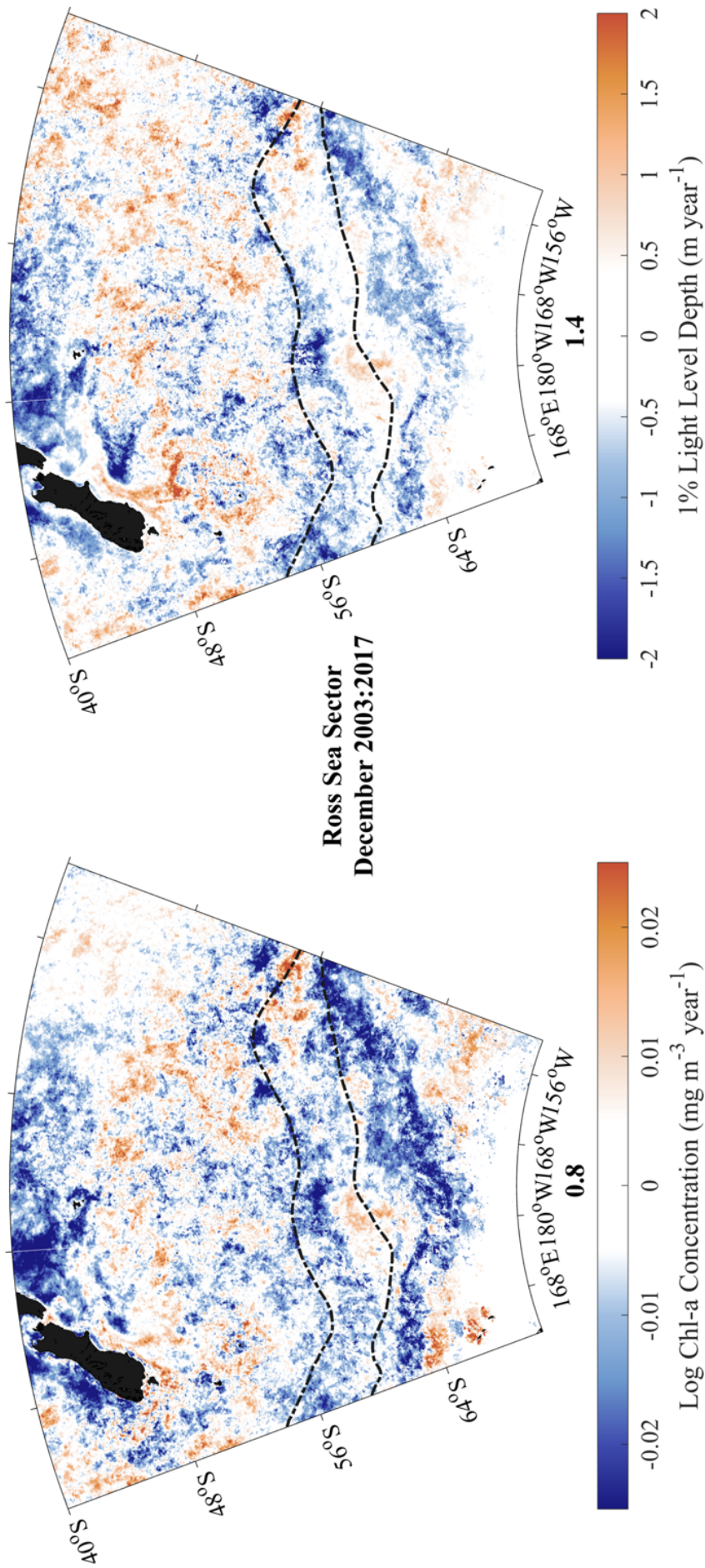


Figure 91: Ross Sea sector (160E - 150W) changes to surface Chl-a concentration and vertical light attenuation for the month of December over the 13-year MODIS time-series. Red represents an increased shallowing of Z_{eu} , Blue represents decreased Chl-a with an associated deepening Z_{eu} . Ratios of [gain : loss] are reported in bold above the colourbar as [increased Chl : decreased Chl-a] and [shallower Z_{eu} ; deeper Z_{eu}] respectively. Values above 1.0 indicate increased Chl and shallower Z_{eu} (more pixels are red), and values less than 1.0 indicate decreased Chl-a and deeper Z_{eu} (more pixels are blue). Results here point to a decrease in surface concentrations of phytoplankton but a modest shallowing of vertical light attenuation over all Decembers in the timeseries.

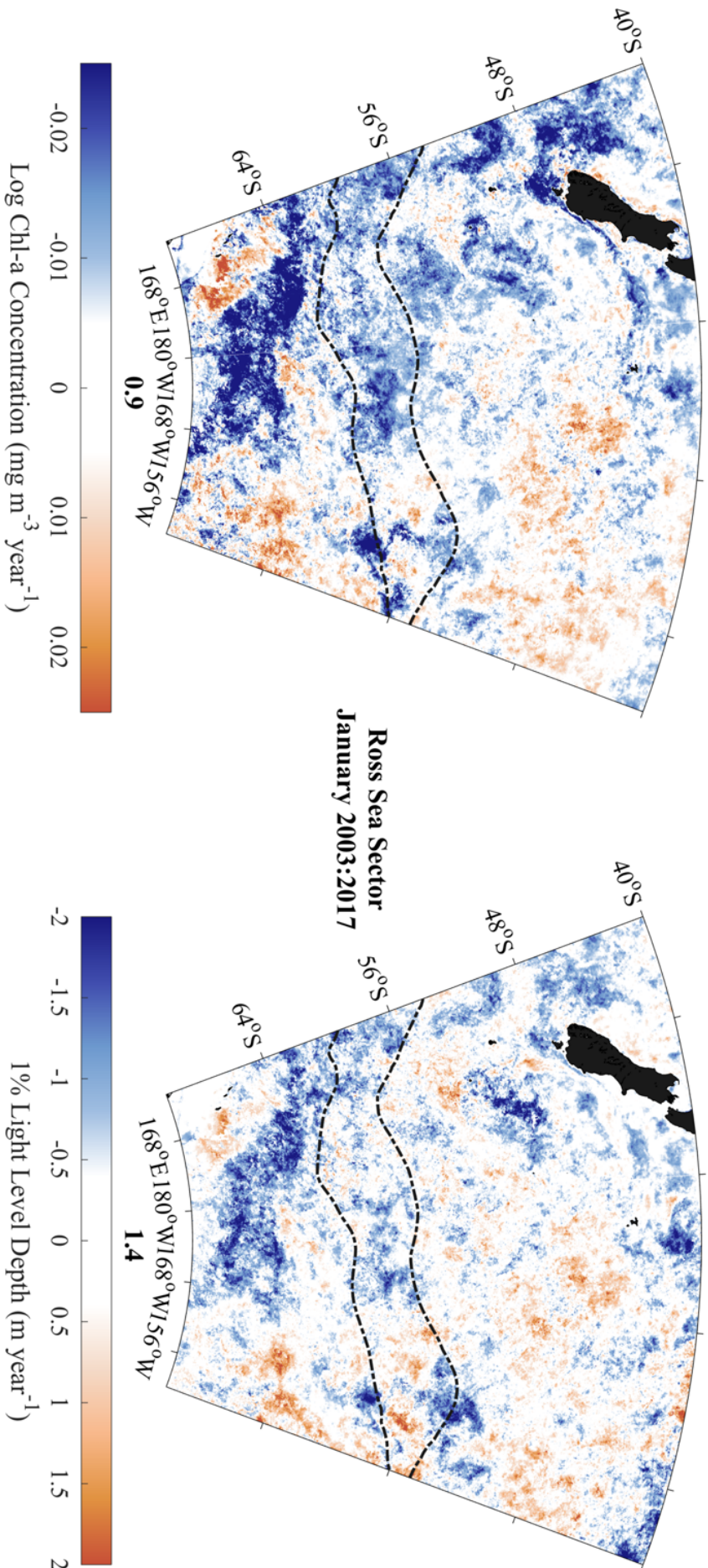


Figure 92: Ross Sea sector (160E - 150W) changes to surface Chl-a concentration and vertical light attenuation for the month of December over the 13-year MODIS time-series. Red represents an increased Chl-a with an associated shallowing of Z_{eu} . Blue represents decreased Chl-a with an associated deepening Z_{eu} . Ratios of [gain : loss] are reported in bold above the colourbar as [increased Chl : decreased Chl-a] and [shallower Z_{eu} : deeper Z_{eu}], respectively. Values above 1.0 indicate increased Chl and shallower Z_{eu} (more pixels are red), and values less than 1.0 indicate decreased Chl-a and deeper Z_{eu} (more pixels are blue). Results here point to a very slight decline in surface concentrations of phytoplankton but a modest shallowing of vertical light attenuation over all Januaries in the timeseries.

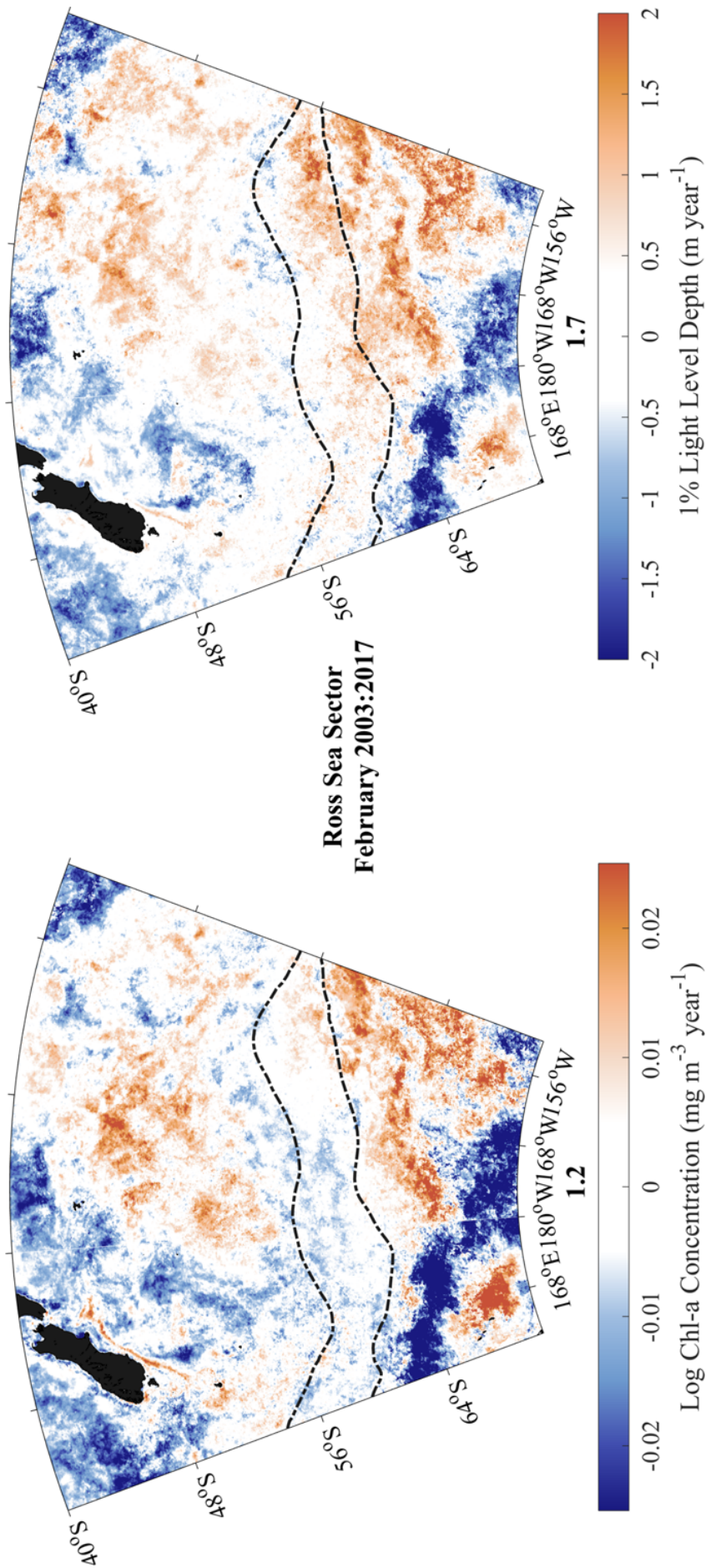


Figure 93: Ross Sea sector (160E - 150W) changes to surface Chl-a concentration and vertical light attenuation for the month of December over the 13-year MODIS time-series. Red represents an increased shallowing of Z_{eu} , Blue represents decreased Chl-a with an associated deepening Z_{eu} . Ratios of [gain : loss] are reported in bold above the colourbar as [increased Chl : decreased Chl-a] and [shallower Z_{eu} ; deeper Z_{eu}] respectively. Values above 1.0 indicate increased Chl and shallower Z_{eu} (more pixels are red), and values less than 1.0 indicate decreased Chl-a and deeper Z_{eu} (more pixels are blue). Results here point to a recovery and slight increase in surface concentrations of phytoplankton, with an associated shallowing of vertical light attenuation over all Februaries in the timeseries.

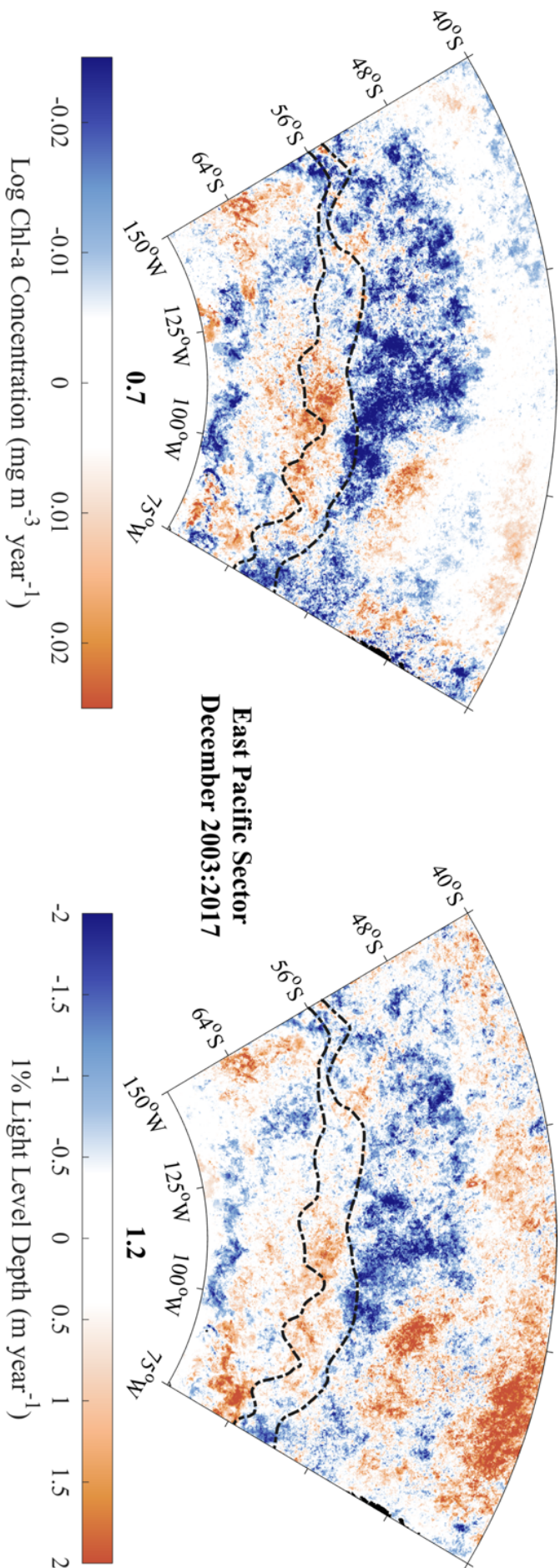


Figure 94: East Pacific Sector (75W – 150W) changes to surface Chl-a concentration and vertical light attenuation for the month of December over the 13-year MODIS time-series. Red represents increased Chl-a with an associated shallowing of Z_{eu} . Blue represents decreased Chl-a with an associated deepening Z_{eu} . Ratios of [red : blue] are reported in bold above the colourbar as [Chl gain : Chl loss] and [shallower Z_{eu} ; deeper Z_{eu}], respectively. Values above 1.0 indicate increased Chl and shallower Z_{eu} (more pixels are red), and values less than 1.0 indicate decreased Chl-a and deeper Z_{eu} (more pixels are blue). Results for the East Pacific Sector over the last 13 years point to a reduction in surface concentrations of phytoplankton but a slight shallowing of vertical light attenuation.

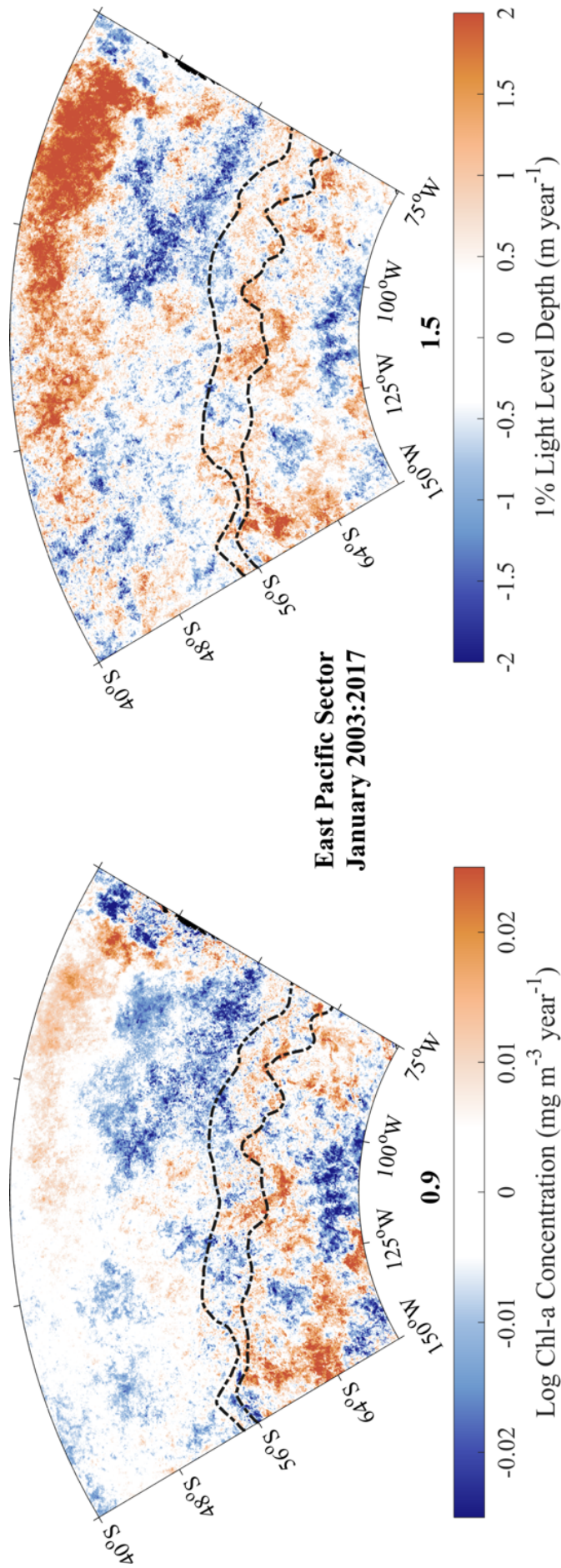


Figure 95: East Pacific Sector (75W – 150W) changes to surface Chl-a concentration and vertical light attenuation for the month of January over the 13-year MODIS time-series. Red represents increased Chl-a with an associated shallowing of Z_{eu} , Blue represents decreased Chl-a with an associated deepening Z_{eu} . Ratios of [red : blue] are reported in bold above the colourbar as [Chl gain : Chl-a loss] and [shallower Z_{eu} ; deeper Z_{eu}], respectively. Values above 1.0 indicate increased Chl and shallower Z_{eu} (more pixels are red), and values less than 1.0 indicate decreased Chl-a and deeper Z_{eu} (more pixels are blue). Results for the East Pacific Sector over the last 13 years point to a small decrease in surface concentrations of phytoplankton, but increases to vertical light attenuation during the month of January. Although well north of the ACC, changes are very interesting along 40S, where moderate increases in [Chl-a] have generated a very strong shallowing of the 1% light level.

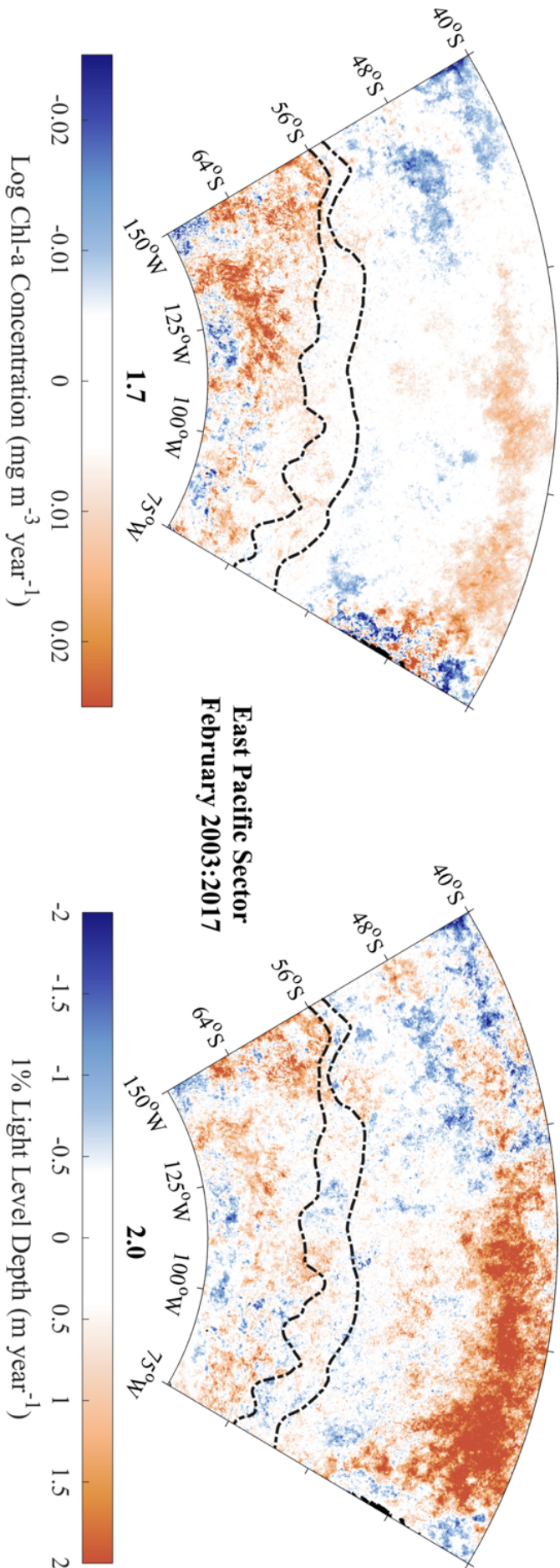


Figure 96: East Pacific Sector ($75^{\circ}\text{W} - 150^{\circ}\text{W}$) changes to surface Chl-a concentration and vertical light attenuation for the month of February over the 13-year MODIS time-series. Red represents increased Chl-a with an associated shallowing of Z_{eu} . Blue represents decreased Chl-a with an associated deepening Z_{eu} . Ratios of [red : blue] are reported in bold above the colourbar as [Chl gain : Chl loss] and [shallower Z_{eu} ; deeper Z_{eu}], respectively. Values above 1.0 indicate increased Chl and shallower Z_{eu} (more pixels are red), and values less than 1.0 indicate decreased Chl-a and deeper Z_{eu} (more pixels are blue). Results for the East Pacific Sector over the last 13 years point to a strong increase in surface concentrations of phytoplankton, with associated increases to vertical light attenuation during the month of February. Changes along 40°S continue to be noteworthy, where increased [Chl-a] has generated a very strong shallowing of the 1% light level.

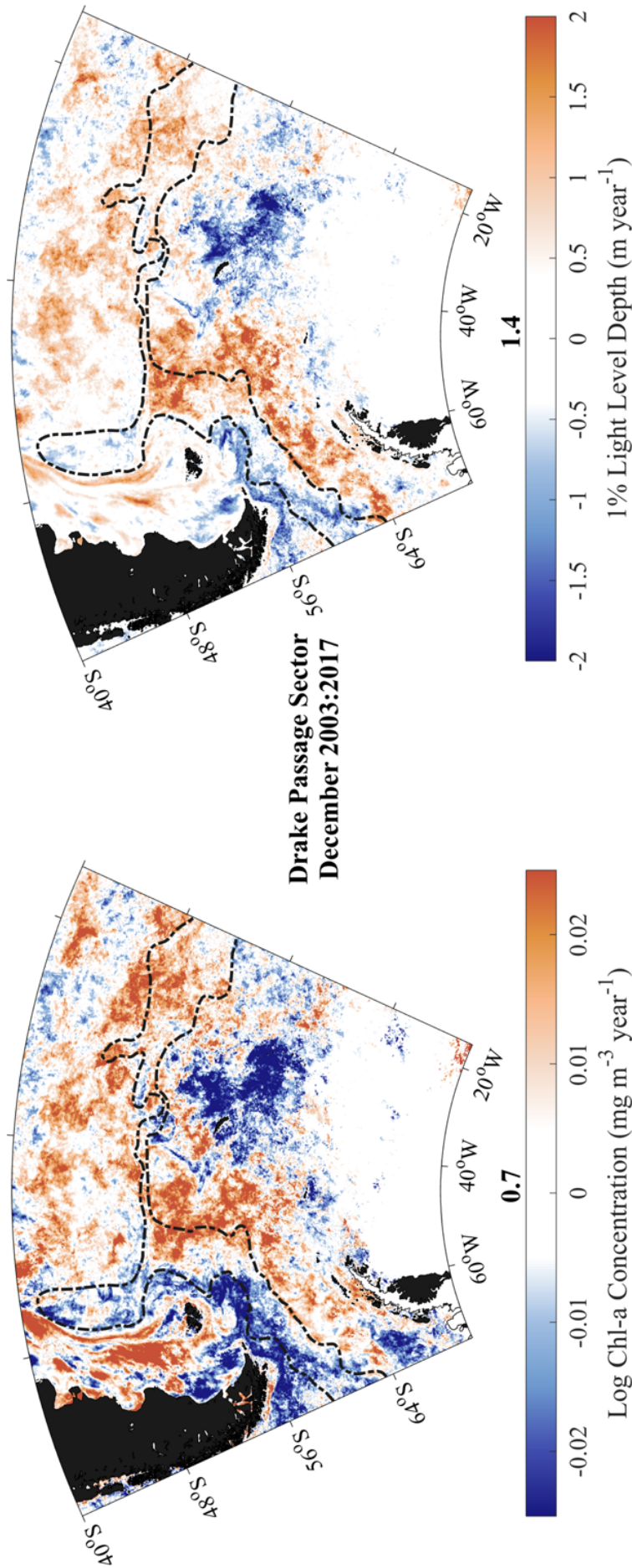


Figure 97: Drake Passage Sector (75W - 15E) changes to surface Chl-a concentration and vertical light attenuation for the month of December over the 13-year MODIS time-series. Red represents increased Chl-a with an associated shallowing of Z_{eu} , Blue represents decreased Chl-a with an associated deepening Z_{eu} . Ratios of [red : blue] are reported in bold above the colourbar as [Chl gain : Chl-a loss] and [shallower Z_{eu} ; deeper Z_{eu}], respectively. Values above 1.0 indicate increased Chl and shallower Z_{eu} (more pixels are red), and values less than 1.0 indicate decreased Chl-a and deeper Z_{eu} (more pixels are blue). Results for Atlantic Sector over the last 13 years point to decreases in surface concentrations of phytoplankton and a shallowing of vertical light attenuation during the month of December.

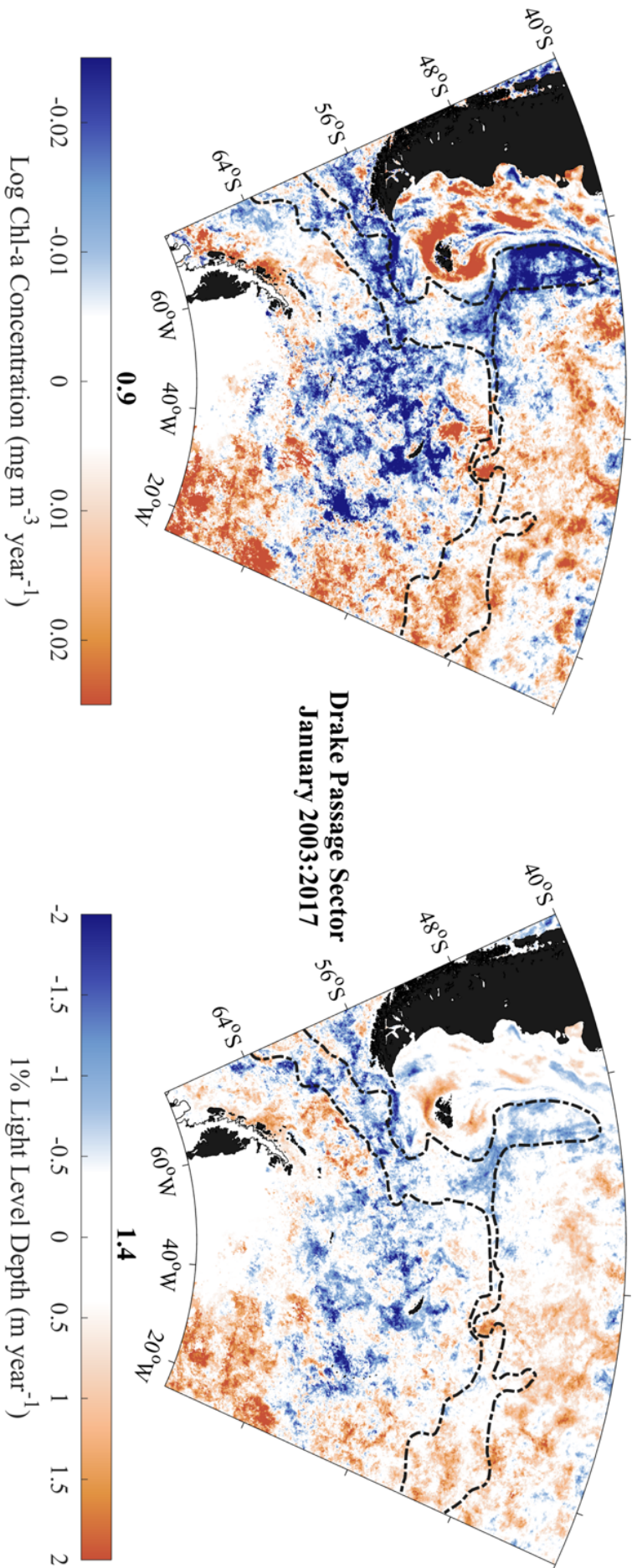


Figure 98: Drake Passage Sector ($75^{\circ}\text{W} - 15^{\circ}\text{E}$) changes to surface Chl-a concentration and vertical light attenuation for the month of January over the 13-year MODIS time-series. Red represents increased Chl-a with an associated shallowing of Z_{eu} . Blue represents decreased Chl-a with an associated deepening Z_{eu} . Ratios of [red : blue] are reported in bold above the colourbar as [Chl gain : Chl loss] and [shallower Z_{eu} ; deeper Z_{eu}], respectively. Values above 1.0 indicate increased Chl and shallower Z_{eu} (more pixels are red), and values less than 1.0 indicate decreased Chl-a and deeper Z_{eu} (more pixels are blue). Results for Atlantic Sector over the last 13 years point to a minor decrease in surface concentrations of phytoplankton and a shallowing of vertical light attenuation during the month of January.

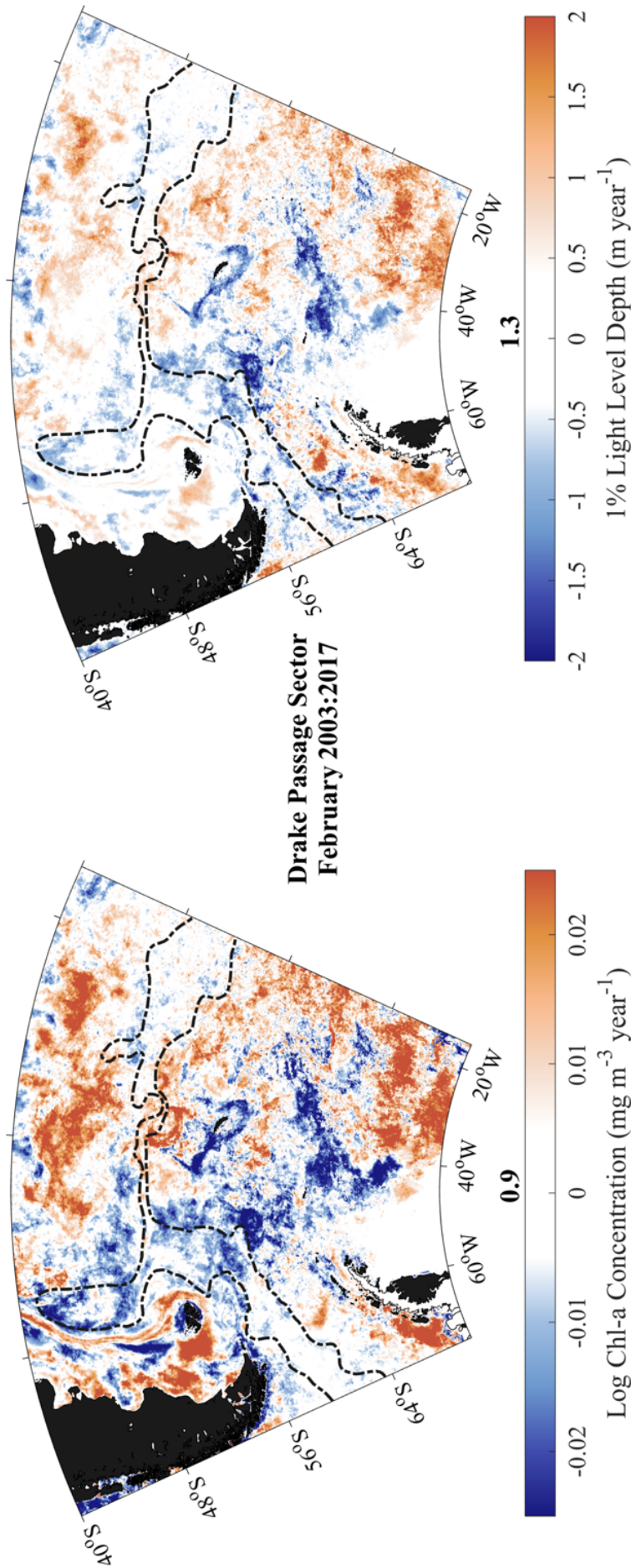


Figure 99: Drake Passage Sector (75W - 15E) changes to surface Chl-a concentration and vertical light attenuation for the month of January over the 13-year MODIS time-series. Red represents increased Chl-a with an associated shallowing of Z_{eu} , Blue represents decreased Chl-a with an associated deepening Z_{eu} . Ratios of [red : blue] are reported in bold above the colourbar as [Chl gain : Chl loss] and [shallower Z_{eu} ; deeper Z_{eu}], respectively. Values above 1.0 indicate increased Chl and shallower Z_{eu} (more pixels are red), and values less than 1.0 indicate decreased Chl-a and deeper Z_{eu} (more pixels are blue). Results for Atlantic Sector over the last 13 years point to little overall change in surface concentrations of phytoplankton and vertical light attenuation during the month of February.

6.3.3.1 December

Examining the resulting R-values, changes in concentration (mg m^{-3}), depth (m) and coverage (%) that correlate to changes in the SAM generally appear to be patchy and/or regional rather than clearly zonal. Spatial patterns from the [Chl-a]-SAM regression are largely mirrored by the Z_{eu} -SAM results. For example, downstream of the Drake Passage and the Falklands, where the general position of the PF steers north, both [Chl-a] and Z_{eu} regressions show strongly significant results, suggesting that positive trends in phytoplankton abundance here may be driven by changes in the SAM. Indeed, for Decembers in the timeseries, this area showed positive trends in [Chl-a] and negative trends in Z_{eu} in the previous analysis (Fig. 75 and Fig. 76, respectively).

In some patches, the Z_{eu} -SAM regression results in stronger signals that are also more spatially distinct. Revisiting the December months in Fig. 75 and Fig. 76, a weakly positive trend in [Chl-a] but distinctly negative trend in Z_{eu} extended across the Pacific to the South American continent. The results from the Z_{eu} -SAM regression appear to match this trend in space and time, but the results from [Chl-a]-SAM regression are again patchier and less intense. Combining these results from the [Chl-a]-SAM and the Z_{eu} -SAM regression, it is perhaps possible to attribute this patchy band as elevated phytoplankton driven by changes in the SAM. However, Z_{eu} is ultimately a measure of water clarity and light attenuation, and can be used in conjunction with [Chl-a] as a proxy for phytoplankton in strictly Case-1 waters. This southern section of the Pacific Ocean is well outside of the ACC and may not conform to Case-1 assumptions. Thus, the results from the Z_{eu} -SAM regression may instead point to an increase in suspended particles through processes that are separate to [Chl-a], but still driven by the SAM.

Overall, the majority of the regression results point to a patchy but general loss of phytoplankton abundance in surface waters of the Southern Ocean. The same is true for the cloud fraction-SAM regression, with a patchy but overall reduction in cover, relative to trends in the SAM. Specific exceptions along the Antarctic continent are Lützow-Holm Bay (Enderby Land), the western arm of the WAP and the Ross Ice Shelf. Exceptions over the ocean include patches of the southern Indian Ocean, as well as a relatively substantial area over the Pacific (east of Tasmania). Notably, this region of the Pacific showing increased cloud does not extend to the west of the South American continent, where the Z_{eu} -SAM relationship was significantly

negative. Thus, it is unlikely that the changes in Z_{eu} relative to the SAM here are 'mechanically' driven by shifts in the amount of light reaching the ocean surface. In other words, the negative results from the Z_{eu} -SAM regression in this region imply a change to the IOP's rather than a straightforward decrease in the amount of solar irradiance reaching the ocean surface.

6.3.3.2 *January*

For Januarys in this timeseries, changes in [Chl-a], Z_{eu} and cloud fraction and that correlate to changes in the SAM are extremely diffuse and patchy. Perhaps more interestingly, the areas where the results from [Chl-a]-SAM and Z_{eu} -SAM regression are significant do not appear to match the regions of the Southern Ocean showing strong changes in trend over time (Fig. 75 and Fig. 76, respectively).

Outside of the ACC, SAM-related changes in [Chl-a] and Z_{eu} suggest an overall reduction of phytoplankton abundance in the surface waters of the south Indian and south Pacific sectors. Although not cohesive, the pattern in the south Atlantic sector is one of little change, with patches of SAM-related increases to surface phytoplankton abundance. This 'flips' south of the SAF, where the south Indian and south Pacific sectors now show patches of SAM-related increases to surface phytoplankton abundance and the south Atlantic sector shows an overall reduction. Specific areas showing positive and negative results from the [Chl-a]-SAM and Z_{eu} -SAM regressions, respectively, include a section of the Malvinas/ Falkland Current, the band of waters between the SAF and the PF for the length of the Pacific sector, and a large area south-east of Kerguelen. SAM-related changes in cloud fraction are extremely diffuse and patchy, but there appears to be broad decline in coverage.

6.3.3.3 *February*

For February of the timeseries, a large region of the Indian sector of the Southern Ocean, within the ACC and south-west of Kerguelen Island, shows a strongly significant relationship between the SAM and Z_{eu} , and the SAM and [Chl-a]. In other words, this region of the ACC appears to show enhanced phytoplankton abundance that is related in some way to the SAM. In the same sector but north of the PF and thus outside of the ACC, the opposite is true with SAM-related changes in [Chl-a] and Z_{eu} suggesting an overall reduction in phytoplankton abundance in surface waters. There is little to indicate that SAM-related changes to cloud fraction contribute

to these shifts in signal, with only small patches in this space resulting in changes to cloud cover over time.

Upstream and within the Drake Passage, waters along the SAF and PF show strongly positive and patchy negative results from the [Chl-a]-SAM and Z_{eu} -SAM regressions, respectively. Results from the cloud fraction-SAM regression in this same area are patchy but show possible SAM-related reductions in cover. However, the most spatially extensive SAM-related increases in cloud cover appear to coincide with a region in the central southern Pacific sector, outside of the ACC, which exhibits possible increases to surface phytoplankton abundance.

Within the 'bud' of the SAF that bulges up and along the Malvinas/ Falkland Current, there appears to be a region of significant change to [Chl-a] and Z_{eu} , relative to the SAM. Interestingly, referring back to the [Chl-a] and Z_{eu} climatology data February in the timeseries for this area (Fig. 75 and Fig. 76), there was a notable dissipation of signal that had been building in the December and January climatologies. In both the climatology and the regression, the Z_{eu} signals are more intense than those of [Chl-a]. This may imply a contribution of non-phytoplankton sources downstream of the South American east coast, such as CDOM.

6.4 CONCLUSIONS

Examining the monthly [Chl-a] and Z_{eu} climatology data shows that, while the Southern Ocean does conform to 'low chlorophyll' assumptions, there are interesting seasonal patterns within these constraints. There are the expected signals associated with features such as fronts, landmasses and islands, as well as the melting ice edge. However, there are also interesting patterns within the Southern Ocean that appear to be independent of these features.

In the Southern Ocean, light shifts from extremely low levels that limit phytoplankton growth, to supersaturating levels that also limit growth. Therefore, changes to cloud cover may have a significant impact on phytoplankton distribution and abundance. Although the Southern Ocean is broadly acknowledged to be the 'cloudiest region on Earth' (McCoy et al., 2015), this extreme cloudiness is not uniform. Indeed, although this region is persistently cloudy, the monthly cloud fraction climatology data shows that different months within the summer timeseries appear to be characterised by distinct patterns of cloudiness.

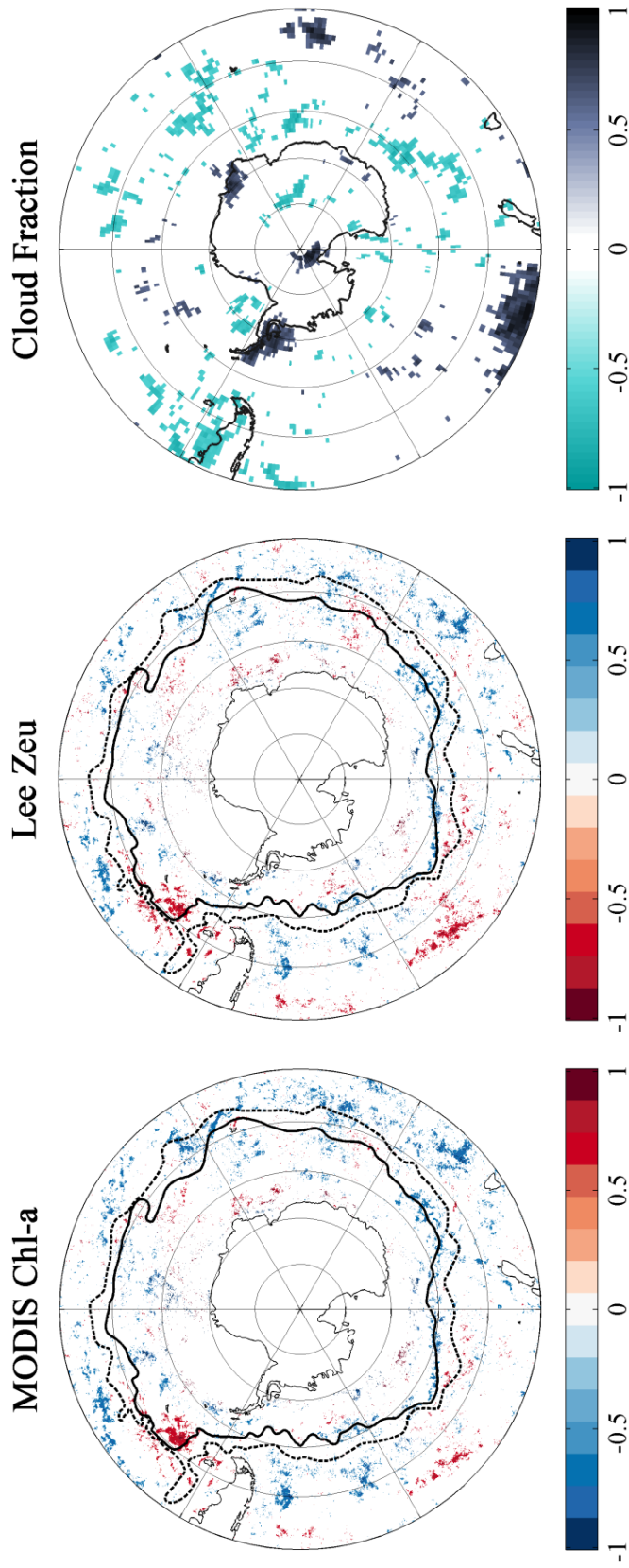


Figure 100: For the months of December, areas where significant ($p < 0.05$) changes are evident in Chl-a, Lee Z_{eu} and Cloud Fraction relative to the SAM. For Chl-a and Z_{eu} , red suggests an increase in surface Chl-a concentration over the 12 consecutive years in the MODIS satellite record (2003 - 2017), while blue suggests a loss. For cloud fraction, black shows an increase in coverage over time, while blue-green shows a decrease in cloud and implies that more light may reach the ocean surface.

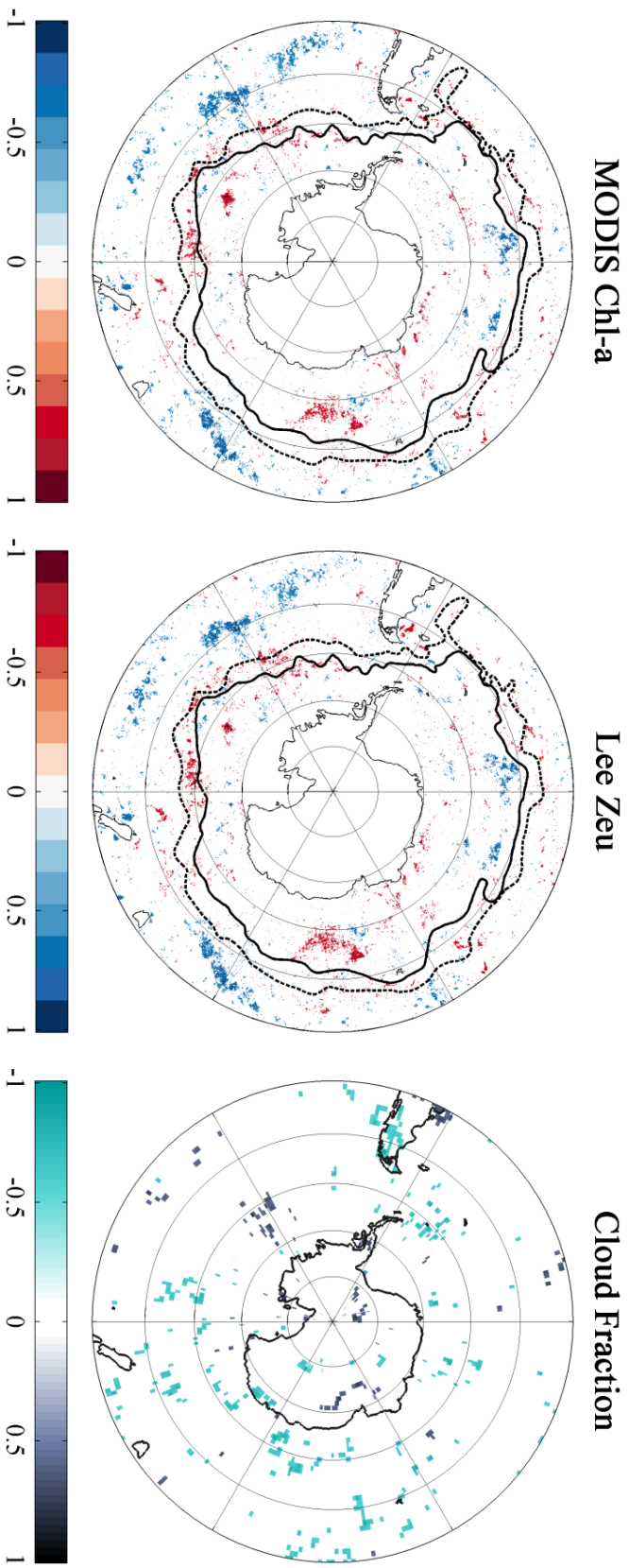


Figure 101: For the months of January, areas where significant ($p < 0.05$) changes are evident in Chl-a, Lee Zeu and Cloud Fraction relative to the SAM. For Chl-a and Z_{eu} , red suggests an increase in surface Chl-a concentration over the 12 consecutive years in the MODIS satellite record (2003 - 2017), while blue suggests a loss. For cloud fraction, black shows an increase in coverage over time, while blue-green shows a decrease in cloud and implies that more light may reach the ocean surface.

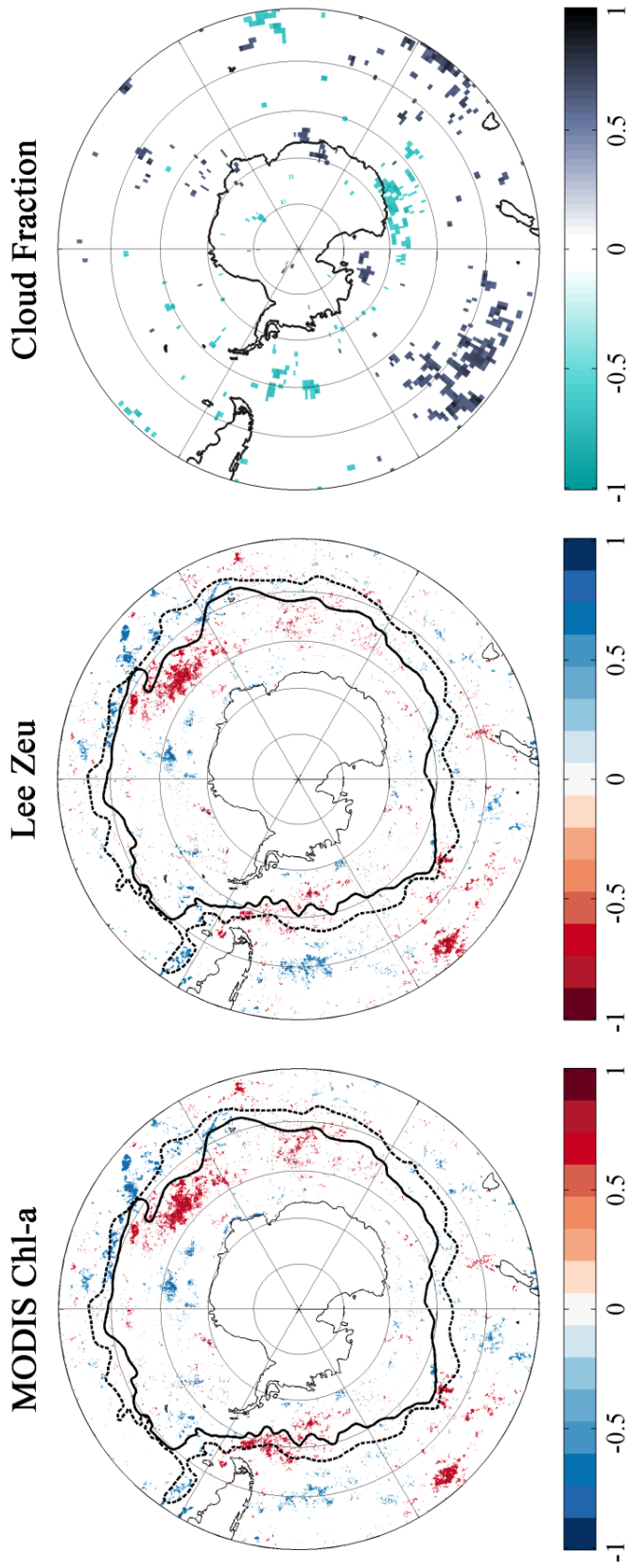


Figure 102: For the months of February, areas where significant ($p < 0.05$) changes are evident in Chl-a, Lee Z_{eu} and Cloud Fraction relative to the SAM. For Chl-a and Z_{eu} , red suggests an increase in surface Chl-a concentration over the 12 consecutive years in the MODIS satellite record (2003 - 2017), while blue suggests a loss. For cloud fraction, black shows an increase in coverage over time, while blue-green shows a decrease in cloud and implies that more light may reach the ocean surface.

Using a simple correlation, Z_{eu} climatology data were examined relative to cloud fraction climatology data. Interestingly, there appeared to be no relationship between the depth of the 1% light level (as a proxy for phytoplankton abundance) and cloud cover. 'Interestingly' not because Z_{eu} is anticipated to be dependent upon mean cloud fraction, but because studies by Meskhidze and Nenes (2006, 2010) and McCoy et al. (2015) have shown that high [Chl-a] (as a proxy for phytoplankton abundance but also a source for aerosols and their precursors) is associated with elevated cloud condensation nuclei (CCN). While measures of CCN are not necessarily equivalent to measures of cloud fraction, it is more likely the 'crudeness' (broad temporal and spatial scales) of this study that masks any seasonally and regionally specific relationships. The correlation in this study was done using climatology data, so any temporally sensitive relationships between proxies of phytoplankton and measures of cloud cover would almost certainly be lost. Having asserted this, Saba et al. (2014) were also unable to find evidence of a relationship between cloud cover and Chl-a using *in situ* data collected around the WAP (Palmer Station). For future work on the open waters of the Southern Ocean, it would be interesting to investigate these relationships (or potential lack thereof) between MODIS [Chl-a], Z_{eu} and cloud fraction with the addition of 8-day data.

Over the last 12 years, trends in [Chl-a] and Z_{eu} for the 'late spring' and summer months of October, November and even December suggest overall declines in surface phytoplankton abundance. While troubling, these trends do not necessarily indicate a net loss of primary biomass. Recalling that [Chl-a] is a surface measurement, reductions in signal may point to a 'migration' of phytoplankton biomass from surface and near-surface waters to depths that cannot be measured by satellite sensors. Furthermore, as detailed in chapter 3, these deep features can also form through photoacclimation processes, where shallow-mixed phytoplankton package relatively little Chl-a due to high light or light-saturating conditions. Recently, Behrenfeld et al. (2015) established that satellite observations documenting declines in surface Chl-a tend to overestimate if this 'packaging effect' is not taken into account. Indeed, measures of [Chl-a] do not linearly translate to measures of phytoplankton biomass, and photoacclimation effects appear to contribute a substantial amount of temporal variability in remotely sensed [Chl-a] (Behrenfeld et al., 2015).

Reduced [Chl-a] and deepening Z_{eu} trends over time may also point to shifts in timing. For future work, it would be worth investigating the 'early spring' months of

August and September to determine if trends in [Chl-a] and Z_{eu} have also changed. These months may be less straightforward to examine due to extensive ice cover confounding MODIS coverage at the highest latitudes. Nonetheless, it may still be possible to determine if the spring bloom is starting earlier and thus perhaps declining earlier too - explaining some of the depressed trends.

By January and February over the 13-year timeseries, there is some respite from overall declines, with trends in [Chl-a] and Z_{eu} suggesting increases to surface phytoplankton abundance. Both positive and negative trends are most intense within the ACC, but positive 'overshadows' negative in terms of spatial coverage. Carranza and Gille (2015) have recently shown that strong winds over the Southern Ocean and ACC correlate significantly with summer Chl-a anomalies. Higher wind speeds were theorised to sustained phytoplankton abundances over the summer months by deepening mixed layers, potentially entraining deeper, colder and more nutrient rich waters (Carranza and Gille, 2015). In agreement with work done by Salle et al. (2010), stronger winds associated with an increasingly positive SAM could also serve to enrich the well-lit surface waters through mixed layers driven deeper. This may explain some of the variability and positive trends over the summer months of January, February and possibly March. By this period of the late summer, while overall trends still point to gains in phytoplankton in surface waters, intensities are noticeably reduced.

Trends in cloud cover are more difficult to monitor or interpret due to the lack of spatial coherence and variability between months. Studies by Meskhidze and Nenes (2006, 2010) and McCoy et al. (2015) have shown that high phytoplankton concentrations act as a source for aerosols and their precursors, and are associated with elevated cloud condensation nuclei (CCN). As a proxy for phytoplankton abundance, areas of elevated [Chl-a] would then possibly be associated with increased cloud cover. However, we did not find a relationship between cloud and [Chl-a]. Instead, it appears that the southern sector of the Atlantic Ocean appears to be getting less cloudy over time, that the southern sector of the Pacific Ocean appears to be getting cloudier over time, and that the southern sector of the Indian Ocean is most changeable between months. Of these trends, only the increase in cloud over the southern Pacific appears to be related to changes to the SAM. Any potentially SAM-related decreases in cover appear constrained to Decembers over the timeseries. Of course, December has previously been shown as the most productive month in terms of overall annual primary production of the Southern Ocean (Arrigo et al., 1998). Thus, even

small changes over this specific time are noteworthy. Results from the [Chl-a]-SAM and Z_{eu} -SAM regressions for Decembers suggest that trends of overall declines in surface phytoplankton abundance may be related to the increasingly positive SAM.

By January, the impact of the SAM appears to have more mixed results, with patches of increased surface phytoplankton within the SAF. Of the three summer months evaluated for this study, February appears to experience the least amount of SAM-related declines. Indeed, there are extensive patches within the ACC and southern sectors of the Pacific Ocean that show positive and negative results from the [Chl-a]-SAM and Z_{eu} -SAM regressions, respectively.

Dominant factors controlling phytoplankton growth in Southern Ocean HNLC waters are mixing, light and, most critically, iron (Boyd et al., 2010; Smetacek et al., 2004). There is growing evidence that the SAM is altering biogeochemical cycling through perturbed, wind-driven mixing in the Southern Ocean. With interplays between mixing, light and iron already so complex in Southern Ocean waters, perturbations related to an increasingly positive SAM are likely to impact on phytoplankton patterns (Hall and Visbeck, 2002; Oke and England, 2004; Watterson, 2000; Lovenduski et al., 2005). However, in no cases were there clearly zonal changes to [Chl-a], Z_{eu} or cloud cover. This was true for trends over time, and for changes that co-varied significantly with the increasingly positive SAM. These results do not support the findings of Lovenduski and Gruber (2010), where SAM-related changes to Chl-a (as well as wind and SST) were shown to be near-zonally symmetrical. However, the asymmetry of the results from this study does echo findings of Sallee et al. (2005), which specifically addressed responses of the MLD (and [Chl-a]) to SAM.

Driven by global climate change and regional climate modes, rises in ocean temperature and localised freshening through enhanced ice melt and increased precipitation appear to be shifting high latitude waters towards stratification (Bindoff et al., 2007; Kemp and Villareal, 2014). Previous chapters of this thesis have already broadly addressed the importance of the vertical dimension when monitoring phytoplankton dynamics in space and time. Patterns within the vertical are, however, difficult to measure. Furthermore, the relationships between phytoplankton abundance, mixing and turbulence and/or stratification are not straightforward.

Within the constraints of this study, many of the factors that may contribute to variability in phytoplankton growth in the Southern Ocean cannot be addressed. Based on the ground-truthing from Chapter 2 and 3, there is some confidence that the

results from this study are not solely attributable to noise. There is high variability around islands (data not shown), but trends are also evident in open waters. With some of the strongest signals evident along the ice-edge, it's probable that changes to ice over are a significant contributing factor. However, the results of this work do strongly suggest that some resolution of the vertical dimension is essential for understanding changes we can 'see' at the surface. Indeed, a reduction in MODIS [Chl-a] over time or relative to the SAM may not imply an overall reduction in phytoplankton biomass. Changes in the ocean colour record at the surface may instead point to conditions that increasingly favour formation of chlorophyll maxima at depth, through photoacclimation effects or vertical migration of the phytoplankton cells themselves.

FROM THE BOTTOM TO THE TOP: LINKING PHYTOPLANKTON ABUNDANCE TO FORAGING PATTERNS OF THE SOUTHERN ELEPHANT SEAL

7.1 BACKGROUND

Tertiary consumers in any given ecosystem are often the most sensitive and responsive to dysfunctions in the food web. This vulnerability is largely thanks to their position at the apex of the food web, and compounded by traits such as specialised diets, low fecundity and unavoidable periods of juvenile dependence (Sergio et al., 2008). For these reasons, top predators are usually the first species to become extinct in perturbed ecosystems (Duffy 2002). As such, as sentinel species for monitoring purposes, marine predators are able to fill the role of ‘condition indicators’; providing clues on the overall health of their supporting marine ecosystem. Sharks, whales, and seabirds are thus often routinely monitored for fluctuations in population size, breeding success, growth rate, foraging behaviour and diet (Boyd and Murray 2001, Ray 2005).

The marine predators, southern elephant seals (*Mirounga leonina*), are no exception to this ‘ecosystem sensitivity’, and fluctuations in their populations appear to be coupled to related changes in the marine environment (McMahon et al., 2005; Biuw et al., 2007).

Between the brief terrestrial-based breeding and moulting phases, where no feeding takes place, adult females characteristically travel thousands of kilometres from their ‘home Island’ to exploit a stochastic marine environment with patchily distributed resources. These predators have been extensively studied from a biological and behavioural perspective so there is a substantial amount of information on their terrestrial phases (McCann, 1980; Bester, 1998; McMahon et al., 2000; Carrick et al., 1962; Le Boeuf and Laws, 1994; Ling, 2013, Postma et al., 2013). Despite these predictable periods where they haul out to breed (around November) or moult (around February), feeding only takes place during the less well understood pelagic phase,

and southern elephant seals spend an average of around 80% of their lives at sea (McIntyre et al., 2010). The post-breeding foraging phase takes place over the austral summer, from November to late January, with little variation. The post-moulting migration is even more extensive, taking up to 8 months and spanning autumn, winter and spring. Throughout each migration, elephant seals dive for approximately 20 - 30 minutes to their preferred depth of between 300 - 400m, surfacing only for short periods of approximately 2 - 3 minutes (Boyd and Arnborn, 1991)

Up to ten times larger than their female counterparts, adult male southern elephant seals are able to dive to 2000m in order to forage benthically (Le Boeuf and Laws, 1994). Females are not able to exploit such deep benthic resources and tend to forage more extensively on horizontal scales. Consequently, they may exhibit clearer correlations to the biogeochemical and physical sea-state in their search for patchy resources. For this reason, only data collected by female southern elephant seals were used in this thesis.

Females also appear to be strongly philopatric, returning to their natal islands (and beaches) for breeding and moulting haul-outs (Hindell, 1991). This results in limited genetic exchange between populations, but the southern elephant seals from Marion Island genetically augment the Kerguelen population (McMahon et al., 2005). The Marion population is one of the northernmost breeding aggregations and their distance from large land masses and the ice edge encourages foraging patterns that are almost exclusively pelagic. The Kerguelen population, on the other hand, are able to take advantage of the shallow plateau that circles the island and extends towards the Antarctic landmass. Nonetheless, the majority still appear to adopt pelagic-dominant foraging (Bailleul et al., 2007; this study).

For this chapter, only the horizontal patterns of female elephant seals tagged with fluorometers (Marion and Kerguelen) and light meters (Kerguelen only) are examined. The vertical dive behaviour of these tagged seals is constituting a second PhD investigation, concurrent to the work being done for this thesis.

Because of the extreme deep-diving and wide-ranging foraging behaviours characteristic to elephant seals, it's impossible to directly observe how these predators interact with the marine environment or their prey. By the time individuals leave the water and haul out for moulting or breeding purposes, stomach contents are often entirely digested, providing few clues on feeding patterns and prey composition (Gal-

lon et al., 2013). For any possible fluctuations in behaviour and diet to be resolved, proxies must therefore be employed to infer shared or common foraging patterns.

The more routinely employed proxies for 'foraging behaviour' are extensive and range from track-based metrics (first passage time, transit rate and turning angle) to dive-based metrics (intensity or type) (LeBoeuf et al., 1988; Bost et al., 2007; Fauchald and Tveraa, 2003; Pinaud and Weimerskirch, 2007). Robinson et al. (2010) assessed all these foraging proxies in northern elephant seals using drift rate, a behaviour-independent measure of foraging success. Speed appeared to be the best single predictor of successful foraging, with periods of slow horizontal transit coinciding with improving body condition (Robinson et al., 2010; Le Boeuf et al., 2000; Crocker et al., 2006; Thums et al., 2011). This supports area restricted search (ARS) and optimal foraging theories, which predict that swimming speeds of marine predators would be measurably affected by the presence of 'hotspots' of high prey abundance (MacArthur and Pianka, 1966; Kareiva and Odell, 1987; Dragon et al., 2010).

Attempting to directly monitor and/or measure the presence, richness and persistence of prey hotspots in our dynamic global oceans is challenging, to say the least. However, it is possible to remotely assess where waters are perhaps most likely to be richest if we use phytoplankton as an indicator.

Phytoplankton form the base of the marine food web. As described and discussed in Chapters 1 – 5 of this thesis, the photosynthetic pigment chlorophyll-a (Chl-a) can be exploited remotely by ocean colour sensors to monitor the distribution and abundance of these microscopic organisms at the ocean surface (Morel and Prieur, 1977; Gordon and Morel, 1983; Falkowski et al., 1998; Henson et al., 2010). Further, as shown in Chapter 6, the depth of the 1% light level can be used to substantiate remotely derived measures of [Chl-a]. However, as additionally detailed in previous chapters, the limitations of remote sensing are substantial on vertical and horizontal scales, as well as temporal and spatial scales.

Previous studies in high latitude waters by Campagna et al (2006, 2007) and Jaud et al. (2012) examined the (fine-scale) diving depths and foraging patterns of tagged southern elephant seals relative to (coarse resolution) satellite-derived concentrations of [Chl-a], with conflicting results. It is quite likely that variability between outcomes is compounded or even exclusively introduced by the multiple steps and lags between the bottom of the food web and the top. However, the inconsistencies could just have well have been caused by the mismatch between the coarse resolution of

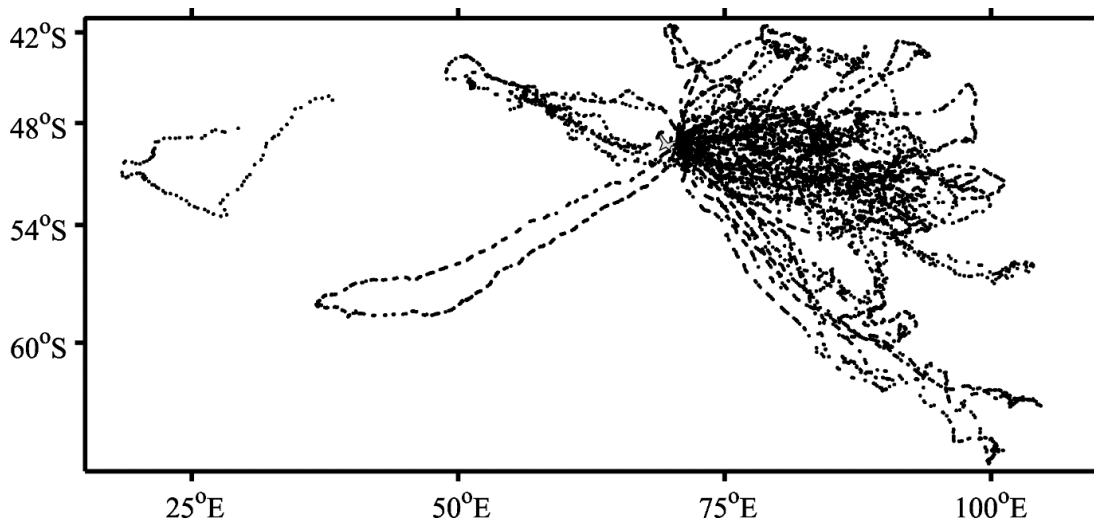


Figure 103: Tracks of all 47 post-breeding adult female southern elephant seals tagged on Kerguelen and Marion Island and instrumented with FCTD tags and TDR light meters. Austral summers span from 2009 to 2014.

the satellite data (and the inherent limitations associated with remote sensing) and the fine-scale tag data.

As tertiary consumers near the top of the Southern Ocean food web, southern elephant seals do not directly feed on phytoplankton. Instead, they predate upon the lanternfish (Myctophidae) and/or squid that predate upon zooplankton and other fish and/or squid, respectively. Indeed, when examining these marine predators, it's essential to be aware of the fact that many links join southern elephant seals to the microscopic phytoplankton cells forming the foundation of their food web. In order to ascertain if variability is due to these many links, or simply from the data resolution mismatch, an alternative proxy for phytoplankton abundance must be tested. Specifically, an alternative proxy that is available on scales and at resolutions that are more closely relatable to the behavioural data.

Recent advances in tagging technology have made it possible to instrument southern elephant seals and track their extensive pelagic phases while measuring a range of oceanographic parameters at similar resolutions and scales (Fig. 103).

Custom-built tags are capable of measuring and relaying salinity and temperature data as the animal moves through the water column (Sea Mammal Research Unit, University of St. Andrews, Scotland). As mentioned in Chapter 2 and 3, light meters and fluorometers have more recently been added to measure vertical light attenuation and chlorophyll, as indicators of phytoplankton distribution and abundance (Charrassin et al., 2010; Xing et al., 2012; Guinet et al., 2013). Because the light

and fluorescence data collected by these tags are retrieved concurrently to the behavioural information, the scales between phytoplankton abundance and foraging behaviour are essentially equivalent. Thus, compared with studies that relied on remotely sensed [Chl-a], errors introduced by differences in scale and resolution should be significantly reduced.

In this chapter, the depth of the 1% light level and fluorescence are introduced as proxies for relative abundance of phytoplankton. Because phytoplankton are the foundation of the marine food web, waters with higher measures of fluorescence should be associated with higher abundances of zooplankton and, thus, a myriad of secondary and tertiary consumers. For this reason, fluorescence is employed as an indicator of 'hotspot' waters in this chapter, where prey species are more likely to be present. Based on results from Robinson et al (2010) and ARS theory, hotspots should thus coincide with phases where the swimming speeds of southern elephant seals are the slowest; suggesting foraging.

In as early as 1998, distinct phases within tracks of southern elephant seals were first identified and described (Jonker and Bester, 1998). These phases were grouped as 'outbound transit' (travel), 'distant foraging' and 'inbound transit' (travel). The question on how to best employ the variable 'speed' to distinguish a foraging phase from a travelling phase is not, however, satisfactorily answered by the literature. Several techniques for finding phase-changes, including first-passage time (Fauchald and Tveraa, 2003), residence time (Barraquand and Benhamou, 2008), moving average (Robinson et al., 2007) and fractal landscape (Tremblay et al., 2007) have been published. Knell and Codling (2012) tested these methods on computer generated movement paths data "designed to replicate the possible paths performed by an animal", and found common limitations with each. Their own partial sum approach, on the other hand, successfully identified phase-changes in the same path data without the constraints inherent to the other methods.

The partial sum method requires both turning angle and speed to find phase-changes. However, track data for this study was not computer generated, and was instead collected by animal-borne tags with battery and data size considerations. Track data collected by FCTD tags are not relayed continuously or even collected on a dive-by-dive basis. For the 1% light level datasets, where measurements are collected every 2 seconds, the method described in Chapter 2 filters off all dives taking place at night, or under low light conditions. For these reasons, movement data from

tagged marine animals are considerably less regular or consistent than those generated by computer, and detecting meaningful changes in turning angle is less likely. Therefore, in order to detect phase changes in these tracks, a method is required that is not highly sensitive to variation introduced by tag/ relay/ filtering limitations, nor reliant on turning angle.

The cumulative sum sequential analysis (CUSUM) developed by Page (1963) is tested as a novel method for detecting phase-changes within tracks of tagged southern elephant seals. Applying Page's "quality number" – in this case, mean speed calculated from a complete foraging trip – the CUSUM method is used to determine deviations from the mean. When plotted on a CUSUM chart, changes in the trend line of cumulative speed suggest that a phase shift has occurred.

Using deviations from the mean travelling speed, tracks can then be grouped into 'outbound transit' (travel), 'potential ARS' (foraging) and 'homeward bound transit' (travel). Thereafter, these behaviour patterns can be examined relative to associated fluorescence and light data to determine if relationships exist between the bottom and the top of the Antarctic marine food web.

If elephant seal foraging patterns are linked to fluorescence and the 1% light level as proxies of phytoplankton, there is future opportunity to predict their at-sea behaviour based on higher resolution ocean colour data (Sentinel 3). Further, if elephant seal at-sea behaviours are associated with phytoplankton patterns, there is also scope for projecting population success or declines under anthropogenic climate change scenarios (the SAM). Indeed, it's possible that southern elephant seals may prove to be a sentinel species for an altering, perturbed Southern Ocean marine ecosystem.

7.2 METHODS

7.2.1 *In-situ datasets*

Adult female southern elephant seals were tagged and monitored for their post-breeding foraging migration only. This marine phase coincides with the height of the austral summer, when primary productivity is relatively high. Research has been done on the relationship between [Chl-a] and distributions of southern elephant seals over the austral winter (Bradshaw et al., 2004). However, there is little to no measur-

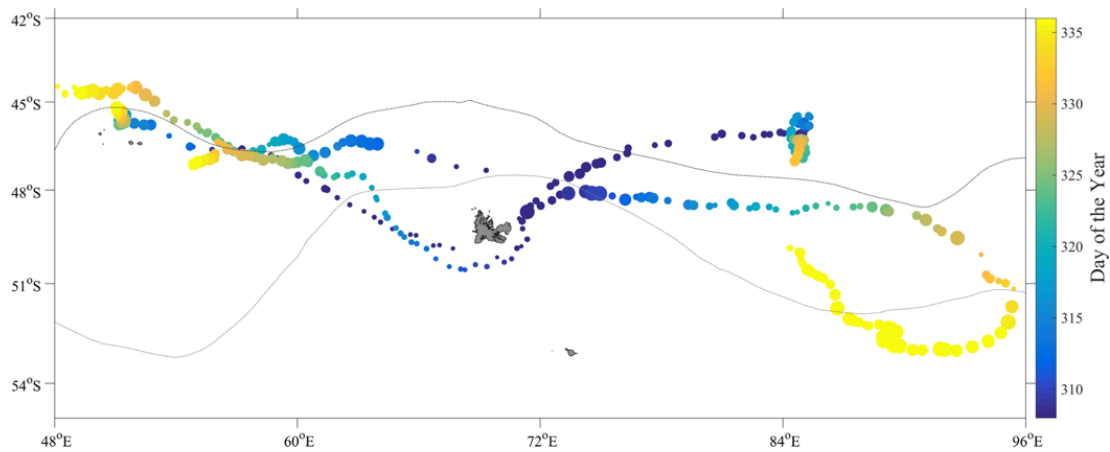


Figure 104: Tracks of the five southern elephant seals not included for the cumulative sums analysis, where instrument failure has resulted in incomplete data collection. Tracks are coloured by day of the year, and larger marker sizes represent higher surface fluorescence yields, as measured by the FCTD-SRDL.

able productivity over these months. Seals tagged for their winter migrations were excluded from this analysis and for this thesis as a whole.

Over the summer months (approximately November - January) spanning 2009 - 2015, seventeen adult female southern elephant seals from Kerguelen and one from Marion Island were tagged with FCTD-SRDLs (Sea Mammal Research Unit, St Andrews University, Scotland). As detailed in Chapters 3 - 5, fluorescence data were adjusted to remove the dark count, and quenching was accounted for using a novel correction method. For this chapter, five of these processed and corrected FCTD datasets were excluded. In these five cases, instrument failure during the at-sea phase resulted in incomplete tracks (Fig. 104). These data could not be used for the cumulative sums analysis because a clear home-bound travel phase is required. Thus, twelve of the seventeen FCTD datasets were retained for further analysis. Quenching-corrected fluorescence yields were integrated with depth per profile to incorporate the vertical dimension.

Over the same period, thirty-five post-breeding female southern elephant seals from Kerguelen Island were tagged with SPLASH₁₀-Fast-Loc GPS instruments; combining a time-depth recorder (TDR), a global positioning system (GPS) logger, an Argos satellite-relay instrument and a data storage logger (Wildlife Computers), collectively referred to as TDR light recorders (Fig. 103). As detailed in Chapter 2, six of these datasets were not retained due to self-shading or instrumentation problems, leaving twenty-nine TDR light level datasets for analysis in this Chapter.

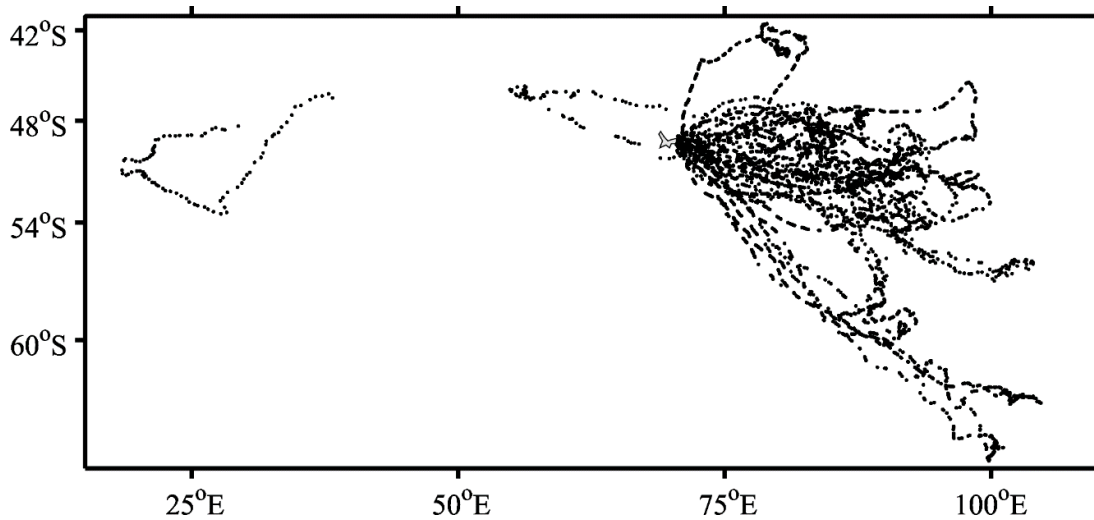


Figure 105: Tracks of the remaining post-breeding adult female southern elephant seals tagged on Kerguelen and Marion Island from 2009 to 2014. Data from both FCTD tags and TDR light meters are shown in this figure.

7.2.2 CUSUM Analysis

From each seal position, speed (km hr^{-1}) was calculated from the distance between successive positions in space. Longer track lengths between positions imply greater speeds. Conversely, short track lengths imply reduced swim speeds and, with ARS in mind, may indicate foraging behaviour.

To find potential phase-changes within the tracks of these wide-ranging marine predators, these speed data were first analysed using a CUSUM analysis. If μ_0 is the target for the 'in-control' mean (Mesnil and Petitgas, 2008) (or Page's "quality number"), then the cumulative sum control chart is formed by plotting the quantity

$$C_i \sum_{j=1}^i (\bar{x} - \mu_0) \quad (5)$$

against the sample i . C_i is called the cumulative sum up to and including the i th sample. For a given temporal interval, the local trend X_{ij} can be deduced from the slope P of C_i . Indeed, between two points, i and j , separated by n values, the local trend can be computed as follows:

$$X_{ij} = P - \mu_0 \quad (6)$$

Travel rates cumulatively faster than the mean speed will result in a positive trend (slope) that is suggestive of a travelling phase. On the other hand, speeds cumulat-

ively slower than the mean speed result in a negative trend (slope), suggestive of a foraging phase. To identify when significant phase changes occur, within a pre-defined window it is necessary to robustly detect where one cumulative trend becomes stochastically dominated by another.

7.2.3 *Spatial Division of Tracks*

For seals carrying FCTD tags, an 8-observation moving average of the instantaneous derivative of cumulative speed was computed, and phase changes were detected using a one-way ANOVA. These tags relay observation/ position every 6 hours, so for a significant phase change to be identified, the behaviour (speeds faster or slower than the mean) would thus have to persist for approximately 2 days.

For seals carrying TDR light meters, all light intensity data are recorded by the tags for the duration of the foraging trip. However, due to the processing of this high resolution fine-scale light data in Chapter 2, the dataset for this CUSUM analysis contains only surfacing events (upcast and downcast) associated with 'viable' measures of the 1% light level. Essentially, this means that only data collected under well-lit day-time conditions were retained. While necessary for ensuring a representative 1% light level over time, the filtering processes applied in Chapter 2 now present a problem with regards to consistency of positional data along a given track. To 'absorb' the introduced but unavoidable within-track variability for the CUSUM analysis in this Chapter, a larger 20-observation moving average of the instantaneous derivative of cumulative speed was used for this one-way ANOVA. There are $\approx 6-11$ observations every 24 hours in these 1% light level datasets, so for a significant phase change to be confirmed by the algorithm in these cases, the behaviour (speeds faster/ slower than the mean) would have to persist for approximately 3 days. The strength of the CUSUM approach is that this problem of irregularly spaced / missing data (night/ dark/ self-shaded) is reduced.

7.2.4 *CUSUM Chart*

Cumulative speeds over time and relative to the mean (quality number) were plotting on CUSUM charts. By using a CUSUM analysis in this study, the expectation is that when a trend in slope changes sign and the new slope trend persists outside of a

pre-determined moving average angle window, a phase change can be considered to have occurred. Detection of statistically significant phase-changes from the one-way ANOVA were compared with phase-changes detected by a Kruskal-Wallis test, which does not rely on normality. Using the CUSUM chart, phase-changes were also confirmed 'by eye' on the CUSUM chart.

Based on the combination of automated and manual detection of phase changes, at-sea behaviour of tagged seals were divided into three phases, namely: outbound transit (travel), potential ARS (foraging) and homebound transit (travel).

During this stage of analysis, it became evident that ten seals tagged with TDR light meters and three with FCTD's did not conform to this 3-phase 'typical' behaviour described by Jonker and Bester (1998). Rather than exhibiting one foraging phase, some of these seals appeared to have several phases of slow speeds nested within high speed phases, indicating that ARS may have taken place sporadically and opportunistically throughout. Other seals exhibited behaviour with substantial bias to slow speeds, with short travel phases highly compressed in space and time (Fig. ??). These datasets were discarded. Overall, data were only retained for further analysis if the slope of the cumulative speeds changed sign in a manner that conformed to 'typical' travel – foraging – travel patterns.

7.2.5 *Processing of the fluorescence and 1% light level data*

Once three clear phases were delineated, corresponding values of depth-integrated fluorescence were examined. For each seal track, the mean fluorescence was calculated per phase, resulting in one mean value for 'outbound transit', one mean value for 'potential ARS' and one mean value for 'homebound travel'. Thereafter, all 'outbound transit' values were grouped, all 'potential ARS' values were grouped and all 'homebound travel' values were grouped. This allowed for the mean fluorescence from each phase to be compared against the other phases with a paired t-test. The analysis serves to determine if grouped fluorescence is significantly different between phases.

The same process was applied to the 1% light level data.

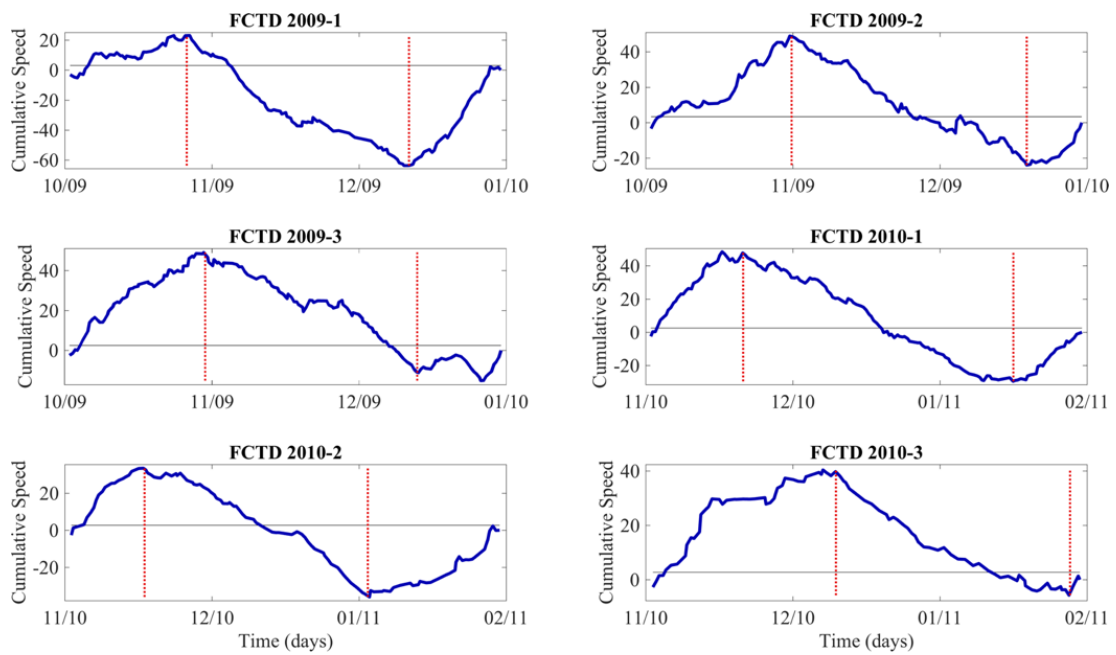


Figure 106: Cumulative sums CUSUM chart for all seals tagged with fluorimeters. The blue line represents the cumulative speeds over time, with the Page Quality Number shown by the black horizontal line and phase changes shown by the vertical red dashed lines. Each plot is labelled by Tag, reported in bold.

7.3 RESULTS

For this study, instrumented seals largely conformed to outbound, foraging and homebound phases characterised by high, low and high speeds, respectively. In most cases, however, the one-way ANOVA and Kruskal-Wallis tests identified short phases of slow speeds within travel phases (Fig. ??). These ‘perturbations’ could have arisen from missing data, from opportunistic foraging, or from searching behaviour within an overall phase. Manual confirmation was required for selection of the two ‘most relevant’ phase changes, highlighting method limitations.

The CUSUM method proved robust at calculating cumulative speeds over time, and showed resilience to variability from changes to speed within phases, or even the resolution of input data. Three seals were tagged with both FCTD-SRDLs and TDR Light Meters, and these datasets provided an opportunity for comparison of resultant CUSUM charts and phase change detections (113)..

Fluorescence is significantly higher during phases where seals are exhibiting cumulative slower speeds (identified as possible foraging), compared with outbound phases where animals are possibly searching for patchily distributed prey (Fig. ??).

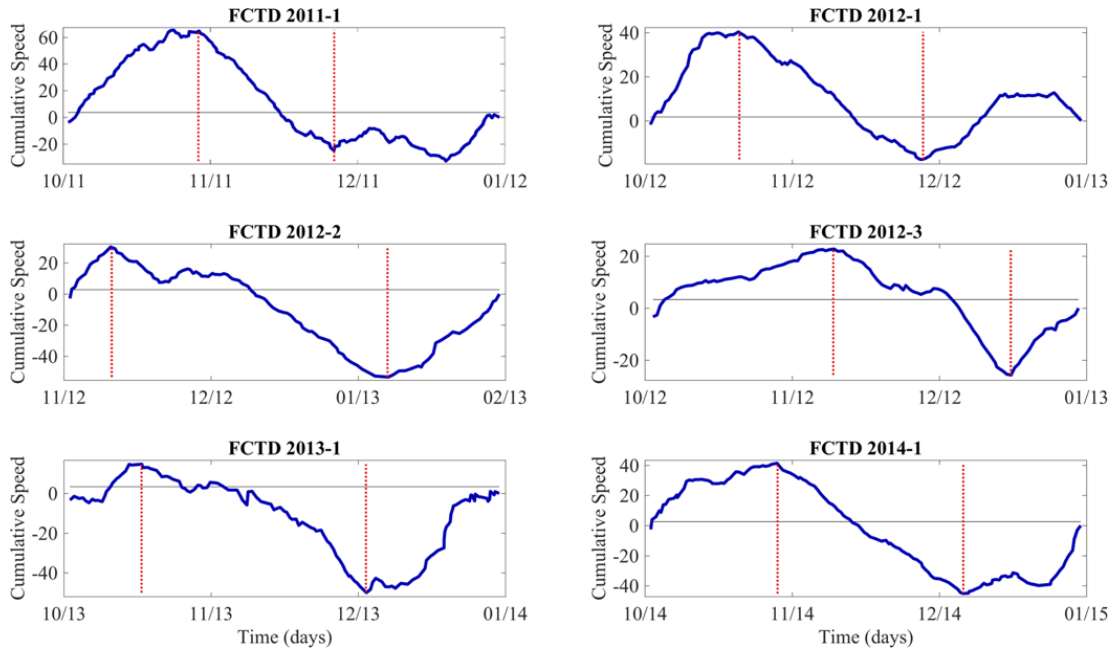


Figure 107: Cumulative sums CUSUM chart for all seals tagged with fluorimeters. The blue line represents the cumulative speeds over time, with the Page Quality Number shown by the black horizontal line and phase changes shown by the vertical red dashed lines. Each plot is labelled by Tag, reported in bold.

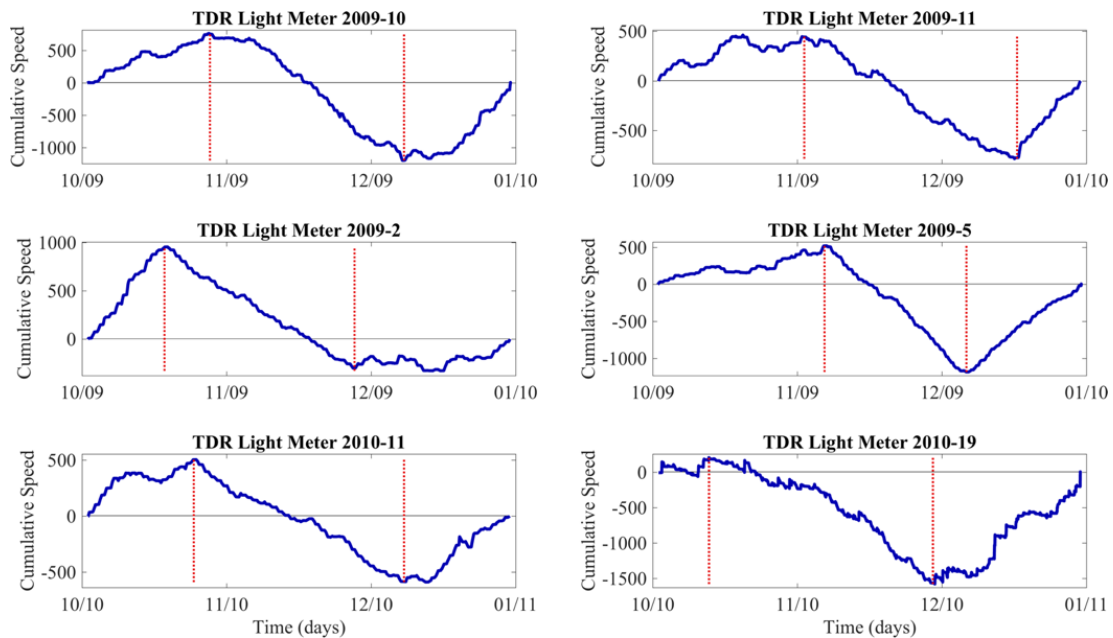


Figure 108: Cumulative sums CUSUM chart for all seals tagged with TDR light meters. The blue line represents the cumulative speeds over time, with the Page Quality Number shown by the black horizontal line and phase changes shown by the vertical red dashed lines. Each plot is labelled by Tag, reported in bold.

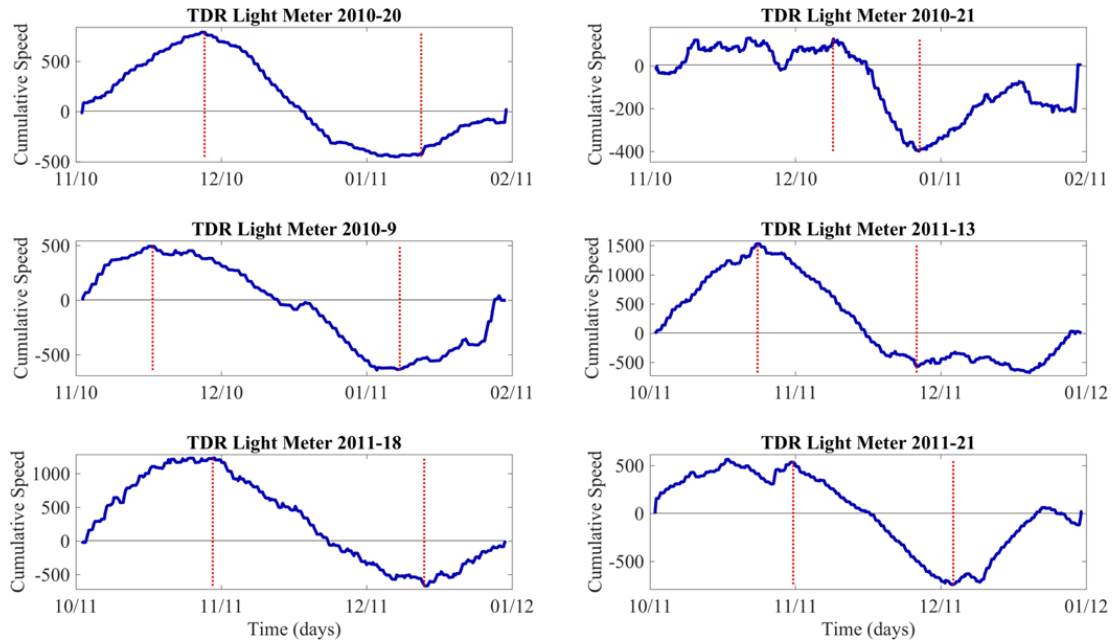


Figure 109: Cumulative sums CUSUM chart for all seals tagged with TDR light meters. The blue line represents the cumulative speeds over time, with the Page Quality Number shown by the black horizontal line and phase changes shown by the vertical red dashed lines. Each plot is labelled by Tag, reported in bold.

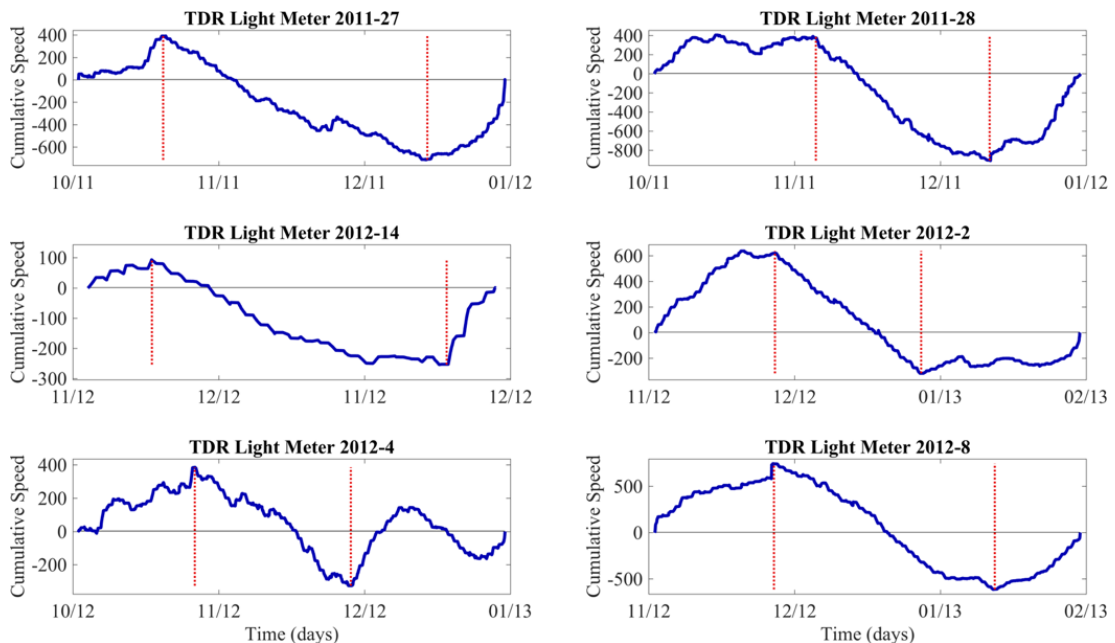


Figure 110: Cumulative sums CUSUM chart for all seals tagged with TDR light meters. The blue line represents the cumulative speeds over time, with the Page Quality Number shown by the black horizontal line and phase changes shown by the vertical red dashed lines. Each plot is labelled by Tag, reported in bold.

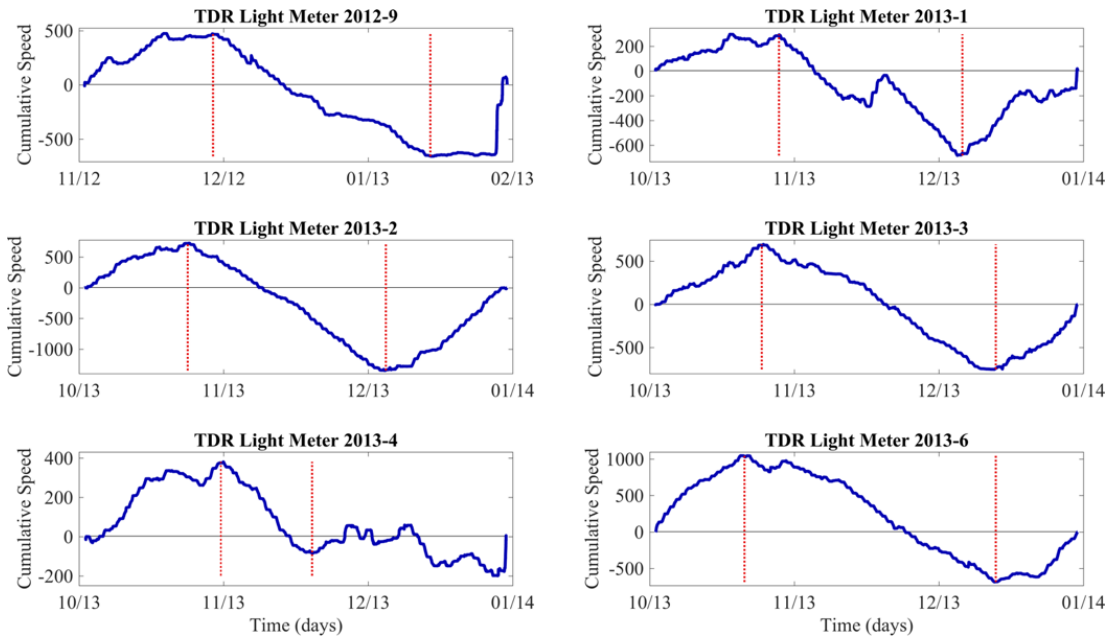


Figure 111: Cumulative sums CUSUM chart for all seals tagged with TDR light meters. The blue line represents the cumulative speeds over time, with the Page Quality Number shown by the black horizontal line and phase changes shown by the vertical red dashed lines. Each plot is labelled by Tag, reported in bold.

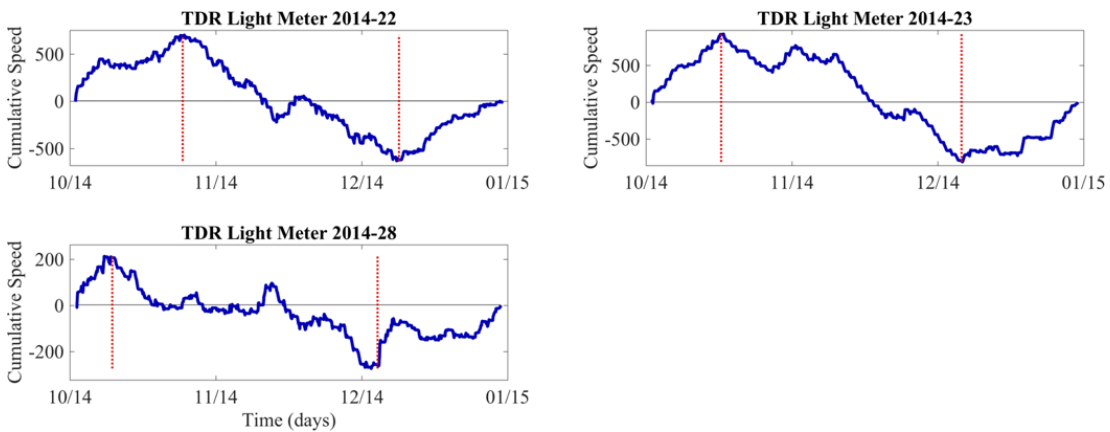


Figure 112: Cumulative sums CUSUM chart for all seals tagged with TDR light meters. The blue line represents the cumulative speeds over time, with the Page Quality Number shown by the black horizontal line and phase changes shown by the vertical red dashed lines. Each plot is labelled by Tag, reported in bold.

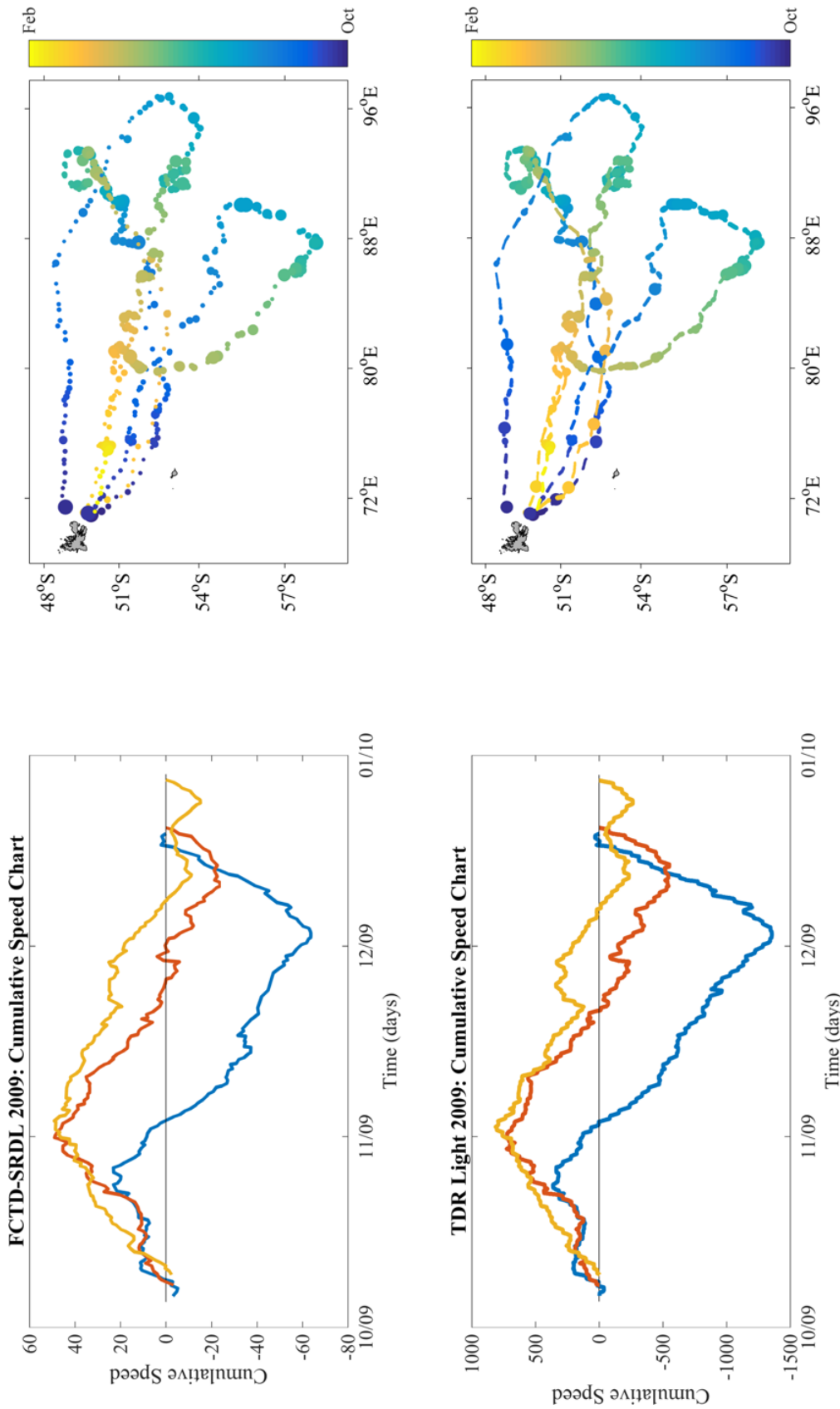


Figure 11.3: Cumulative speeds from the three seals tagged with both FCTD-SRDLS and TDR Light Meters in 2009. The top panel shows cumulative speeds calculated using FCTD data only. With these tags, data are only collected from the deepest dive recorded over 6-hourly windows. The CUSUM chart shows cumulative speed around the Page Quality number (horizontal black line), and the corresponding tracks represent true speed (highest speeds represented by the smallest marker sizes, and visa versa). The bottom panel shows the same, but based on data collected by the TDR light meters. With these tags, data are collected every 2 seconds, however, all low light data (night or very overcast) have been filtered out. The CUSUM chart and tracks calculated using FCTD data matches the CUSUM chart and tracks calculated using TDR Light Meter data, despite differences in resolution.

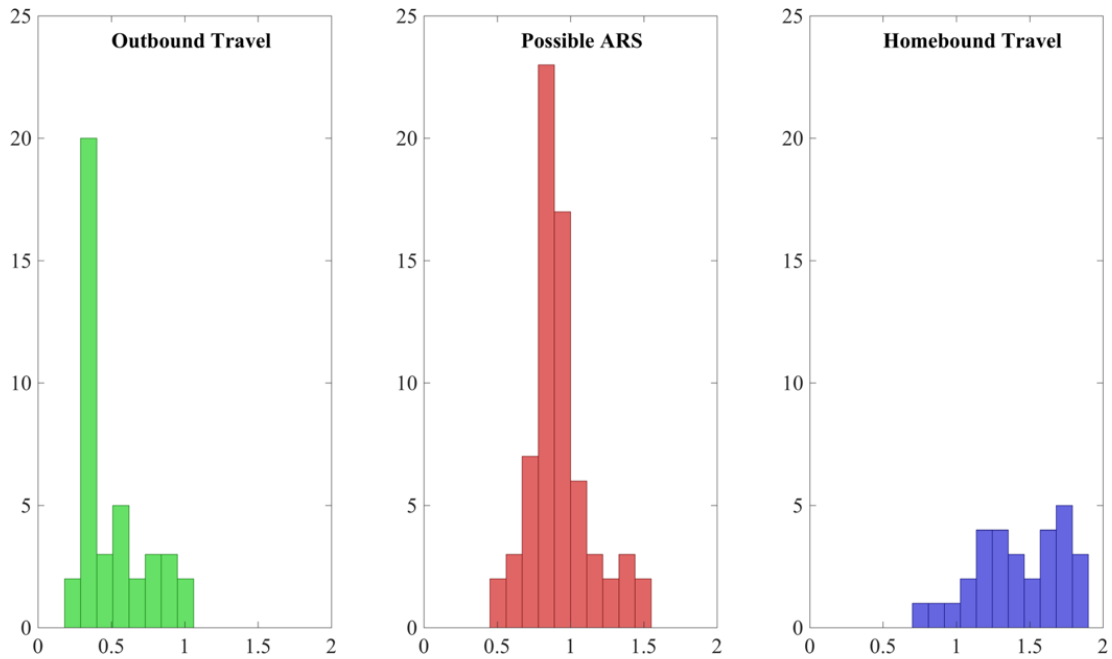


Figure 114: Histograms of fluorescence data collected by twelve southern elephant seals during three at-sea phases, namely: outbound (green), possible area-restricted search (ARS) foraging (red), and homebound (blue). Fluorescence values are lowest during the outbound phase and are highest during the homebound phase. Fluorescence data collected during the foraging phase are approximately normally distributed around a mean of 1.

In the previous chapter, we saw that phytoplankton appears to bloom from December, and it is possible that fluorescence is higher during the foraging phase primarily because of this timing. Indeed, the difference between fluorescence during potential foraging and home-bound travel is not significantly different, and the homeward phase is characterised by higher maximum fluorescence values. However, it is also characterised by highest variability. As seals return to Kerguelen, they are also returning to naturally iron-fertilised waters where phytoplankton concentrations will remain elevated until light-limited. I would suggest that if foraging behaviour is related to phytoplankton, seals would target areas of elevated fluorescence during their outbound trip and remain within/near 'hotspots', resulting in slowed speeds coinciding with high fluorescence. The return journey would be characterised by variable speeds indicative of opportunistic foraging, and variable fluorescence with maximum values nearest the island. This is evident in figures 115 to 120.

The light data are unfortunately more difficult to assess during the different phases. Mean depth of the 1% light level was shallower at the distal end of tracks in open waters (possible ARS). However, differences between light levels and phases are not signi-

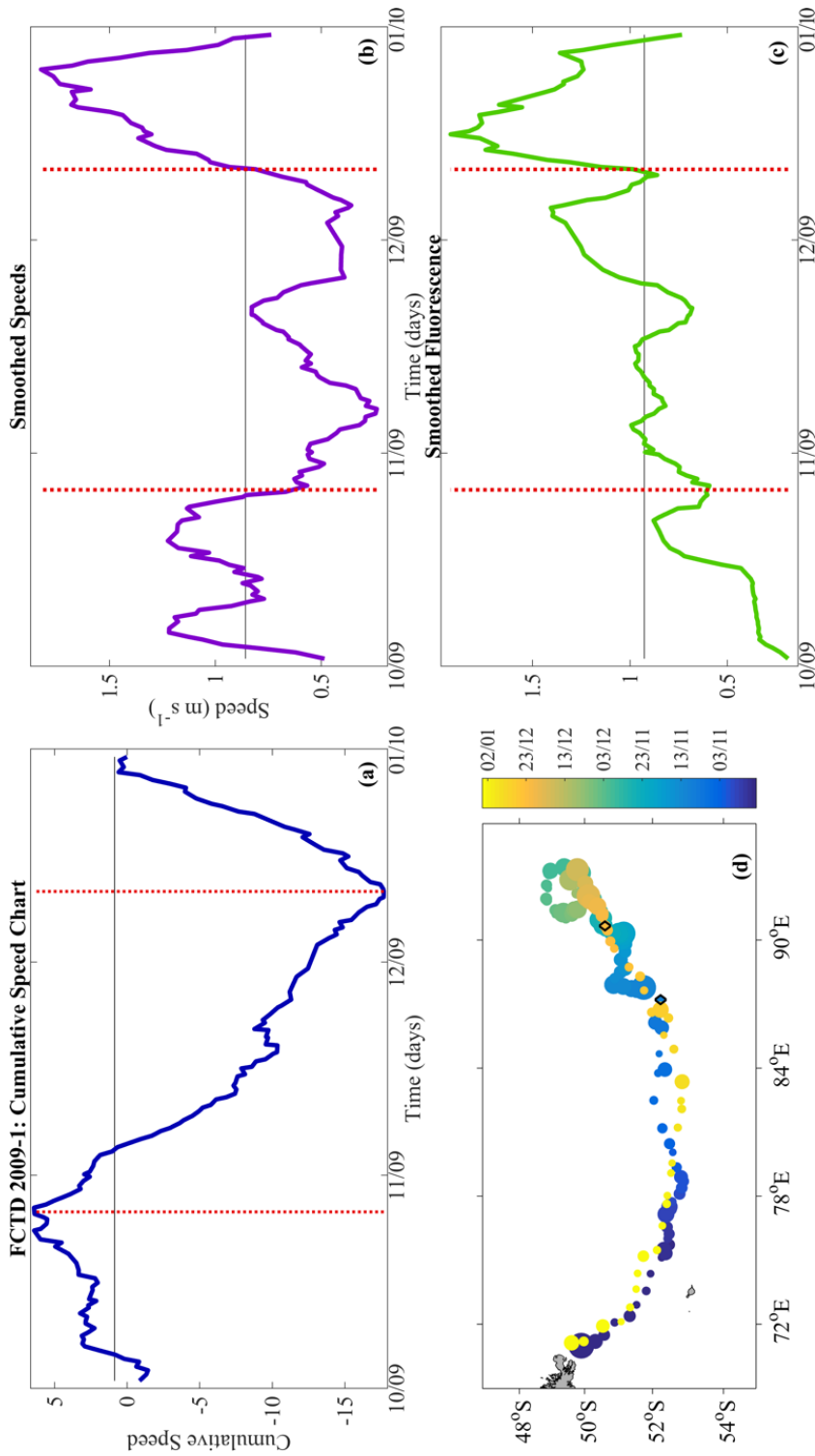


Figure 115: Visualising speed and phase changes for FCTD tag 2009-1. In (a), the CUSUM chart shows cumulative speed relative to the Page Quality Number, represented by the black horizontal line. The two dashed, vertical red lines represent the phase changes from travel to foraging, and then to travel again. Phase changes were detected automatically using a Kruskal-Wallis test, with manual confirmation. The same phase change lines are plotted in (b), which shows the same track data over the same x-axis, but reported as m/s on the y-axis. The phase changes detected on the CUSUM chart are an exact match for when speeds drop below the mean (horizontal black line). Speed has been smoothed using a boxcar filter with window of 4, and is represented by the purple line. For comparison, vertically integrated fluorescence in green (c) has been smoothed using the same boxcar filter, and is plotted over the same x-axis with CUSUM phase change lines in red. Mean fluorescence is shown by the horizontal black line. For context, seal tracks are shown in (d). Larger marker sizes represent slower speeds, and visa-versa. The two black diamonds represent when in time the phase changes were detected on the CUSUM chart.

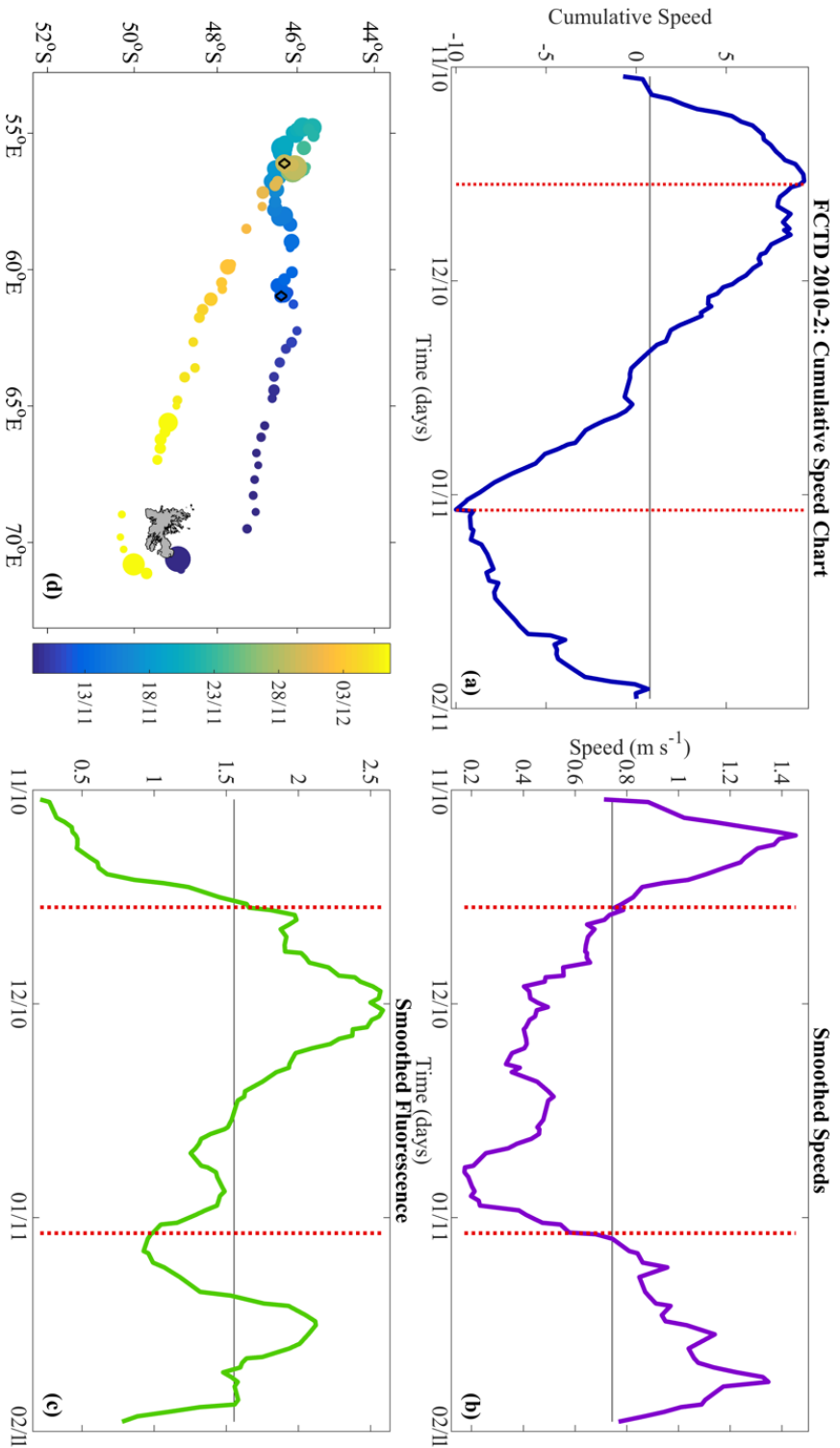


Figure 116: Visualising speed and phase changes for FCTD tag 2010-1. In (a), the CUSUM chart shows cumulative speed relative to the Page Quality Number, represented by the black horizontal line. The two dashed, vertical red lines represent the phase changes from travel to foraging, and then to travel again. Phase changes were detected automatically using a Kruskal-Wallis test, with manual confirmation. The same phase change lines are plotted in (b), which shows the same track data over the same x-axis, but reported as m/s on the y-axis. The phase changes detected on the CUSUM chart are an exact match for when speeds drop below the mean (horizontal black line). Speed has been smoothed using a boxcar filter with window of 4, and is represented by the purple line. For comparison, vertically integrated fluorescence in green (c) has been smoothed using the same boxcar filter, and is plotted over the same x-axis with CUSUM phase change lines in red. Mean fluorescence is shown by the horizontal black line. For context, seal tracks are shown in (d). Larger marker sizes represent slower speeds, and *visa-versa*. The two black diamonds represent when in time the phase changes were detected on the CUSUM chart.

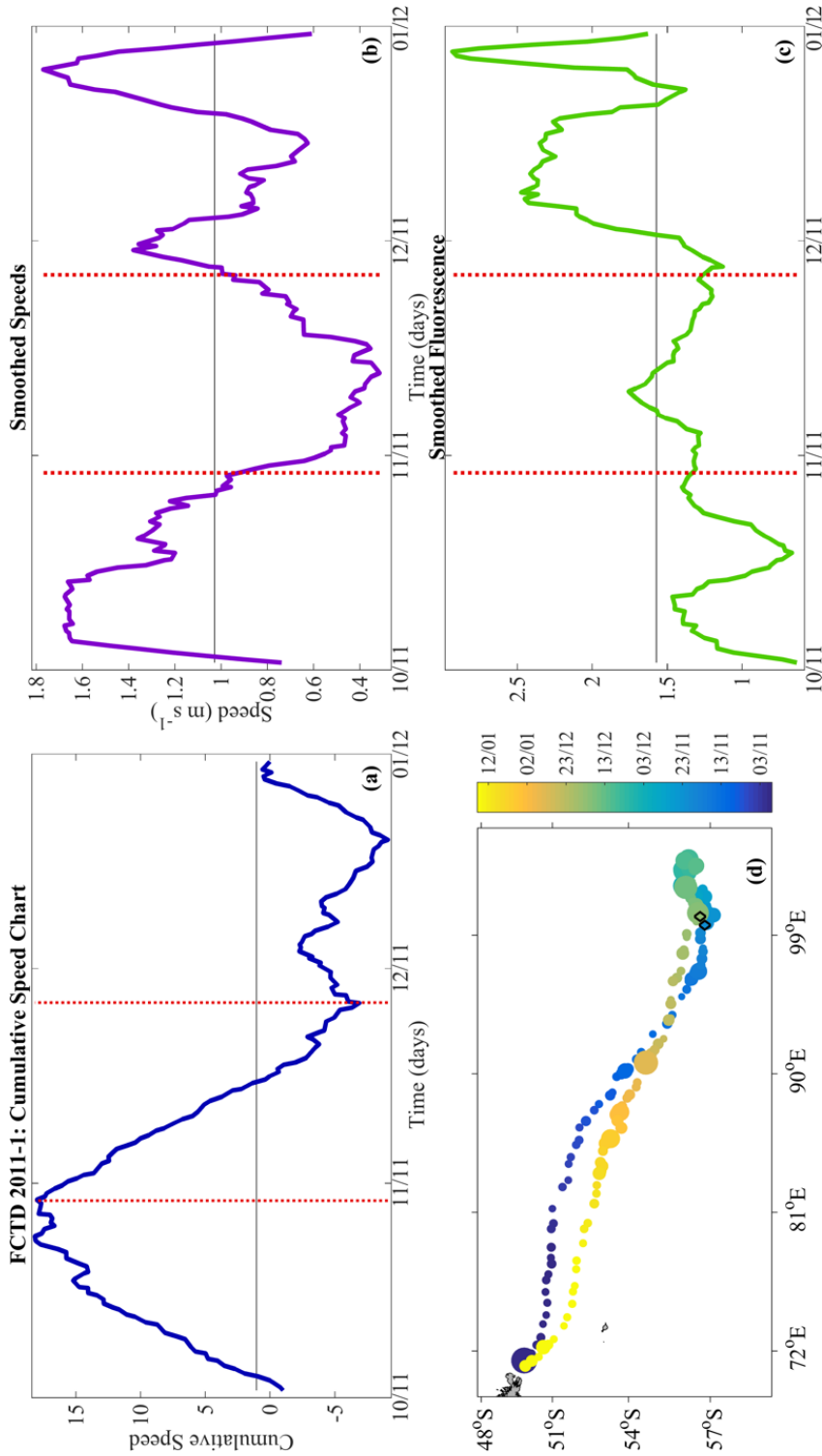


Figure 117: Visualising speed and phase changes for FCTD tag 2011-1. In (a), the CUSUM chart shows cumulative speed relative to the Page Quality Number, represented by the black horizontal line. The two dashed, vertical red lines represent phase changes from travel to foraging, and to travel again. Phase changes were detected automatically using a Kruskal-Wallis test, with manual confirmation. The same phase change lines are plotted in (b), which shows the track data over the same x-axis, but reported as m/s on the y-axis. The phase changes detected on the CUSUM chart are a match for when speeds drop below the mean (horizontal black line). Speed has been smoothed using a boxcar filter with window of 4, and is represented by the purple line. For comparison, vertically integrated fluorescence in green (c) has been smoothed using the same boxcar filter, and is plotted over the same x-axis with CUSUM phase change lines in red. Mean fluorescence is shown by the horizontal black line. For context, seal tracks are shown in (d). Larger marker sizes represent slower speeds, and visa-versa. The two black diamonds represent when in time the phase changes were detected on the CUSUM chart.

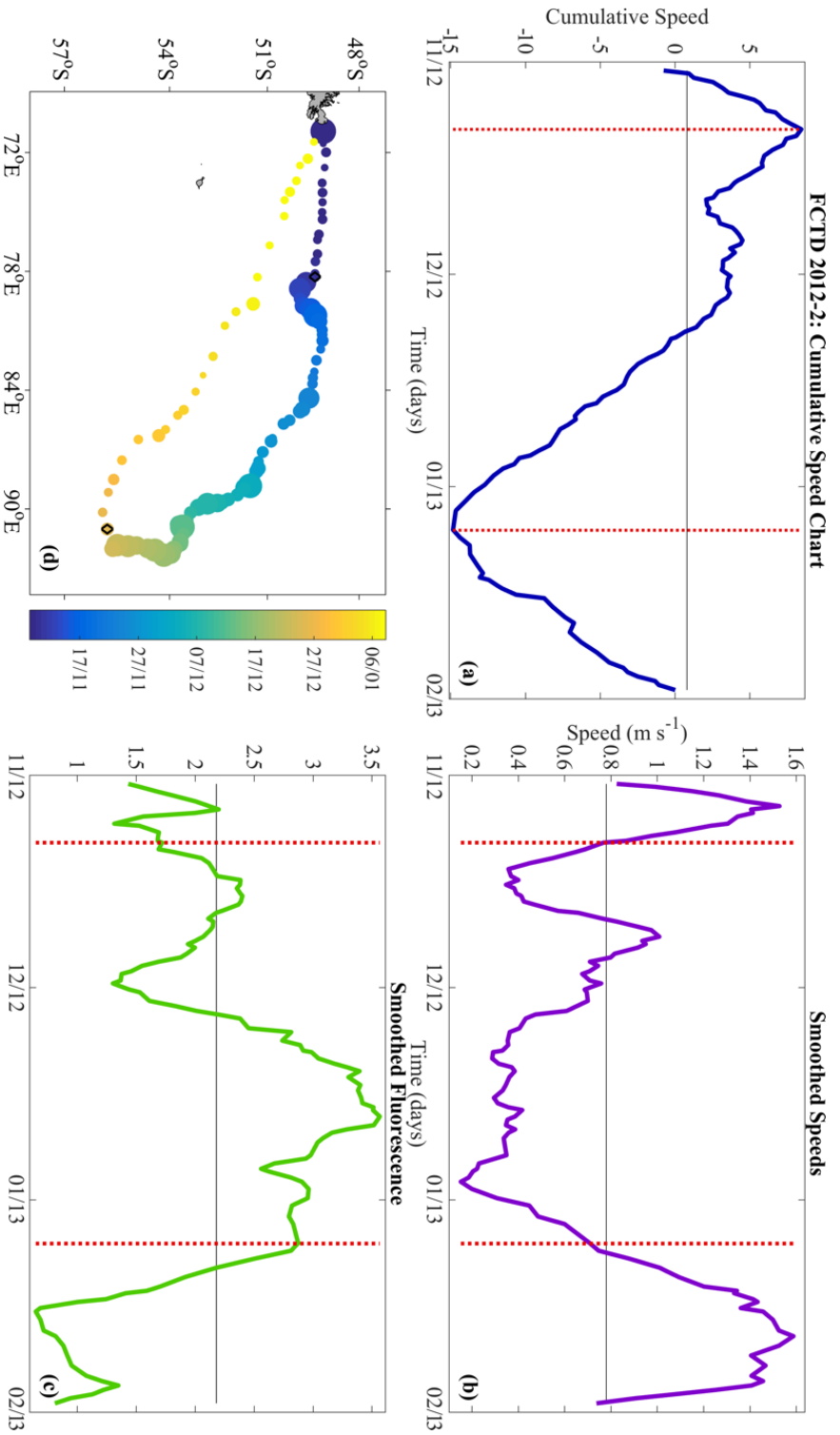


Figure 118: Visualising speed and phase changes for FCTD tag 2012-2. In (a), the CUSUM chart shows cumulative speed relative to the Page Quality Number, represented by the black horizontal line. The two dashed, vertical red lines represent phase changes from travel to foraging, and to travel again. Phase changes were detected automatically using a Kruskal-Wallis test, with manual confirmation. The same phase change lines are plotted in (b), which shows the track data over the same x-axis, but reported as m/s on the y-axis. The phase changes detected on the CUSUM chart are a match for when speeds drop below the mean (horizontal black line). Speed has been smoothed using a boxcar filter with window of 4, and is represented by the purple line. For comparison, vertically integrated fluorescence in green (c) has been smoothed using the same boxcar filter, and is plotted over the same x-axis with CUSUM phase change lines in red. Mean fluorescence is shown by the horizontal black line. For context, seal tracks are shown in (d). Larger marker sizes represent slower speeds, and *visa-versa*. The two black diamonds represent when in time the phase changes were detected on the CUSUM chart. This is the clearest example of the inverse relationship speed may have to phytoplankton, and there are short foraging phases within travel phases that appear related to patches of increased fluorescence.

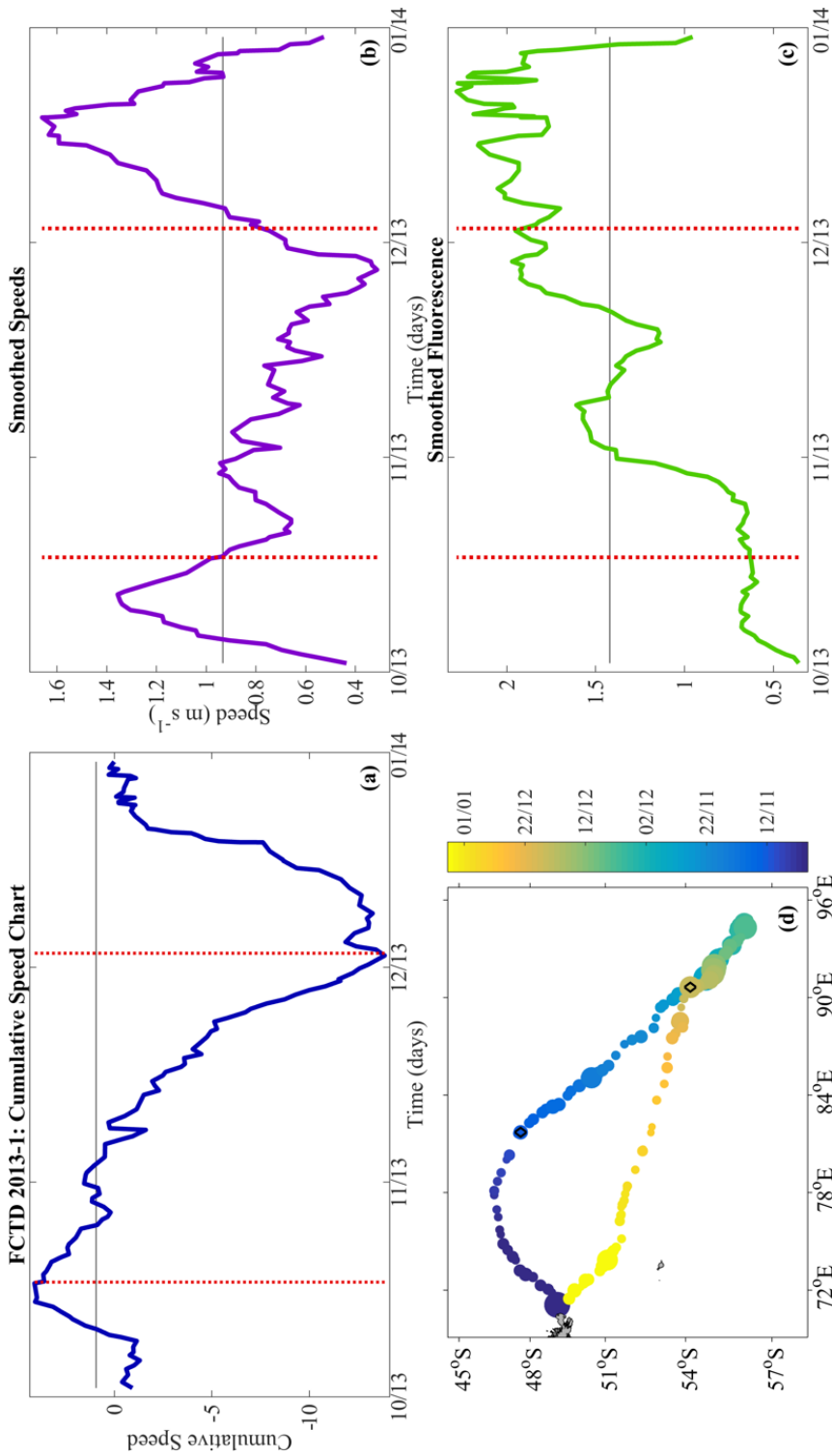


Figure 119: Visualising speed and phase changes for FCTD tag 2013-1. In (a), the CUSUM chart shows cumulative speed relative to the Page Quality Number, represented by the black horizontal line. The two dashed, vertical red lines represent phase changes from travel to foraging, and to travel again. Phase changes were detected automatically using a Kruskal-Wallis test, with manual confirmation. The same phase change lines are plotted in (b), which shows the track data over the same x-axis, but reported as m/s on the y-axis. The phase changes detected on the CUSUM chart are a match for when speeds drop below the mean (horizontal black line). Speed has been smoothed using a boxcar filter with window of 4, and is represented by the purple line. For comparison, vertically integrated fluorescence in green (c) has been smoothed using the same boxcar filter, and is plotted over the same x-axis with CUSUM phase change lines in red. Mean fluorescence is shown by the horizontal black line. For context, seal tracks are shown in (d). Larger marker sizes represent slower speeds, and visa-versa. The two black diamonds represent when in time the phase changes were detected on the CUSUM chart.

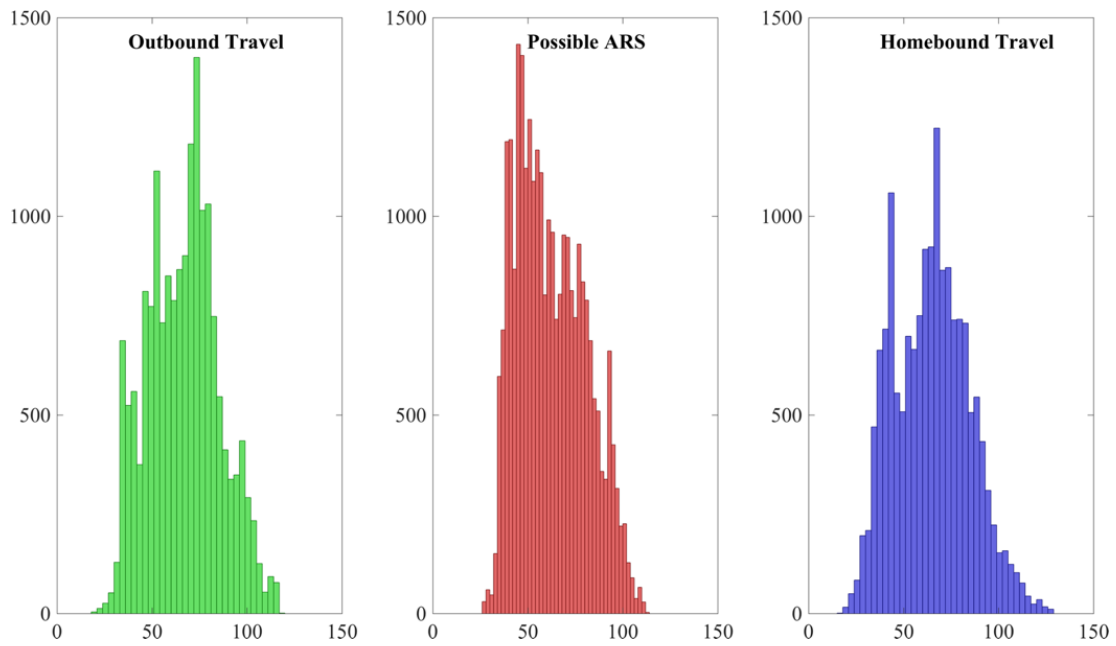


Figure 121: Histograms of light level data collected by southern elephant seals tagged with TDR light meters during three at-sea phases: outbound (green), possible area-restricted search foraging (red), and homebound (blue). Lower 1% light level depths in meters (x-axis) are indicative of phytoplankton or other materials in surface waters.

ficant. Within the outbound and homeward bound phases, it is possible that light levels are impacted by suspended sediment and run-off from Kerguelen. This would confound any possible relationships.

7.4 DISCUSSION

In this final data chapter, I have attempted to gauge if the at-sea behaviour of southern elephant seals from Kerguelen is independent of fluorescence and the 1% light level, as proxies of phytoplankton abundance. As discussed at length in this thesis, there are caveats associated with comparing coarse resolution satellite data with fine-scale *in situ* data. Results from previous studies that have attempted to compare behavioural data with satellite data do not always agree (e.g.: Jaud et al., 2012; Vacqu e-Garcia et al., 2015; Campagna et al., 2006 and 2007). For this reason, in this chapter, I have exclusively used *in situ* data collected by the tags. However, this does not fully resolve the problem of mismatches, and there is still the expectation of spatial and temporal lags. In this case, between phytoplankton concentration measured in the water column, and a possible behavioural response.

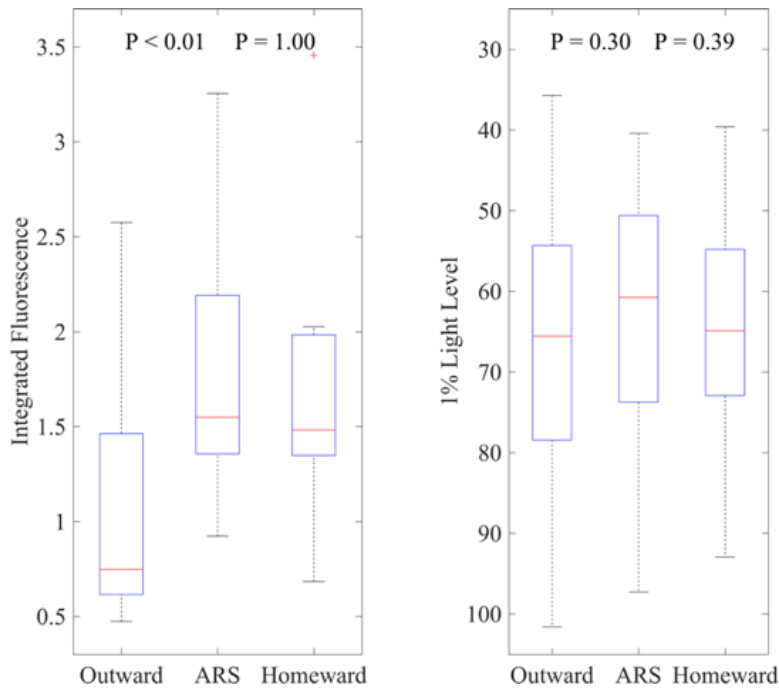


Figure 122: Boxplot showing median, interquartile ranges and outliers of fluorescence (left) and the 1% light level (right) for three phases: outbound travel, potential foraging and homebound travel.

Spatio-temporal lags between phytoplankton and elephant seals are inevitable because these marine mammals predate upon fish and squid, rather than the primary producers themselves. However, phytoplankton hotspots tend to be associated with elevated zooplankton such as krill (Weber and El-Sayed, 1985), which attract the prey that southern elephant seals target. Perturbations to phytoplankton patterns would be expected to impact on all these networks (Henson et al., 2009). Indeed, despite the gap between primary production and tertiary consumption, growing evidence suggests that distributions of marine predators are not independent of the physics or biogeochemistry (Boyd and Arnborn, 1991; Bradshaw et al., 2004; Bailleul et al., 2007; Biuw et al., 2007; Simmons et al., 2007; Biuw et al., 2010; Maxwell et al., 2011; Jaud et al., 2012; Vacquie-Garcia et al., 2012; Dragon et al., 2012; Costa et al., 2010).

Because of the deep-diving and wide-ranging foraging behaviours characteristic to elephant seals, we are unable to directly observe how they interact with the marine environment or their prey. However, marine phases make up around 80% of their lives (Le Boeuf and Laws, 1994; McIntyre et al., 2010). Adult females often travel thousands of kilometres from their natal island, traversing shelf seas, open waters, frontal systems and eddies, as well seamounts, ridges and continental shelf edges (McConnell et al., 1992; Campagna et al., 2007). These waters will differ in turbu-

lence, mixing and light penetration, as well as in phytoplankton, zooplankton and prey abundance. It is unlikely that a single variables would drive foraging behaviour, and it is more reasonable to suggest that a range of factors are involved. After all, Southern elephant seals are mammals. Foraging strategies are likely to be adaptive and flexible, and this question of behaviour is itself an entire field of research.

Bearing this in mind, my results do show some evidence that foraging behaviour is not independent of phytoplankton abundance. Using a cumulative sums analysis based on speed only, the method was reasonably successful at determining travelling from foraging phases. Data tested from three seals tagged with fluorometers and TDR light meters confirmed that the CUSUM method was successful at finding change points in datasets at different resolutions, or when gaps are present. When seals were examined individually, relationships between speed and fluorescence were often not clear. Nonetheless, fluorescence between outbound and foraging phases was significantly different.

Results between phases and the 1% light level were not significant, but there were small differences in means between foraging and travelling. It is unclear if this is due to different optical complexities of Southern Ocean waters, but the shallower (albeit non-significant) mean during the foraging phase is interesting. In open waters, there is less likely to be sediment or CDOM. Light attenuation is therefore most likely to be primarily altered by phytoplankton. Around Kerguelen, surface waters may be more turbid as a result of island run-off. I was unable to resolve this question, but future studies would benefit from better resolved optical properties of the waters around the island.

Results from a recent study on movement patterns of southern elephant seals showed that if trajectories are not corrected for the impact of the current, methods for detecting intensive foraging areas (ARS) may be misleading by (Della Penna et al., 2015). Tracked trajectories of elephant seals and other fast-swimming species have been understood to be largely independent of current effects, based on altimetry and model data (Bailleul et al., 2010; Sleeman et al., 2010). The work done for this chapter did not take displacement, drifting and passive advection into account, and it is beyond the scope of the CUSUM method to address such variables. Based on the most recent evidence that elephant seals travel mostly vertically during intensive foraging, and “horizontal displacements” are a function only of their moving frame

of reference, I would suggest that currents and dive shapes are included for future studies.

In closing: results from this chapter present tentative evidence that the at-sea behaviour of southern elephant seals is not independent of phytoplankton abundance. Within the context of an increasingly positive Southern Annular Mode, which is acting to perturb spatio-temporal patterns of phytoplankton in the Southern Ocean, this bears more investigation.

SUMMARY

8.1 CONTEXT

In Southern Ocean waters, our understandings of patterns of phytoplankton are still incomplete. Conflicting, strongly supported theories exist on why overall phytoplankton abundance is low. There is evidence for iron and light co-limitation, but also for mixing, stratification and high light stress (Sallee et al., 2015; Boyd et al., 2010; Smetacek et al., 2004; Moore et al., 1999; Sokolov and Rintoul, 2007; Sallee et al., 2010; Krishnamurthy et al. 2008; Lovenduski and Gruber, 2005). Secondly, contributions of deep chlorophyll maxima (DCM) to carbon flux and primary productivity are only now gaining support for being loci of sustained blooms with high export (Kemp and Villareal, 2013). For the purposes of monitoring phytoplankton over time, satellites can be used to examine ocean colour at spatial scales unmatched by other methods (Dierssen and Smith, 2000; McClain, 2009). However, the Southern Ocean is cloudy, and passively sensed data are often associated with high uncertainty. Furthermore, DCM present at depths that cannot be measured by satellite. To ground truth' satellite data and improve uncertainty on surface and vertical scales, continued collection of *in situ* data is essential.

Due to its convenience, fluorescence is widely utilised to measure vertical phytoplankton patterns (Lorenzen, 1966; Cullen and Eppley, 1981; Falkowski and Kolber, 1995; Lavigne et al., 2012). However, this method of data collection has its own drawbacks, and this has been particularly true for this study. Fluorescence data were collected without concurrent backscatter and/or PAR, instruments were not pre-calibrated in Southern Ocean waters, and calibration in the Mediterranean showed high variability between instruments. Nonetheless, in such under-sampled waters, there is motivation to process all *in situ* datasets to make them as representative as possible. For this body of work, the main requirement for processing fluorescence data was to correct for quenching at the surface, while preserving as much of the vertical di-

mension as possible. This required development of a bespoke method that relied on knowledge of the depth of the 1% light level.

8.2 SOME LIGHT ON THE MATTER

Over the same years that seals were tagged with fluorometers, other seals were also tagged with TDR light meters. Only 3 seals were tagged with both at the same time, meaning an alternative of estimating the 1% light level was necessary. Until 2016, NASA provided two evaluative products for estimating this depth. To test their representability, both needed to be tested against the 1% light level data collected by the tagged seals. However, processing the raw *in situ* light data did not prove to be a straightforward step. Understanding the impact that light sensor placement had on the collected data proved to be an essential part of the self-shading quality control process. To my knowledge, nothing has been formally published on this, but my results may serve to improve or optimise tagging and subsequent data acquisition for future deployments.

Examining relationships between the very fine scale *in situ* measures of the 1% light level and coarse resolution MODIS Z_{eu} demonstrated that satellite products tend to underestimate. This was useful; however, correlation was ultimately not the most appropriate method for examining relationships. Instead, examining 'the shape' of the two datasets when plotted over time allowed for a clearer match-up. This approach was less sensitive to differences in resolution and proved sufficient for examining broad relationships between the two datasets over time. It was not clear how much variability could be attributed to the MODIS remote sensor, and how much was contributed by the TDR light sensors. However, some improvement was evident using Lee's algorithm. The addition of IOP's improved retrieval of 1% light level estimates, despite Case 1 assumptions for Southern Ocean waters. My results contradict those of Soppa et al. (2013) but support findings of Shang et al. (2011).

8.3 QUENCHING CORRECTION

Based on these results, Lee Z_{eu} was used as a reference depth from which to correct for quenching. At the surface, corrected fluorescence values differed from those generated using the Xing et al. (2012) MLD method, but not significantly. Interestingly,

this suggests that DCM in the mixed layer (be it from floristic shifts or packaging effects) do not have a substantial impact on surface values. Results here proved valuable in later chapters, when comparing surface and vertically integrated fluorescence data with MODIS [Chl-a].

8.4 VERTICAL DIMENSION AND DCM

The vertical dimension and horizontal dynamics were addressed in two separate chapters, respectively. On vertical scales, around a quarter of all fluorescence profiles collected by tagged seals showed evidence of distinct deep chlorophyll maxima within or below MLD. Phytoplankton tend to be motile, but diatoms dominate in Southern Ocean waters and they are non-motile. It is tempting to suggest that differences between DCM and homogeneous profiles arise from shifts in community structure, with dinoflagellates dominating where vertical patchiness is evident. However, non-motile phytoplankton are not as passive as historically believed, and they are able to change their buoyancy to actively respond to light, nutrient levels or stresses (Arrieta et al., 2015). Particularly at night, DCM may be due to non-motile and motile phytoplankton overcoming high turbulence to create “strong fractal patchiness” (Durham et al., 2013). As much as grazing was not within the scope of this study, vertical migration would allow phytoplankton cells to move deeper at night, where risk of predation is reduced.

Alternatively, turbulence strength within the upper mixed layers of the Southern Ocean may not be high or uniform with depth (Franks, 2015). This seems counter-intuitive because topographic roughness, current speed, and wind speed are cited as the main factors controlling mixing in the Southern Ocean (Meyer et al., 2015). The waters around Kerguelen are impacted by all three. I strongly agree with the assertion of Meyer et al. (2015) that the dynamics and intensities of mixing here “require more attention”. Further, I suggest that vertical patterns of heterogeneity and homogeneity within these fluorescence data may add to information on spatial and temporal variability of turbulence and mixing.

8.5 HORIZONTAL DYNAMICS

Horizontal dynamics based on fluorescence and [Chl-a] were addressed in a dedicated chapter. *In situ* fluorescence data were corrected for quenching but were not transformed to chlorophyll-a concentrations for comparison with MODIS [Chl-a]. The absence of instrument calibration or concurrent ship-based sampling in the Southern Ocean prevented a conversion of fluorescence to chlorophyll-a. However, there is no universal relationship between fluorescence and chlorophyll-a concentration (Cullen, 1982). Had *in situ* calibration data been available, transforming fluorescence would have little obvious benefit.

Examining the fine scale *in situ* fluorescence against the coarse resolution MODIS [Chl-a] followed similar methods to those used to examine the 1% light level against Z_{eu} . Correlation demonstrated that satellite products tend to underestimate; however, correlation was ultimately not the most appropriate method for examining relationships. As was shown with the light data, examining 'the shape of the two datasets over time allowed for a clearer match-up. This is a relative rather than a quantitative approach; less sensitive to differences in resolution and sufficient for examining broad relationships between the two datasets over time. In this case, I'd suggest that the MODIS product was not the primary source of variability. Early calibration in the Mediterranean showed large differences between instruments that could not be resolved through subtraction of the dark count. For this reason, tag-to-tag variability remained the source of highest uncertainty.

At this point, it's fair to ask if the ground-truthing steps have added confidence to use of MODIS [Chl-a] and Z_{eu} as proxies of phytoplankton and light attenuation. I propose that they have. Satellite data at coarse spatial and temporal resolutions have shown relative relationships to high resolution data collected by animal-borne sensors that are still under development. Any perturbations to [Chl-a] and Lee Z_{eu} over the MODIS record can perhaps be approached with more certainty than if the ground-truthing steps had not been done.

8.6 A CHANGING OCEAN?

Henson et al. (2010) found that a time series of at least 40 years would be required to distinguish global warming signals from natural, interannual or decadal variability. I

do not dispute this. However, for this study, the focus is not on global climate change. In this case, the focus is on perturbations that may be associated with an increasingly positive SAM.

To this end, MODIS [Chl-a] data were examined for changes to phytoplankton over the 13-year timeseries, and relative to the SAM index. As a complementary product to MODIS [Chl-a], Lee Z_{eu} was used as an indicator of phytoplankton and other particles suspended in surface waters. In using Z_{eu} , I made no assumptions about water Case classifications. There is also a case for Z_{eu} not being proportional to changes in [Chl-a]. Minor increases in [Chl-a] had disproportionate impacts on Z_{eu} when waters were previously clear of suspended materials. Large declines in [Chl-a], on the other hand, showed little impact to Z_{eu} if phytoplankton, their detrital products, or indeed CDOM, were still present in some quantity.

For the whole of the Southern Ocean, trends in [Chl-a] from November to December suggest a slight decline in phytoplankton abundance. By February, this trend has changed sign and there appears to be a recovery of phytoplankton levels. Results point to a possible shift of timing of the bloom. However, trends are measured from over a relatively short timeseries and are mostly not significant, suggesting interannual to decadal scale variability. Nonetheless, some regional changes do appear to be associated with the increasingly positive SAM. Relative to this climate mode, overall declines in phytoplankton abundance in surface waters are significant 'only' over Decembers – historically the most productive month in terms of annual primary production in the Southern Ocean (Arrigo et al., 1998). Impacts of the SAM have more mixed results over January. By February, however, the overall decline has changed sign with extensive regions showing increases in phytoplankton abundance. Again, this points to a possible shift in the timing of the bloom.

Cloud fraction was included to investigate if it changes would be related to the anomalous low pressure and high pressure bands associated with a positive SAM. However, results were patchy. The southern sector of the Atlantic Ocean appears to be getting less cloudy over time, the southern Pacific appears to be getting cloudier over time, and the southern sector of the Indian Ocean is most variable between months. Relative to the SAM, increases in cloudiness over the southern Pacific was significant over December. Unlike the studies by Meskhidze and Nenes (2006, 2010) and McCoy et al. (2015), where high [Chl-a] was associated with elevated cloud condensation nuclei (CCN), no relationship was evident between cloud fraction and Z_{eu} or [Chl-a].

Saba et al. (2014) were also unable to find evidence of a relationship between cloud cover and phytoplankton abundance.

In no cases did changes to [Chl-a], Z_{eu} or cloud cover appear to be zonal. These results contradict the findings of Lovenduski and Gruber (2010), where SAM-related changes to satellite [Chl-a] (as well as wind and SST) were shown to be near-zonally symmetrical. However, the asymmetry of the results from this work echoes the studies by Lefebvre et al. (2004) and Sallee et al. (2005), who found non-annular responses of the Southern Ocean to this annular mode.

Declines in phytoplankton abundance over time or relative to the SAM may not point to net losses in biomass, but rather to increases in DCM. This supports by Behrenfeld et al. (2015), suggesting that changes in remotely sensed global [Chl-a] patterns are related to chlorophyll packaging, and are not indicative of phytoplankton decline. If decreases at the surface translate to increased formation of DCM, rates of photosynthesis, productivity, and export through sinking may not decline (Kemp and Villareal, 2013).

8.7 SEALS AND LITTLE GREEN CELLS

To examine if changes to phytoplankton patterns may have consequences for higher consumers in the ecosystem, it is first necessary to establish if at-sea predator behaviour can be related to the base of the marine food web. A range of proxies for detecting 'foraging behaviour' on horizontal scales exist. These include track-based metrics like first passage time, transit rate, and turning angle (LeBoeuf et al., 1988; Bost et al., 2007; Fauchald and Tveraa, 2003). Robinson et al. (2010) assessed all these foraging proxies using northern elephant seal data. Drift rate, a behaviour-independent measure of foraging success, was compared with when and where track-based metrics had flagged foraging behaviour. Speed was consistently the best single predictor, with periods of slow horizontal transit coinciding with improving body condition (Robinson et al., 2010; Le Boeuf et al., 2000; Crocker et al., 2006; Thums et al., 2011). Results from Robinson et al. (2010) support area restricted search (ARS) theories, which predict that swim speeds of marine predators would be measurably affected by the presence of prey 'hotspots' (MacArthur and Pianka, 1966; Kareiva and Odell, 1987; Dragon et al., 2010). Based on these results, I using speed as a single metric of

foraging behaviour. Applying a basic cumulative sums method proved efficient for detecting travel (high speeds) from potential foraging (slow).

Jonker and Bester (1998) were the first to identify and describe three-phase at-sea behaviour in tagged southern elephant seals. I followed this grouping and delineated all seal tracks into 'outbound transit' (travel), 'distant foraging' (potential ARS) and 'inbound transit' (travel). However, this chapter would have benefited from some relaxation of these three criteria. Although seals do largely exhibit the phases described by Jonker and Bester (1998), shorter, less intense foraging behaviour does appear to take place within travel phases. These smaller foraging phases are often clear on the CUSUM chart and are detected by the Kruskal-Wallis phase change test. Because they are shorter in length, I would suggest that they are opportunistic relative to the 'distant' ARS phase. Moreover, they appear to coincide with patches of higher fluorescence. For future work, examining in-travel phase foraging relative to fluorescence may reduce some of the variability in the relationship between speed and fluorescence.

In this chapter, fluorescence and the depth of the 1% light level were used as proxies of phytoplankton abundance. These variables were collected at the same as the behavioural data, which resolves mismatches in resolution that have hindered other studies (Biuw et al., 2007). Despite anticipated spatio-temporal lags between elephant seal behaviour and the bottom of the marine food web, foraging was not independent of phytoplankton abundance between outbound and potential ARS phases. On the other hand, although mean depth was shallower at the distal end of tracks in open waters (ARS), differences between light level and phases were not significant. Within outbound and homeward bound phases, light levels may be impacted by suspended sediment from Kerguelen itself, confounding any relationships. However, it's also possible that foraging is unrelated to light levels. It's equally possible that phytoplankton is higher in foraging phases because December and January tend to be characterised by elevated phytoplankton abundances. Further investigation may answer some of these questions.

In closing, based on this PhD work, a number of results may be of relevance to the global scientific community. Firstly, MODIS [Chl-a] and Lee Z_{eu} products can be related to fine-scale fluorescence and light data collected by tagged seals. I would tentatively suggest that the remotely sensed data are possibly not sufficient for quantitative comparisons with *in situ* data, but correlations do confirm that MODIS underestim-

ates. Secondly, with some confidence afforded by the ground-truthing steps, phytoplankton patterns in some regions of the Southern Ocean do not appear independent of atmospheric variability dominated by the SAM. It is likely that these perturbations are mediated by the strengthening winds and altered mixing regimes associated with the SAM positive trend. Finally, results on behavioural patterns are less clear, but they provide some evidence that foraging behaviours of southern elephant seals are not be independent of phytoplankton abundance and distribution.

8.8 RECOMMENDATIONS FOR FUTURE DEPLOYMENTS

For improving or avoiding quenching correction: The method I've presented for correcting quenching is only applicable under specific circumstances, and makes assumptions about homogeneity within Z_{eu} . As animal-borne tags begin to integrate increasingly miniaturised instruments, I recommend the addition of PAR and backscatter for improved quenching correction methods. It may, however, just be simpler for tags to be programmed to collect data at night. This would allow for more data from more dives to be collected over the relatively short night-time, and with substantially greater confidence. All night and overcast data are discarded from the light level datasets with little to no negative impact, so this is a viable suggestion.

For calculating the Dark Count: Fluorometers do need to start collecting data from below 200m. Removing the offset does not resolve variability between tags, but a more accurate dark count would prove useful for calculating error and confidence per tag.

BIBLIOGRAPHY

- Ainley, D. G. et al. (1991). 'The structure of upper level pelagic food webs in the Antarctic: Effect of phytoplankton distribution'. In: *Journal of Marine Systems* 2.1-2, pp. 111–122. ISSN: 09247963. DOI: [10.1016/0924-7963\(91\)90017-0](https://doi.org/10.1016/0924-7963(91)90017-0).
- Aksnes, Dag L., Mark D. Ohman and Pascal Rivière (2007). 'Optical effect on the nitracline in a coastal upwelling area'. In: *Limnology and Oceanography* 52.3, pp. 1179–1187. ISSN: 0024-3590. DOI: [10.4319/lo.2007.52.3.1179](https://doi.org/10.4319/lo.2007.52.3.1179).
- Alderkamp, Anne-Carlijn Carlijn et al. (2011). 'Short-term photoacclimation effects on photoinhibition of phytoplankton in the Drake Passage (Southern Ocean)'. In: *Deep-Sea Research Part I: Oceanographic Research Papers* 58.9, pp. 943–955. ISSN: 09670637. DOI: [10.1016/j.dsr.2011.07.001](https://doi.org/10.1016/j.dsr.2011.07.001). URL: <http://linkinghub.elsevier.com/retrieve/pii/S0967063711001233>.
- Alderkamp, Anne-Carlijn et al. (2010). 'Can photoinhibition control phytoplankton abundance in deeply mixed water columns of the Southern Ocean?' In: *Limnology and Oceanography* 55.3, pp. 1248–1264. ISSN: 00243590. DOI: [10.4319/lo.2010.55.3.1248](https://doi.org/10.4319/lo.2010.55.3.1248). URL: <http://doi.wiley.com/10.4319/lo.2010.55.3.1248>.
- Arrieta J., Barreira A. and I. Tuval (2015). 'Microscale patches of nonmotile phytoplankton'. In: *Physical review letters* 114(12).
- Arrigo, Kevin R. and Gert L. van Dijken (2011). 'Secular trends in Arctic Ocean net primary production'. In: *Journal of Geophysical Research* 116.C9, pp. 1–15. ISSN: 0148-0227. DOI: [10.1029/2011JC007151](https://doi.org/10.1029/2011JC007151).
- Arrigo, Kevin R., Gert L. van Dijken and Seth Bushinsky (2008). 'Primary production in the Southern Ocean, 1997-2006'. In: *Journal of Geophysical Research* 113.Co8004, doi:10.1029/2007JC004551. ISSN: 0148-0227. DOI: [10.1029/2007JC004551](https://doi.org/10.1029/2007JC004551). URL: <http://doi.wiley.com/10.1029/2007JC004551>.
- Arrigo, Kevin R. et al. (1998). 'Primary production in Southern Ocean waters'. In: *Journal of Geophysical Research* 103, pp. 15587–15600. ISSN: 0148-0227. DOI: [10.1029/98JC00930](https://doi.org/10.1029/98JC00930).
- Arrigo, Kevin R. et al. (2010). 'Photophysiology in two major southern ocean phytoplankton taxa: Photosynthesis and growth of *Phaeocystis antarctica* and *Fragilariopsis cylindrus* under different irradiance levels'. In: *Integrative and Comparative*

- ive Biology*. Vol. 50. 6, pp. 950–966. ISBN: 1557-7023 (Electronic)\r1540-7063 (Linking). DOI: [10.1093/icb/icq021](https://doi.org/10.1093/icb/icq021).
- Bailleul, Frédéric et al. (2007). 'Successful foraging zones of southern elephant seals from the Kerguelen Islands in relation to oceanographic conditions'. In: *Philosophical Transactions of the Royal Society B: Biological Sciences* 362.1487, pp. 2169–2181. ISSN: 0962-8436. DOI: [10.1098/rstb.2007.2109](https://doi.org/10.1098/rstb.2007.2109). URL: <http://www.pubmedcentral.nih.gov/articlerender.fcgi?artid=2442861&tool=pmcentrez&rendertype=abstract>.
- Barraquand, Frédéric and Simon Benhamou (2008). 'Animal movements in heterogeneous landscapes: Identifying profitable places and homogeneous movement bouts'. In: *Ecology* 89.12, pp. 3336–3348. ISSN: 00129658. DOI: [10.1890/08-0162.1](https://doi.org/10.1890/08-0162.1).
- Beaulieu, C. et al. (2013). 'Factors challenging our ability to detect long-term trends in ocean chlorophyll'. In: *Biogeosciences* 10.4, pp. 2711–2724. ISSN: 17264170. DOI: [10.5194/bg-10-2711-2013](https://doi.org/10.5194/bg-10-2711-2013).
- Behrenfeld, M. J. et al. (2009). 'Satellite-detected fluorescence reveals global physiology of ocean phytoplankton'. In: *Biogeosciences* 6.5, pp. 779–794. ISSN: 1726-4189. DOI: [10.5194/bg-6-779-2009](https://doi.org/10.5194/bg-6-779-2009). URL: <http://www.biogeosciences.net/6/779/2009/>.
- Behrenfeld, Michael J (2010). 'Abandoning sverdrup's critical depth hypothesis on phytoplankton blooms'. In: *Ecology* 91.4, pp. 977–989. ISSN: 00129658. DOI: [10.1890/09-1207.1](https://doi.org/10.1890/09-1207.1).
- Behrenfeld, Michael J. and Emmanuel Boss (2006). 'Beam attenuation and chlorophyll concentration as alternative optical indices of phytoplankton biomass'. In: *Journal of Marine Research* 64.3, pp. 431–451. ISSN: 00222402. DOI: [10.1357/002224006778189563](https://doi.org/10.1357/002224006778189563).
- Behrenfeld, Michael J. and Paul G. Falkowski (1997). 'Photosynthetic rates derived from satellite-based chlorophyll concentration'. In: *Limnology and Oceanography* 42.1, pp. 1–20. ISSN: 0024-3590. DOI: [10.4319/lo.1997.42.1.0001](https://doi.org/10.4319/lo.1997.42.1.0001).
- Behrenfeld, Michael J et al. (2006). 'Climate-driven trends in contemporary ocean productivity.' In: *Nature* 444.7120, pp. 752–755. ISSN: 0028-0836. DOI: [10.1038/nature05317](https://doi.org/10.1038/nature05317).
- Behrenfeld, Michael J. et al. (2015). 'Revaluating ocean warming impacts on global phytoplankton'. In: *Nature Climate Change* October. ISSN: 1758-678X. DOI: [10.1038/nclimate2838](https://doi.org/10.1038/nclimate2838). URL: <http://www.nature.com/doifinder/10.1038/nclimate2838>.

- Bester, M.N. (1988). 'Marking and monitoring studies of the Kerguelen stock of southern elephant seals *Mirounga leonina* and their bearing on biological research in the Vestfold Hills'. In: *Biology of the Vestfold Hills, Antarctica*, pp. 269–277.
- Biermann, L. et al. (2015). 'An alternative method for correcting fluorescence quenching'. English. In: *Ocean Science* 11.1, pp. 83–91. ISSN: 18120792. DOI: [10.5194/os-11-83-2015](https://doi.org/10.5194/os-11-83-2015). URL: <http://www.ocean-sci.net/11/83/2015/os-11-83-2015.html>.
- Bindoff, Nathaniel L et al. (2007). 'Observations: oceanic climate change and sea level'. In: *Intergovernmental Panel on Climate Change Fifth Assessment Report Climate Change 2013: The Physical Science Basis*. ISSN: 0521880092. URL: <http://nora.nerc.ac.uk/id/eprint/15400>.
- Biuw, M et al. (2007). 'Variations in behavior and condition of a Southern Ocean top predator in relation to in situ oceanographic conditions.' In: *Proceedings of the National Academy of Sciences of the United States of America* 104.34, pp. 13705–10. ISSN: 0027-8424. DOI: [10.1073/pnas.0701121104](https://doi.org/10.1073/pnas.0701121104). URL: <http://www.pnas.org/content/104/34/13705.full>.
- Biuw, Martin et al. (2010). 'Effects of hydrographic variability on the spatial, seasonal and diel diving patterns of Southern Elephant seals in the Eastern Weddell sea'. In: *PLoS ONE* 5.11. ISSN: 19326203. DOI: [10.1371/journal.pone.0013816](https://doi.org/10.1371/journal.pone.0013816).
- Bjornsson, H and S. a. Venegas (1997). 'A Manual for EOF and SVD Analysis of Climatic Data'. In: *CCGCR Report* 97, p. 52. ISSN: 0717-6163. DOI: [10.1002/elps.200700001](https://doi.org/10.1002/elps.200700001). arXiv: 9809069v1 [arXiv:gr-qc]. URL: <http://ci.nii.ac.jp/naid/10019979757/>.
- Block, B a et al. (2011). 'Tracking apex marine predator movements in a dynamic ocean.' In: *Nature* 475.7354, pp. 86–90. ISSN: 0028-0836. DOI: [10.1038/nature10082](https://doi.org/10.1038/nature10082). URL: <http://dx.doi.org/10.1038/nature10082><http://dx.doi.org/10.1038/nature10082><http://www.nature.com/doifinder/10.1038/nature10082>.
- Block, Barbara A. et al. (2002). 'Revealing pelagic habitat use: The tagging of Pacific pelagics program'. In: *Oceanologica Acta* 25.5, pp. 255–266. ISSN: 03991784. DOI: [10.1016/S0399-1784\(02\)01212-4](https://doi.org/10.1016/S0399-1784(02)01212-4).
- Boehme, L. et al. (2008a). 'Antarctic circumpolar current frontal system in the South Atlantic: Monitoring using merged Argo and animal-borne sensor data'. In: *Journal of Geophysical Research: Oceans* 113.9. ISSN: 21699291. DOI: [10.1029/2007JC004647](https://doi.org/10.1029/2007JC004647).

- Boehme, L et al. (2008b). 'Monitoring Drake Passage with elephant seals: Frontal structures and snapshots of transport'. In: *Limnology and Oceanography* 53.5, pp. 2350–2360. ISSN: 00243590. DOI: [10.4319/lo.2008.53.5\(part2\).2350](https://doi.org/10.4319/lo.2008.53.5(part2).2350). URL: <http://GotoISI://WOS:000261355400022>.
- Boehme, L. et al. (2009). 'Technical note: Animal-borne CTD-satellite relay data loggers for real-time oceanographic data collection'. In: *Ocean Science* 5, pp. 685–695. ISSN: 1812-0784. DOI: [10.5194/osd-6-1261-2009](https://doi.org/10.5194/osd-6-1261-2009). URL: <http://nora.nerc.ac.uk/10788/>.
- Boehme L., Thorpe S. E. Biuw M. Fedak M. and M. P. Meredith (2008). 'Monitoring Drake Passage with elephant seals: Frontal structures and snapshots of transport'. In: *Limnology and Oceanography* 53(5), p. 2350.
- Bopp, L et al. (2005). 'Response of diatoms distribution to global warming and potential implications: A global model study - art. no. L19606'. In: *Geophysical Research Letters* 32.19, p. 19606. ISSN: 0094-8276. DOI: [10.1029/2005GL023653](https://doi.org/10.1029/2005GL023653).
- Bost, C. A. et al. (2007). 'Changes in dive profiles as an indicator of feeding success in king and Ad??lie penguins'. In: *Deep-Sea Research Part II: Topical Studies in Oceanography* 54.3-4, pp. 248–255. ISSN: 09670645. DOI: [10.1016/j.dsr2.2006.11.007](https://doi.org/10.1016/j.dsr2.2006.11.007).
- Boyce, Daniel G, Marlon R Lewis and Boris Worm (2010). 'Global phytoplankton decline over the past century.' In: *Nature* 466.7306, pp. 591–596. ISSN: 1476-4687. DOI: [10.1038/nature09268](https://doi.org/10.1038/nature09268). URL: <http://dx.doi.org/10.1038/nature09268http://www.ncbi.nlm.nih.gov/pubmed/20671703>.
- Boyd, I. L. and T. Arnbohm (1991). 'Diving behaviour in relation to water temperature in the southern elephant seal: foraging implications'. In: *Polar Biology* 11.4, pp. 259–266. ISSN: 07224060. DOI: [10.1007/BF00238460](https://doi.org/10.1007/BF00238460).
- Boyd, I. L. and A. W A Murray (2001). 'Monitoring a marine ecosystem using responses of upper trophic level predators'. In: *Journal of Animal Ecology* 70.5, pp. 747–760. ISSN: 00218790. DOI: [10.1046/j.0021-8790.2001.00534.x](https://doi.org/10.1046/j.0021-8790.2001.00534.x).
- Bradshaw, Corey J A et al. (2004a). 'Loyalty pays: Potential life history consequences of fidelity to marine foraging regions by southern elephant seals'. In: *Animal Behaviour* 68.6, pp. 1349–1360. ISSN: 00033472. DOI: [10.1016/j.anbehav.2003.12.013](https://doi.org/10.1016/j.anbehav.2003.12.013).
- Bradshaw, Corey J a et al. (2004b). 'At-sea distribution of female southern elephant seals relative to variation in ocean surface properties'. In: *ICES Journal of Marine*

- Science* 61.6, pp. 1014–1027. ISSN: 10543139. DOI: [10.1016/j.icesjms.2004.07.012](https://doi.org/10.1016/j.icesjms.2004.07.012).
- Bruyn, T McIntyre P J N De and I J Ansorge M N Bester (2010). 'A lifetime at depth : vertical distribution of southern elephant seals in the water column'. In: pp. 1037–1048. DOI: [10.1007/s00300-010-0782-3](https://doi.org/10.1007/s00300-010-0782-3).
- Buiron D., Stenni B. Chappellaz J. Landais A. Baumgartner M. Bonazza M. Capron E. Frezzotti M. Kageyama M. Lemieux-Dudon B. and V. Masson-Delmotte (2012). 'Regional imprints of millennial variability during the MIS 3 period around Antarctica'. In: *Quaternary Science Reviews* 48, pp. 99–112.
- Cai, Wenju et al. (2005). 'The response of the Southern Annular Mode, the East Australian Current, and the southern mid-latitude ocean circulation to global warming'. In: *Geophysical Research Letters* 32.23, pp. 1–4. ISSN: 00948276. DOI: [10.1029/2005GL024701](https://doi.org/10.1029/2005GL024701). URL: <http://doi.wiley.com/10.1029/2005GL024701>.
- Campagna, Claudio et al. (2006). 'Southern elephant seal trajectories, fronts and eddies in the Brazil/Malvinas Confluence'. In: *Deep-Sea Research Part I: Oceanographic Research Papers* 53.12, pp. 1907–1924. ISSN: 09670637. DOI: [10.1016/j.dsr.2006.08.015](https://doi.org/10.1016/j.dsr.2006.08.015).
- Campagna, Claudio et al. (2007). 'Deep divers in shallow seas: Southern elephant seals on the Patagonian shelf'. In: *Deep-Sea Research Part I: Oceanographic Research Papers* 54.10, pp. 1792–1814. ISSN: 09670637. DOI: [10.1016/j.dsr.2007.06.006](https://doi.org/10.1016/j.dsr.2007.06.006).
- Campbell, JW (1995). 'The lognormal distribution as a model for bio-optical variability in the sea'. In: *Journal of Geophysical Research* 100.C7, pp. 13237–13254. ISSN: 0148-0227. URL: <http://onlinelibrary.wiley.com/doi/10.1029/95JC00458/full>.
- Carpenter, E J et al. (1995). 'The dinoflagellate *Dinophysis-Norvegica* - biological and ecological observations in the Baltic Sea'. In: *European Journal of Phycology* 30.1, pp. 1–9. ISSN: 0967-0262. DOI: [10.1080/09670269500650751](https://doi.org/10.1080/09670269500650751). URL: [GotoISI://A1995QJ40100001](http://www.isi.com/doi/10.1080/09670269500650751).
- Carranza, Magdalena M. and Sarah T. Gille (2015). 'Southern Ocean wind-driven entrainment enhances satellite chlorophyll-a through the summer'. In: *Journal of Geophysical Research C: Oceans* 120.1, pp. 304–323. ISSN: 21699291. DOI: [10.1002/2014JC010203](https://doi.org/10.1002/2014JC010203).
- Carrick, R and SE Ingham (1962). 'Studies on the southern elephant seal, *Mirounga leonina* (L.). V. Population dynamics and utilization'. In: *CSIRO Wildlife Research*

- 7.2, pp. 198–206. ISSN: 0007-9103. DOI: [10.1071/CWR9620198](https://doi.org/10.1071/CWR9620198). URL: <http://www.publish.csiro.au/?paper=CWR9620198>.
- Chan, Augustine T. (1980). 'Comparative physiological study of marine diatoms and dinoflagellates in relation to irradiance and cell size: II relationship between photosynthesis, growth, and carbon/chlorophyll a ratio'. In: *Journal of Phycology* 16.3, pp. 428–432. ISSN: 1529-8817. DOI: [10.1111/j.1529-8817.1980.tb03056.x](https://doi.org/10.1111/j.1529-8817.1980.tb03056.x). URL: <http://dx.doi.org/10.1111/j.1529-8817.1980.tb03056.x>.
- Charrassin, J. B. , Roquet, F. , Park, Y. H. , Bailleul, F. , Guinet, C. , Meredith, M. , Nicholls, K. , Thorpe, S. , Tremblay, Y. , Costa, D. , Göbel, M. , Muelbert, M. , Bestler, M. N. , Plötz, J. , Bornemann, H. , Timmermann, R. , Hindell, M. , Meijers, C. (2010). 'New Insights into Southern Ocean Physical and Biological Processes Revealed by Instrumented Elephant Seals'. In: *Proceedings of OceanObs'09: Sustained Ocean Observations and Information for Society* 2.9296, pp. 154–165. DOI: [10.5270/OceanObs09.cwp.15](https://doi.org/10.5270/OceanObs09.cwp.15). URL: <http://www.oceanobs09.net/proceedings/cwp/cwp15>.
- Chiswell, Stephen M. (2011). 'Annual cycles and spring blooms in phytoplankton: Don't abandon Sverdrup completely'. In: *Marine Ecology Progress Series* 443, pp. 39–50. ISSN: 01718630. DOI: [10.3354/meps09453](https://doi.org/10.3354/meps09453).
- Chiswell, Stephen M., Paulo H R Calil and Philip W. Boyd (2015). 'Spring blooms and annual cycles of phytoplankton: a unified perspective'. In: *Journal of Plankton Research* 37.3, pp. 500–508. ISSN: 0142-7873. DOI: [10.1093/plankt/fbv021](https://doi.org/10.1093/plankt/fbv021). URL: <http://www.plankt.oxfordjournals.org/cgi/doi/10.1093/plankt/fbv021>.
- Claustre, H. et al. (2008). 'Gross community production and metabolic balance in the South Pacific Gyre, using a non intrusive bio-optical method'. In: *Biogeosciences* 5.2, pp. 463–474. ISSN: 1726-4189. DOI: [10.5194/bgd-4-3089-2007](https://doi.org/10.5194/bgd-4-3089-2007). URL: <http://hal.archives-ouvertes.fr/hal-00330701>.
- Clementson L. A., Parslow J. S. Turnbull A. R. McKenzie D. C. and C. E. Rathbone (2001). 'Optical properties of waters in the Australasian sector of the Southern Ocean'. In: *Journal of Geophysical Research*.
- Costa, Daniel P. et al. (2010). 'Approaches to studying climatic change and its role on the habitat selection of antarctic pinnipeds'. In: *Integrative and Comparative Biology*. Vol. 50. 6, pp. 1018–1030. ISBN: 1540-7063. DOI: [10.1093/icb/icq054](https://doi.org/10.1093/icb/icq054).
- Cullen, J J and R W Eppley (1981). 'Chlorophyll Maximum Layers of the Southern-California Bight and Possible Mechanisms of their Formation and Maintenance'. In: *Oceanologica Acta* 4.1, pp. 23–32.

- Cullen, John J. (1982). 'The deep chlorophyll maximum: comparing vertical profiles of chlorophyll'. In: *Deep Sea Research Part B. Oceanographic Literature Review* 29.12, p. 787. ISSN: 01980254. DOI: [10.1016/0198-0254\(82\)90274-6](https://doi.org/10.1016/0198-0254(82)90274-6).
- Davies-Colley, R. J. and D. G. Smith (2001). 'Turbidity, Suspended Sediment, and Water Clarity: a Review'. In: *American Water Resources Association* 37.5, pp. 1085–1101. ISSN: 1093-474X. DOI: [10.1111/j.1752-1688.2001.tb03624.x](https://doi.org/10.1111/j.1752-1688.2001.tb03624.x).
- Della Penna, Alice et al. (2015). 'Quasi-planktonic behavior of foraging top marine predators.' In: *Scientific reports* 5.November, p. 18063. ISSN: 2045-2322. DOI: [10.1038/srep18063](https://doi.org/10.1038/srep18063). URL: <http://www.pubmedcentral.nih.gov/articlerender.fcgi?artid=4678296&tool=pmcentrez&rendertype=abstract>.
- Dierssen, H. M. and R. C. Smith (2000). 'Bio-optical properties and remote sensing ocean color algorithms for Antarctic Peninsula waters'. In: *Journal of Geophysical Research* 105.C11, p. 26301. ISSN: 0148-0227. DOI: [10.1029/1999JC000296](https://doi.org/10.1029/1999JC000296). URL: <http://doi.wiley.com/10.1029/1999JC000296>.
- Dong, Shenfu et al. (2008). 'Southern ocean mixed-layer depth from Argo float profiles'. In: *Journal of Geophysical Research: Oceans* 113.6. ISSN: 21699291. DOI: [10.1029/2006JC004051](https://doi.org/10.1029/2006JC004051).
- Dragon, Anne Cecile et al. (2010). 'Linking foraging behaviour to physical oceanographic structures: Southern elephant seals and mesoscale eddies east of Kerguelen Islands'. In: *Progress in Oceanography* 87.1-4, pp. 61–71. ISSN: 00796611. DOI: [10.1016/j.pocean.2010.09.025](https://doi.org/10.1016/j.pocean.2010.09.025).
- Duffy, J Emmett (2002). 'Biodiversity and ecosystem function: the consumer connection'. In: *Oikos* 99.2, pp. 201–219. ISSN: 0030-1299. DOI: [10.1034/j.1600-0706.2002.990201.x](https://doi.org/10.1034/j.1600-0706.2002.990201.x). URL: <http://dx.doi.org/10.1034/j.1600-0706.2002.990201.x>.
- Dufour, Carolina et al. (2013). 'Interannual variability of primary production and air-sea CO₂ flux in the Atlantic and Indian sectors of the Southern Ocean.' In: 15, p. 8634.
- Durham, William M et al. (2013). 'Turbulence drives microscale patches of motile phytoplankton.' In: *Nature communications* 4, p. 2148. ISSN: 2041-1723. DOI: [10.1038/ncomms3148](https://doi.org/10.1038/ncomms3148). URL: <http://www.ncbi.nlm.nih.gov/pubmed/23852011>.
- Estrada, M. et al. (1993). *Variability of deep chlorophyll maximum characteristics in the northwestern Mediterranean*. DOI: [10.3354/meps092289](https://doi.org/10.3354/meps092289).

- Fairbanks, Richard G. et al. (1982). 'Vertical distribution and isotopic fractionation of living planktonic foraminifera from the Panama Basin'. In: *Nature* 298.5877, pp. 841–844. ISSN: 0028-0836. DOI: [10.1038/298841a0](https://doi.org/10.1038/298841a0). arXiv: [arXiv:1011.1669v3](https://arxiv.org/abs/1011.1669v3).
- Falkowski, Paul G., Richard T. Barber and Victor Smetacek (1998). 'Biogeochemical controls and feedbacks on ocean primary production'. In: *Science* 281, pp. 200–206. ISSN: 1095-9203. DOI: [10.1126/science.281.5374.200](https://doi.org/10.1126/science.281.5374.200).
- Falkowski, Pg and Z Kolber (1995). 'Variations in Chlorophyll Fluorescence Yields in Phytoplankton in the World Oceans'. In: *Australian Journal of Plant Physiology* 22.2, p. 341. ISSN: 0310-7841. DOI: [10.1071/PP9950341](https://doi.org/10.1071/PP9950341).
- Fauchald, Per and Torkild Tveraa (2003). 'Using first-passage time in the analysis of area-restricted search and habitat selection'. In: *Ecology* 84.2, pp. 282–288. ISSN: 00129658. DOI: [10.1890/0012-9658\(2003\)084\[0282:UFPTIT\]2.0.CO;2](https://doi.org/10.1890/0012-9658(2003)084[0282:UFPTIT]2.0.CO;2).
- Fedak, M. A. (2013). 'The impact of animal platforms on polar ocean observation'. In: *Deep-Sea Research Part II: Topical Studies in Oceanography* 88-89, pp. 7–13. ISSN: 09670645. DOI: [10.1016/j.dsr2.2012.07.007](https://doi.org/10.1016/j.dsr2.2012.07.007).
- Fedak, Mike (2004). 'Marine animals as platforms for oceanographic sampling: a ? win / win ? situation for biology and operational oceanography'. In: *Memoirs of the National Institute for Polar Research, Special Issue* 58, pp. 133–147.
- Finkel, Zoe V. (2014). 'Marine Net Primary Production'. In: *Global Environmental Change*. Dordrecht: Springer Netherlands, pp. 117–124. ISBN: 978-94-007-5783-7. DOI: [10.1007/978-94-007-5784-4_{_}42](https://doi.org/10.1007/978-94-007-5784-4_{_}42). URL: http://link.springer.com/10.1007/978-94-007-5784-4http://link.springer.com/10.1007/978-94-007-5784-4_{_}42.
- Franks, Peter J S (2015). 'Has Sverdrup's critical depth hypothesis been tested? Mixed layers vs. turbulent layers'. In: *ICES Journal of Marine Science* 72.6, pp. 1897–1907. ISSN: 10959289. DOI: [10.1093/icesjms/fsu175](https://doi.org/10.1093/icesjms/fsu175). URL: <http://icesjms.oxfordjournals.org/lookup/doi/10.1093/icesjms/fsu175>.
- Fu, G, K S Baith and C R McClain (1998). 'SeaDAS: The SeaWiFS Data Analysis System'. In: *Proceedings of the Fourth Ocean Remote Sensing Conference*, pp. 73–77.
- Gallon, S. et al. (2013). 'Identifying foraging events in deep diving southern elephant seals, *Mirounga leonina*, using acceleration data loggers'. In: *Deep-Sea Research Part II: Topical Studies in Oceanography* 88-89, pp. 14–22. ISSN: 09670645. DOI: [10.1016/j.dsr2.2012.09.002](https://doi.org/10.1016/j.dsr2.2012.09.002).

- Ganachaud, A. and C. Wunsch (2000). 'Improved estimates of global ocean circulation, heat transport and mixing from hydrographic data.' In: *Nature* 408.6811, pp. 453–457. ISSN: 0028-0836. DOI: [10.1038/35044048](https://doi.org/10.1038/35044048).
- Garcia, V. M T and D. A. Purdie (1992). 'The influence of irradiance on growth, photosynthesis and respiration of *Gyrodinium cf. aureolum*'. In: *Journal of Plankton Research* 14.9, pp. 1251–1265. ISSN: 01427873. DOI: [10.1093/plankt/14.9.1251](https://doi.org/10.1093/plankt/14.9.1251). URL: <http://plankt.oxfordjournals.org/cgi/doi/10.1093/plankt/14.9.1251>.
- Gille, Sarah T (2002). 'Warming of the Southern Ocean since the 1950s.' In: *Science* 295.2002, pp. 1275–1277. ISSN: 00368075. DOI: [10.1126/science.1065863](https://doi.org/10.1126/science.1065863).
- Gille, Sarah T. (2003). 'Float Observations of the Southern Ocean. Part I: Estimating Mean Fields, Bottom Velocities, and Topographic Steering'. In: *Journal of Physical Oceanography* 33.6, pp. 1167–1181. ISSN: 0022-3670. DOI: [10.1175/1520-0485\(2003\)033<1167:F00TS0>2.0.CO;2](https://doi.org/10.1175/1520-0485(2003)033<1167:F00TS0>2.0.CO;2).
- Gille, Sarah T (2014a). 'Meridional displacement of the Antarctic Circumpolar Current.' In: *Philosophical transactions. Series A, Mathematical, physical, and engineering sciences* 372.2019, p. 20130273. ISSN: 1364-503X. DOI: [10.1098/rsta.2013.0273](https://doi.org/10.1098/rsta.2013.0273). URL: <http://www.pubmedcentral.nih.gov/articlerender.fcgi?artid=4032512&tool=pmcentrez&rendertype=abstract>.
- Gille, Sarah T (2014b). 'Meridional displacement of the Antarctic Circumpolar Current.' In: *Philosophical transactions. Series A, Mathematical, physical, and engineering sciences* 372.2019, p. 20130273. ISSN: 1364-503X. DOI: [10.1098/rsta.2013.0273](https://doi.org/10.1098/rsta.2013.0273). URL: <http://www.pubmedcentral.nih.gov/articlerender.fcgi?artid=4032512&tool=pmcentrez&rendertype=abstract>.
- Gillett, N P, T D Kell and P D Jones (2006). 'Regional climate impacts of the Southern Annular Mode'. In: *Geophysical Research Letters* 33.23, pp. 1–4. ISSN: 00948276. DOI: [10.1029/2006GL027721](https://doi.org/10.1029/2006GL027721).
- Gordon, Arnold L et al. (2001). 'Interocean exchange'. In: *Ocean circulation and climate observing and modelling the global ocean* 77, pp. 303–314.
- Gordon, H R and A Morel (1983). 'Remote assessment of ocean color for interpretation of satellite visible imagery: A review'. In: *Lecture Notes on Coastal and Estuarine Study* 4, pp. 1–114. ISSN: 0025-3154. DOI: [10.1029/LN004](https://doi.org/10.1029/LN004).
- Graham R. M., Boer A. M. Heywood K. J. Chapman M. R. and D. P. Stevens (2012). 'Southern Ocean fronts: Controlled by wind or topography?' In: *Journal of Geophysical Research: Oceans* 117(C8).

- Guinet, C. et al. (2013). 'Calibration procedures and first dataset of Southern Ocean chlorophyll a profiles collected by elephant seals equipped with a newly developed CTD-fluorescence tags'. In: *Earth System Science Data* 5.1, pp. 15–29. ISSN: 18663508. DOI: [10.5194/essd-5-15-2013](https://doi.org/10.5194/essd-5-15-2013).
- Hahn-Woernle, L., H. A. Dijkstra and H. J. Van Der Woerd (2014). 'Sensitivity of phytoplankton distributions to vertical mixing along a North Atlantic transect'. In: *Ocean Science* 10.6, pp. 993–1011. ISSN: 18120792. DOI: [10.5194/os-10-993-2014](https://doi.org/10.5194/os-10-993-2014). URL: <http://www.ocean-sci-discuss.net/11/839/2014/>.
- Hall, Alex and Martin Visbeck (2002). 'Synchronous variability in the Southern Hemisphere atmosphere, sea ice, and ocean resulting from the annular mode'. In: *Journal of Climate* 15.21, pp. 3043–3057. ISSN: 08948755. DOI: [10.1175/1520-0442\(2004\)017<2249:CO SVIT>2.0.CO;2](https://doi.org/10.1175/1520-0442(2004)017<2249:CO SVIT>2.0.CO;2).
- Heerah K., Hindell M. Guinet C. and J. B. Charrassin (2014). 'A new method to quantify within dive foraging behaviour in marine predators'. In: *PLoS One* 9(6), e99329.
- Henson, S.a. et al. (2010). 'Detection of anthropogenic climate change in satellite records of ocean chlorophyll and productivity'. In: *Biogeosciences*, pp. 621–640. ISSN: 1726-4189. DOI: [10.5194/bg-7-621-2010](https://doi.org/10.5194/bg-7-621-2010). URL: <http://eprints.soton.ac.uk/154065/>.
- Henson, Stephanie A., John P. Dunne and Jorge L. Sarmiento (2009). 'Decadal variability in North Atlantic phytoplankton blooms'. In: *Journal of Geophysical Research: Oceans* 114.4, pp. 1–11. ISSN: 21699291. DOI: [10.1029/2008JC005139](https://doi.org/10.1029/2008JC005139).
- Hindell, M A, D J Slip and H R Burton (1991). 'The Diving Behavior of Adult Male and Female Southern Elephant Seals, *Mirounga-leonina* (Pinnipedia, Phocidae)'. In: *Australian Journal of Zoology* 39.5, pp. 595–619. DOI: [Doi10.1071/Zo9910595](https://doi.org/10.1071/Zo9910595). URL: <http://www.publish.csiro.au/?paper=Z09910595>.
- Ho, M., A. S. Kiem and D. C. Verdon-Kidd (2012). *The Southern Annular Mode: A comparison of indices*. DOI: [10.5194/hess-16-967-2012](https://doi.org/10.5194/hess-16-967-2012). URL: <http://www.hydro-earth-syst-sci.net/16/967/2012/>.
- Hobbs, William R. and Marilyn N. Raphael (2010). 'Characterizing the zonally asymmetric component of the SH circulation'. In: *Climate Dynamics* 35.5, pp. 859–873. ISSN: 09307575. DOI: [10.1007/s00382-009-0663-z](https://doi.org/10.1007/s00382-009-0663-z).

- Holm-Hansen, Osmund and Christopher D. Hewes (2004). *Deep chlorophyll-a maxima (DCMs) in Antarctic waters: I. Relationships between DCMs and the physical, chemical, and optical conditions in the upper water column*. DOI: [10.1007/s00300-004-0641-1](https://doi.org/10.1007/s00300-004-0641-1).
- Huisman, Jef, Paul van Oostveen and Franz J. Weissing (1999). 'Species Dynamics in Phytoplankton Blooms: Incomplete Mixing and Competition for Light'. In: *The American Naturalist* 154.1, pp. 46–68. ISSN: 0003-0147. DOI: [10.1086/303220](https://doi.org/10.1086/303220).
- Humphries, Nicolas E et al. (2010). 'Environmental context explains Lévy and Brownian movement patterns of marine predators.' In: *Nature* 465.7301, pp. 1066–1069. ISSN: 0028-0836. DOI: [10.1038/nature09116](https://doi.org/10.1038/nature09116). URL: <http://dx.doi.org/10.1038/nature09116>.
- Jaud, Thomas et al. (2012). 'Relationship between Chlorophyll a Concentration, Light Attenuation and Diving Depth of the Southern Elephant Seal *Mirounga leonina*'. In: *PLoS ONE* 7.10, e47444. ISSN: 1932-6203. DOI: [10.1371/journal.pone.0047444](https://doi.org/10.1371/journal.pone.0047444). URL: <http://dx.plos.org/10.1371/journal.pone.0047444>.
- Jena, B. (2016). 'Satellite remote sensing of the island mass effect on the Sub-Antarctic Kerguelen Plateau, Southern Ocean'. In: *Frontiers of Earth Science* 10(3), pp. 479–486.
- Johnson, Kenneth et al. (2009). 'Observing Biogeochemical Cycles at Global Scales with Profiling Floats and Gliders: Prospects for a Global Array'. In: *Oceanography* 22.3, pp. 216–225. ISSN: 10428275. DOI: [10.5670/oceanog.2009.81](https://doi.org/10.5670/oceanog.2009.81).
- Jonker, F. C. and M. N. Bester (1998). 'Seasonal movements and foraging areas of adult southern female elephant seals, *Mirounga leonina*, from Marion Island'. In: *Antarctic Science* 10.1, pp. 21–30. ISSN: 0954-1020. DOI: [10.1017/S0954102098000042](https://doi.org/10.1017/S0954102098000042).
- Kara, A. Birol (2003). 'Mixed layer depth variability over the global ocean'. In: *Journal of Geophysical Research* 108.C3, pp. 1–15. ISSN: 0148-0227. DOI: [10.1029/2000JC000736](https://doi.org/10.1029/2000JC000736).
- Kara, a. Birol, Peter a. Rochford and Harley E. Hurlburt (2000). 'An optimal definition for ocean mixed layer depth'. In: *Journal of Geophysical Research* 105.C7, p. 16803. ISSN: 0148-0227. DOI: [10.1029/2000JC900072](https://doi.org/10.1029/2000JC900072).
- Kareiva, Peter and Garrett Odell (1987). 'Swarms of Predators Exhibit "Preytaxis" if Individual Predators Use Area-Restricted Search'. In: *The American Naturalist* 130.2, p. 233. ISSN: 0003-0147. DOI: [10.1086/284707](https://doi.org/10.1086/284707).
- Karsten, Richard H. and John Marshall (2002). 'Constructing the Residual Circulation of the ACC from Observations'. In: *Journal of Physical Oceanography* 32.1951,

- pp. 3315–3327. ISSN: 0022-3670. DOI: [10.1175/1520-0485\(2002\)032<3315:CTRCOT>2.0.CO;2](https://doi.org/10.1175/1520-0485(2002)032<3315:CTRCOT>2.0.CO;2).
- Kemp, Alan E S and Tracy A. Villareal (2013). 'High diatom production and export in stratified waters - A potential negative feedback to global warming'. In: *Progress in Oceanography* 119, pp. 4–23. ISSN: 00796611. DOI: [10.1016/j.pocean.2013.06.004](https://doi.org/10.1016/j.pocean.2013.06.004). URL: <http://linkinghub.elsevier.com/retrieve/pii/S0079661113000852>.
- Kidson, J. W. and M. R. Sinclair (1995). 'The influences of persistent anomalies on Southern Hemisphere storm tracks'. In: *Journal of Climate* 8.8, pp. 1938–1950. ISSN: 08948755. DOI: [10.1175/1520-0442\(1995\)008<1938:TIOPA0>2.0.CO;2](https://doi.org/10.1175/1520-0442(1995)008<1938:TIOPA0>2.0.CO;2).
- King, J. C and J.: Turner (1997). *Antarctic meteorology and climatology*, p. 9701264. ISBN: 9780521465601. DOI: [10.1029/98E000122](https://doi.org/10.1029/98E000122). URL: <http://adsabs.harvard.edu/abs/1997amc..book.....K>.
- King, Michael D. et al. (1992). 'Remote Sensing of Cloud, Aerosol, and Water Vapor Properties from the Moderate Resolution Imaging Spectrometer (MODIS)'. In: *IEEE Transactions on Geoscience and Remote Sensing* 30.1, pp. 2–27. ISSN: 15580644. DOI: [10.1109/36.124212](https://doi.org/10.1109/36.124212).
- King, Michael D. et al. (2003). 'Cloud and aerosol properties, precipitable water, and profiles of temperature and water vapor from MODIS'. In: *IEEE Transactions on Geoscience and Remote Sensing* 41.2 PART 1, pp. 442–456. ISSN: 01962892. DOI: [10.1109/TGRS.2002.808226](https://doi.org/10.1109/TGRS.2002.808226).
- King, Michael D. et al. (2013). 'Spatial and temporal distribution of clouds observed by MODIS onboard the terra and aqua satellites'. In: *IEEE Transactions on Geoscience and Remote Sensing* 51.7, pp. 3826–3852. ISSN: 01962892. DOI: [10.1109/TGRS.2012.2227333](https://doi.org/10.1109/TGRS.2012.2227333).
- Kirk, John T.O. (1994). 'Estimation of the absorption and the scattering coefficients of natural waters by use of underwater irradiance measurements.' In: *Applied optics* 33.15, pp. 3276–3278. ISSN: 0003-6935. DOI: [10.1364/AO.33.003276](https://doi.org/10.1364/AO.33.003276).
- Knell, Andrew S. and Edward A. Codling (2012). 'Classifying area-restricted search (ARS) using a partial sum approach'. In: *Theoretical Ecology* 5.3, pp. 325–339. ISSN: 18741738. DOI: [10.1007/s12080-011-0130-4](https://doi.org/10.1007/s12080-011-0130-4).
- Korhonen, Hannele et al. (2010). 'Aerosol climate feedback due to decadal increases in southern hemisphere wind speeds'. In: *Geophysical Research Letters* 37.2. ISSN: 19448007. DOI: [10.1029/2009GL041320](https://doi.org/10.1029/2009GL041320).

- Krause, G H and E Weis (1991). 'Chlorophyll Fluorescence and Photosynthesis: The Basics'. In: *Annual Review of Plant Physiology and Plant Molecular Biology* 42.1, pp. 313–349. ISSN: 1040-2519. DOI: [10.1146/annurev.pp.42.060191.001525](https://doi.org/10.1146/annurev.pp.42.060191.001525).
- Kropuenske, Lindsey R. et al. (2009). 'Photophysiology in two major Southern Ocean phytoplankton taxa: Photoprotection in *Phaeocystis antarctica* and *Fragilariopsis cylindrus*'. In: *Limnology and Oceanography* 54.4, pp. 1176–1196. ISSN: 00243590. DOI: [10.4319/lo.2009.54.4.1176](https://doi.org/10.4319/lo.2009.54.4.1176). URL: http://www.aslo.org/lo/toc/vol{_}54/issue{_}4/1176.html.
- Kropuenske, Lindsey R. et al. (2010). 'Strategies and rates of photoacclimation in two major southern ocean phytoplankton taxa: *Phaeocystis Antarctica* (haptophyta) and *Fragilariopsis Cylindrus* (bacillariophyceae)'. In: *Journal of Phycology* 46.6, pp. 1138–1151. ISSN: 00223646. DOI: [10.1111/j.1529-8817.2010.00922.x](https://doi.org/10.1111/j.1529-8817.2010.00922.x). URL: <http://doi.wiley.com/10.1111/j.1529-8817.2010.00922.x>.
- Lavigne, H. et al. (2012). 'Towards a merged satellite and in situ fluorescence ocean chlorophyll product'. In: *Biogeosciences* 9.6, pp. 2111–2125. ISSN: 17264170. DOI: [10.5194/bg-9-2111-2012](https://doi.org/10.5194/bg-9-2111-2012).
- Lavigne, H. et al. (2015). 'On the vertical distribution of the chlorophyll a concentration in the Mediterranean Sea: A basin-scale and seasonal approach'. In: *Biogeosciences* 12.16, pp. 5021–5039. ISSN: 17264189. DOI: [10.5194/bg-12-5021-2015](https://doi.org/10.5194/bg-12-5021-2015).
- Le Boeuf, B J et al. (1988). 'Continuous, Deep Diving in Female Northern Elephant Seals, *Mirounga angustirostris*'. In: *Canadian Journal of Zoology* 66, pp. 446–458. ISSN: 0008-4301. DOI: [10.1139/z88-064](https://doi.org/10.1139/z88-064). URL: <http://www.nrcresearchpress.com/doi/abs/10.1139/z88-064>.
- Le Boeuf, B.J. and R.M. Laws (1994). 'Elephant seals: An introduction to the genus'. In: *Elephant Seals: Population Ecology, Behavior, and Physiology*, pp. 1–26. DOI: <http://ark.cdlib.org/ark:/13030/ft7b69p131/>.
- LeBoeuf, B.J. et al. (2000). 'Foraging ecology of northern elephant seals'. In: *Ecological Monographs* 70.3, pp. 353–382.
- Lee, ZhongPing P. et al. (2005). 'Penetration of solar radiation in the upper ocean: A numerical model for oceanic and coastal waters'. In: *Journal of Geophysical Research C: Oceans* 110.9, pp. 1–12. ISSN: 01480227. DOI: [10.1029/2004JC002780](https://doi.org/10.1029/2004JC002780).
- Lee, ZhongPing P. et al. (2007). 'Euphotic zone depth: Its derivation and implication to ocean-color remote sensing'. In: *Journal of Geophysical Research: Oceans* 112.3,

- p. C03009. ISSN: 21699291. DOI: [10.1029/2006JC003802](https://doi.org/10.1029/2006JC003802). URL: <http://doi.wiley.com/10.1029/2006JC003802>.
- Lee, Zhongping et al. (2014). 'Usable solar radiation and its attenuation in the upper water column'. In: *Journal of Geophysical Research: Oceans* 119.2, pp. 1488–1497. ISSN: 21699291. DOI: [10.1002/2013JC009507](https://doi.org/10.1002/2013JC009507).
- Lenton, A. and R. J. Matear (2007). 'Role of the southern annular mode (SAM) in Southern Ocean CO₂ uptake'. In: *Global Biogeochemical Cycles* 21(2).
- Levitus, Sydney (1983). 'Climatological Atlas of the World Ocean'. In: *Eos, Transactions American Geophysical Union* 64.49, p. 962. ISSN: 0096-3941. DOI: [10.1029/E0064i049p00962-02](https://doi.org/10.1029/E0064i049p00962-02). URL: <http://doi.wiley.com/10.1029/E0064i049p00962-02>.
- Lewis, Marlon R et al. (1990). 'Influence of penetrating solar radiation on the heat budget of the equatorial Pacific Ocean'. In: *Nature* 347, pp. 543–545.
- Ling, John K. (2012). 'The skin and hair of the southern elephant seal, *Mirounga leonina* (Linn.). IV. Annual cycle of pelage follicle activity and moult'. In: *Australian Journal of Zoology* 60.4, pp. 259–271. ISSN: 0004959X. DOI: [10.1071/Z012049](https://doi.org/10.1071/Z012049).
- Logan, BA, B Demmig-Adams and Adams WW III (2014). 'Context quantification and measurement guide for non photochemical quenching of chlorophyll fluorescence'. In: *Non-photochemical quenching and energy dissipation in plant, algae and cyanobacteria. Advances in photosynthesis and respiration*, pp. 187–201.
- Longhurst, Alan R (2006). *Role of the marine biosphere in the Global Carbon Cycle*. DOI: [10.4319/lo.1991.36.8.1507](https://doi.org/10.4319/lo.1991.36.8.1507). URL: [papers2://publication/uuid/587A5D5D-784D-40B4-9B07-F0225CFA5F5B\\$\\backslash\\$http://faculty.washington.edu/jkeister/Zooplankton{_}course/Longhurst{_}{_}91.pdf](papers2://publication/uuid/587A5D5D-784D-40B4-9B07-F0225CFA5F5B$\\backslash$http://faculty.washington.edu/jkeister/Zooplankton{_}course/Longhurst{_}{_}91.pdf).
- Lorenzen, Carl J (1966). 'A method for the continuous measurement of in vivo chlorophyll concentration'. In: *Deep sea research* 13, pp. 223–227. ISSN: 00117471. DOI: [10.1016/0011-7471\(66\)91102-8](https://doi.org/10.1016/0011-7471(66)91102-8). URL: http://www.whoi.edu/cms/files/Lorenzen{_}1966{_}DSR{_}1-s2.0-0011747166911028-main{_}180924.pdf.
- Lovenduski, Nicole S. and Nicolas Gruber (2005). 'Impact of the Southern Annular Mode on Southern Ocean circulation and biology'. In: *Geophysical Research Letters* 32.11, pp. 1–4. ISSN: 00948276. DOI: [10.1029/2005GL022727](https://doi.org/10.1029/2005GL022727). URL: <http://doi.wiley.com/10.1029/2005GL022727>.
- Lovenduski, Nicole Suzanne (2007). 'Impact of the Southern Annular Mode on Southern Ocean Circulation and Biogeochemistry by'. In:

- MacArthur, R H and E R Planka (1966). 'On optimal use of a patchy environment'. In: *The American Naturalist* 100.96, pp. 603–609.
- Macías, Diego, Adolf Stips and Elisa Garcia-Gorriz (2014). 'The relevance of deep chlorophyll maximum in the open Mediterranean Sea evaluated through 3D hydrodynamic-biogeochemical coupled simulations'. In: *Ecological Modelling* 281, pp. 26–37. ISSN: 03043800. DOI: [10.1016/j.ecolmodel.2014.03.002](https://doi.org/10.1016/j.ecolmodel.2014.03.002).
- Marrari, Marina, Chuanmin Hu and Kendra Daly (2006). 'Validation of SeaWiFS chlorophyll a concentrations in the Southern Ocean: A revisit'. In: *Remote Sensing of Environment* 105.4, pp. 367–375. ISSN: 00344257. DOI: [10.1016/j.rse.2006.07.008](https://doi.org/10.1016/j.rse.2006.07.008).
- Marshall, Gareth J. (2003). 'Trends in the Southern Annular Mode from observations and reanalyses'. In: *Journal of Climate* 16.24, pp. 4134–4143. ISSN: 08948755. DOI: [10.1175/1520-0442\(2003\)016<4134:TITSAM>2.0.CO;2](https://doi.org/10.1175/1520-0442(2003)016<4134:TITSAM>2.0.CO;2).
- Martin, Johannie et al. (2010). 'Prevalence, structure and properties of subsurface chlorophyll maxima in Canadian Arctic waters'. In: *Marine Ecology Progress Series* 412, pp. 69–84. ISSN: 01718630. DOI: [10.3354/meps08666](https://doi.org/10.3354/meps08666).
- Martinez, Elodie et al. (2009). 'Climate-driven basin-scale decadal oscillations of oceanic phytoplankton.' In: *Science (New York, N.Y.)* 326.5957, pp. 1253–1256. ISSN: 0036-8075. DOI: [10.1126/science.1177012](https://doi.org/10.1126/science.1177012).
- Maxwell, Sara M. et al. (2012). 'Benthic foraging on seamounts: A specialized foraging behavior in a deep-diving pinniped'. In: *Marine Mammal Science* 28.3. ISSN: 08240469. DOI: [10.1111/j.1748-7692.2011.00527.x](https://doi.org/10.1111/j.1748-7692.2011.00527.x).
- May, Christine L. et al. (2003). 'Effects of spatial and temporal variability of turbidity on phytoplankton blooms'. In: *Marine Ecology Progress Series* 254, pp. 111–128. ISSN: 01718630. DOI: [10.3354/meps254111](https://doi.org/10.3354/meps254111).
- McCann, T.S. (1980). 'Population structure and social organization of southern elephant seals, *Mirounga leonina* (L.)' In: *Biological Journal of the Linnean Society* 14(1), pp. 133–150.
- McClain, Charles R (2009). 'A decade of satellite ocean color observations.' In: *Annual review of marine science* 1, pp. 19–42. ISSN: 1941-1405. DOI: [10.1146/annurev.marine.010908.163650](https://doi.org/10.1146/annurev.marine.010908.163650).
- McClain, Charles R. et al. (2006). 'Satellite data for ocean biology, biogeochemistry, and climate research'. In: *Eos, Transactions American Geophysical Union* 87.34, pp. 337–343. ISSN: 2324-9250. DOI: [10.1029/2006E0340002](https://doi.org/10.1029/2006E0340002).

- McConnell, B J, C Chambers and M A Fedak (1992). 'Foraging Ecology of Southern Elephant Seals in Relation to the Bathymetry and Productivity of the Southern Ocean'. In: *Antarctic Science* 4.4, pp. 393–398. ISSN: 0954-1020. DOI: [10.1017/S0954102092000580](https://doi.org/10.1017/S0954102092000580). URL: GotoISI://A1992KA15500005.
- McConnell, Bernie et al. (2002). 'Movements and foraging areas of naive, recently weaned southern elephant seal pups'. In: *Journal of Animal Ecology* 71.1, pp. 65–78. ISSN: 0021-8790. DOI: [10.1046/j.0021-8790.2001.00576.x](https://doi.org/10.1046/j.0021-8790.2001.00576.x). URL: <http://doi.wiley.com/10.1046/j.0021-8790.2001.00576.x>.
- McCoy, D. T. et al. (2015). 'Natural aerosols explain seasonal and spatial patterns of Southern Ocean cloud albedo'. In: *Science Advances* 1, e1500157. ISSN: 2375-2548. DOI: [10.1126/sciadv.1500157](https://doi.org/10.1126/sciadv.1500157). URL: <http://advances.sciencemag.org/content/1/6/e1500157.abstract>.
- McIntyre T. de Bruyn P.J.N., Ansorge I.J. Bester M.N. Bornemann H. Plotz J. and Tosh C.A. (2010). 'A lifetime at depth: vertical distribution of southern elephant seals in the water column'. In: *Polar biology* 33(8), 1037–1048.
- McMahon C.R., Burton H.R. and M.N. Bester (2000). 'Weaning mass and the future survival of juvenile southern elephant seals, *Mirounga leonina*, at Macquarie Island'. In: *Antarctic Science* 12(02), pp. 149–153.
- McMahon, Clive R. et al. (2005). *Population status, trends and a re-examination of the hypotheses explaining the recent declines of the southern elephant seal *Mirounga leonina**. DOI: [10.1111/j.1365-2907.2005.00055.x](https://doi.org/10.1111/j.1365-2907.2005.00055.x).
- Mckitrick, Ross (1999). 'The mann et al. northern hemisphere ?hockey stick? climate index a t'. In: *Hemisphere*, pp. 20–48.
- Mellard, Jarad P. et al. (2011). 'The vertical distribution of phytoplankton in stratified water columns'. In: *Journal of Theoretical Biology* 269.1, pp. 16–30. ISSN: 00225193. DOI: [10.1016/j.jtbi.2010.09.041](https://doi.org/10.1016/j.jtbi.2010.09.041).
- Mengesha, Semeneh et al. (1998). 'Seasonal variation of phytoplankton community structure and nitrogen uptake regime in the Indian Sector of the Southern Ocean'. In: *Polar Biology* 20.4, pp. 259–272. ISSN: 07224060. DOI: [10.1007/s003000050302](https://doi.org/10.1007/s003000050302).
- Mesnil, Benoit and Pierre Petitgas (2009). 'Detection of changes in time-series of indicators using CUSUM control charts'. In: *Aquatic Living Resources* 22, pp. 187–192. ISSN: 0990-7440. DOI: [10.1051/alr/2008058](https://doi.org/10.1051/alr/2008058).

- Meyer, Amelie et al. (2015). 'Mixing Variability in the Southern Ocean'. In: *Journal of Physical Oceanography* 45.4, pp. 966–987. ISSN: 0022-3670. DOI: [10.1175/JPO-D-14-0110.1](https://doi.org/10.1175/JPO-D-14-0110.1). URL: <http://dx.doi.org/10.1175/JPO-D-14-0110.1>.
- Mignot, A. et al. (2011). 'From the shape of the vertical profile of in vivo fluorescence to Chlorophyll-a concentration'. In: *Biogeosciences* 8.8, pp. 2391–2406. ISSN: 17264170. DOI: [10.5194/bg-8-2391-2011](https://doi.org/10.5194/bg-8-2391-2011).
- Mikaloff Fletcher SE, Gruber N, Jacobson AR, Gloor M, Doney SC, Dutkiewicz S, Gerber M, Follows M, Joos F, Lindsay K, Menemenlis D. (2006). 'Inverse estimates of anthropogenic CO₂ uptake, transport, and storage by the ocean'. In: *Global Biogeochemical Cycles* 20.2.
- Mikaloff Fletcher, S. E. et al. (2007). 'Inverse estimates of the oceanic sources and sinks of natural CO₂ and the implied oceanic carbon transport'. In: *Global Biogeochemical Cycles* 21.1. ISSN: 08866236. DOI: [10.1029/2006GB002751](https://doi.org/10.1029/2006GB002751).
- Miller, J R (1976). 'The salinity effect in a mixed layer ocean model'. In: *J. Phys. Oceanogr.* 6, pp. 29–35.
- Milligan, Allen J., Uriel A. Aparicio and Michael J. Behrenfeld (2012). 'Fluorescence and nonphotochemical quenching responses to simulated vertical mixing in the marine diatom *Thalassiosira weissflogii*'. In: *Marine Ecology Progress Series* 448, pp. 67–78. ISSN: 01718630. DOI: [10.3354/meps09544](https://doi.org/10.3354/meps09544). URL: <http://www.int-res.com/abstracts/meps/v448/p67-78/>.
- Monterey, G. I. and Sydney Levitus (1997). *Climatological cycle of mixed layer depth in the world ocean*. NOAA Atlas NESDIS 14.
- Moore T. S., Dowell M. D. and B. A. Franz (2012). 'Detection of coccolithophore blooms in ocean colour satellite imagery: A generalized approach for use with multiple sensors'. In: *Remote Sensing of Environment* 117, pp. 249–263.
- Morel, A and B Gentili (2004). 'Radiation transport within oceanic (case 1) water'. In: *Journal Of Geophysical Research-Oceans* 109.C6, art. no.–C6008. URL: [GotoISI: ://000221954900007](https://doi.org/10.1029/2000JC00007).
- Morel, Anclré and Louis Prieur (1977). 'Analysis of variations in ocean color'. In: *Limnology and Oceanography* 22.4, pp. 709–722. ISSN: 1939-5590. DOI: [10.4319/lo.1977.22.4.0709](https://doi.org/10.4319/lo.1977.22.4.0709). URL: <http://dx.doi.org/10.4319/lo.1977.22.4.0709>.
- Morel, André (1988). 'Optical modeling of the upper ocean in relation to its biogenous matter content (case I waters)'. In: *Journal of Geophysical Research* 93.8, p. 10749. ISSN: 0148-0227. DOI: [10.1029/JC093iC09p10749](https://doi.org/10.1029/JC093iC09p10749).

- Morel, Andre (2009). 'Are the empirical relationships describing the bio-optical properties of case 1 waters consistent and internally compatible?' In: *Journal of Geophysical Research: Oceans* 114.1, pp. 1–15. ISSN: 21699291. DOI: [10.1029/2008JC004803](https://doi.org/10.1029/2008JC004803).
- Morel, André and Jean-Francois Berthon (1989). 'Surface pigments, algal biomass profiles, and potential production of the euphotic layer: Relationships reinvestigated in view of remote-sensing applications'. In: *Limnology and Oceanography* 34.8, pp. 1545–1562. ISSN: 00243590. DOI: [10.4319/lo.1989.34.8.1545](https://doi.org/10.4319/lo.1989.34.8.1545). URL: <http://doi.wiley.com/10.4319/lo.1989.34.8.1545>.
- Morel, André et al. (2007). 'Optical properties of the ??clearest?? natural waters'. In: *Limnology and Oceanography* 52.1, pp. 217–229. ISSN: 0003-6935. DOI: [10.4319/lo.2007.52.1.0217](https://doi.org/10.4319/lo.2007.52.1.0217).
- Müller, P, X P Li and K K Niyogi (2001). 'Non-photochemical quenching. A response to excess light energy.' In: *Plant physiology* 125.4, pp. 1558–1566. ISSN: 0032-0889. DOI: [10.1104/pp.125.4.1558](https://doi.org/10.1104/pp.125.4.1558).
- Murnane, R. J., J. L. Sarmiento and C. Le Quere (1999). 'Spatial distribution of air-sea CO₂ fluxes and the interhemispheric transport of carbon by the oceans'. In: *Global Biogeochemical Cycles* 13.2, pp. 287–305. ISSN: 19449224. DOI: [10.1029/1998GB900009](https://doi.org/10.1029/1998GB900009).
- Nan, Sulan and Jianping Li (2003). 'The relationship between the summer precipitation in the Yangtze River valley and the boreal spring Southern Hemisphere annular mode'. In: *Geophysical Research Letters* 30.24, pp. 1–4. ISSN: 0094-8276. DOI: [10.1029/2003GL018381](https://doi.org/10.1029/2003GL018381).
- Nowlin, W. D. and J. M. Klinck (1986). 'The Physics of the Antarctic Circumpolar Current'. In: *Reviews of Geophysics* 24.3, p. 469. ISSN: 8755-1209. DOI: [10.1029/RG024i003p00469](https://doi.org/10.1029/RG024i003p00469). URL: <http://www.agu.org/pubs/crossref/1986/RG024i003p00469.shtml>.
- O'Reilly, John E. et al. (1998). 'Ocean color chlorophyll algorithms for SeaWiFS'. In: *Journal of Geophysical Research* 103.C11, p. 24937. ISSN: 0148-0227. DOI: [10.1029/98JC02160](https://doi.org/10.1029/98JC02160).
- Oke, Peter R. and Matthew H. England (2004). 'Oceanic response to changes in the latitude of the Southern Hemisphere subpolar westerly winds'. In: *Journal of Climate* 17.5, pp. 1040–1054. ISSN: 08948755. DOI: [10.1175/1520-0442\(2004\)017<1040:ORTCIT>2.0.CO;2](https://doi.org/10.1175/1520-0442(2004)017<1040:ORTCIT>2.0.CO;2).

- Olbers, Dirk et al. (2004). 'The dynamical balance, transport and circulation of the Antarctic Circumpolar Current'. In: *Antarctic Science* 16.4, pp. 439–470. ISSN: 0954-1020. DOI: [10.1017/S0954102004002251](https://doi.org/10.1017/S0954102004002251).
- Palmer, Molly a. et al. (2013). 'Light and nutrient control of photosynthesis in natural phytoplankton populations from the Chukchi and Beaufort seas, Arctic Ocean'. In: *Limnology and Oceanography* 58.6, pp. 2185–2205. ISSN: 00243590. DOI: [10.4319/lo.2013.58.6.2185](https://doi.org/10.4319/lo.2013.58.6.2185). URL: http://apps.webofknowledge.com.ez.statsbiblioteket.dk:2048/full{_}record.do?product=WOS{\&}search{_}mode=GeneralSearch{\&}qid=1{\&}SID=Y1KFfwkPxvzIgyKKUZx{\&}page=1{\&}doc=9{\&}cacheurlFromRightClick=no.
- Photopoulou T., Lovell P. Fedak M. A. Thomas L. and J. Matthiopoulos (2015). 'Efficient abstracting of dive profiles using a broken?stick model'. In: *Methods in Ecology and Evolution* 6(3), pp. 278–288. DOI: [10.1111/2041-210X.12328](https://doi.org/10.1111/2041-210X.12328).
- Photopoulou, Theoni et al. (2015). 'Efficient abstracting of dive profiles using a broken-stick model'. In: *Methods in Ecology and Evolution* 6.3, pp. 278–288. ISSN: 2041210X. DOI: [10.1111/2041-210X.12328](https://doi.org/10.1111/2041-210X.12328).
- Pinaud, David and Henri Weimerskirch (2007). 'At-sea distribution and scale-dependent foraging behaviour of petrels and albatrosses: A comparative study'. In: *Journal of Animal Ecology* 76.1, pp. 9–19. ISSN: 00218790. DOI: [10.1111/j.1365-2656.2006.01186.x](https://doi.org/10.1111/j.1365-2656.2006.01186.x).
- Pollard, R. T., M. I. Lucas and J. F. Read (2002). 'Physical controls on biogeochemical zonation in the Southern Ocean'. In: *Deep-Sea Research Part II: Topical Studies in Oceanography* 49.16, pp. 3289–3305. ISSN: 09670645. DOI: [10.1016/S0967-0645\(02\)00084-X](https://doi.org/10.1016/S0967-0645(02)00084-X).
- Pollard, R. T. and J. F. Read (2001). 'Circulation pathways and transports of the Southern Ocean in the vicinity of the Southwest Indian Ridge'. In: *Journal of Geophysical Research* 106.C2, pp. 2881–2898. ISSN: 0148-0227. DOI: [10.1029/2000JC900090](https://doi.org/10.1029/2000JC900090). URL: <http://doi.wiley.com/10.1029/2000JC900090>.
- Quéguiner, Bernard (2013). 'Iron fertilization and the structure of planktonic communities in high nutrient regions of the Southern Ocean'. In: *Deep-Sea Research Part II: Topical Studies in Oceanography* 90, pp. 43–54. ISSN: 09670645. DOI: [10.1016/j.dsr2.2012.07.024](https://doi.org/10.1016/j.dsr2.2012.07.024).

- Rasmus, K.E., W. Granéli and S.-Å. Wängberg (2004). 'Optical studies in the Southern Ocean'. In: *Deep Sea Research Part II: Topical Studies in Oceanography* 51.22-24, pp. 2583–2597. ISSN: 09670645. DOI: [10.1016/j.dsr2.2001.01.004](https://doi.org/10.1016/j.dsr2.2001.01.004).
- Reason, C. J C and M. Rouault (2005). 'Links between the Antarctic Oscillation and winter rainfall over western South Africa'. In: *Geophysical Research Letters* 32.7, pp. 1–4. ISSN: 00948276. DOI: [10.1029/2005GL022419](https://doi.org/10.1029/2005GL022419).
- Richardson, Anthony J and David S Schoeman (2004). 'Climate impact on plankton ecosystems in the Northeast Atlantic.' In: *Science (New York, N.Y.)* 305.5690, pp. 1609–12. ISSN: 1095-9203. DOI: [10.1126/science.1100958](https://doi.org/10.1126/science.1100958). URL: <http://www.ncbi.nlm.nih.gov/pubmed/15361622>.
- Robinson, P. W. et al. (2007). 'A comparison of indirect measures of feeding behaviour based on ARGOS tracking data'. In: *Deep-Sea Research Part II: Topical Studies in Oceanography* 54.3-4, pp. 356–368. ISSN: 09670645. DOI: [10.1016/j.dsr2.2006.11.020](https://doi.org/10.1016/j.dsr2.2006.11.020).
- Robinson, P. W. et al. (2010). 'Measurements of foraging success in a highly pelagic marine predator, the northern elephant seal'. In: *Journal of Animal Ecology* 79.6, pp. 1146–1156. ISSN: 00218790. DOI: [10.1111/j.1365-2656.2010.01735.x](https://doi.org/10.1111/j.1365-2656.2010.01735.x).
- Rogers, Jeffery C. and Harry van Loon (1982). 'Spatial Variability of Sea Level Pressure and 500 mb Height Anomalies over the Southern Hemisphere'. In: *Monthly Weather Review* 110.10, pp. 1375–1392. ISSN: 0027-0644. DOI: [10.1175/1520-0493\(1982\)110<1375:SVOSLP>2.0.CO;2](https://doi.org/10.1175/1520-0493(1982)110<1375:SVOSLP>2.0.CO;2).
- Roquet, Fabien et al. (2014). 'A Southern Indian Ocean database of hydrographic profiles obtained with instrumented elephant seals.' In: *Scientific data* 1, p. 140028. ISSN: 2052-4463. DOI: [10.1038/sdata.2014.28](https://doi.org/10.1038/sdata.2014.28). URL: <http://www.nature.com/articles/sdata201428>.
- Ross, Robin M. et al. (2008). 'Palmer LTER: Patterns of distribution of five dominant zooplankton species in the epipelagic zone west of the Antarctic Peninsula, 1993-2004'. In: *Deep-Sea Research Part II: Topical Studies in Oceanography* 55.18-19, pp. 2086–2105. ISSN: 09670645. DOI: [10.1016/j.dsr2.2008.04.037](https://doi.org/10.1016/j.dsr2.2008.04.037).
- Ryther, John H and David W Menzel (2010). 'Light Adaptation by Marine Phytoplankton'. In: 4.4, pp. 492–497.
- S., Sokolov and Rintoul S.R. (2007). 'Multiple jets of the Antarctic circumpolar current south of Australia'. In: *Journal of Physical Oceanography* 37(5), 1394–1412.

- Sabine, Christopher L. et al. (2004). 'The Oceanic Sink for Anthropogenic CO₂'. In: *Science* 305.5682, pp. 367–371. ISSN: 0036-8075. DOI: [10.1126/science.1097403](https://doi.org/10.1126/science.1097403). arXiv: [9809069 \[gr-qc\]](https://arxiv.org/abs/gr-qc/9809069). URL: <http://arxiv.org/abs/gr-qc/9809069> <http://www.tandfonline.com/doi/abs/10.1080/01422419908228843> <http://www.sciencemag.org/cgi/doi/10.1126/science.1097403>.
- Sackmann, B. S., M. J. Perry and C. C. Eriksen (2008). 'Seaglider observations of variability in daytime fluorescence quenching of chlorophyll-a in Northeastern Pacific coastal waters'. In: *Biogeosciences Discussions* 5.4, pp. 2839–2865. ISSN: 1810-6285. DOI: [10.5194/bgd-5-2839-2008](https://doi.org/10.5194/bgd-5-2839-2008).
- Saijo D., Mitani Y. Abe T. Sasaki H. Goetsch C. Costa D. P. and K. Miyashita (2016). 'Linking mesopelagic prey abundance and distribution to the foraging behavior of a deep-diving predator, the northern elephant seal'. In: *Deep Sea Research Part II: Topical Studies in Oceanography*.
- Sallée, J. B., K. G. Speer and S. R. Rintoul (2010). 'Zonally asymmetric response of the Southern Ocean mixed-layer depth to the Southern Annular Mode'. In: *Nature Geoscience* 3.4, pp. 273–279. ISSN: 1752-0894. DOI: [10.1038/ngeo812](https://doi.org/10.1038/ngeo812). URL: <http://dx.doi.org/10.1038/ngeo812>.
- Sallée, J. B., K. Speer and R. Morrow (2008). 'Response of the antarctic circumpolar current to atmospheric variability'. In: *Journal of Climate* 21.12, pp. 3020–3039. ISSN: 08948755. DOI: [10.1175/2007JCLI1702.1](https://doi.org/10.1175/2007JCLI1702.1).
- Sallée, J. B. et al. (2013). 'Assessment of Southern Ocean mixed-layer depths in CMIP5 models: Historical bias and forcing response'. In: *Journal of Geophysical Research: Oceans* 118.4, pp. 1845–1862. ISSN: 21699291. DOI: [10.1002/jgrc.20157](https://doi.org/10.1002/jgrc.20157).
- Sallée, Jean Baptiste et al. (2015). 'Characterization of distinct bloom phenology regimes in the Southern Ocean'. In: *ICES Journal of Marine Science* 72.6, pp. 1985–1998. ISSN: 10959289. DOI: [10.1093/icesjms/fsv069](https://doi.org/10.1093/icesjms/fsv069). URL: <http://icesjms.oxfordjournals.org/lookup/doi/10.1093/icesjms/fsv069>.
- Sall J. B., Speer K. and R. Morrow (2008). 'Response of the Antarctic Circumpolar Current to atmospheric variability'. In: *Journal of Climate* 21(12), pp. 3020–3039.
- Sarmiento, Jorge L. et al. (1998). 'Simulated response of the ocean carbon cycle to anthropogenic climate warming'. In: *Nature* 393.6682, pp. 245–249. ISSN: 0028-0836. DOI: [10.1038/30455](https://doi.org/10.1038/30455). URL: papers2://publication/uuid/CEEFF4EC-05EC-4234-BB83-243FE1300035.

- Saulquin, Bertrand et al. (2013). 'Estimation of the diffuse attenuation coefficient KdPAR using MERIS and application to seabed habitat mapping'. In: *Remote Sensing of Environment* 128, pp. 224–233. ISSN: 00344257. DOI: [10.1016/j.rse.2012.10.002](https://doi.org/10.1016/j.rse.2012.10.002).
- Sergio, Fabrizio et al. (2008a). 'Top Predators as Conservation Tools: Ecological Rationale, Assumptions, and Efficacy'. In: *Annual Review of Ecology, Evolution, and Systematics* 39.1, pp. 1–19. ISSN: 1543-592X. DOI: [10.1146/annurev.ecolsys.39.110707.173545](https://doi.org/10.1146/annurev.ecolsys.39.110707.173545).
- (2008b). 'Top Predators as Conservation Tools: Ecological Rationale, Assumptions, and Efficacy'. In: *Annual Review of Ecology, Evolution, and Systematics* 39.1, pp. 1–19. ISSN: 1543-592X. DOI: [10.1146/annurev.ecolsys.39.110707.173545](https://doi.org/10.1146/annurev.ecolsys.39.110707.173545).
- Shang, Shaoling, Zhongping Lee and Guomei Wei (2011). 'Characterization of MODIS-derived euphotic zone depth: Results for the China Sea'. In: *Remote Sensing of Environment* 115.1, pp. 180–186. ISSN: 00344257. DOI: [10.1016/j.rse.2010.08.016](https://doi.org/10.1016/j.rse.2010.08.016). URL: <http://linkinghub.elsevier.com/retrieve/pii/S0034425710002567>.
- Shindell, Drew T. and Gavin A. Schmidt (2004). 'Southern Hemisphere climate response to ozone changes and greenhouse gas increases'. In: *Geophysical Research Letters* 31.18. ISSN: 00948276. DOI: [10.1029/2004GL020724](https://doi.org/10.1029/2004GL020724).
- Simmons, Samantha E. et al. (2007). 'Linking foraging behaviour of the northern elephant seal with oceanography and bathymetry at mesoscales'. In: *Marine Ecology Progress Series* 346, pp. 265–275. ISSN: 01718630. DOI: [10.3354/meps07014](https://doi.org/10.3354/meps07014).
- Sims, D.W. David W et al. (2008). 'Scaling laws of marine predator search behaviour'. In: *Nature* 451.7182, pp. 1098–102. ISSN: 1476-4687. DOI: [10.1038/nature06518](https://doi.org/10.1038/nature06518). URL: <http://www.ncbi.nlm.nih.gov/pubmed/18305542> \backslash\$ nhttp://www.nature.com/nature/journal/v451/n7182/abs/nature06518.html.
- Sleeman, Jai C. et al. (2010). 'To go or not to go with the flow: Environmental influences on whale shark movement patterns'. In: *Journal of Experimental Marine Biology and Ecology* 390.2, pp. 84–98. ISSN: 00220981. DOI: [10.1016/j.jembe.2010.05.009](https://doi.org/10.1016/j.jembe.2010.05.009).
- Sokolov, S. and S. R. Rintoul (2003). 'Subsurface structure of interannual temperature anomalies in the Australian sector of the Southern Ocean'. In: *Journal of Geophysical Research* 108.C9, p. 3285. ISSN: 0148-0227. DOI: [10.1029/2002JC001494](https://doi.org/10.1029/2002JC001494). URL: <http://www.agu.org/pubs/crossref/2003/2002JC001494.shtml>.

- Sokolov, Serguei and Stephen R. Rintoul (2009). 'Circumpolar structure and distribution of the antarctic circumpolar current fronts: 2. Variability and relationship to sea surface height'. In: *Journal of Geophysical Research: Oceans* 114.11, pp. 1–15. ISSN: 21699291. DOI: [10.1029/2008JC005248](https://doi.org/10.1029/2008JC005248).
- Son, S-W et al. (2008). 'The impact of stratospheric ozone recovery on the Southern Hemisphere westerly jet.' In: *Science (New York, N.Y.)* 320.5882, pp. 1486–1489. ISSN: 0036-8075. DOI: [10.1126/science.1155939](https://doi.org/10.1126/science.1155939).
- Soppa, M. A. et al. (2013). 'Satellite derived euphotic depth in the Southern Ocean: Implications for primary production modelling'. In: *Remote Sensing of Environment* 137, pp. 198–211. ISSN: 00344257. DOI: [10.1016/j.rse.2013.06.017](https://doi.org/10.1016/j.rse.2013.06.017). URL: <http://linkinghub.elsevier.com/retrieve/pii/S0034425713002101>.
- Steele, J H (1967). 'A study of production in the Gulf of Mexico'. In: *Journal of Marine Research* 22.3, pp. 211–223.
- Stevick, P. T., B. J. McConnell and P. S. Hammond (2002). 'Patterns of movement'. In: *Marine mammal biology: an evolutionary approach*. Vol. 101. 1-2, pp. 185–216. ISBN: 0632052325. URL: movementpatterns.pbworks.com/Patterns-of-Movement[//books.google.com/books?hl=es{\&}lr={\&}id=5{_}G608B-zTwC{\&}pgis=1](http://books.google.com/books?hl=es&lr=&id=5{_}G608B-zTwC{\&}pgis=1).
- Sturman, Andrew P. and N. J. Tapper (1996). 'The weather and climate of Australia and New Zealand'. In:
- Sverdrup, Hu (1953). 'On conditions for the vernal blooming of phytoplankton'. In: *Journal du Conseil* 18, pp. 287–295. ISSN: 15415856. DOI: [10.4319/lom.2007.5.269](https://doi.org/10.4319/lom.2007.5.269).
- Taylor, John R. and Raffaele Ferrari (2011). 'Shutdown of turbulent convection as a new criterion for the onset of spring phytoplankton blooms'. In: *Limnology and Oceanography* 56.6, pp. 2293–2307. ISSN: 00243590. DOI: [10.4319/lo.2011.56.6.2293](https://doi.org/10.4319/lo.2011.56.6.2293).
- Teo, Slh et al. (2009). 'Estimating chlorophyll profiles from electronic tags deployed on pelagic animals'. In: *Aquatic Biology* 5.May, pp. 195–207. ISSN: 1864-7782. DOI: [10.3354/ab00152](https://doi.org/10.3354/ab00152).
- Thompson, Andrew F and Kelvin J Richards (2011). 'Low frequency variability of Southern Ocean jets'. In: *Journal of Geophysical Research* 116.C9, pp. 1–17. ISSN: 0148-0227. DOI: [10.1029/2010JC006749](https://doi.org/10.1029/2010JC006749). URL: papers://137dc921-963a-4293-adcf-8602be5dd4d2/Paper/p7890<http://europa.agu.org/?view=article{\&}uri=/journals/jc/jc1109/2010JC006749/2010JC006749.xml{\&}t=2010JC006749>.

- Thompson, D W J and J M Wallace (2000). 'Annular Mode in the Extratropical Circulation. Part I : Month-to-Month Variability'. In: *Journal of Climate* 13,1999, pp. 1000–1016. DOI: [http://dx.doi.org/10.1175/1520-0442\(2000\)013<1000:AMITEC>2.0.CO;2](http://dx.doi.org/10.1175/1520-0442(2000)013<1000:AMITEC>2.0.CO;2). URL: <papers2://publication/uuid/9A9E1710-F09C-4477-B3E2-BB99F78E6CA4>.
- Thompson, D W J et al. (2011). 'Signatures of the Antarctic ozone hole in Southern Hemisphere surface climate change'. In: *Nature Geoscience* 4,11, pp. 741–749. ISSN: 1752-0894. DOI: [Doi10.1038/Ngeo1296](https://doi.org/10.1038/Ngeo1296). URL: [ISI:000296723500009](https://www.isinet.com/doi/10.1038/Ngeo1296).
- Thums, Michele, Corey J A Bradshaw and Mark A. Hindell (2011). 'In situ measures of foraging success and prey encounter reveal marine habitat-dependent search strategies'. In: *Ecology* 92,6, pp. 1258–1270. ISSN: 00129658. DOI: [10.1890/09-1299.1](https://doi.org/10.1890/09-1299.1).
- Timmermans, Klaas R. et al. (2001). 'Growth rates of large and small Southern Ocean diatoms in relation to availability of iron in natural seawater'. In: *Limnology and Oceanography* 46,2, pp. 260–266. ISSN: 00243590. DOI: [10.4319/lo.2001.46.2.0260](https://doi.org/10.4319/lo.2001.46.2.0260).
- Todd, Robert E., Daniel L. Rudnick and Russ E. Davis (2009). 'Monitoring the greater San Pedro Bay region using autonomous underwater gliders during fall of 2006'. In: *Journal of Geophysical Research: Oceans* 114,6, pp. 1–13. ISSN: 21699291. DOI: [10.1029/2008JC005086](https://doi.org/10.1029/2008JC005086).
- Toggweiler, J R and Joellen Russell (2008). 'Ocean circulation in a warming climate'. In: *Nature* 451,7176, pp. 286–288. ISSN: 0028-0836. DOI: [10.1038/nature06590](https://doi.org/10.1038/nature06590). URL: <http://dx.doi.org/10.1038/nature06590>.
- Toggweiler, J R and B Samuels (1993). 'New radiocarbon constraints on the upwelling of abyssal water to the ocean's surface'. In: *The Global Carbon Cycle I* 15, pp. 334–366.
- Tomczak M, Godfrey JS (1994). *Regional oceanography: an introduction*. ISBN: 0080410200. DOI: [10.1016/0278-4343\(95\)00021-6](https://doi.org/10.1016/0278-4343(95)00021-6). arXiv: [arXiv:1011.1669v3](https://arxiv.org/abs/1011.1669v3).
- Treguier, a. M. and J. C. McWilliams (1990). 'Topographic Influences on Wind-Driven, Stratified Flow in a β -Plane Channel: An Idealized Model for the Antarctic Circumpolar Current'. In: *Journal of Physical Oceanography* 20,3, pp. 321–343. ISSN: 0022-3670. DOI: [10.1175/1520-0485\(1990\)020<0321:TIOWDS>2.0.CO;2](https://doi.org/10.1175/1520-0485(1990)020<0321:TIOWDS>2.0.CO;2).
- Tremblay, Yann, Antony J Roberts and Daniel P Costa (2007). 'Fractal landscape method: an alternative approach to measuring area-restricted searching behavior.'

- In: *The Journal of experimental biology* 210.Pt 6, pp. 935–945. ISSN: 0022-0949. DOI: [10.1242/jeb.02710](https://doi.org/10.1242/jeb.02710).
- Tripathy, S. C. et al. (2015). 'Deep chlorophyll maximum and primary productivity in Indian Ocean sector of the Southern Ocean: Case study in the Subtropical and Polar Front during austral summer 2011'. In: *Deep-Sea Research Part II: Topical Studies in Oceanography* 118, pp. 240–249. ISSN: 09670645. DOI: [10.1016/j.dsr2.2015.01.004](https://doi.org/10.1016/j.dsr2.2015.01.004). URL: <http://www.sciencedirect.com/science/article/pii/S0967064515000053>.
- Turner, J and Gareth J Marshall (2011). 'Climate Change in the Polar Regions'. In: pp. 1–428.
- Turner, John et al. (2013). 'Antarctic climate change and the environment: an update'. In: *Polar Record* 50.3, pp. 1–23. ISSN: 0032-2474. DOI: [doi:10.1017/S0032247413000296](https://doi.org/10.1017/S0032247413000296). URL: http://journals.cambridge.org/abstract{_}S0032247413000296.
- Vacquie-Garcia, Jade et al. (2015). 'Delineation of the southern elephant seal's main foraging environments defined by temperature and light conditions'. In: *Deep-Sea Research Part II: Topical Studies in Oceanography* 113, pp. 145–153. ISSN: 09670645. DOI: [10.1016/j.dsr2.2014.10.029](https://doi.org/10.1016/j.dsr2.2014.10.029).
- Vargas, Colomban de (2015). 'Eukaryotic plankton diversity in the sunlit ocean'. In: *Science* 348.MAY, pp. 1–12. ISSN: 0717-6163. DOI: [10.1007/s13398-014-0173-7.2](https://doi.org/10.1007/s13398-014-0173-7.2). arXiv: [9809069v1](https://arxiv.org/abs/9809069v1) [arXiv:gr-qc].
- Venables, Hugh J., Andrew Clarke and Michael P. Meredith (2013). 'Wintertime controls on summer stratification and productivity at the western Antarctic Peninsula'. In: *Limnology and Oceanography* 58.3, pp. 1035–1047. ISSN: 00243590. DOI: [10.4319/lo.2013.58.3.1035](https://doi.org/10.4319/lo.2013.58.3.1035). URL: <http://doi.wiley.com/10.4319/lo.2013.58.3.1035>.
- W.D., Nowlin and Clifford M. (1982). 'The kinematic and thermohaline zonation of the Antarctic circumpolar current at drake passage'. In: *J. Mar. Res* 40, 481?50.
- Wang, Guojian and Wenju Cai (2013). 'Climate-change impact on the 20th-century relationship between the Southern Annular Mode and global mean temperature.' In: *Scientific reports* 3, p. 2039. ISSN: 2045-2322. DOI: [10.1038/srep02039](https://doi.org/10.1038/srep02039). URL: <http://www.pubmedcentral.nih.gov/articlerender.fcgi?artid=3687247{\&}tool=pmcentrez{\&}rendertype=abstract>.
- Watson, Andrew J., Geoffrey K. Vallis and Maxim Nikurashin (2015). 'Southern Ocean buoyancy forcing of ocean ventilation and glacial atmospheric CO₂'. In: *Nature*

- Geoscience* 8.11, pp. 861–864. ISSN: 1752-0894. DOI: [10.1038/ngeo2538](https://doi.org/10.1038/ngeo2538). URL: <http://www.nature.com.libezproxy.open.ac.uk/ngeo/journal/v8/n11/full/ngeo2538.html>.
- Watson, Andrew J et al. (2014). 'The Southern Ocean , carbon and climate The Southern Ocean , carbon and climate'. In: June.
- Watterson, I. G. (2000). 'Southern midlatitude zonal wind vacillation and its interaction with the ocean in GCM simulations'. In: *Journal of Climate* 13.3, pp. 562–578. ISSN: 08948755. DOI: [10.1175/1520-0442\(2000\)013<0562:SMZWVA>2.0.CO;2](https://doi.org/10.1175/1520-0442(2000)013<0562:SMZWVA>2.0.CO;2).
- Xing, X G et al. (2012). 'Quenching correction for in vivo chlorophyll fluorescence acquired by autonomous platforms: A case study with instrumented elephant seals in the Kerguelen region (Southern Ocean)'. In: *Limnology and Oceanography-Methods* 10, pp. 483–495. ISSN: 15415856. DOI: [10.4319/lom.2012.10.483](https://doi.org/10.4319/lom.2012.10.483). URL: [GotoISI://WOS:000307929300003](http://www.wos.org/000307929300003).
- Xing, Xiaogang et al. (2011). 'Combined processing and mutual interpretation of radiometry and fluorimetry from autonomous profiling Bio Argo floats: Chlorophyll a retrieval'. In: *Journal of Geophysical Research-Oceans* 116, p. C06020. ISSN: 0148-0227. DOI: [10.1029/2010JC006899](https://doi.org/10.1029/2010JC006899). URL: <http://dx.doi.org/10.1029/2010JC006899>.
- Yentsch, Charles S (1960). 'The influence of phytoplankton pigments on the colour of sea water'. In: *Deep Sea Research (1953)* 7.1, pp. 1–9. ISSN: 01466313. DOI: [10.1016/0146-6313\(60\)90002-2](https://doi.org/10.1016/0146-6313(60)90002-2). URL: <http://linkinghub.elsevier.com/retrieve/pii/0146631360900022>.
- Yoshiyama, Kohei et al. (2009). 'Phytoplankton competition for nutrients and light in a stratified water column.' In: *The American naturalist* 174.2, pp. 190–203. ISSN: 0003-0147. DOI: [10.1086/600113](https://doi.org/10.1086/600113).
- Zheng, Fei, Jianping Li and Ting Liu (2014). 'Some advances in studies of the climatic impacts of the southern hemisphere annular mode'. In: *Journal of Meteorological Research* 28.5, pp. 820–835. ISSN: 21980934. DOI: [10.1007/s13351-014-4079-2](https://doi.org/10.1007/s13351-014-4079-2).
- de Boyer Montégut, Clément et al. (2004). 'Mixed layer depth over the global ocean: An examination of profile data and a profile-based climatology'. In: *Journal of Geophysical Research C: Oceans* 109.12, pp. 1–20. ISSN: 01480227. DOI: [10.1029/2004JC002378](https://doi.org/10.1029/2004JC002378).

van Wijk EM, Riser S, Rintoul SR, Speer K, Klatt O, Boebel O, Owens B, Gascard JC, Freeland H, Wijffels S, Roemmich D (2009). *Observing High Latitudes : extending the core Argo array*. Tech. rep. August, p. 2009. DOI: [10.1029/2005GL023740](https://doi.org/10.1029/2005GL023740).Rintoul.

Candidate's declaration

I, Lauren Biermann, do hereby certify that this thesis, submitted for the degree of PhD, which is approximately 64,865 words in length, has been written by me, and that it is the record of work carried out by me, or principally by myself in collaboration with others as acknowledged, and that it has not been submitted in any previous application for any degree.

I was admitted as a research student at the University of St Andrews in June 2012.

I received funding from an organisation or institution and have acknowledged the funder(s) in the full text of my thesis.

06/06/2018

Date

Signature of candidate

Supervisor's declaration

I hereby certify that the candidate has fulfilled the conditions of the Resolution and Regulations appropriate for the degree of PhD in the University of St Andrews and that the candidate is qualified to submit this thesis in application for that degree.

06/06/2018

Date

Signature of supervisor

Permission for publication

In submitting this thesis to the University of St Andrews we understand that we are giving permission for it to be made available for use in accordance with the regulations of the University Library for the time being in force, subject to any copyright vested in the work not being affected thereby. We also understand, unless exempt by an award of an embargo as requested below, that the title and the abstract will be published, and that a copy of the work may be made and supplied to any bona fide library or research worker, that this thesis will be electronically accessible for personal or research use and that the library has the right to migrate this thesis into new electronic forms as required to ensure continued access to the thesis.

I, Lauren Biermann, confirm that my thesis does not contain any third-party material that requires copyright clearance.

The following is an agreed request by candidate and supervisor regarding the publication of this thesis:

Printed copy

No embargo on print copy.

Electronic copy

No embargo on electronic copy.

06/06/2018

Date

Signature of candidate

06/06/2018

Date

Signature of supervisor

Underpinning Research Data or Digital Outputs

Candidate's declaration

I, Lauren Biermann, hereby certify that no requirements to deposit original research data or digital outputs apply to this thesis and that, where appropriate, secondary data used have been referenced in the full text of my thesis.

06/06/2018

Date

Signature of candidate

DECLARATION

I declare that the contents of this thesis entitled *An assessment of MODIS products in the Southern Ocean using tagged southern elephant seals, in the context of an increasingly positive Southern Annular Mode* was undertaken and completed by myself, unless otherwise acknowledged and has not been submitted in support of an application for another degree or qualification in this or any other university or institution.

Scotland, February 2016

Lauren Biermann

COLOPHON

This document was typeset using the typographical look-and-feel `classicthesis` developed by André Miede. The style was inspired by Robert Bringhurst's seminal book on typography "*The Elements of Typographic Style*". `classicthesis` is available for both \LaTeX and \LyX :

<https://bitbucket.org/amiede/classicthesis/>

Happy users of `classicthesis` usually send a real postcard to the author, a collection of postcards received so far is featured here:

<http://postcards.miede.de/>

Final Version as of 18th May 2017 (`classicthesis` version 1).